frontiers | Research Topics

Future directions in novel laser source development: Dynamical properties, and beam manipulation

Edited by
Xing Fu, Tijmen Euser, Shu-Wei Huang, Nicolas Joly
and Shangran Xie

Published in
Frontiers in Physics

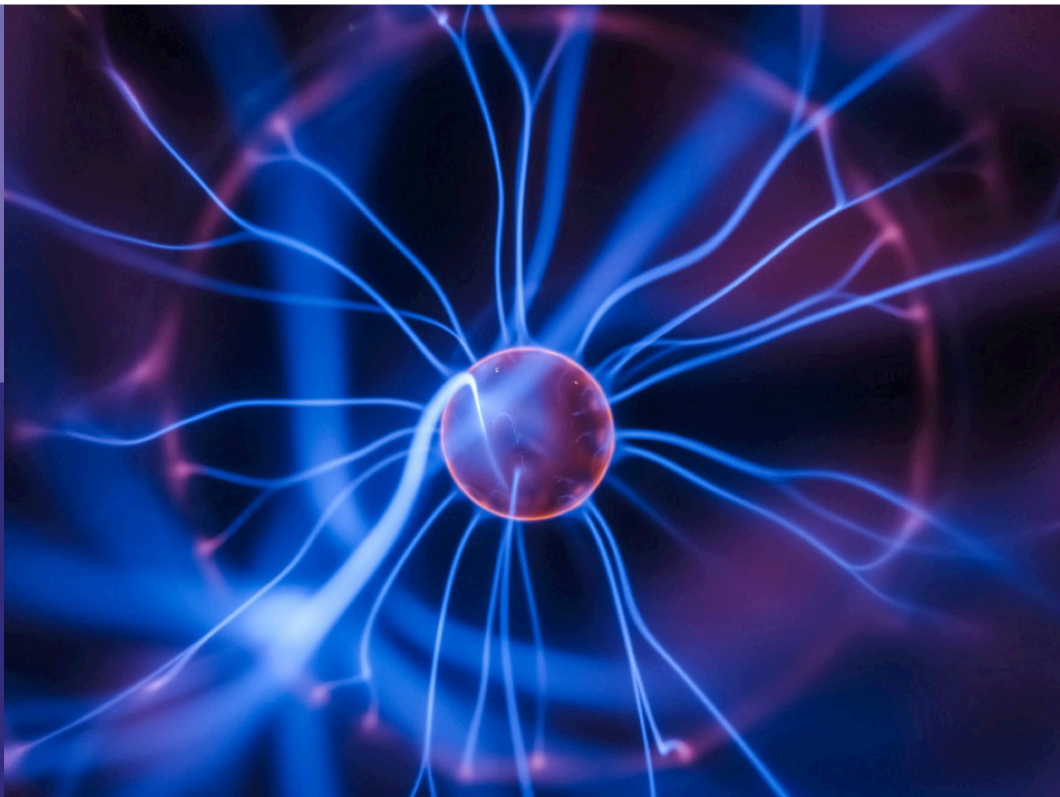

ISSN 1664-8714
ISBN 978-2-83250-937-1
DOI 10.3389/978-2-83250-937-1

About Frontiers

Frontiers is more than just an open access publisher of scholarly articles: it is a pioneering approach to the world of academia, radically improving the way scholarly research is managed. The grand vision of Frontiers is a world where all people have an equal opportunity to seek, share and generate knowledge. Frontiers provides immediate and permanent online open access to all its publications, but this alone is not enough to realize our grand goals.

Frontiers journal series

The Frontiers journal series is a multi-tier and interdisciplinary set of open-access, online journals, promising a paradigm shift from the current review, selection and dissemination processes in academic publishing. All Frontiers journals are driven by researchers for researchers; therefore, they constitute a service to the scholarly community. At the same time, the *Frontiers journal series* operates on a revolutionary invention, the tiered publishing system, initially addressing specific communities of scholars, and gradually climbing up to broader public understanding, thus serving the interests of the lay society, too.

Dedication to quality

Each Frontiers article is a landmark of the highest quality, thanks to genuinely collaborative interactions between authors and review editors, who include some of the world's best academicians. Research must be certified by peers before entering a stream of knowledge that may eventually reach the public - and shape society; therefore, Frontiers only applies the most rigorous and unbiased reviews. Frontiers revolutionizes research publishing by freely delivering the most outstanding research, evaluated with no bias from both the academic and social point of view. By applying the most advanced information technologies, Frontiers is catapulting scholarly publishing into a new generation.

What are Frontiers Research Topics?

Frontiers Research Topics are very popular trademarks of the *Frontiers journals series*: they are collections of at least ten articles, all centered on a particular subject. With their unique mix of varied contributions from Original Research to Review Articles, Frontiers Research Topics unify the most influential researchers, the latest key findings and historical advances in a hot research area.

Find out more on how to host your own Frontiers Research Topic or contribute to one as an author by contacting the Frontiers editorial office: frontiersin.org/about/contact

Future directions in novel laser source development: Dynamical properties, and beam manipulation

Topic editors
Xing Fu — Tsinghua University, China
Tijmen Euser — University of Cambridge, United Kingdom
Shu-Wei Huang — University of Colorado Boulder, United States
Nicolas Joly — University of Erlangen Nuremberg, Germany
Shangran Xie — Beijing Institute of Technology, China

Citation
Fu, X., Euser, T., Huang, S.-W., Joly, N., Xie, S., eds. (2022). *Future directions in novel laser source development: Dynamical properties, and beam manipulation*. Lausanne: Frontiers Media SA. doi: 10.3389/978-2-83250-937-1

Table of contents

frontiers | Frontiers in Physics

TYPE Editorial
PUBLISHED 18 November 2022
DOI 10.3389/fphy.2022.1052461

Check for updates

OPEN ACCESS

EDITED AND REVIEWED BY
Lorenzo Pavesi,
University of Trento, Italy

*CORRESPONDENCE
Xing Fu,
fuxing@tsinghua.edu.cn
Tijmen Euser,
te287@cam.ac.uk
Shu-Wei Huang,
ShuWei.Huang@colorado.edu
Nicolas Y. Joly,
nicolas.joly@fau.de
Shangran Xie,
sxie@bit.edu.cn

SPECIALTY SECTION
This article was submitted to Optics and Photonics,
a section of the journal
Frontiers in Physics

RECEIVED 24 September 2022
ACCEPTED 07 November 2022
PUBLISHED 18 November 2022

CITATION
Fu X, Euser T, Huang S-W, Joly NY and Xie S (2022), Editorial: Future directions in novel laser source development: Dynamical properties, and beam manipulation.
Front. Phys. 10:1052461.
doi: 10.3389/fphy.2022.1052461

Editorial: Future directions in novel laser source development: Dynamical properties, and beam manipulation

Xing Fu[1]*, Tijmen Euser[2]*, Shu-Wei Huang[3]*, Nicolas Y. Joly[4,5]* and Shangran Xie[6]*

[1]Department of Precision Instrument, Tsinghua University, Beijing, China, [2]Nanophotonics Centre, Department of Physics, Cavendish Laboratory, University of Cambridge, Cambridge, United Kingdom, [3]Department of Electrical, Computer, and Energy Engineering, University of Colorado Boulder, Boulder, CO, United States, [4]Friedrich-Alexander-Universität Erlangen-Nürnberg (FAU), Erlangen, Germany, [5]Max-Planck Institute for the Science of Light, Erlangen, Germany, [6]School of Optics and Photonics, Beijing Institute of Technology, Beijing, China

KEYWORDS

laser source, beam manipulation, laser application, laser dynamics, novel laser development

Editorial on the Research Topic
Future Directions in Novel Laser Source Development: Dynamical Properties, and Beam Manipulation

Lasers, which are ubiquitous in everyday life, have revolutionized the world in the fields of manufacturing, communication, metrology, sensing, display, directed energy, and others. Tremendous technological breakthroughs in laser sources have been reported to meet the ever-increasing demands for improved laser performance [1]. Today, new trends for laser development are emerging, including advanced laser sources with specially tailored attributes (such as spatial patterns, spectral properties, pulse shapes, wavelength coverage, etc.). A variety of laser applications has called for these new sources. As a result, remarkable progresses have been made in this direction over the past decades.

Complete characterization and control of laser outputs among multiple domains and degrees of freedom is the key for practical laser-matter interactions. In this context, better control over laser properties has a vast range of new laser application scenarios, such as: adapting spatial beam profiles to achieve super-resolution imaging of living cells [2], tailoring pulse shapes and wavelength range to generate optical frequency rulers with unprecedented precision [3], employing the angular momentum of laser beams to realize contactless and multi-dimensional motion control of nano-particles [4], to name a few. In addition, recent technological progress has created new paradigms, such as on-chip lasers and photonics [5], metasurface lasers [6], topological lasers [7], biological lasers [8], and air lasing [9], offering abundant dynamics and enabling applications to be explored. The goal of this Research Topic is to take a snapshot of the current frontier of dynamics and manipulation of novel laser sources. Furthermore, we aim to build connections between experts from different backgrounds to gather the current state-of-the-art and to ensure that researchers in distinct sub-areas can learn from each other's progress.

This Research Topic includes thirteen original research articles covering the laser sources, beam manipulation and applications. At the cutting edge of newly developed lasers, Wang et al. demonstrated the broadest tuning range of the femtosecond Cr:ZnSe/ZnS lasers, which may be applied to medical diagnostics and molecular spectroscopies. Zhang et al. reported the generation of the 335.5 nm wavelength laser based on a home-built resonant cavity, having a high-peak-power density up to 20.86 MW/cm^2. The source is ready for the generation of narrow-linewidth 167.75 nm vacuum ultraviolet (VUV) single-frequency continuous wave (CW) laser, towards angle-resolved photoemission spectroscopy (ARPES) with high energy resolution. Echarri et al. demonstrated results of photo-ionization experiments driven by a newly developed compact tunable diamond Raman laser. It exhibited comparable performance with commonly used Ti:sapphire lasers in terms of produced ion current. For developing near-infrared high energy laser source, Jiang et al. reported a nanosecond single-aperture Nd:YAG laser producing 10 J energy at the repetition rate of 50 Hz. In addition, Lei et al. introduced hybrid nanosecond laser oscillator and amplifier with gain crystal combination of Nd:YAG and Nd:LuAG, and analyzed the influence of overlapping gain spectra. To obtain multi-beam repetition-rated regenerative amplifiers with high performance, Gao et al. reported the detailed design method, and obtained eight-beam output with uniform energy and high energy stabilities (RMS of 0.3%–0.9%) over 2 hours.

Several authors presented their recent work on beam manipulation and propagation properties of laser beam. Wang et al. studied the distinct characteristics and properties of optical lattice patterns in transverse mode locking (TML) and non-TML states, which can be distinguished by intensity comparison, interferometry, and beat frequency spectrum. Zhang et al. explored the effect of thermal blooming induced by the propagation of higher-order laser mode from fiber array. They investigated the influence of beamlet arrangement on the energy focusability under thermal blooming. Liu et al. reported the propagation properties of a novel twisted Hermite-Gaussian correlated Schell-model beam, as a new type of partially coherent twisted beam. Then they discussed the enhancement on the self-reconstruction capability by the twist phase. Lu et al. studied the behavior of partially coherent beam in nonlinear media, indicating the threshold condition of coherence size related to the self-focusing phenomenon.

Finally, we should remember the famous statement from the early stages of lasers, which was considered a solution looking for a problem [10]. Applications of laser are numerous. For this Research Topic, Wen et al. showed that the advanced laser plasma shockwave cleaning enhanced the fabrication quality of black silicon, which is crucial for large-scale industrial preparation. Liu et al. proposed and verified an augmented reality holographic stereogram, by simultaneously rendering the obtained scene model and virtual scene. Peng et al. demonstrated the imaging through random scatter medium. They carried out the spatial coherence measurement, and reconstructed the image information with the help of iterative phase retrieval algorithm in the Fresnel domain.

In summary, this Research Topic collects a vast range of latest progresses on the novel laser source development, serving as a worth reading reference for the researchers in the related fields.

Author contributions

All authors listed have made a substantial, direct, and intellectual contribution to the work and approved it for publication.

Conflict of interest

The authors declare that the research was conducted in the absence of any commercial or financial relationships that could be construed as a potential conflict of interest.

Publisher's note

References

1. Hitz CB, Ewing JJ, Hecht J. *Introduction to laser technology*. John Wiley & Sons (2012).

2. Schermelleh L, Ferrand A, Huser T, Eggeling C, Sauer M, Biehlmaier O, et al. Super-resolution microscopy demystified. *Nat Cel Biol* (2019) 21:72–84. doi:10.1038/s41556-018-0251-8

3. Fortier T, Baumann E. 20 years of developments in optical frequency comb technology and applications. *Commun Phys* (2019) 2:1–16. doi:10.1038/s42005-019-0249-y

4. Shen Y, Wang X, Xie Z, Min C, Fu X, Liu Q, et al. Optical vortices 30 years on: OAM manipulation from topological charge to multiple singularities. *Light Sci Appl* (2019) 8:90. doi:10.1038/s41377-019-0194-2

5. Zhou Z, Yin B, Michel J. On-chip light sources for silicon photonics. *Light Sci Appl* (2015) 4:e358. doi:10.1038/lsa.2015.131

6. Sroor H, Huang YW, Sephton B, Naidoo D, Vallés A, Ginis V, et al. High-purity orbital angular momentum states from a visible metasurface laser. *Nat Photon* (2020) 14:498–503. doi:10.1038/s41566-020-0623-z

7. Bandres MA, Wittek S, Harari G, Parto M, Ren J, Segev M, et al. Topological insulator laser: Experiments. *Science* (2018) 359:eaar4005. doi:10.1126/science.aar4005

8. Chen YC, Fan X. Biological lasers for biomedical applications. *Adv Opt Mater* (2019) 7:1900377. doi:10.1002/adom.201900377

9. Polynkin P, Cheng Y. *Air lasing*. Springer International Publishing (2018).

10. Hecht J. A Short history of laser development. *Appl Opt* (2010) 49:F99–F122. doi:10.1117/1.3483597

ORIGINAL RESEARCH
published: 03 January 2022
doi: 10.3389/fphy.2021.807542

Self-Focusing Property of Partially Coherent Beam With Non-Uniform Correlation Structure in Non-Linear Media

Lu Lu[1†], Zhiqiang Wang[2,3†], Jiayi Yu[4], Chunhong Qiao[5], Rong Lin[4,6] and Yangjian Cai[4,7]*

[1]Jiangsu Key Lab of Opto-Electronic Technology, School of Physics and Technology, Nanjing Normal University, Nanjing, China, [2]National Astronomical Observatories/Nanjing Institute of Astronomical Optics and Technology, Chinese Academy of Sciences, Nanjing, China, [3]CAS Key Laboratory of Astronomical Optics and Technology, Nanjing Institute of Astronomical Optics and Technology, Nanjing, China, [4]Shandong Provincial Engineering and Technical Center of Light Manipulations & Shandong Provincial Key Laboratory of Optics and Photonic Device, School of Physics and Electronics, Shandong Normal University, Jinan, China, [5]Key Laboratory of Atmospheric Optics, Anhui Institute of Optics and Fine Mechanics, Chinese Academy of Sciences, Hefei, China, [6]College of Physics and Electronic Engineering, Heze University, Heze, China, [7]School of Physical Science and Technology, Soochow University, Suzhou, China

Coherence in a light beam has the potential to serve as a degree of freedom for manipulating the beam. In this work, the self-focusing property of a partially coherent beam with a non-uniform correlation structure propagating in a non-linear medium is investigated. The analysis of the evolution of beam width reveals that the coherence structure plays a vital role in the self-focusing formation. A threshold condition for the coherence radius is proposed for the first time, and the relation of self-focusing length and initial coherence radius is studied numerically and analytically. It is shown that a feasible approach for manipulating the self-focusing length by adjusting the initial coherence radius is achieved.

Keywords: partially coherent beam, non-uniform correlation structure, optical coherence, coherence radius, self-focusing length

OPEN ACCESS

Edited by:
Xing Fu,
Tsinghua University, China

Reviewed by:
Xinzhong LI,
Henan University of Science and Technology, China
Shiyao Fu,
Beijing Institute of Technology, China

****Correspondence:***
Yangjian Cai
yangjiancai@suda.edu.cn

†These authors have contributed equally to this work

Specialty section:
This article was submitted to Optics and Photonics, a section of the journal Frontiers in Physics

Received: *02 November 2021*
Accepted: *17 November 2021*
Published: *03 January 2022*

Citation:
Lu L, Wang Z, Yu J, Qiao C, Lin R and Cai Y (2022) Self-Focusing Property of Partially Coherent Beam With Non-Uniform Correlation Structure in Non-Linear Media. Front. Phys. 9:807542. doi: 10.3389/fphy.2021.807542

INTRODUCTION

Spatial coherence is a crucial intrinsic characteristic of light. Optical coherence is now the subject of a well-developed theory [1]; the laser beam with decreased spatial coherence has been analyzed in depth, and it has been labeled as the partially coherent beam (PCB) [2]. By adjusting the spatial coherence of PCBs, novel properties can be exhibited that play a significant role in the light–matter interaction and have attracted the attention of researchers [1, 3]. In the past few decades, intense interest has been focused on the design of different types of PCBs and the interaction between PCBs and various media. To date, many PCBs with uniform or non-uniform correlation structures have been introduced [4], and their propagation properties in turbulence and uniaxial crystal media have been studied [5, 6]. Although these works have been extensive and might seem to be complete, the investigations have not exhausted all possibilities. The non-linear effect can significantly affect the essence of PCB propagation; in practical terms, the Kerr effect strongly exists when an intense laser beam is present in non-linear media.

There are several approaches to describe the propagation of PCBs in a non-linear medium, for example, the coherent density approach [7], multimode decomposition [8], the geometric optics approach [9], and the mutual coherence function [1]. At present, the Gaussian–Schell source model

(GSM) of a partially coherent beam propagating in a non-linear medium is frequently used [10–14]. With a spatially variant correlation function proposed by Gori et al. [15], PCBs with a non-uniform correlation structure not only exhibit self-focusing and self-shifting properties [16–19] but also produce lower scintillation in turbulence [20, 21] than that of GSM beams. The self-focusing property of non-uniformly correlated PCBs (NUC-PCBs) may spark extensive interest owing to their wide application in many fields, such as laser filamentation [10], lightening control [22], high-power atmospheric propagation [23], optical micromanipulation [24], optical communications [25], and optical coherence encryption [26]. Thus, the investigation of the self-focusing property of NUC-PCBs has potential application prospects.

Spatial coherence is regarded as a significant element of a laser beam, and it is vital to achieve the manipulation of self-focusing domain, especially for the control of filamentation one. Until now, the well-known methods for controlling the filamentation domain are as follows: modulating the laser pulse power [27], adjusting the divergence angle of initial laser [28], launching negatively chirped ultrashort pulses [29], and double-lens setup [23]. It is worth mentioning that the input peak intensity is the easiest quantity to change and control precisely [30]; however, the laser power is still limited in the practical scene. If the spatial coherence can be used to control the self-focusing length, it may provide an alternative route to realize the manipulation of filamentation domain. It not only fills in the gap of spatial coherence to control the length of self-focusing but also proposes a feasible solution to obtain the long-range filament propagation. Therefore, it is time to explore an avenue for achieving the manipulation of self-focusing length by adjusting the coherence.

In this work, the self-focusing property of an NUC-PCB propagating in a non-linear medium is investigated. Combining with the non-linear Schrödinger (NLS) equation and mutual coherence function, an analytical expression for beam width is derived. By analyzing the evolution of beam width, the result illustrates that the coherence structure is a key element for self-focusing formation. Furthermore, with the first proposal of the threshold condition of coherence radius, the analytical formula of self-focusing length is obtained. More importantly, it is found that a feasible approach for manipulating the self-focusing length by adjusting the initial coherence radius is realized. These new findings may provide a theoretical and numerical basis in optical communication, optical encryption, optical micro-fabrication, and related areas.

THEORY

The propagation dynamics of laser beams in a Kerr medium is described by the NLS equation. Under the slowly varying amplitude approximation, the NLS equation for a two-dimensional quasi-monochromatic partially coherent beam is [10]

$$\mathrm{i}\frac{\partial \mathbf{E}}{\partial z} + \frac{\beta}{2}\nabla^2\mathbf{E} + \frac{n_2 k}{n_0}\langle \mathbf{E}\mathbf{E}^*\rangle \mathbf{E} = 0, \tag{1}$$

where $\mathrm{E} = \mathrm{E}(\mathrm{r}, z)$ is the amplitude of the electric field, β is the diffraction or second-order dispersion coefficient, $\nabla^2 = \partial^2/\partial x^2 + \partial^2/\partial y^2$ is the transverse Laplacian, n_0 (n_2) is the linear (non-linear) refractive index, $k = 2\pi/\lambda$ is the wavenumber related to the wavelength, $\langle\bullet\rangle$ denotes the statistical ensemble average, and $*$ is the conjugation operator.

Using a PCB as the laser source, **Eq. 1** is unable to correctly describe the propagation evolution in a non-linear medium. Spatial coherence refers to the correlation of complex fields at the same time but at different transverse points r_1 and r_2. To clarify and emphasize the influence of spatial coherence, the temporal coherence will not be involved here. If **Eq. 1** is applied to $\mathrm{E}(\mathrm{r}_1, z)$ and multiplied through by $\mathrm{E}^*(\mathrm{r}_2, z)$, followed by subtracting a similar expression, which is the equation applied to $\mathrm{E}^*(\mathrm{r}_2, z)$ and multiplied through by $\mathrm{E}(\mathrm{r}_1, z)$, and the statistical ensemble averaging the resulting expression [10, 12], one obtains

$$\begin{aligned}\mathrm{i}\frac{\partial\langle \mathbf{E}(\mathbf{r}_1)\mathbf{E}^*(\mathbf{r}_2)\rangle}{\partial z} &+ \frac{\beta}{2}\left(\nabla_1^2 - \nabla_2^2\right)\langle \mathbf{E}(\mathbf{r}_1)\mathbf{E}^*(\mathbf{r}_2)\rangle \\ &+ \frac{n_2 k}{n_0}\left[|\mathbf{E}(\mathbf{r}_2)|^2 - |\mathbf{E}(\mathbf{r}_1)|^2\right]\langle \mathbf{E}(\mathbf{r}_1)\mathbf{E}^*(\mathbf{r}_2)\rangle = 0.\end{aligned} \tag{2}$$

Mutual coherence function, i.e., $\mathbf{W}(\mathbf{r}_i, \mathbf{r}_j) = \langle \mathbf{E}(\mathbf{r}_i)\mathbf{E}^*(\mathbf{r}_j)\rangle$ $(i, j = 1, 2)$, is a common method to solve PCBs in propagation media [1, 31–34]. **Equation 2** can be converted to [10, 12–14]

$$\begin{aligned}\mathrm{i}\frac{\partial \mathbf{W}(\mathbf{r}_1, \mathbf{r}_2)}{\partial z} &+ \frac{\beta}{2}\left(\nabla_1^2 - \nabla_2^2\right)\mathbf{W}(\mathbf{r}_1, \mathbf{r}_2) \\ &+ \frac{n_2 k}{n_0}\left[\mathbf{W}(\mathbf{r}_2, \mathbf{r}_2) - \mathbf{W}(\mathbf{r}_1, \mathbf{r}_1)\right]\mathbf{W}(\mathbf{r}_1, \mathbf{r}_2) = 0.\end{aligned} \tag{3}$$

Considering the PCB with non-uniform correlation function, i.e., assuming Gaussian weight and kernel functions in the spatial domain, the mutual coherence function at the source plane is [17, 18]

$$\begin{aligned}\mathbf{W}(\mathbf{r}_1, \mathbf{r}_2, 0) &= \exp\left[-\left(\mathbf{r}_1^2 + \mathbf{r}_2^2\right)/2w_0^2\right] \\ &\times \exp\left\{-\left[(\mathbf{r}_2 - \mathbf{r}_0)^2 - (\mathbf{r}_1 - \mathbf{r}_0)^2\right]^2/\sigma_0^4\right\},\end{aligned} \tag{4}$$

with the initial coherence radius σ_0 and the maximum intensity being in the region centered at $\mathbf{r}_0$.

By setting $\mathbf{u} = (\mathbf{r}_1 + \mathbf{r}_2)/2$ and $\mathbf{v} = \mathbf{r}_1 - \mathbf{r}_2$ in **Eq. 4**, we obtain from **Eq. 3**

$$\left\{\frac{\partial}{\partial z} - \mathrm{i}\beta\nabla_u\nabla_v + \frac{2\mathrm{i}n_2 \mathrm{k}\mathbf{u}\mathbf{v}}{n_0 w_0^2}\right\}\mathbf{W}(\mathbf{u}, \mathbf{v}, z) = 0, \tag{5}$$

where

$$\mathbf{W}(\mathbf{u}, \mathbf{v}, z) = I_z \exp\left(-\mathbf{u}^2/w_z^2 - \mathbf{v}^2/w_z^2 - 4\mathbf{u}^2\mathbf{v}^2/\sigma_z^2 + \mathrm{i}\mathbf{u}\mathbf{v}\varphi_z\right).$$

Inserting initial conditions (beam width $w_{z=0} = w_0$, coherence radius $\sigma_{z=0} = \sigma_0$, phase $\varphi_{z=0} = 0$, and intensity $I_{z=0} = 1$) into **Eq. 5**, a set of coupled equations for these quantities is obtained:

$$\frac{\mathrm{d}w_z}{\mathrm{d}z} = \beta\varphi_z w_z, \tag{6}$$

$$\frac{\mathrm{d}\sigma_z}{\mathrm{d}z} = \beta\varphi_z \sigma_z, \tag{7}$$

$$\frac{\mathrm{d}\varphi_z}{\mathrm{d}z} = \beta/w_z^4 - \beta\varphi_z^2 - 16\beta/\sigma_z^4 - 2n_2k/n_0w_z^2, \tag{8}$$

$$\frac{\mathrm{d}I_z}{\mathrm{d}z} = -\beta\varphi_z I_z. \tag{9}$$

Combining **Eqs. 6**, **8**, the dynamics of beam width of an NUC-PCB is

$$\frac{\mathrm{d}^2 w_z}{\mathrm{d}z^2} = \frac{\beta^2(1-\gamma^2)}{w_z^3} - \frac{2\beta n_2 k}{n_0 w_z}, \tag{10}$$

with the boundary condition $(\mathrm{d}w_z/\mathrm{d}z)|_{z=0} = 0$; **Equation 10** can then be formulated as

$$\left(\frac{\mathrm{d}w_z}{\mathrm{d}z}\right)^2 + \beta^2(1-\gamma^2)\left(\frac{1}{w_z^2} - \frac{1}{w_0^2}\right) + \frac{4\beta n_2 k}{n_0}\ln\left(\frac{w_z}{w_0}\right) = 0. \tag{11}$$

To ensure the NUC-PCB with a minimum beam width (without collapse), the first and second derivatives of beam width should satisfy the following requirements: $\mathrm{d}w_z/\mathrm{d}z = 0$ and $\mathrm{d}^2w_z/\mathrm{d}z^2 > 0$, i.e.,

$$\begin{cases} \beta^2(1-\gamma^2)\left(\frac{1}{w_z^2} - \frac{1}{w_0^2}\right) + \frac{4\beta n_2 k}{n_0}\ln\left(\frac{w_z}{w_0}\right) = 0, \\ \frac{\beta^2(1-\gamma^2)}{2w_0^2} - \frac{\beta n_2 k}{n_0} > 0. \end{cases} \tag{12}$$

Based on **Eq. 12**, the critical coherence radius for the formation of self-focusing is given by

$$\frac{1}{\sigma_{cr}^4} = \frac{1}{16w_0^4} - \frac{n_2 k}{8\beta n_0 w_0^2}. \tag{13}$$

Here, the initial coherence radius should be considered as $\sigma_0 < \sigma_{cr}$.

With boundary conditions $w_{z=0} = w_0$ and $(\mathrm{d}w_z/\mathrm{d}z)|_{z=0} = 0$, an analytical expression for beam width is obtained:

$$w_z^2 = w_0^2 + \frac{\beta^2(1-\gamma^2)z^2}{w_0^2} - \frac{2\beta n_2 k(1+2\alpha)z^2}{n_0}. \tag{14}$$

Physically, the evolution of beam width is determined by a competition for two main factors: 1) spreading induced by free-space diffraction and 2) self-focusing caused by the non-uniform correlation structure and non-linearity of the medium. Here, the parameters are recorded as $\gamma = 4w_0^2/\sigma_0^2 = 4w_z^2/\sigma_z^2$, $\alpha = \ln(\sigma_z/\sigma_0)$, and the focusing case with $n_2 > 0$ is considered.

When the critical coherence radius is satisfied, the self-focusing length can be expressed as

$$z_f = \frac{\left(\sigma_0^2/\sigma_{cr}^2 - 1\right)}{\sqrt{\beta^2(1-\gamma^2)/w_0^4 - 2\beta n_2 k[1+2\ln(\sigma_0/\sigma_{cr})]/n_0 w_0^2}}, \tag{15}$$

where a variable substitution is used, due to the common range of variables $\sigma_z/\sigma_0 \in (0,1]$ and $\sigma_0/\sigma_{cr} \in (0,1]$.

NUMERICAL CALCULATIONS AND ANALYSIS

Using the fast Fourier transform split-step method [35], the initial parameters are chosen as follows: wavelength $\lambda = 0.8$ µm, initial beam width $w_0 = 0.8$ mm, Rayleigh length for PCBs $z_R = kw_0\sigma_0/2$[12], coefficient $\beta = 1/n_0k$, propagation length $z = 0.6z_R$, linear refractive index of the medium $n_0 = 1$, transverse size $20w_0$, grid number $N = 512$, and step number $M = 2000$.

The self-focusing length for the NUC-PCB in the linear and non-linear media is investigated numerically, where the non-linear refractive index is $n_2 = 3\times10^{-21}$ m^2/W, the critical coherence radius for self-focusing is satisfied with $\sigma_{cr} = 2w_0$, and the initial coherence radius is $\sigma_0 = 0.25\sigma_{cr}$. Due to the existence of non-linearity, the self-focusing length in a linear medium (**Figure 1A**, i.e., $z = 0.1056z_R$) is shorter than that in a non-linear medium (**Figure 1B**, i.e., $z = 0.1935z_R$), and the peak intensity for the linear case is lower than that of the non-linear one (**Figure 1D**). It shows that the property of propagation medium can affect the self-focusing length, and in a medium with $n_2 > 0$, that length can be extended. Besides, the propagation property for the GSM is mentioned; there is no self-focusing phenomenon seen in **Figure 1C** because the peak intensity is located at the source plane (blue curve in **Figure 1D**). It may be predicted that the non-uniform coherence structure plays a vital role in the formation of self-focusing.

For the analytical expression of beam width (i.e., **Eq. 14**), it is obvious that the propagation dynamics are determined by a balance of three elements, i.e., diffraction (or dispersion), coherence structure of beam, and property of propagation medium. Similarly, the beam width for the GSM beam is derived as $w_G^2 = w_0^2 + \beta^2(1+\gamma)z^2/w_0^2 - 2\beta n_2 k(1+2\alpha)z^2/n_0$. The critical coherence radius is $1/\sigma_G^2 = n_2k/2n_0\beta - 1/4w_0^2$, which shows that there is no real root in the GSM case, i.e., there is no beam focusing. For the same non-linear refractive index, the GSM beam spreads (magenta curve in **Figure 2**), while the NUC-PCB is focused (green curve in **Figure 2**). For NUC-PCBs, a higher non-linear refractive index causes a more obvious beam focusing (red curve in **Figure 2**). It illustrates that the formation of self-focusing is more affected by the non-uniform correlation structure than by the non-linearity of the medium. The numerical and analytical analysis indicates that the coherence structure is the core element for the self-focusing formation. Besides, with the initial coherence radius increased, the beam spreading of GSM becomes significant, and the self-focusing effect for NUC-PCBs is gradually reduced.

Based on the analysis of the beam width's dependence on the coherence structure, it appears that the initial coherence radius can be regarded as a degree of freedom for manipulating the self-focusing length. To verify this hypothesis, the numerical and analytical methods were successively used. In the numerical calculation, the initial coherence radii are selected as follows: $\sigma_0 = 0.2\sigma_{cr}$, $0.4\sigma_{cr}$, $0.6\sigma_{cr}$, and $0.8\sigma_{cr}$; the non-linear refractive index is $n_2 = 3\times10^{-23}$ m^2/W. **Figure 3** shows that the corresponding self-focusing lengths are approximately $0.085z_R$,

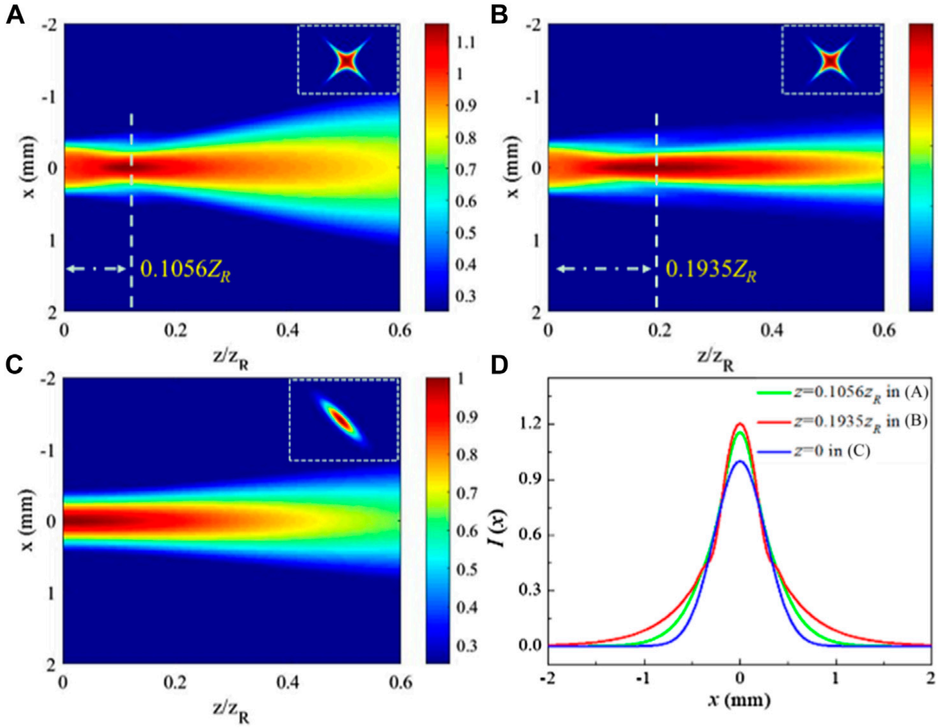

FIGURE 1 | Propagation evolution of three cases: **(A)** NUC-PCB in a linear medium, **(B)** NUC-PCB in a non-linear medium, and **(C)** GSM beam in a non-linear medium, where **(D)** shows the corresponding intensity distribution at the locations of maximum intensity in **(A–C)**. The insets represent the mutual coherence function (or cross-spectral density) at the source plane.

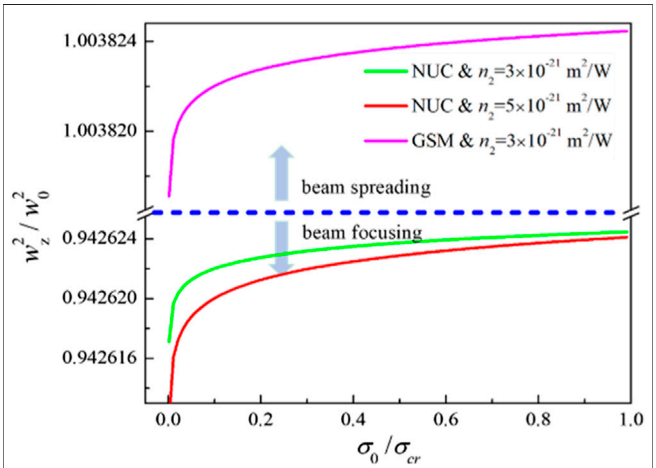

FIGURE 2 | Dependence of the beam width on the initial coherence radius.

$0.1596z_R$, $0.2052z_R$, and $0.2064z_R$, respectively. With the aid of numerical results, the initial coherence radius can change the self-focusing length to some extent, but the specific relation is not clarified. Therefore, the analytical relation of the self-focusing length and initial coherence radius was studied. Based on **Eq. 15**, the relative self-focusing length z_f/z_R is investigated. It is shown that the dependence of the relative self-focusing length on the initial coherence radius is not monotonic, and the maximum of the relative self-focusing length is located at $\sigma_0 = 0.71\sigma_{cr}$. It is found that the relative self-focusing length can be continuously controlled by varying the initial coherence radius; thus, the conclusion that the initial coherence radius may be regarded as a degree of freedom for manipulating the self-focusing length is established. In addition, by a modestly sized change in parameters such as the initial beam width and wavelength, the self-focusing length may be tunable in the range from microns to kilometers, and it is even possible to realize controllability from the micro to macro domains. It is worth mentioning that the correctness of the analytical expression is verified by comparing numerical and analytical results, and the results show that two methods have a good agreement with each other, as shown in **Figure 4** (i.e., magenta dots).

CONCLUSION AND DISCUSSIONS

In summary, the self-focusing property of a partially coherent beam with a non-uniform correlation structure propagating in a non-linear medium was investigated using numerical and analytical methods. It is found that the non-uniform correlation structure plays a core role in the self-focusing formation. Furthermore, with the threshold condition of initial coherence radius proposed for the first time, the analytical

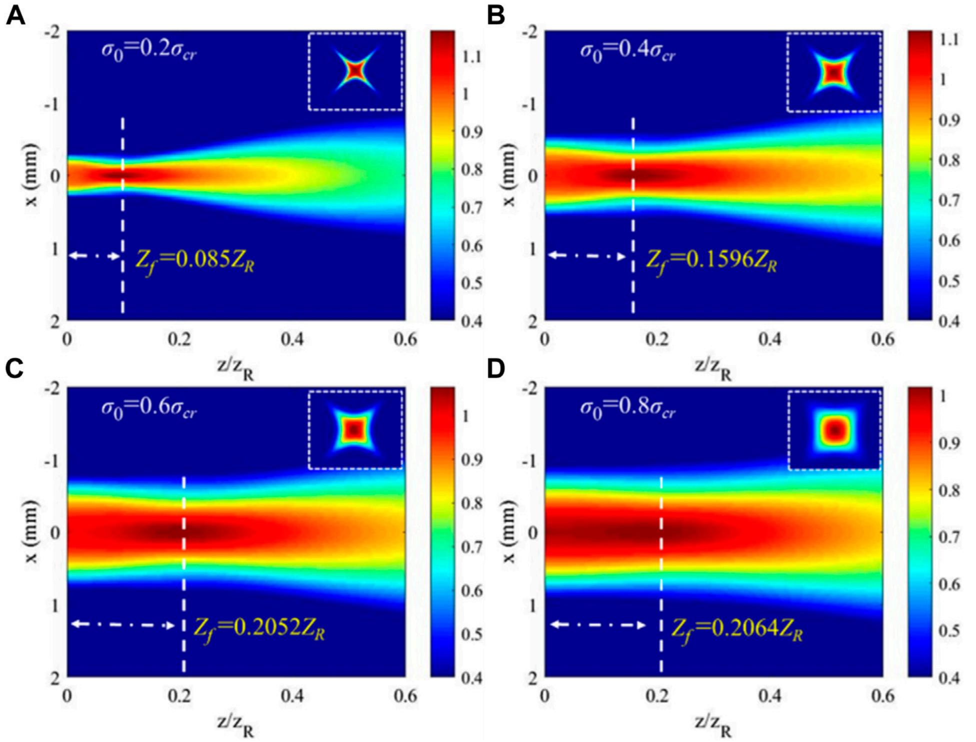

FIGURE 3 | Self-focusing length with various initial coherence radii: **(A)** $\sigma_0 = 0.2\sigma_{cr}$, **(B)** $\sigma_0 = 0.4\sigma_{cr}$, **(C)** $\sigma_0 = 0.6\sigma_{cr}$, and **(D)** $\sigma_0 = 0.8\sigma_{cr}$, where the insets represent the mutual coherence function (or cross-spectral density) at the source plane.

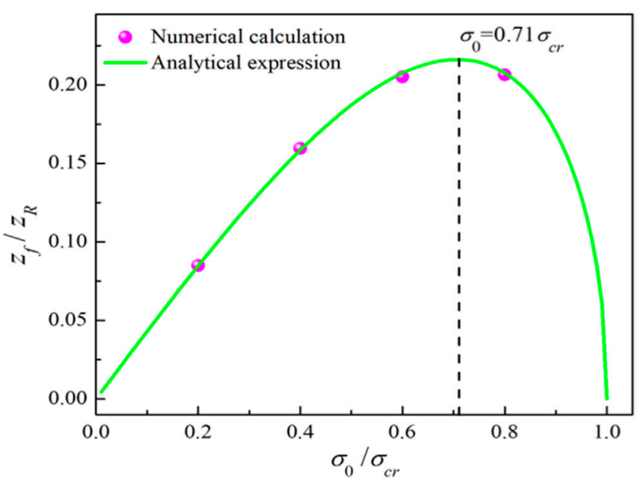

FIGURE 4 | Dependence of the relative self-focusing length on the initial coherence radius. The magenta dots correspond to the cases in **Figure 3**.

formula for the self-focusing length is obtained. The result shows that the relation of relative self-focusing length and initial coherence radius is not monotonic, and it can be continuously controlled by changing the initial coherence radius. More significantly, a feasible approach for manipulating the self-focusing length by adjusting the initial coherence radius has been realized. These findings may have potential applications in optical communication, optical encryption, all-optical signal processing, and related areas. For example, it is known that the polarization [36–38] and orbital angular momentum [39] can be used as a carrier basis of signals for optical communication links. Herein, spatial coherence is regarded as the degree of freedom of a light beam as well, and it may provide another dimension for data-coding. In addition, the self-focusing length can be manipulated by varying the initial coherence radius of NUC-PCBs, benefiting for a controllable high-power laser atmospheric propagation for moving targets.

DATA AVAILABILITY STATEMENT

The original contributions presented in the study are included in the article, and further inquiries can be directed to the corresponding authors.

AUTHOR CONTRIBUTIONS

All authors listed have made a substantial, direct, and intellectual contribution to the work and approved it for publication.

FUNDING

We acknowledge the National Key Research and Development Project of China (2019YFA0705000), National Natural Science Foundation of China (91750201, 11974218, 11804234, 11903062, 12192254, and 11904087), Innovation Group of Jinan (2018GXRC010), and Local Science and Technology Development Project of the Central Government (YDZX20203700001766). We appreciate the valuable comments from reviewers.

REFERENCES

1. Mandel L, Wolf E. *Optical Coherence and Quantum Optics*. Cambridge, UK: Cambridge University Press (1995).
2. Cai Y, Chen Y, Yu J, Liu X, Liu L. Generation of Partially Coherent Beams. *Prog Opt* (2017) 62:157–223. doi:10.1016/bs.po.2016.11.001
3. Chen Y, Norrman A, Ponomarenko SA, Friberg AT. Optical Coherence and Electromagnetic Surface Waves. *Prog Opt* (2020) 65:105–72. doi:10.1016/bs.po.2019.11.001
4. Cai Y, Chen Y, Wang F. Generation and Propagation of Partially Coherent Beams with Nonconventional Correlation Functions: a Review [Invited]. *J Opt Soc Am A* (2014) 31(9):2083–96. doi:10.1364/josaa.31.002083
5. Gbur G. Partially Coherent Beam Propagation in Atmospheric Turbulence [Invited]. *J Opt Soc Am A* (2014) 31(9):2038–45. doi:10.1364/josaa.31.002038
6. Lin R, Chen M, Liu Y, Zhang H, Gbur G, Cai Y, et al. Measuring Refractive Indices of a Uniaxial crystal by Structured Light with Non-uniform Correlation. *Opt Lett* (2021) 46(10):2268–71. doi:10.1364/ol.424259
7. Christodoulides DN, Coskun TH, Mitchell M, Segev M. Theory of Incoherent Self-Focusing in Biased Photorefractive Media. *Phys Rev Lett* (1997) 78:646–9. doi:10.1103/physrevlett.78.646
8. Christodoulides DN, Coskun TH, Mitchell M, Segev M. Multimode Incoherent Spatial Solitons in Logarithmically Saturable Nonlinear Media. *Phys Rev Lett* (1998) 80:2310–3. doi:10.1103/physrevlett.80.2310
9. Snyder AW, Mitchell DJ. Big Incoherent Solitons. *Phys Rev Lett* (1998) 80: 1422–4. doi:10.1103/physrevlett.80.1422
10. Królikowski W, Edmundson D, Bang O. Unified Model for Partially Coherent Solitons in Logarithmically Nonlinear media. *Phys Rev E* (2000) 61:3122–6. doi:10.1103/physreve.61.3122
11. Mendonça JT, Tsintsadze NL. Analog of the Wigner-Moyal Equation for the Electromagnetic Field. *Phys Rev E* (2000) 62:4276–82. doi:10.1103/physreve.62.4276
12. Nayyar VP. Propagation of Partially Coherent Gaussian Schell-Model Sources in Nonlinear media. *J Opt Soc Am B* (1997) 14(9):2248–53. doi:10.1364/josab.14.002248
13. Wang H, Ji X-L, Zhang H, Li X-Q, Deng Y. Propagation Formulae and Characteristics of Partially Coherent Laser Beams in Nonlinear media. *Opt Lett* (2019) 44(4):743–6. doi:10.1364/ol.44.000743
14. Wang H, Ji X-L, Deng Y, Li X-Q, Yu H. Theory of the Quasi-Steady-State Self-Focusing of Partially Coherent Light Pulses in Nonlinear media. *Opt Lett* (2020) 45(3):710–3. doi:10.1364/ol.379902
15. Gori F, Santarsiero M. Devising Genuine Spatial Correlation Functions. *Opt Lett* (2007) 32(24):3531–3. doi:10.1364/ol.32.003531
16. Lajunen H, Saastamoinen T. Propagation Characteristics of Partially Coherent Beams with Spatially Varying Correlations. *Opt Lett* (2011) 36(20):4104–6. doi:10.1364/ol.36.004104
17. Tong Z, Korotkova O. Nonuniformly Correlated Light Beams in Uniformly Correlated media. *Opt Lett* (2012) 37(15):3240–2. doi:10.1364/ol.37.003240
18. Lajunen H, Saastamoinen T. Non-uniformly Correlated Partially Coherent Pulses. *Opt Express* (2013) 21(1):190–5. doi:10.1364/oe.21.000190
19. Yu J, Cai Y, Gbur G. Rectangular Hermite Non-uniformly Correlated Beams and its Propagation Properties. *Opt Express* (2018) 26(21):27894–906. doi:10.1364/oe.26.027894
20. Yu J, Wang F, Liu L, Cai Y, Gbur G. Propagation Properties of Hermite Non-uniformly Correlated Beams in Turbulence. *Opt Express* (2018) 26(13): 16333–43. doi:10.1364/oe.26.016333
21. Gu Y, Gbur G. Scintillation of Nonuniformly Correlated Beams in Atmospheric Turbulence. *Opt Lett* (2013) 38(9):1395–7. doi:10.1364/ol.38.001395
22. Houard A, D'Amico C, Liu Y, Andre YB, Franco M, Prade B, et al. High Current Permanent Discharges in Air Induced by Femtosecond Laser Filamentation. *Appl Phys Lett* (2007) 90:171501. doi:10.1063/1.2734396
23. Fibich G, Sivan Y, Ehrlich Y, Louzon E, Fraenkel M, Eisenmann S, et al. Control of the Collapse Distance in Atmospheric Propagation. *Opt Express* (2006) 14(12):4946–57. doi:10.1364/oe.14.004946
24. Zhao C, Cai Y, Lu X, Eyyuboğlu HT. Radiation Force of Coherent and Partially Coherent Flat-Topped Beams on a Rayleigh Particle. *Opt Express* (2009) 17(3): 1753–65. doi:10.1364/oe.17.001753
25. Yu J, Zhu X, Lin S, Wang F, Gbur G, Cai Y. Vector Partially Coherent Beams with Prescribed Non-uniform Correlation Structure. *Opt Lett* (2020) 45(13): 3824–7. doi:10.1364/ol.397316
26. Peng D, Huang Z, Liu Y, Chen Y, Wang F, Ponomarenko SA, et al. Optical Coherence Encryption with Structured Random Light. *PhotoniX* (2021) 2(1):6. doi:10.1186/s43074-021-00027-z
27. Houard A, Franco M, Prade B, Durécu A, Lombard L, Bourdon P, et al. Femtosecond Filamentation in Turbulent Air. *Phys Rev A* (2008) 78:033804. doi:10.1103/physreva.78.033804
28. Jin Z, Zhang J, Xu MH, Lu X, Li YT, Wang ZH, et al. Control of Filamentation Induced by Femtosecond Laser Pulses Propagating in Air. *Opt Express* (2005) 13(25):10424–30. doi:10.1364/opex.13.010424
29. Sprangle P, Peñano JRB, Hafizi B. Propagation of Intense Short Laser Pulses in the Atmosphere. *Phys Rev E Stat Nonlin Soft Matter Phys* (2002) 66:046418. doi:10.1103/PhysRevE.66.046418
30. Buryak A, Trapani PD, Skryabin DV, Trillo S. Optical Solitons Due to Quadratic Nonlinearities: from Basic Physics to Futuristic Applications. *Phys Rep* (2002) 370(2):63–235. doi:10.1016/s0370-1573(02)00196-5
31. Wolf E. A Macroscopic Theory of Interference and Diffraction of Light from Finite Sources II. Fields with a Spectral Range of Arbitrary Width. *Proc Roy Soc* (1955) A230:246.
32. Born M, Wolf E. *Principles of Optics*. New York: Pergamon Press (1959).
33. Wolf E. *Introduction to the Theory of Coherence and Polarization of Light*. Cambridge, UK: Cambridge University Press (2007).
34. Andrews LC, Phillips RL. *Laser Beam Propagation through Random Media*. Bellingham: SPIE Press (2005).
35. Hermansson B, Yevick D, Friberg AT. Optical Coherence Calculations with the Split-step Fast Fourier Transform Method. *Appl Opt* (1986) 25(16):2645–7. doi:10.1364/ao.25.002645
36. Andrews MR, Mitra PP, deCarvalho R. Tripling the Capacity of Wireless Communications Using Electromagnetic Polarization. *Nature* (2001) 409(6818):316–8. doi:10.1038/35053015
37. Turpin A, Loiko Y, Kalkandjiev TK, Mompart J. Free-space Optical Polarization Demultiplexing and Multiplexing by Means of Conical Refraction. *Opt Lett* (2012) 37(20):4197–9. doi:10.1364/ol.37.004197
38. Lu L, Wang Z, Cai Y. Propagation Properties of Phase-Locked Radially-Polarized Vector fields Array in Turbulent Atmosphere. *Opt Express* (2021) 29(11):16833–44. doi:10.1364/oe.427003

39. Zou L, Gu X, Wang L. High-dimensional Free-Space Optical Communications Based on Orbital Angular Momentum Coding. *Opt Commun* (2010) 410: 333–7. doi:10.1016/j.optcom.2017.10.035

Conflict of Interest: The authors declare that the research was conducted in the absence of any commercial or financial relationships that could be construed as a potential conflict of interest.

Publisher's Note: All claims expressed in this article are solely those of the authors and do not necessarily represent those of their affiliated organizations, or those of the publisher, the editors, and the reviewers. Any product that may be evaluated in this article, or claim that may be made by its manufacturer, is not guaranteed or endorsed by the publisher.

ORIGINAL RESEARCH
published: 03 January 2022
doi: 10.3389/fphy.2021.801916

Investigation on the Formation of Laser Transverse Pattern Possessing Optical Lattices

Xin Wang[1,2,3], *Zilong Zhang*[1,2,3]*, *Yuan Gao*[1,2,3], *Suyi Zhao*[1,2,3], *Yuchen Jie*[1,2,3] *and Changming Zhao*[1,2,3]

[1]*School of Optics and Photonics, Beijing Institute of Technology, Beijing, China,* [2]*Key Laboratory of Photoelectronic Imaging Technology and System, Ministry of Education of People's Republic of China, Beijing, China,* [3]*Key Laboratory of Photonics Information Technology, Ministry of Industry and Information Technology, Beijing, China*

Optical lattices (OLs) with diverse transverse patterns and optical vortex lattices (OVLs) with special phase singularities have played important roles in the fields of atomic cooling, particle manipulation, quantum entanglement, and optical communication. As a matter of consensus until now, the OL patterns are generated by coherently superimposing multiple transverse modes with a fixed phase difference through the transverse mode locking (TML) effect. There are phase singularities in the dark area of this kind of OL pattern, so it is also called OVL pattern. However, in our research, it is found that some high-order complex symmetric OL patterns can hardly be analyzed by TML model. Instead, the analysis method of incoherent superposition of mode intensity could be applied. The OL pattern obtained by this method can be regarded as in non-TML state. Therefore, in this article, we mainly study the distinct characteristics and properties of OL patterns in TML and non-TML states. Through intensity comparison, interferometry, and beat frequency spectrum, we can effectively distinguish OL pattern in TML and non-TML states, which is of significance to explore the formation of laser transverse pattern possessing OL.

Keywords: laser transverse patterns, optical lattice, optical vortex lattice, transverse mode locking, structured light

OPEN ACCESS

Edited by:
Xing Fu,
Tsinghua University, China

Reviewed by:
Yijie Shen,
University of Southampton, United Kingdom
Yuanjie Yang,
University of Electronic Science and Technology of China, China

***Correspondence:**
Zilong Zhang
zlzhang@bit.edu.cn

Specialty section:
This article was submitted to Optics and Photonics, a section of the journal Frontiers in Physics

Received: *26 October 2021*
Accepted: *05 November 2021*
Published: *03 January 2022*

Citation:
Wang X, Zhang Z, Gao Y, Zhao S, Jie Y and Zhao C (2022) Investigation on the Formation of Laser Transverse Pattern Possessing Optical Lattices. Front. Phys. 9:801916. doi: 10.3389/fphy.2021.801916

INTRODUCTION

Optical lattices (OLs) refer to the periodic potential well in the laser standing wave field [1, 2]. The spatial period of the potential well is the order of laser wavelength, making it available to capture, cool, and trap atoms in the potential well array [3, 4]. In 1990s, a two-dimensional OL pattern with spatiotemporal chaos was found in Na_2 laser, whereas the time-averaged intensity was stable, wherein the transverse dynamics was ruled by the competition of two modes (each one of them possessing a cylindrical symmetry) [5]. Then, following the OL patterns generated in CO_2 laser and theoretical speculations on spontaneous symmetry breaking phenomena, it was pointed out that the spatiotemporal behavior of a laser in the low-dimensional regimen crucially depends on symmetries and that most of the dynamic features can be directly captured as consequences of spontaneous symmetry breaking mechanism [6, 7]. For the high-dimensional case, patterns in a CO_2 laser with a large Fresnel number are characterized by a high degree of complexity and by the absence of zeroes in the intensity profile [8, 9]. In addition, in the research of OL pattern generated in a Na_2 laser, the phase singularities similar to that studied in hydrodynamics [10] were found, which possesses the same properties as the optical vortex discovered by Coullet et al in 1989 [11], thus naming this kind of OL with special phase singularities as optical vortex lattice (OVL). The transverse patterns with special phase singularities were then found to be generated in vertical-cavity-surface–emitting lasers (VCSELs) [12]. Here, the generated low-order OVL is experimentally interfered with the plane wave. It is found that there were bifurcation fringes in the dark region, which reveals the existence of phase singularities. Subsequently, the high-order OVL was found in microchip laser with large Fresnel number by Chen and Lan [13, 14]. And it is pointed out that with the inherent nonlinear properties of laser cavity, multiple transverse modes can be spontaneously locked, so as to generate high-order vortex lattice. The further generation laws of OVL are summarized in Refs. [15–17]; that is, by actively selective pumping and gain distribution such as adjusting the pump power, pump distance, and the size of pump spot on the gain crystal, the OVL patterns from low order to high order could be generated and switched. Optical lattices with special transverse distribution play an important part in atomic cooling and trapping [18–20], whereas the OVLs with unique phase singularity have also broadened the applications in particle manipulation [21–25], quantum entanglement [26], and optical communications [27–29].

The exploration of the essence of transverse pattern formation of OL can be traced back to 1970s. By simplifying the laser equations for the class A case to the complex Ginzburg–Landau (CGL) equation, the relationship between superfluid and laser dynamics was established. In view of this common theoretical description, it was expected that the dynamics of pattern formation in lasers and the dynamics of superfluid would show identical features [30]. Later, the generation and spatial stability of special laser transverse patterns were analyzed through Maxwell–Bloch (MB) equations [31, 32]. Moreover, the vortex solution was solved through MB equations [11], which could be applied in the formation of OVL. Subsequently, with the derivation of laser Ginzburg–Landau equations in class A lasers [33] and complex Swift–Hohenberg (CSH) equations in class B lasers [34], vortex solutions could also be obtained, thus generating OVL. It is worth noting that the numerical analytical solutions of these spatiotemporal multivariate nonlinear partial differential equations need to allocate complex parameters in the actual laser system. Therefore, the method to analyze the output OL patterns by superposition of some laser modes (such as Hermite–Gaussian [HG], Laguerre–Gaussian [LG], and Ince–Gaussian [IG] modes) is proposed [16, 17, 35–38]. There are two main types of superposition analysis methods. The first is to analyze the output OL pattern through the superposition of intensities of composed modes alone. It is pointed that in multi–transverse-mode lasers, the coupling between transverse modes occurs through their intensity rather than their field amplitude, and these modes are arranged together according to the principle of "transverse hole burning" to maximize energy coexistence and minimize intensity distribution overlap [35]. The OL patterns though the first analysis method can be observed in CO_2 laser, most of which are high-order symmetrical patterns [7, 8]. The second kind of analysis method involves the transverse mode locking (TML) effect [31], which includes frequency locking and phase locking. The output OL pattern is analyzed by superimposing the electric field of multiple modes with the locking phase. Moreover, with the assistance of the inherent nonlinearity of the laser cavity, the frequencies of the composed modes are pulled to the same value [12, 16, 17]. The second TML method is commonly used. Through this analysis method, the OL with both high order and low order, as well as symmetric and asymmetric patterns, could be obtained, which have a wide range of applications. In addition, it is found that there are phase singularities in the dark region of OL pattern analyzed by TML method [12, 16], which could also be called OVL patterns. In contrast, the OL patterns obtained by intensity superposition alone could be regarded as the OL pattern in non-TML state. Whether there are phase singularities in the OL pattern in non-TML state has not been specially studied. Although the experimental higher-order OL patterns similar to the analyzed OL patterns in non-TML state have been generated in VCSEL [12] and microchip lasers [13, 14], the existence of phase singularity has not been discussed in these researches. Interferometric observation of the phase singularity in OL is a common detection method, which introduces a reference beam to interfere with the measured beam [39, 40], or splits the measured beam to interfere with each other [41–44]. Then, the existence of the phase singularity could be determined by observing whether the interference fringes are misaligned. In recent years, most of the analyses of OL and OVL patterns are to correspond the numerically simulation by TML model and the experimentally measured patterns. Then, the consistence of intensity correspondence is used to analyze the properties of the generated OL patterns [17]. Furthermore, interference experiments are applied to analyze whether there are phase singularities in the dark area of the generated OL patterns [12, 16]. However, these analyses are all based on the premise that OL patterns are in TML state, whereas the properties of OL patterns in non-TML state are rarely studied in these years. In our study, OL patterns in TML state and non-TML state are both analyzed by mode superposition method, rather than by solving complex nonlinear equations. For the OL patterns in non-TML state through our method, we not only analyze the numerical transverse patterns obtained by solving equations, but also obtain the same high-order symmetrical patterns as the output of CO_2 lasers [7, 8], microchip lasers [13, 14], and solid-state lasers [17, 45]. In addition, if the TML state is satisfied, strictly speaking, the frequency of the composed modes should be locked to the same value. Then, measuring the beat frequency spectrum of the output pattern could also be used as a method to assist in judging the properties of OL patterns.

Consequently, the aim of this article is threefold. First, we theoretically analyze the difference through intensity profile between OL in TML and non-TML states in a more complete and rigorous way. Numerical simulations reveal that the OL pattern intensity in TML state varies greatly with the locking phase, and there are both symmetrical and asymmetrical patterns. For OL in non-TML states, as only intensity superposition is performed, it has nothing to do with the relative phase of the composed modes, and the pattern is always symmetrical. For the two-mode composed patterns, some intensity distributions of OL in TML and non-TML states are the same. However, when the composition modes reach more than two, their patterns produced by the approaches of TML and non-TML superposition are totally different. Second, interferometry is applied to distinguish OL patterns in TML and non-TML states. For OL patterns in TML state, after interfering with a plane wave, it is shown that all dark zones possess interference bifurcation fringes, revealing the phase singularities. This is consistent with previous research results [12, 16]. Nevertheless, for the interference between OL in non-TML states and a plane wave, we find that some dark regions of the pattern possess interference bifurcations, but some do not. Moreover, the existence of their interference bifurcation is related to the phase of the composed modes. Third, a peculiar assistant method is proposed to judge the states in OL formation through the beat frequency spectra. For the various beat frequency spectra observed in the experiment, including null-component spectra, several-spike spectra, two-cluster spectra, and periodic spectra, we theoretically and experimentally correspond to each state including TML, non-TML, only-phase-locking, and prelocking states in OL formation. Therefore, through the three methods introduced in our article, namely, the intensity comparison, interferometry, and beat frequency spectrum, the OL in TML or non-TML states could be effectively distinguished, which is of great significance for the understanding of the essence of laser transverse pattern possessing OL.

NUMERICAL CHARACTERIZATIONS AND THEORIES

Intensity of the OL Patterns

For theoretical analysis of OL generation, the traditional method is to numerically solve the nonlinear MB equations [31] and the CGL [33] and CSH [34] equations. As a result, numerical solutions could be obtained to describe OL and OVL patterns. However, for this set of space–time multivariate nonlinear partial differential equations, the solution process is cumbersome, and it is tough to assign various parameters to a specific laser system. Furthermore, another analysis method is proposed, which is to perform coherent superposition of HG, LG, or IG modes with different locking phases to fulfill the analysis and simulation [37]. By matching the result of the simulation with the actual output pattern, it can confirm whether the OL is in TML state or not, which is the previous judging method [12, 16, 17]. In most cases, this correspondence is unique and can be applied to determine the TML state. However, we found that for two-mode composed patterns in TML state with some locking phases, the beam pattern is similar to that of their non-TML state.

Then, we would like to present the TML theoretical models by coherent superposition of HG or LG modes with different locked phases. The expressions of HG and LG modes are as follows [37].

$$HG_{m,n}(x,y,z) = \frac{C_{m,n}^{HG}}{\omega^2(z)}\exp\left(-\frac{x^2+y^2}{\omega^2(z)}\right)H_m\left(\frac{\sqrt{2}x}{\omega(z)}\right)H_m\left(\frac{\sqrt{2}y}{\omega(z)}\right)\exp\left[ikz+ik\frac{x^2+y^2}{2R(z)}-i(m+n+1)\Psi(z)\right] \tag{1}$$

$$LG_{p,l}(r,\phi,z) = \frac{C_{p,l}^{LG}}{\omega(z)}\left(\frac{\sqrt{2}r}{\omega(z)}\right)^{|l|}\exp\left(-\frac{r^2}{\omega^2(z)}\right)L_p^{|l|}\left(\frac{2r^2}{\omega^2(z)}\right)\exp(il\phi)\exp\left[ikz+ik\frac{r^2}{2R(z)}-i(2p+|l|+1)\Psi(z)\right] \tag{2}$$

where the HG and LG modes are individually expressed with Cartesian coordinates and cylindrical coordinates. $C_{m,n}^{HG}$ and $C_{p,l}^{LG}$ are the normalization constants for the HG and LG modes, respectively. $H_m(\cdot)$ [or $H_n(\cdot)$] is the Hermite polynomial of mth (or nth) order. $\omega(z)$ is the beam half width at position z and $\omega^2 = \omega_0^2(z_R^2+z^2)/z_R^2$. ω_0 is the radius of the beam waist of the fundamental mode, and z_R is the Rayleigh length. $R(z)$ is the z-dependent radius of curvature, and $\Psi(z) = \arctan(z/z_R)$ is the Gouy phase.

For the perspective of the perfect TML state of OL, apart from the phase locking, the frequencies of the participating transverse modes are supposed to be locked to a common value to establish cooperative frequency locking [31]. It is available under the assistance of nonlinearity in class B lasers [34]. In this case, the TML progress can be expressed by the coherent superposition of HG or LG modes with a specific locking phase as follows.

$$E_{\mathrm{TML}} = \sum_{m,n} a_{m,n}HG_{m,n}(\cdot)\exp\left(i\phi_{m,n}+ikz+ik\frac{x^2+y^2}{R(z)}-iq\Psi(z)\right) \tag{3}$$

Or

$$E_{\mathrm{TML}} = \sum_{p,l} b_{p,l}LG_{p,l}(\cdot)\exp\left(i\phi_{p,l}+ikz+ik\frac{x^2+y^2}{R(z)}-iq\Psi(z)\right) \tag{4}$$

where $HG_{m,n}(\cdot)$ and $LG_{p,l}(\cdot)$ are the pure intensity items of HG and LG modes, respectively. $a_{m,n}$ and $b_{p,l}$ are the coefficients of each mode. $\phi_{m,n}$ and $\phi_{p,l}$ are the locking phases of HG and LG modes. q is the total index. For HG modes, $q = m+n+1$, $m, n = 0, 1, 2\ldots$, whereas for LG modes, $q = 2p+|l|+1$, $p = 0, 1, 2\ldots$; $l = 0, \pm1, \pm2\ldots$.

Afterward, if we perform the non-TML superposition of the intensity of HG and LG modes, we can obtain the total intensity by

$$I_{\mathrm{non-TML}} = \sum_{m,n} a_{m,n}HG_{m,n}(x,y,z)\cdot HG_{m,n}^*(x,y,z) \tag{5}$$

Or

$$I_{\mathrm{non-TML}} = \sum_{p,l} b_{p,l}LG_{p,l}(r,\phi,z)\cdot LG_{p,l}^*(r,\phi,z) \tag{6}$$

where $HG_{m,n}(x,y,z)$ and $LG_{p,l}(r,\phi,z)$ are from **Eqs 1, 2**. $HG_{m,n}^*(x,y,z)$ and $LG_{p,l}^*(r,\phi,z)$ are the conjugate item of $HG_{m,n}(x,y,z)$ and $LG_{p,l}(r,\phi,z)$, respectively. And the total intensity has nothing to do with the phase of each composed mode. Through the numerical simulation of **Eq. 5**, we can get the patterns of OL in non-TML state as shown in **Figure 1**.

In the first column of **Figures 1A–E**, it can be found that for OL pattern in non-TML state composed of total HG modes with the same order, the intensity of the pattern shows concentric-ring distribution. In addition, for OL pattern in non-TML state of partial HG modes with the same order, it can easily form patterns similar to that simulated by MB equations [31], as well as experimentally generated in CO_2 laser [7, 8], microchip lasers [13, 14], and solid-state lasers [45–48]. Rows A–E, respectively, show the OL patterns in non-TML state composed of HG modes with Fresnel numbers from 2 to 6.

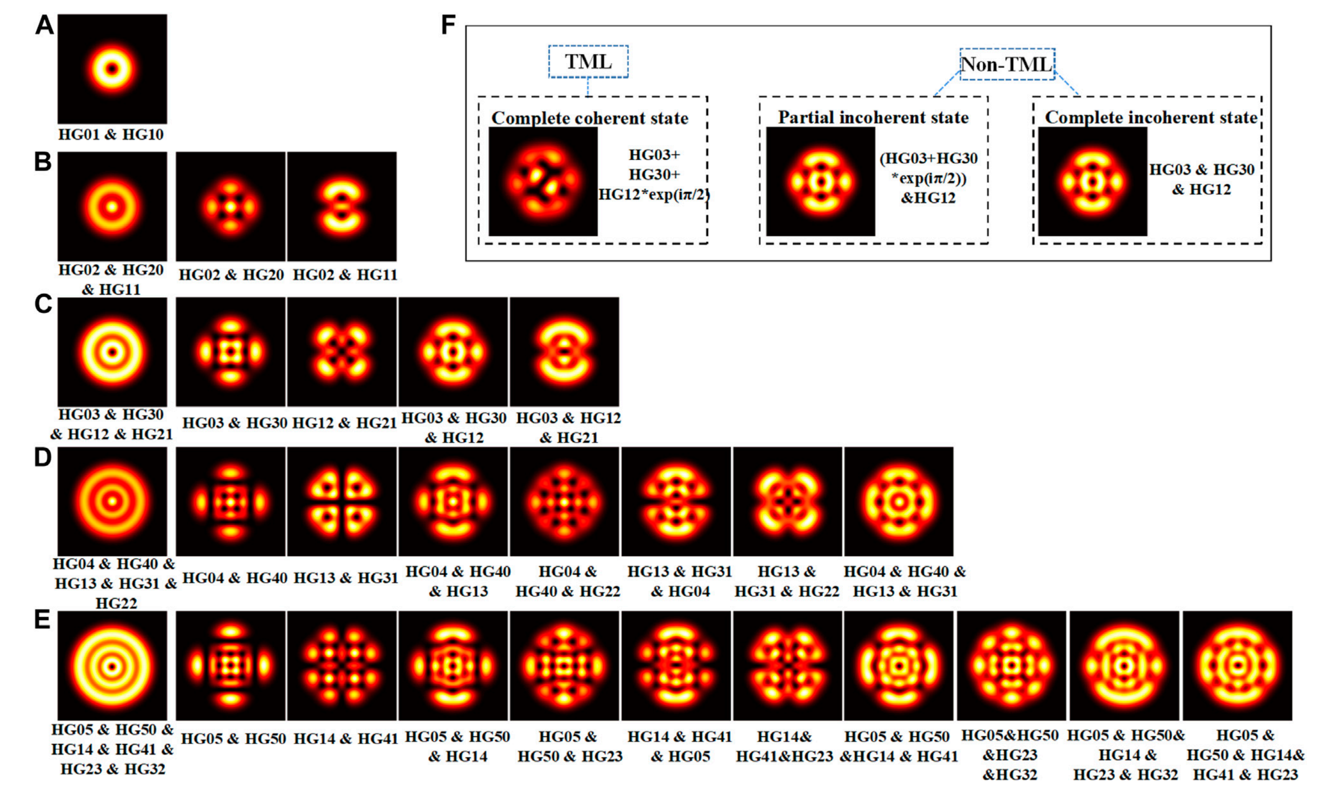

FIGURE 1 | (A–E) Simulated beam patterns in non-TML state. **(F)** The complete coherent superposition belongs to TML state, whereas partial and complete incoherent superpositions are two special kinds of non-TML states. The symbol "+" indicates the coherent superposition between transverse modes, that is, the TML state, and the symbol "&" indicates the incoherent superposition between transverse modes, that is, the non-TML state.

Next, we would like to show the intensity of OL patterns in TML state, which is obtained by coherent superposition between the transverse modes. Select one pattern in non-TML state from **Figure 1**, and use **Eq. 3** to perform TML simulation with different locking phases by coherently superimposing the corresponding composed modes; the results can be obtained in **Figure 2**.

As shown in **Figure 2**, for the case of the combination of HG_{03}, HG_{30}, and HG_{12} modes, their pattern in non-TML state is a regular symmetrical pattern, whereas by conducting the composed modes to TML operations with different locking phases, it can be found that the obtained patterns are quite different with each other. In most cases, if the composition modes reach more than two, their patterns in TML and non-TML state are totally different, whereas for the two-mode composed pattern, simulation results based on **Eqs 1–6** contrastively show the intensity of OL patterns in TML and non-TML state in **Figure 3**.

As shown in **Figures 3A–C**, abundant beam patterns in TML states composed of only two HG eigenmodes are simulated with different locking phases. The patterns in the same ring of **Figure 3** are composed of HG modes in the same order, whereas the orders of HG eigenmodes in different rings are different, with the values being 1 to 4 from the inner most ring ($m + n = 1$) to the outer most one ($m + n = 4$). The patterns located between two rings are composed of two HG eigenmodes with different but adjacent orders. α, β, and γ represent the phase items with locking phase of $\pi/4$, $\pi/2$, and π, respectively. Comparing **Figures 3B,C** with **Figure 3D**, it can be discovered that the patterns in TML state with locking phase of $\pi/2$ are basically the same as the corresponding patterns in non-TML state when the composed modes are in the same order, whereas in different orders, the patterns of two HG mode composed beams in non-TML state are the same as those in TML state with locking phase of π. Throughout the simulation results, we can find that for most cases, it is feasible to describe the formation of OL through the intensity distribution with the coherent superposition of HG modes in TML state. However, if the output light intensity can be characterized by TML and non-TML states simultaneously, it is tough to judge the exact state by the intensity distribution alone.

Interference Method to Distinguish OL Patterns

In this section, we show the difference between OL patterns in TML and non-TML states through interference method with a plane wave. The theoretical analysis of interference between OL pattern composed of HG modes in TML or non-TML state and a plane wave is investigated in **Supplementary Appendix SA**. Then, we can get the intensity of the interference result as follows:

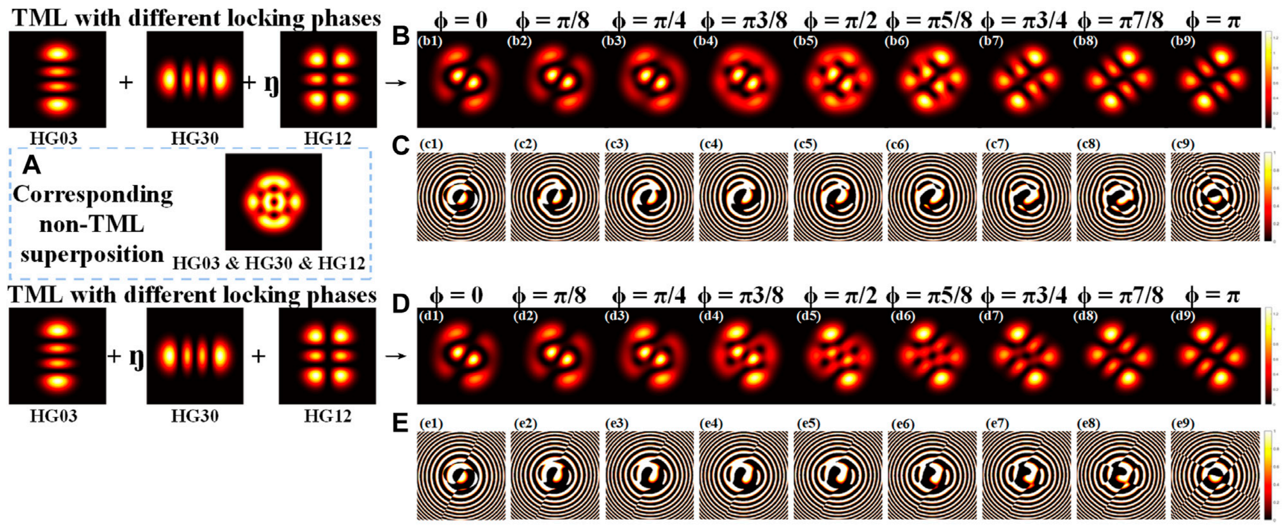

FIGURE 2 | (B–E) Simulated beam patterns composed of HG_{03}, HG_{30}, and HG_{12} modes in TML states with different locking phases. **(A)** Corresponding pattern in non-TML state. $\eta = \exp(i\phi)$, (X1)–(X9) correspond to the TML results with locking phase from 0 to π, X = b, c, d, e. **(C)** and **(E)** are simulated phases of **(B)** and **(D)**, respectively.

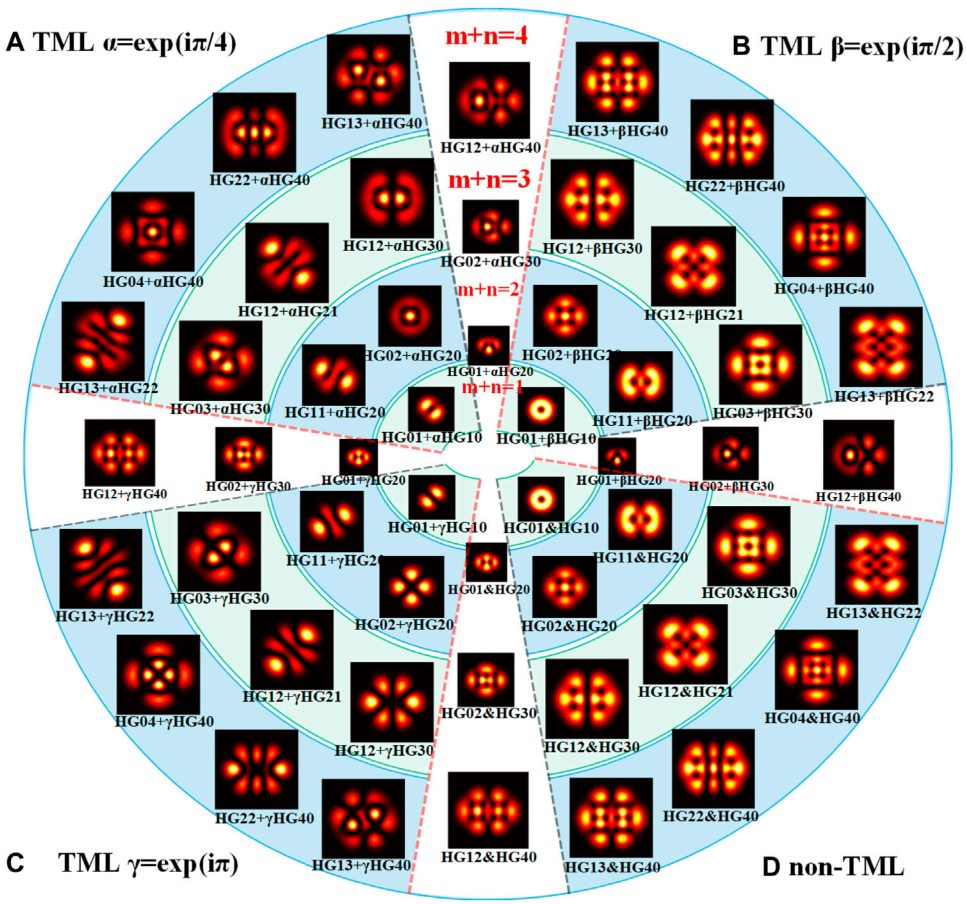

FIGURE 3 | Simulated far field beam patterns in TML and non-TML states composed of two HG modes. **(A–C)** Patterns in TML state with locking phases of $\pi/4$, $\pi/2$, and π, respectively. **(D)** Patterns in non-TML state composed of corresponding HG modes.

$$
\begin{aligned}
I_{\text{non-TML-int}} &= \left[HG_1 \cdot \exp(i\phi) + \exp(ikz)\right] \times conj\left[HG_1 \right.\\
&\quad \left. \cdot \exp(i\phi) + \exp(ikz)\right] + \left[HG_2 + \exp(ikz)\right] \\
&\quad \times conj\left[HG_2 + \exp(ikz)\right] \\
&= \mathrm{Re}^2\{HG_1\} + \mathrm{Im}^2\{HG_1\} + 1 \\
&\quad + 2\sqrt{\mathrm{Re}^2\{HG_1\} + \mathrm{Im}^2\{HG_1\}} \cdot \sin(kz - \phi + \beta) \\
&\quad + \mathrm{Re}^2\{HG_2\} + \mathrm{Im}^2\{HG_2\} + 1 \\
&\quad + 2\sqrt{\mathrm{Re}^2\{HG_2\} + \mathrm{Im}^2\{HG_2\}} \cdot \sin(kz + \beta)
\end{aligned} \tag{7}
$$

$$
\begin{aligned}
I_{\text{TML-int}} &= \left[HG_1 \cdot \exp(i\phi) + HG_2 + \exp(ikz)\right] \times conj\left[HG_1 \right.\\
&\quad \left. \cdot \exp(i\phi) + HG_2 + \exp(ikz)\right] \\
&= \mathrm{Re}^2\{HG_1\} + \mathrm{Im}^2\{HG_1\} + 1 \\
&\quad + 2\sqrt{\mathrm{Re}^2\{HG_1\} + \mathrm{Im}^2\{HG_1\}} \sin(kz - \phi + \beta) \\
&\quad + \mathrm{Re}^2\{HG_2\} + \mathrm{Im}^2\{HG_2\} + 1 + 2\sqrt{A^2 + B^2} \sin(\phi + \gamma)
\end{aligned} \tag{8}
$$

where **Eqs 7, 8** correspond to Eqs. A6, A7 in **Supplementary Appendix SA**, respectively. Comparing **Eq. 8** with **Eq. 7**, we find that the interferences between plane wave and OL in the two states of TML and non-TML are both related to the phase item of the composed modes. However, **Eq. 8** indicates that there are two last items related to the phase ϕ in the interference between plane wave and OL in TML state, whereas there is only one related phase item $2\sqrt{\mathrm{Re}^2\{HG_1\} + \mathrm{Im}^2\{HG_1\}} \sin(kz - \phi + \beta)$ in **Eq. 7** of interference between plane wave and OL in non-TML state. In order to observe the influence of phase item on interference results more intuitively, we make simulations according to **Eqs 7, 8**, and the simulated interference results can be obtained as shown in **Figure 4**.

As shown in **Figure 4**, although the OL pattern in TML and non-TML states may have same intensity distributions, their interference patterns with plane wave are different. The simulated interference results of the OL pattern in TML state with a plane wave show that there are bifurcations at all the dark regions [see **Figure 4**(a1)–(a9), (d1)–(d5), (g1)–(g4)]. In contrast, some dark regions of the interference pattern of OL in non-TML state with a plane wave do not have bifurcations, revealing no phase singularities there [see **Figure 4**(b3), (b7), (b9), (e1)–(e5), (h2), (h3)]. These are the main differences between OL patterns in TML and non-TML states through interference method. In addition, to further study the interference characteristic of the OL in non-TML state, we selected two beams from **Figure 1** and performed the interference simulations. Different relative phases of the HG modes that comprise the OL pattern are also considered in the simulations. The results are depicted in **Figure 5**.

It can be found from the previous discussion that the intensity distribution of OL in non-TML state is independent of the phase of combined modes. Therefore, the intensities of OL composed of HG modes with different locking phases before interference with the plane wave in **Figures 5B–D,F–H** are the same as those in **Figures 5A,E**, respectively. By comparing the interference patterns between wave plane and OL in non-TML state under different phases, we find that the interference bifurcations show new features. For example, the interference fringes in the case of **Figure 5B** show no obvious bifurcation, but only slight relative displacement between fringe and dark area center can be observed. In contrast, **Figure 5**(c1)–(c5), (d1)–(d5) shows clear interference bifurcation fringes. Similarly, in **Figures 5F–H**, there are no forked stripes in the dark area of the beam pattern, enlarged as **Figure 5**(f2), (f4), (f6), (g2), (g6), (h1), and (h4), whereas other dark areas possess interference bifurcations. Therefore, for the OL in non-TML state, although its beam intensity distribution is independent of the phase, the phase item of the composed modes still affects their interference patterns, which is consistent with Eq. A6 in **Supplementary Appendix SA**. This is different from the previous understanding that all dark areas have phase singularities [15, 16]. For beams with intensity distribution similar to OL, it may be a non-TML superposition state of several HG modes. In this case, although there is fringe bifurcation in the interference pattern, it still comes from the superposition of unlocked modes, so necessarily there is no vortex phase at this position. In fact, combining **Figures 4**, **5**, it is seen that the dark zone of OL in TML state possesses phase singularity, whereas the existence and distribution of phase singularity of OL in non-TML state vary with the phases of composed HG modes.

Beat Frequency Spectra Method to Distinguish OL Patterns

In this section, we propose the method by observing the characteristic of beat frequency spectra, which could be applied to further distinguish OL in TML or non-TML state. First, for OL in TML state, it is assumed that frequencies of the transverse modes involved in the locking are pulled to the same value by the cooperative frequency locking effect with the aid of cavity nonlinearity [31]. As the frequencies are pulled to the same, it is obvious for no beat frequency components. Then, for the case of OL in non-TML state, the intensities of composed modes are superimposed, whereas their frequencies compete with each other, resulting in several-spike beat frequency spectra. Actually, in addition to the aforementioned TML and non-TML states, there are two other states of OL in actual multi–transverse-mode laser, which we call the only-phase-locking and prelocking states. The most common case we find is the only-phase-locking state. In this case, the intensity of OL pattern is stable, and the phase is locked, generally not π/2, whereas the frequencies of the composed modes are not completely locked at the same value, resulting in two-cluster spectra. The prelocking state corresponds to the periodic beat frequency spectra. It takes place when the frequency interval of the transverse modes involved in the locking is decreased close to the value meeting the cooperative locking frequency effect. The harmonic content of the mode-beat signal strongly increases if its frequency difference ν_B is reduced. While ν_B becomes comparable to or smaller than the homogeneous line width of the gain medium, the oscillating modes involved share a large part of the nonhomogeneously broadened population inversion. As a

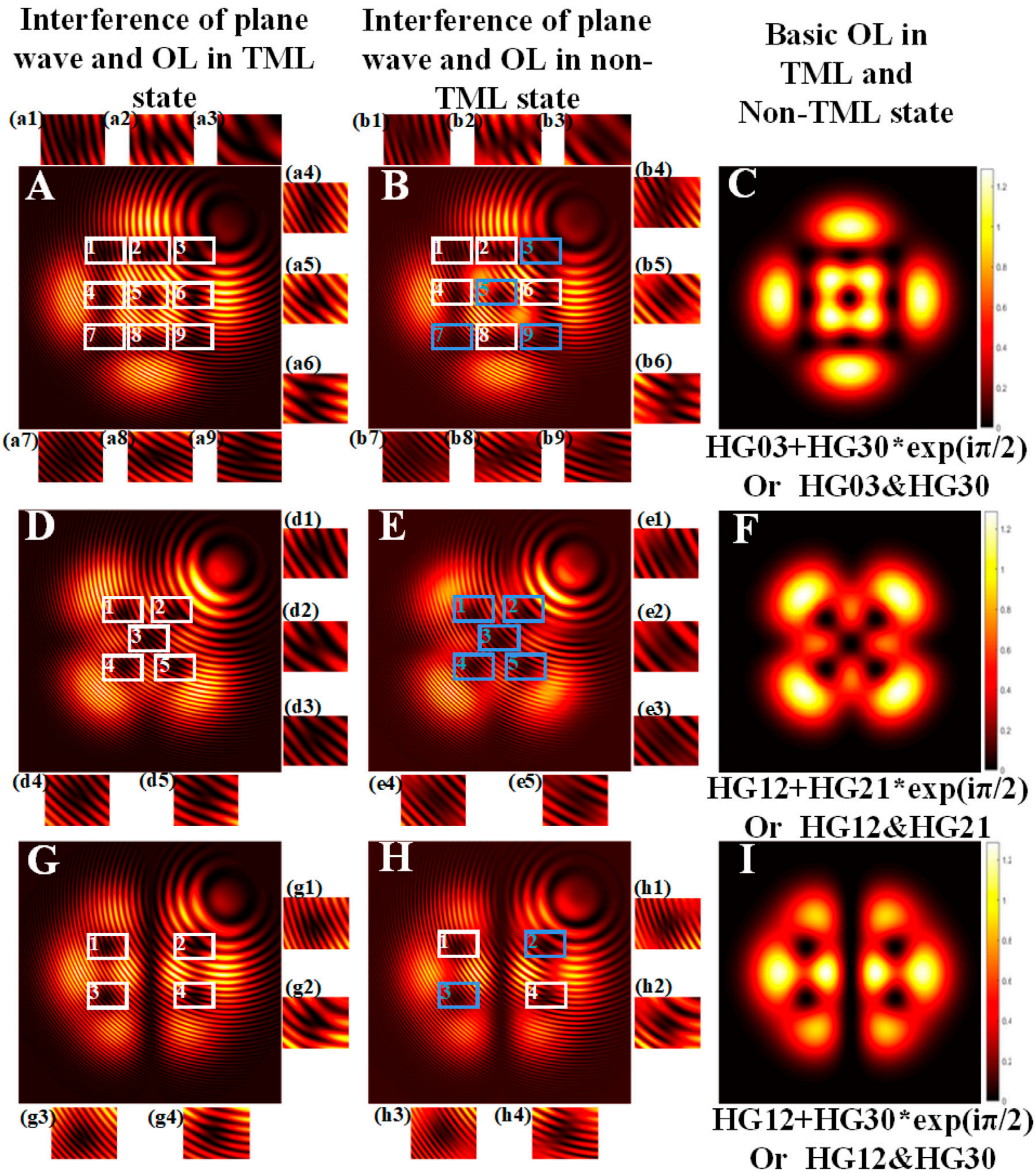

FIGURE 4 | Simulated interference patterns between plane wave and OL in TML states **(A)**, **(C)**, and **(G)** and non-TML states **(B)**, **(E)**, and **(H)**. **(C)**, **(F)**, and **(I)** are the corresponding OL patterns selected from **Figure 3**. The inserts show the enlarged area of the interference fringes.

result, this situation is known to lead to an increase in the effective mode pushing. When reaching a prelocking but not perfectly locking state, the beat frequency spectra will periodically oscillate with this frequency difference ν_B as the interval [49, 50]. The relationship between the intensity of each mode and the oscillation frequency satisfies the Cooperative Frequency Shift law [51], which is expressed by

$$\sum_n \left(\overline{\omega_n} - \nu_n\right)\left|f_n\right|^2 = 0 \tag{9}$$

where $\overline{\omega_n}$ is the pulled frequency of the nth mode, ν_n is the oscillation frequency, and f_n is the amplitude of the field. If the participating modes are ideally locked to the same frequency ν_{cf}, by substituting ν_{cf} into **Eq. 9**, we can obtain

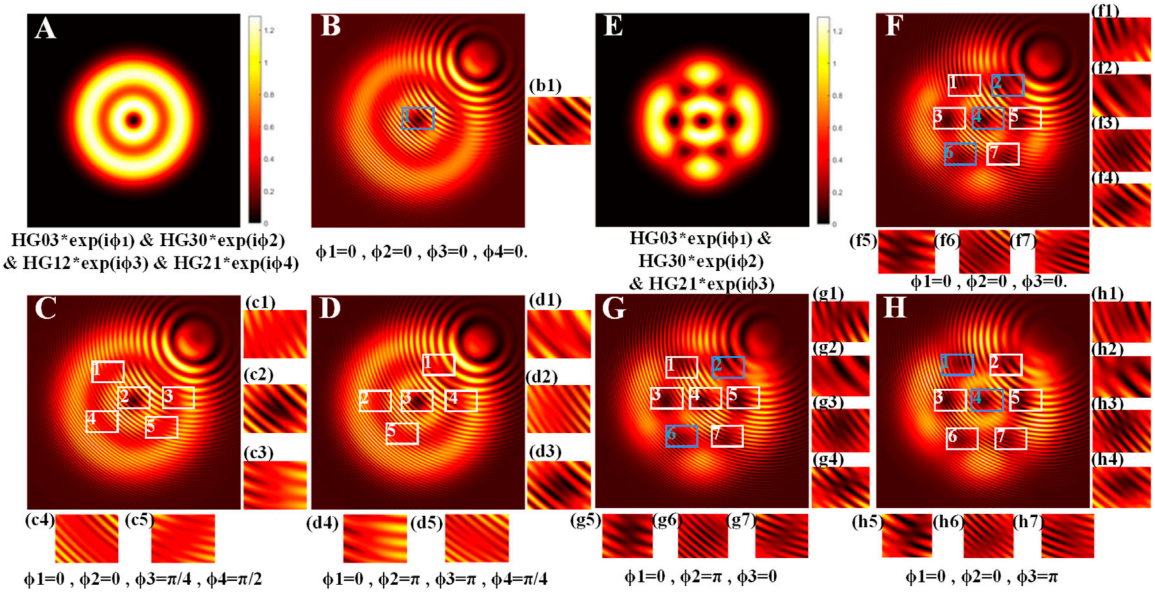

FIGURE 5 | Simulated interference results in non-TML states with different phases. The inserts show the enlarged figures of the interference fringes.

$$\sum_n \left(\overline{\omega_n} - \nu_{cf}\right)\left|f_n\right|^2 = 0 \tag{10}$$

$$\nu_{cf} = \frac{\sum_n \overline{\omega_n}\left|f_n\right|^2}{\sum_n \left|f_n\right|^2} \tag{11}$$

Accordingly, after prelocking state, if the frequencies of the composed modes are pulled to the same value by cooperative frequency locking effect, this value would be the average of frequency weighted by the intensity of each mode, thus leading no beat frequency components and reaching TML state.

EXPERIMENTAL SETUP AND RESULTS

In order to verify the above theory and simulation analysis, we carried out experimental verification based on microchip solid-state laser with large Fresnel number. The schematic diagram of experimental setup is shown in **Figure 6**. The designed microchip cavity for OVL generation is composed of a 0.4-mm-thick 1.0 at% doped Nd:YAG chip and a 1-mm-thick x-cut $LiTO_3$ chip [52]. The cross-section dimensions of the chips are of 5×5 mm^2. The two chips are stacked together to form the laser cavity, with 5% reflection coating at 1,064 nm on the surface of $LiTO_3$ chip, and high transmission coating at 808 nm and high reflection coating at 1,064 nm on the surface of Nd:YAG chip. The microchip cavity is placed in a copper heat sink to transfer the generated heat. In addition, a 0.01°C temperature controller is applied on the copper heat sink to keep the cavity under stable thermal conditions. Besides, a fiber coupled 808-nm laser diode with maximum output power of 10 W is used as the pump source. Then, the pump beam delivered from the tail fiber with 100-μm core diameter is focused into the microchip cavity by a 1:1 free space optical coupler. The coupling system is fixed in the precise adjustment stage. Under a fixed pump power, OL can be switched by adjusting the pump angle Δθ. The beam profile of the pump beam at the beam waist is a super-Gaussian one close to a flattop [53]. A Mach–Zehnder interferometer is set up to observe the interference fringes of the laser beams. After passing through the beam splitter (BS) 1, the transmitted light is the generated OL pattern, whereas the reflected light becomes a plane wave after being modulated by the aperture diaphragm and lens, and the two beams interfere at BS2. If observing only the intensity distribution of the generated OL pattern, the obstacle board in the figure can be lowered to cover the plane wave. Afterward, the beam passed through BS2 is split into two beams by BS3. For the transmitted beam, the light intensity distribution can be observed on the CCD after the attenuation sheet. By contrast, the reflected beam can be directly detected by a photodetector to detect the beat frequency. No obvious difference was found on the spectra when the photodetector was shifted to measure the mode beat at different positions in a beam cross section. Furthermore, to ensure the RF range of beat frequency of the transverse modes in our setup, a 3-GHz bandwidth photodetector was also used to observe the mode beats of a quite complex series of transverse modes, showing that most of the mode-beat frequencies were located at the 0- to 500-MHz range. Consequently, a 400-MHz bandwidth is enough for all the modes discussed in this article. Last but not least, it should be noticed that the microchip cavity we used is quite thin with a longitudinal interval of about 50 GHz. As a result, it is available for a near-single longitudinal mode operation to prevent influence from the longitudinal modes. The whole experimental setup is shown in **Figure 6**, with a pump power of 5 W and the pump angle ranging from 0° to 10°, as well as the controlled temperature of 22°C.

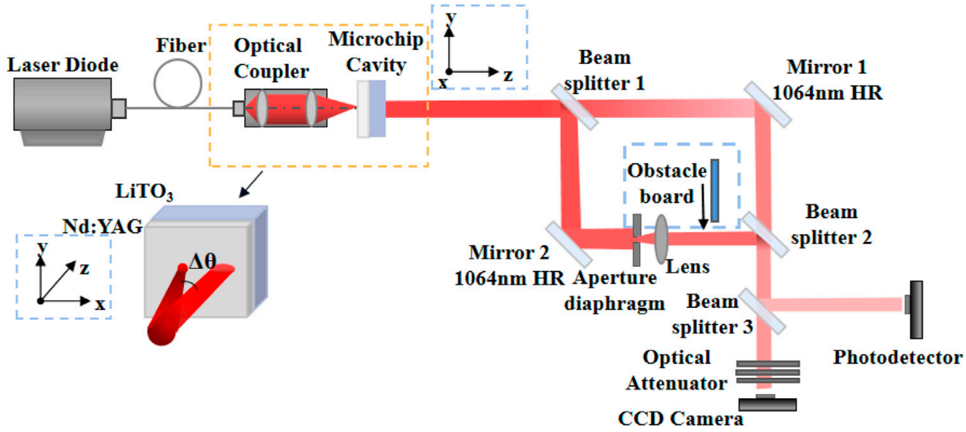

FIGURE 6 | Schematic illustration of experimental arrangement used for OL generation and measurement.

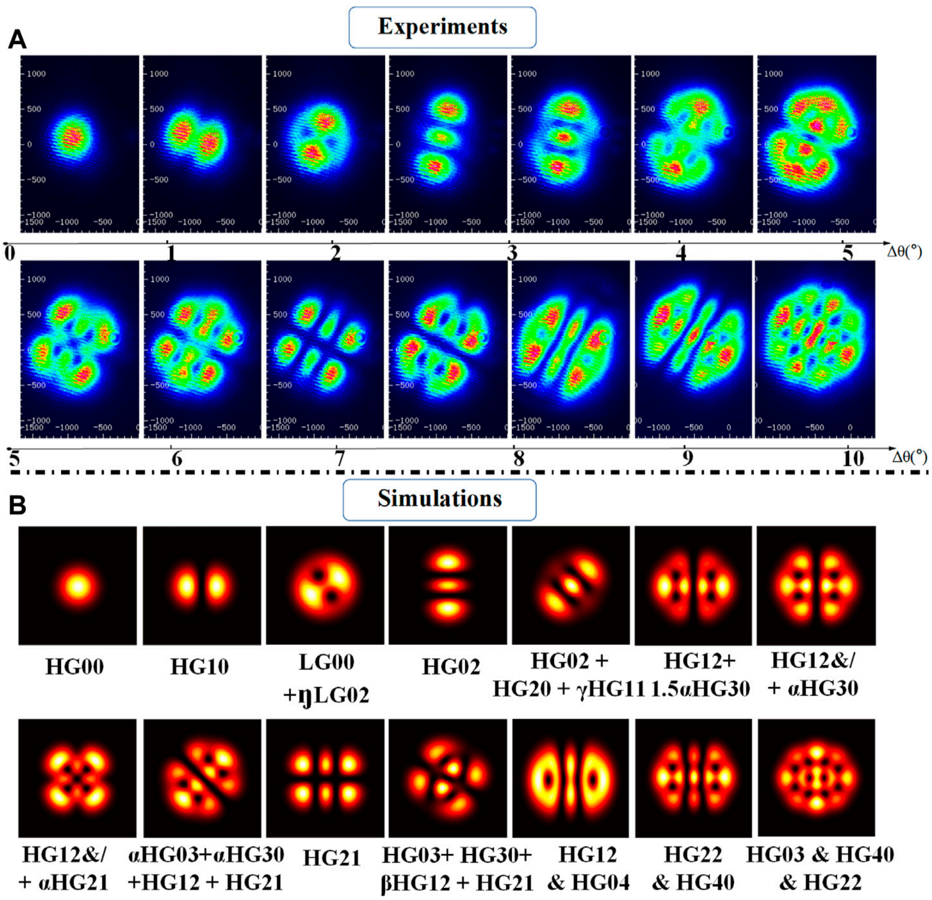

FIGURE 7 | (A) Experimental and **(B)** simulated results of OL patterns versus the change of pump angle $\Delta\theta$ ranging from 0° to 10°, whereas $\alpha = \exp(i\pi/4)$, $\beta = \exp(i\pi/2)$, $\gamma = \exp(i\pi 3/4)$, and ŋ = $\exp(i\pi 3/8)$. The symbol "&/+" indicates that the pattern can be described by both TML and non-TML models.

Abundant OL patterns generated from our microchip laser are investigated by the pump angle tuning. **Figure 7** summarizes the experimentally obtained patterns at various pumping angles, as well as the corresponding simulated results to show the exact mode composition of the OL pattern.

In **Figure 7**, the HG_{00} mode is generated with a pump beam diameter of about 100 μm in the cavity with a normal pump incident. Afterward, through increasing the pump angle $\Delta\theta$ to achieve the enlarged pump area or Fresnel number, OL patterns can be obtained and switched without increasing the pump

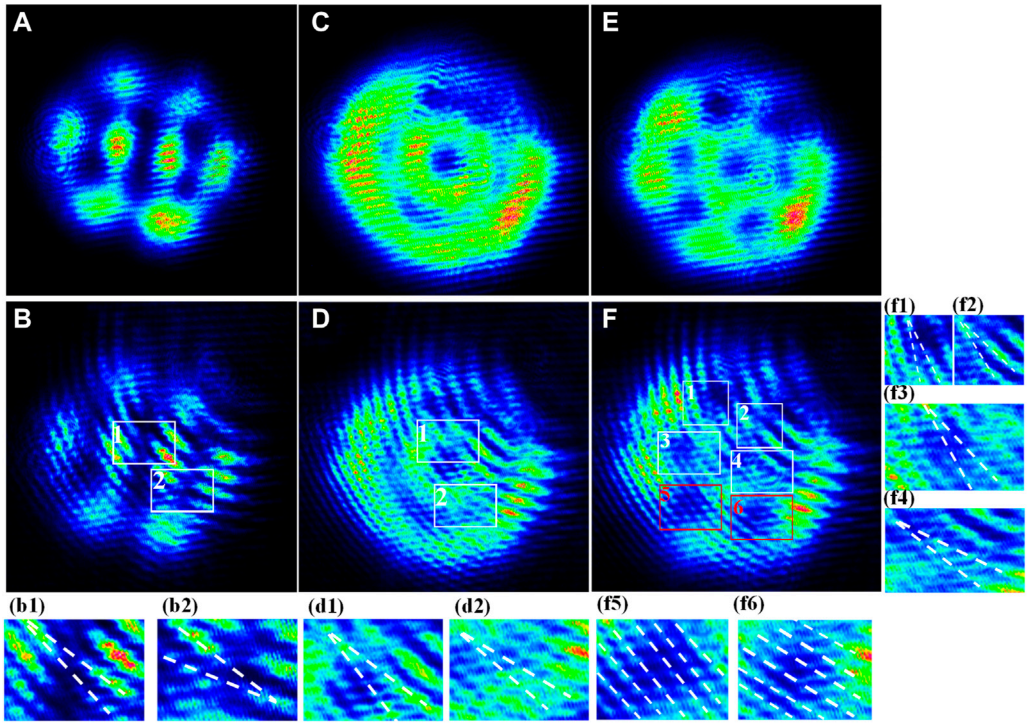

FIGURE 8 | Experimental results of interference between OL patterns in non-TML state and a plane wave, which corresponded to **Figures 4G,H, 5**. The inserts show the enlarged regions of the interference fringes.

power. Therefore, the order of the generated OL increases with the increase of the pump angle within a certain range. As shown in **Figures 7A,B**, the generated convertible OL patterns include basic single HG modes and other patterns in TML or non-TML states.

To investigate the states of the obtained OL patterns from the microchip cavity, the interference characteristic of the OL pattern is experimentally studied, corresponding to the theoretical analysis in *Numerical Characterizations and Theories*. As the research on the interference between plane wave and OVL in TML state has been discussed in Ref. [12], and it shows that all the dark regions have interference bifurcation, so here we mainly study the interference characteristics of plane wave and OL in non-TML state. We have selected several OL patterns in non-TML state from **Figures 4H**, **5**. The beam patterns and corresponding interference fringes are shown in **Figure 8**. Comparing **Figures 8B,D,F** with **Figures 4G,H** and **Figures 5B–D,F–H** respectively, it can be seen that the number and position of the interference fringes do not correspond to those of the dark areas of the OL pattern. First, for **Figure 8B**, it can be seen that only the dark area in the enlarged area has bifurcation stripes, but not elsewhere. Then, there is a bifurcated stripe at the central dark area [enlarged shown in subfigure (d1)] of the concentric ring pattern in **Figure 8D**. And for the dark ring of the beam, a bifurcated stripe appears only at the bottom [enlarged shown in subfigure (d2)]. In addition, the interference results in **Figure 8F** show that two dark regions (f5) and (f6) do not possess bifurcated stripe. These results indicate not all dark areas of the OL patterns in non-TML state possess phase singularity, which is consistent with our theoretical analysis and simulation.

At last, we would like to show the experimentally measured beat frequency spectra results of the OL patterns in TML, non-TML, only-phase-locking, and prelocking states in **Figure 9**.

To begin with, we studied the beat frequency spectra of OL in TML state in **Figure 9B**. In this case, the frequencies of the participating modes were pulled to the same value with the aid of nonlinearity. For this purpose, the beat frequency spectra in TML state are supposed to be the same as those of the single mode (see **Figure 9A**); that is, there is no extra beat frequency component. Subsequently, in the process of increasing the pump angle to switch the OL pattern, we found that it is tough to adjust it to the state of no beat frequency spectra for the OL in higher order. This reveals that the high-order OL is not in TML state to a large extent, but it is in the non-TML state. As shown in **Figure 9**(c3), a beat frequency component (approximately 100 MHz) always exists, which is the frequency difference of the two composed modes HG_{22} and HG_{40} in non-TML state. In addition, the frequency spectra in **Figure 9**(d3) are superimposed with three beat frequency components (approximately 40, 80, and 110 MHz) due to the pairwise beat frequencies of the three participating modes. Then, for the case when only the phases of the composed modes are locked, but the frequencies are not, as shown in **Figures 9E,F**, there comes the OL in only-phase-locking state. Comparing the experimentally obtained patterns in **Figure 9**(e2), (f2) with the simulations in **Figure 9**(e1), (f1), it is found that the phase difference of composed modes is locked to

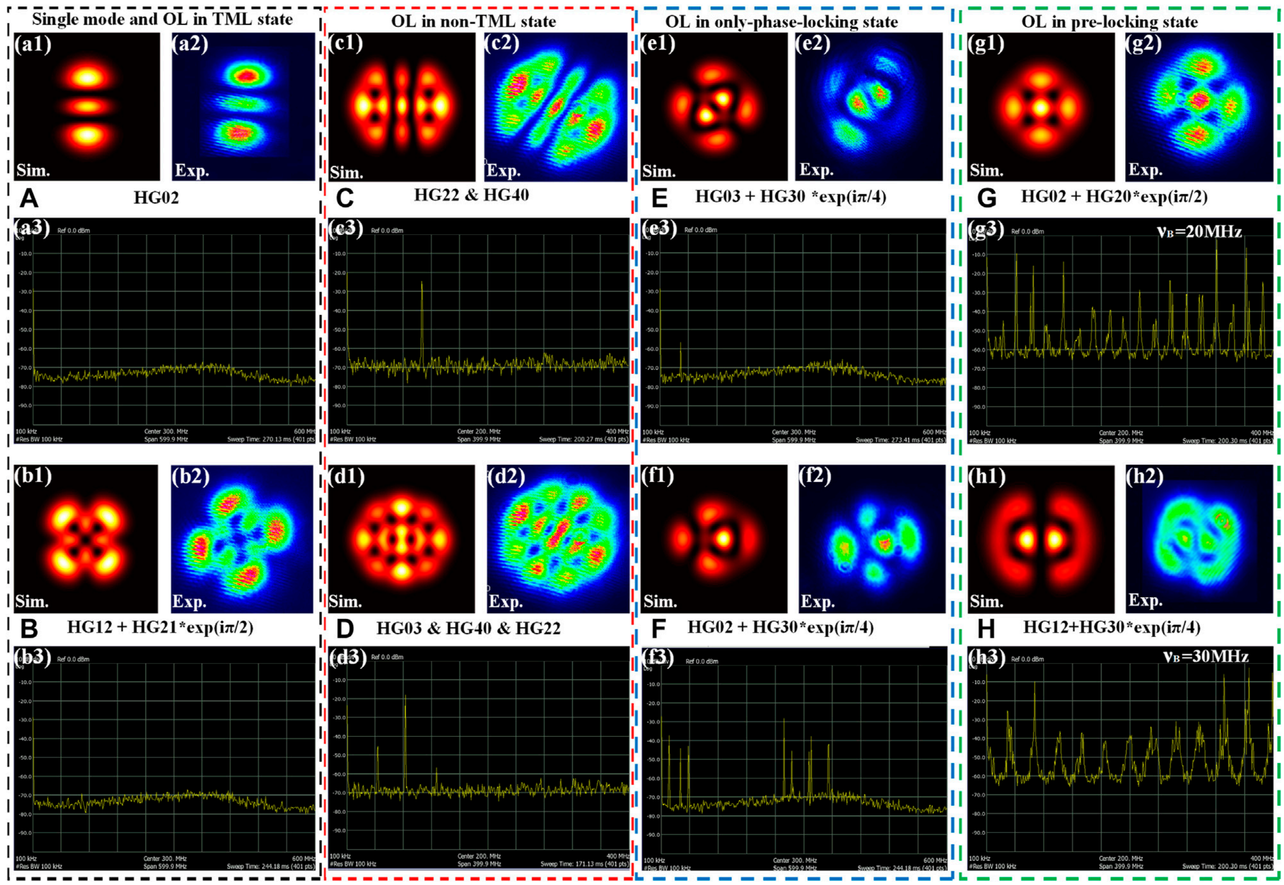

FIGURE 9 | Simulated and experimental results of OL with complex beat frequency spectra in TML and non-TML states. **(A)** Single mode. **(B)** OL in TML state. **(C, D)** OL in non-TML state. **(E, F)** OL in only-phase-locking state. **(G, H)** OL in prelocking state.

a constant value π/4, whereas the frequencies of composed modes are not perfectly locked together, resulting in the beat spectrum as shown in **Figure 9**(e3), (f3). For **Figure 9**(f3), the multispectra may be due to the two-order transverse mode families participating in oscillation. The frequency difference between the two transverse mode families is relatively large, resulting in two clusters of frequency spectra, and then the coupling of the modes in two orders leads to the appearance of multiple frequency spectra. Last but not the least, we found that in the lower-order OL switching process, there was a transitional stage from prelocking to locking. **Figures 9G,H** indicates the intensities and periodic spectra of OL in prelocking state, which are the superposition of transverse modes in the second degenerated family ($m + n = 2$) and the third degenerated family ($m + n = 3$), respectively. As discussed in *Numerical Characterizations and Theories*, the prelocking state occurs when the frequency interval of the transverse modes involved in the locking is decreased close to the value meeting the cooperative locking frequency effect. The harmonic content of the mode-beat signal strongly increases if its frequency difference ν_B is further reduced. When reaching a prelocking but not perfectly locking state, the beat frequency spectra will periodically oscillate with this frequency difference ν_B as the interval, and ν_B in (g3) and (h3) of **Figure 9** is 20 and 30 MHz, respectively.

CONCLUSION

In summary, we have successfully demonstrated the distinction methods of OL patterns in TML state and non-TML state. First, through the intensity, the OL pattern in TML state varies greatly with the locking phase, and there are both symmetrical and asymmetrical patterns. Whereas for OL pattern in non-TML state, as only intensity superposition is performed, it has nothing to do with the relative phase of the composed modes, and the intensity pattern is always symmetrical. Next, through simulations and experiments on the interference between OL patterns and the plane wave, the OL patterns in the above two states could be distinguished. When the OL is in TML state, all the dark zones possess phase singularity. In contrast, the phase singularity of OL in non-TML state varies with the phases of the composed modes, and some dark regions of OL in non-TML state do not possess phase singularity. At last, an OL state judgment with the beat frequency spectra is proposed as an auxiliary means. For TML and non-TML state, our analysis shows that the corresponding beat frequency spectra are supposed to be null-component spectra and several-spike spectra, respectively. In addition, the other two types of OL states with beat frequency spectra are summarized; that is, the extra-component and two-cluster spectra correspond to only-phase-locking state, and the periodic spectra correspond to prelocking state. The OL patterns and interference patterns can be predicted by the established theoretical model and are in consonance with the experimental results. With the summarization of such three ingenious methods including intensity comparison, interferometry, and beat frequency spectrum to distinguish OL patterns in TML or non-TML states, it is beneficial for further rigorously understanding the physical mechanism of laser transverse pattern possessing OL.

DATA AVAILABILITY STATEMENT

The original contributions presented in the study are included in the article/**Supplementary Material**, further inquiries can be directed to the corresponding author.

AUTHOR CONTRIBUTIONS

XW and ZZ conceived the idea and performed analytical derivations. XW and ZZ performed numerical simulations and experiments. XW wrote the manuscript. All authors provided critical feedback and helped shape the research, analysis and manuscript.

FUNDING

ZZ acknowledges financial support *via* National Natural Science Foundation of China (NSFC), (61805013).

SUPPLEMENTARY MATERIAL

The Supplementary Material for this article can be found online at: https://www.frontiersin.org/articles/10.3389/fphy.2021.801916/full#supplementary-material

REFERENCES

1. Ungar PJ, Weiss DS, Riis E, Chu S Optical Molasses and Multilevel Atoms: Theory. *J Opt Soc Am B* (1989) 6:2058–71. doi:10.1364/JOSAB.6.002058
2. Weiss DS, Riis E, Shevy Y, Ungar PJ, Chu S Optical Molasses and Multilevel Atoms: experiment. *J Opt Soc Am B* (1989) 6:2072–83. doi:10.1364/JOSAB.6.002072
3. Jessen PS, Gerz C, Lett PD, Phillips WD, Rolston SL, Spreeuw RJC, et al. Observation of Quantized Motion of Rb Atoms in an Optical Field. *Phys Rev Lett* (1992) 69:49–52. doi:10.1103/PhysRevLett.69.49
4. Verkerk P, Lounis B, Salomon C, Cohen-Tannoudji C, Courtois J-Y, Grynberg G Dynamics and Spatial Order of Cold Cesium Atoms in a Periodic Optical Potential. *Phys Rev Lett* (1992) 68:3861–4. doi:10.1103/PhysRevLett.68.3861
5. Klische W, Weiss CO, Wellegehausen B Spatiotemporal Chaos from a continuousNa2laser. *Phys Rev A* (1989) 39:919–22. doi:10.1103/PhysRevA.39.919
6. Tredicce JR, Quel EJ, Ghazzawi AM, GreenPernigo CA, Pernigo MA, Narducci LM, et al. And Lugiato LA. Spatial and Temporal Instabilities in a CO_2 LaserSpatial and Temporal Instabilities in aCO2laser. *Phys Rev Lett* (1989) 62:1274–7. doi:10.1103/PhysRevLett.62.1274
7. Dangoisse D, Hennequin D, Lepers C, Louvergneaux E, Glorieux P Two-dimensional Optical Lattices in aCO2laser. *Phys Rev A* (1992) 46:5955–8. doi:10.1103/PhysRevA.46.5955
8. Huyet G, Martinoni MC, Tredicce JR, Rica S Spatiotemporal Dynamics of Lasers with a Large Fresnel Number. *Phys Rev Lett* (1995) 75:4027–30. doi:10.1103/PhysRevLett.75.4027
9. Huyet G, Tredicce JR Spatio-temporal Chaos in the Transverse Section of Lasers. *Physica D: Nonlinear Phenomena* (1996) 96:209–14. doi:10.1016/0167-2789(96)00021-8
10. Brambilla M, Battipede F, Lugiato LA, Penna V, Prati F, Tamm C, et al. Transverse Laser Patterns. I. Phase Singularity Crystals. *Phys Rev A* (1991) 43:5090–113. doi:10.1103/PhysRevA.43.5090
11. Coullet P, Gil L, Rocca F Optical Vortices. *Opt Commun* (1989) 73:403–8. doi:10.1016/0030-4018(89)90180-6
12. Scheuer J, Orenstein M Optical Vortices Crystals: Spontaneous Generation in Nonlinear Semiconductor Microcavities. *Science* (1999) 285:230–3. doi:10.1126/science.285.5425.230
13. Chen YF, Lan YP Formation of Optical Vortex Lattices in Solid-State Microchip Lasers: Spontaneous Transverse Mode Locking. *Phys Rev A* (2001) 64:063807. doi:10.1103/PhysRevA.64.063807
14. Chen YF, Lan YP Transverse Pattern Formation of Optical Vortices in a Microchip Laser with a Large Fresnel Number. *Phys Rev A* (2001) 65:013802. doi:10.1103/PhysRevA.65.013802
15. Otsuka K, Ko J-Y, Makino H, Ohtomo T, Okamoto A Transverse Effects in a Microchip Laser with Asymmetric End-Pumping: Modal Interference and Dynamic Instability. *J Opt B: Quan Semiclass. Opt.* (2003) 5:R137–R145. doi:10.1088/1464-4266/5/3/202
16. Otsuka K, Chu S-C Generation of Vortex Array Beams from a Thin-Slice Solid-State Laser with Shaped Wide-Aperture Laser-Diode Pumping. *Opt Lett* (2009) 34:10–2. doi:10.1364/OL.34.000010
17. Shen Y, Wan Z, Fu X, Liu Q, Gong M Vortex Lattices with Transverse-Mode-Locking States Switching in a Large-Aperture off-axis-pumped Solid-State Laser. *J Opt Soc Am B* (2018) 35:2940–4. doi:10.1364/JOSAB.35.002940
18. Jaksch D, Bruder C, Cirac JI, Gardiner CW, Zoller P Cold Bosonic Atoms in Optical Lattices. *Phys Rev Lett* (1998) 81:3108–11. doi:10.1103/PhysRevLett.81.3108
19. Greiner M, Mandel O, Esslinger T, Hänsch TW, Bloch I Quantum Phase Transition from a Superfluid to a Mott Insulator in a Gas of Ultracold Atoms. *Nature* (2002) 415:39–44. doi:10.1038/415039a
20. Maher-Mcwilliams C, Douglas P, Barker PF Laser-driven Acceleration of Neutral Particles. *Nat Photon* (2012) 6:386–90. doi:10.1038/nphoton.2012.87
21. Padgett M, Bowman R Tweezers with a Twist. *Nat Photon* (2011) 5:343–8. doi:10.1038/nphoton.2011.81
22. Kuo C-F, Chu S-C Numerical Study of the Properties of Optical Vortex Array Laser Tweezers. *Opt Express* (2013) 21:26418–31. doi:10.1364/oe.21.026418
23. Woerdemann M, Alpmann C, Esseling M, Denz C Advanced Optical Trapping by Complex Beam Shaping. *Laser Photon Rev* (2013) 7:839–54. doi:10.1002/lpor.201200058
24. Shen Y, Wang X, Xie Z, Min C, Fu X, Liu Q, et al. Optical Vortices 30 Years on: OAM Manipulation from Topological Charge to Multiple Singularities. *Light Sci Appl* (2019) 8:1–29. doi:10.1038/s41377-019-0194-2
25. Yang Y, Ren Y-X, Chen M, Arita Y, Rosales-Guzmán C Optical Trapping with Structured Light: a Review. *Adv Photon* (2021) 3:034001. doi:10.1117/1.AP.3.3.034001
26. Mair A, Vaziri A, Weihs G, Zeilinger A Entanglement of the Orbital Angular Momentum States of Photons. *Nature* (2001) 412:313–6. doi:10.1038/35085529
27. Wang J, Yang J-Y, Fazal IM, Ahmed N, Yan Y, Huang H, et al. Terabit Free-Space Data Transmission Employing Orbital Angular Momentum Multiplexing. *Nat Photon* (2012) 6:488–96. doi:10.1038/nphoton.2012.138
28. Wang J Advances in Communications Using Optical Vortices. *Photon Res* (2016) 4:B14–28. doi:10.1364/prj.4.000b14

29. Gong L, Zhao Q, Zhang H, Hu X-Y, Huang K, Yang J-M, et al. Optical Orbital-Angular-Momentum-Multiplexed Data Transmission under High Scattering. *Light Sci Appl* (2019) 8:268–78. doi:10.1038/s41377-019-0140-3
30. Graham R, Haken H Laserlight ? First Example of a Second-Order Phase Transition Far Away from thermal Equilibrium. *Z Physik* (1970) 237:31–46. doi:10.1007/BF01400474
31. Lugiato LA, Narducci LM, Oldano C Cooperative Frequency Locking and Stationary Spatial Structures in Lasers. *J Opt Soc Am B* (1988) 5:879–88. doi:10.1364/josab.5.000879
32. Lugiato LA, Oppo GL, Tredicce JR, Narducci LM, Pernigo MA Instabilities and Spatial Complexity in a Laser. *J Opt Soc Am B* (1990) 7:1019–33. doi:10.1364/josab.7.001019
33. Staliunas K, Weiss CO Tilted and Standing Waves and Vortex Lattices in Class-A Lasers. *Physica D: Nonlinear Phenomena* (1995) 81:79–93. doi:10.1016/0167-2789(94)00193-T
34. Staliunas K, Weiss CO Nonstationary Vortex Lattices in Large-Aperture Class B Lasers. *J Opt Soc Am B* (1995) 12:1142–9. doi:10.1364/JOSAB.12.001142
35. Louvergneaux E, Hennequin D, Dangoisse D, Glorieux P Transverse Mode Competition in aCO2laser. *Phys Rev A* (1996) 53:4435–8. doi:10.1103/physreva.53.4435
36. D'Alessandro G, Papoff F, Louvergneaux E, Glorieux P Average Patterns and Coherent Phenomena in Wide Aperture Lasers. *Phys Rev E* (2004) 69:066212. doi:10.1103/PhysRevE.69.066212
37. Wan Z, Shen Y, Gong M, Fu X Quadrant-separable Multi-Singularity Vortices Manipulation by Coherent Superposed Mode with Spatial-Energy Mismatch. *Opt Express* (2018) 26:34940. doi:10.1364/OE.26.034940
38. Zhang Z, Zhao C Spontaneous Phase and Frequency Locking of Transverse Modes in Different Orders. *Phys Rev Appl* (2020) 13:024010. doi:10.1103/PhysRevApplied.13.024010
39. Huang H, Ren Y, Yan Y, Ahmed N, Yue Y, Bozovich A, et al. Phase-shift Interference-Based Wavefront Characterization for Orbital Angular Momentum Modes. *Opt Lett* (2013) 38:2348–50. doi:10.1364/OL.38.002348
40. Shen Y, Meng Y, Fu X, Gong M Hybrid Topological Evolution of Multi-Singularity Vortex Beams: Generalized Nature for Helical-Ince-Gaussian and Hermite-Laguerre-Gaussian Modes. *J Opt Soc Am A* (2019) 36:578–87. doi:10.1364/JOSAA.36.000578
41. Sztul HI, Alfano RR Double-slit Interference with Laguerre-Gaussian Beams. *Opt Lett* (2006) 31:999–1001. doi:10.1364/OL.31.000999
42. Emile O, Emile J Young's Double-Slit Interference Pattern from a Twisted Beam. *Appl Phys B* (2014) 117:487–91. doi:10.1007/s00340-014-5859-1
43. Leach J, Padgett MJ, Barnett SM, Franke-Arnold S, Courtial J Measuring the Orbital Angular Momentum of a Single Photon. *Phys Rev Lett* (2002) 88: 257901. doi:10.1103/PhysRevLett.88.257901
44. Gao C, Qi X, Liu Y, Xin J, Wang L Sorting and Detecting Orbital Angular Momentum States by Using a Dove Prism Embedded Mach-Zehnder Interferometer and Amplitude Gratings. *Opt Commun* (2011) 284:48–51. doi:10.1016/j.optcom.2010.08.083
45. Rao AS, Miyamoto K, Omatsu T Direct Generation of Vortex Lattice Modes from an Intracavity Frequency Doubled Pr:YLF Laser. In: Conference on Lasers and Electro-Optics. San Jose, CA: OSA Technical DigestOptical Society of America (2021). paper STh1B.2. doi:10.1364/CLEO_SI.2021.STh1B.2
46. Ma Y, Vallés A, Tung J-C, Chen Y-F, Miyamoto K, Omatsu T Direct Generation of Red and orange Optical Vortex Beams from an off-axis Diode-Pumped Pr3+: YLF Laser. *Opt Express* (2019) 27:18190. doi:10.1364/OE.27.018190
47. Liang H-C, Lin H-Y Generation of Resonant Geometric Modes from off-axis Pumped Degenerate Cavity Nd:YVO4 Lasers with External Mode Converters. *Opt Lett* (2020) 45:2307–10. doi:10.1364/OL.390278
48. Rao AS, Miike T, Miyamoto K, Omatsu T Optical Vortex Lattice Mode Generation from a Diode-Pumped Pr3+:LiYF4 Laser. *J Opt* (2021) 23: 075502. doi:10.1088/2040-8986/ac067d
49. Brunel M, Emile O, Alouini M, Le Floch A, Bretenaker F Experimental and Theoretical Study of Longitudinally Monomode Vectorial Solid-State Lasers. *Phys Rev A* (1999) 59:831–40. doi:10.1103/PhysRevA.59.831
50. Tamm C Frequency Locking of Two Transverse Optical Modes of a Laser. *Phys Rev A* (1988) 38:5960–3. doi:10.1103/PhysRevA.38.5960
51. Wolf E, Agarwal GS Coherence Theory of Laser Resonator Modes. *J Opt Soc Am A* (1984) 1:541–6. doi:10.1364/JOSAA.1.000541
52. Zhang Z, Gui K, Zhao C, Zhang H, Xing Y Direct Generation of Vortex Beam with a Dual-Polarization Microchip Laser. *IEEE Photon Technol Lett* (2019) 31: 1221–4. doi:10.1109/LPT.2019.2922428
53. Yan X, Liu Q, Wang D, Gong M Combined Guiding Effect in the End-Pumped Laser Resonator. *Opt Express* (2011) 19:6883–902. doi:10.1364/OE.19.006883

Conflict of Interest: The authors declare that the research was conducted in the absence of any commercial or financial relationships that could be construed as a potential conflict of interest.

Publisher's Note: All claims expressed in this article are solely those of the authors and do not necessarily represent those of their affiliated organizations, or those of the publisher, the editors and the reviewers. Any product that may be evaluated in this article, or claim that may be made by its manufacturer, is not guaranteed or endorsed by the publisher.

ORIGINAL RESEARCH
published: 11 January 2022
doi: 10.3389/fphy.2021.828487

Imaging Through Random Scatterer with Spatial Coherence Structure Measurement

Deming Peng[1], Xuan Zhang[1], Yonglei Liu[2], Yimeng Zhu[1], Yahong Chen[1]*, Fei Wang[1]* and Yangjian Cai[1,2]*

[1]Institute of Optics, School of Physical Science and Technology, Soochow University, Suzhou, China, [2]Shandong Provincial Engineering and Technical Center of Light Manipulation and Shandong Provincial Key Laboratory of Optics and Photonic Devices, School of Physics and Electronics, Shandong Normal University, Jinan, China

Optical coherence is becoming an efficient degree of freedom for light field manipulations and applications. In this work, we show that the image information hidden a distance behind a random scattering medium is encoded in the complex spatial coherence structure of a partially coherent light beam that generates after the random scatterer. We validate in experiment that the image information can be well recovered with the spatial coherence measurement and the aid of the iterative phase retrieval algorithm in the Fresnel domain. We find not only the spatial shape but also the position including the lateral shift and longitudinal distances of the image hidden behind the random scatterer can be reconstructed, which indicates the potential uses in three-dimensional optical imaging through random scattering media.

Keywords: optical coherence, optical imaging, random scatterer, spatial coherence measurement, iterative phase retrieval

OPEN ACCESS

Edited by:
Xing Fu,
Tsinghua University, China

Reviewed by:
Wen Chen,
Hong Kong Polytechnic University, Hong Kong SAR, China
Huaibin Zheng,
Xi'an Jiaotong University, China

****Correspondence:***
Yahong Chen
yahongchen@suda.edu.cn
Fei Wang
fwang@suda.edu.cn
Yangjian Cai
yangjiancai@suda.edu.cn

Specialty section:
This article was submitted to Optics and Photonics, a section of the journal Frontiers in Physics

Received: *03 December 2021*
Accepted: *16 December 2021*
Published: *11 January 2022*

Citation:
Peng D, Zhang X, Liu Y, Zhu Y, Chen Y, Wang F and Cai Y (2022) Imaging Through Random Scatterer with Spatial Coherence Structure Measurement. Front. Phys. 9:828487. doi: 10.3389/fphy.2021.828487

1 INTRODUCTION

Spatial coherence is an important characteristic to describe the statistical properties of random light fields, and it has played a vital role in understanding interference, propagation, and light-matter interaction of both classical and quantum wave fields [1–3]. Nowadays, the spatial coherence has already been viewed as an efficient tool for light field manipulations and applications [4]. For instance, by simply adjusting the spatial coherence width, i.e., decreasing the spatial coherence of a laser beam, the generated partially (lowly) coherent beams can help reduce the turbulence-induced signal distortion in free-space optical communication [5, 6], and can restrict speckles in optical imaging [7] and beam shaping applications [8]. Since the pioneering work by Gori and his colleagues [9–11], it has been well recognized that by modulating the spatial coherence structure of light source, the partially coherent beams will display many extraordinary propagation properties [12] including self-splitting, self-focusing, self-shaping, and self-reconstruction effects. The spatial coherence structure engineering has found applications in sub-Rayleigh imaging [13], robust microscopy imaging [14], and robust far-field imaging [15].

The methods for modulating the spatial coherence structure can be divided into two types. The first type is based on the famous Wolf's coherent-mode representation [1], in which the partially coherent beam is viewed as an incoherent superposition of a set of spatially coherent modes. By controlling the modal weight and the complex field distribution of each mode, the spatial coherence structure of the synthesized partially coherent beam can be controlled [16–21]. The second approach is based on the (generalized) van Cittert–Zernike theorem, which indicates that a partially coherent secondary source can be generated by propagating a spatially incoherent source in free space or other media [22]. In this approach, the spatial coherence structure of the secondary partially coherent source can be modulated by controlling the intensity distribution of the incoherent source and the response function of the optical system [12, 23].

In the second approach, the incoherent source is typically generated in the experiment by passing a fully coherent structured light through a dynamic random scatterer, e.g., a rotating ground glass disk [4, 23]. Based on the van Cittert–Zernike theorem, the intensity distribution $p(\mathbf{v})$ of the fully coherent structured light before the random scatterer has a determinate relation with the complex spatial coherence structure $\mu(\mathbf{r}_1, \mathbf{r}_2)$ of the generated partially coherent secondary source. For example, when the optical system between the random scatterer and the secondary source is formed by a Fourier lens, $p(\mathbf{v})$ and $\mu(\mathbf{r}_1, \mathbf{r}_2)$ form the Fourier transform pair. Thus, by measuring the complex spatial coherence structure of the partially coherent source, the image information encoded in the fully coherent light hidden behind the random scatterer can be well recovered. Huang and coauthors showed that both the transverse position and the spatial shape of a moving object hidden behind the rotating ground glass disk can be well reconstructed with the complex spatial coherence measurement [24]. Later, Dong and coauthors showed that the polarization properties of the hidden image can be obtained with the spatial coherence matrix measurement [25]. When the optical system is formed by a fractional Fourier transform system, it is found that the image information can be recovered by measuring the complex spatial coherence structure only when the fractional order used in recovery is correct, which indicates the potential application in coherence-based optical encryption and decryption [26].

However, in the above studies, only the image information projected on the random scatterer can be recovered by complex spatial coherence measurement since the restriction of the van Cittert–Zernike theorem. In other words, only the two-dimensional (2D) image information hidden behind the random scatterer can be extracted from the spatial coherence measurement, which limits the application in three-dimensional (3D) optical imaging through random media. To solve this limitation, a question is naturally raised: whether the information of an image (or object) at a certain distance from the random scatterer can be recovered? In this work, we show that with the help of the spatial coherence measurement and the iterative phase retrieval algorithm in the Fresnel domain, the image information hidden a distance behind the rotating ground glass disk can be well reconstructed. Further, it is demonstrated that not only the spatial shape and the lateral shift but also the longitudinal position of the hidden image can be well recovered.

We remark that the research on optical imaging through random media is a historical topic since the early study was carried out by Goodman et al. in the 1960s [27, 28]. However, this topic today is still attracting wide attention from the researchers due to the broad range of its applications from biomedical to astronomical imaging [29, 30]. Different methods have been proposed to realize the optical imaging through scattering media. The most straightforward approaches utilize ballistic photons [31–33]. However, strongly scattering media reduce the number of ballistic photons and lower the signal tremendously. Thus, these methods are used mostly for imaging static objects through a weakly scattering medium. Some methods, such as the wavefront shaping techniques [34–37] and the transmission matrix measurement methods [38, 39], require the transmission properties of the random scatterer itself before imaging. Another approach relies on the memory effect of light through scattering medium [40, 41]. Within the memory effect region, the intensity autocorrelation of the scattered light is identical to the autocorrelation of the object image hidden behind the scatterer [42–46]. Thus, the object can be reconstructed well by using the phase retrieval algorithm [47].

However, the above methods are mainly dealt with optical imaging through a *static* medium [48, 49]. In this work, we propose a different method for optical imaging through a *dynamic* scattering medium. We remark that a few of technologies for optical imaging through dynamic scattering media have been proposed recently [50, 51]. Their methods are based on the intensity correlations of the speckles. Thus, the image information can be reconstructed only when the random fluctuations of the dynamic scatterer obey Gaussian statistics [52]. For the random scattering media having non-Gaussian statistics, e.g., the turbulent atmosphere [53], the proposed method cannot be used anymore. However, our method is based on measuring the second-order field-field correlation (spatial coherence) of a partially coherent light beam. The relation between the image information and the spatial coherence is independent of the statistics of the random medium. In other words, the image information encoded in the spatial coherence structure can be recovered well for the random media with any statistical properties. Thus, our coherence-based method shows robustness in the complex environment, which we have showed in [26].

This work is organized as follows. In **Section 2**, we present our basic principle for encoding the image information hidden behind the random scatterer into the spatial coherence structure of a random light that generates after the random medium and we show the iterative phase retrieval algorithm used in our experiment. In **Section 3**, we present our experimental verification and discuss how to measure the complex spatial coherence of a random light beam with the intensity-intensity cross-correlations. The experimental results to demonstrate the feasibility of our method are presented in **Section 4**. We summarize our findings in **Section 5**.

2 PRINCIPLE

The schematic diagram of the encoding system is shown in **Figure 1A**, in which the image is hidden a distance z in front of the scattering medium. The image is illuminated by a fully coherent light beam. Based on the Huygens-Fresnel diffraction integral formula, the optical field on the front surface of the scattering medium is expressed as

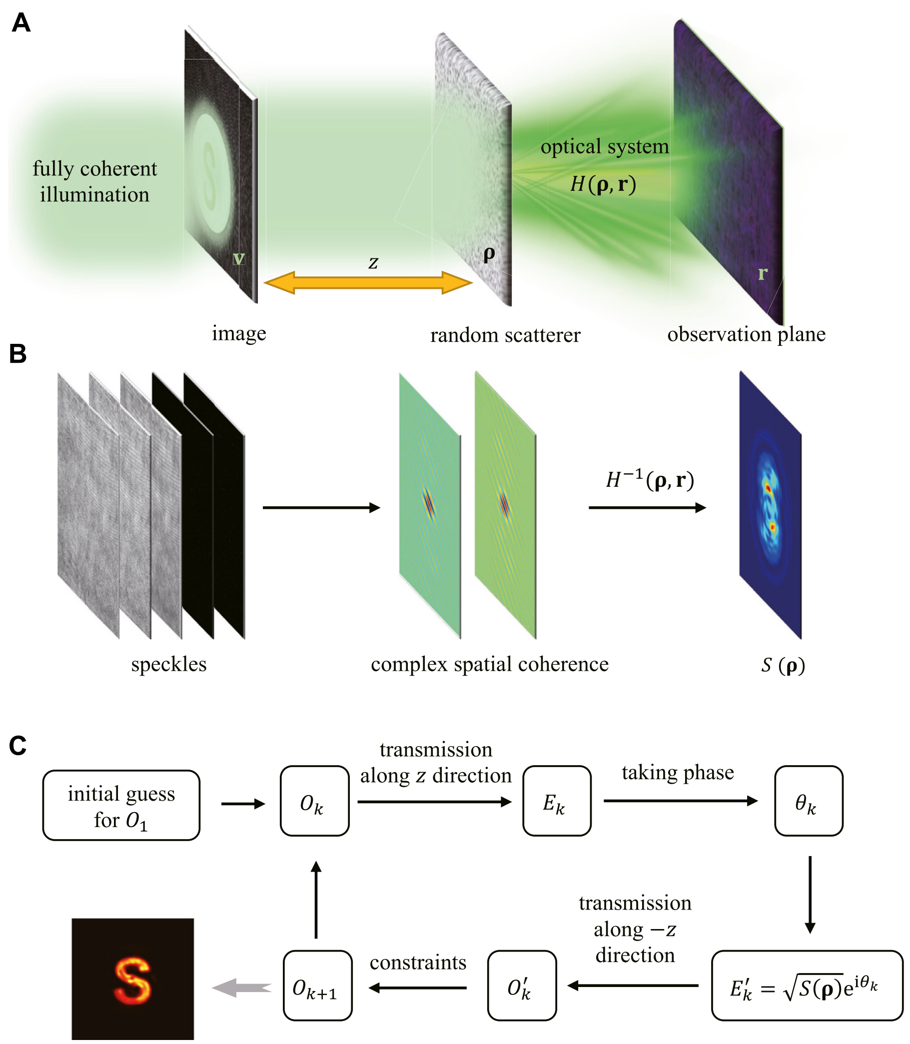

FIGURE 1 | Schematic diagram of optical imaging through a random scattering medium. **(A)** The image hidden a distance z behind a random scatterer is illuminated by a fully coherent light. The scattered light from the random medium passes through an optical system with response function $H(\rho, \mathbf{r})$. The complex spatial coherence structure is measured in the observation plane. **(B)** The intensity $S(\rho)$ on the front surface of the random scatterer can be recovered through inverse transform $H^{-1}(\rho, \mathbf{r})$ of the measured complex spatial coherence. **(C)** The flowchart of the iterative phase retrieval algorithm.

$$E(\boldsymbol{\rho}) = -\frac{\mathrm{i}}{\lambda z}\exp(\mathrm{i}kz)\iint O(\mathbf{v})\exp\left[\frac{\mathrm{i}k}{2z}(\boldsymbol{\rho}-\mathbf{v})^2\right]\mathrm{d}^2\mathbf{v}, \quad (1)$$

where λ denotes the wavelength, $k = 2\pi/\lambda$ is the wavenumber, and $O(\mathbf{v})$ denotes the transmission function of the image. Above, $\mathbf{v}$ and $\boldsymbol{\rho}$ are the spatial coordinates of the cross section where the image and the random scattering medium are located, respectively.

After the beam passes through the random scattering medium, the fully coherent light becomes spatially incoherent if we assume the beam spot on the random scatterer is larger than the inhomogeneity scale of the random scatterer [52]. The statistical properties for a spatially incoherent light are characterized by the cross-spectral density function (in spatial-frequency domain) [1], i.e.

$$W(\boldsymbol{\rho}_1, \boldsymbol{\rho}_2) = \sqrt{S(\boldsymbol{\rho}_1)S(\boldsymbol{\rho}_2)}\delta(\boldsymbol{\rho}_1 - \boldsymbol{\rho}_2), \quad (2)$$

where $S(\boldsymbol{\rho}) = |E(\boldsymbol{\rho})|^2$ denotes the averaged spectral density of the incoherent source and $\delta(\boldsymbol{\rho}_1 - \boldsymbol{\rho}_2)$ is a Dirac delta function, which indicates that the fields at two different spatial positions $\boldsymbol{\rho}_1$ and $\boldsymbol{\rho}_2$ are uncorrelated. Based on the pseudo-mode representation theory [54], the cross-spectral density function in **Eq. 2** can be expanded as

$$W(\boldsymbol{\rho}_1, \boldsymbol{\rho}_2) = \sum_n \alpha_n E_n^*(\boldsymbol{\rho}_1)E_n(\boldsymbol{\rho}_2), \quad (3)$$

where $E_n(\boldsymbol{\rho})$ and α_n stand for the modal function and its modal weight, respectively, for the nth mode. Such pseudo-mode representation indicates that a incoherent (or partially coherent) light can be viewed as a superposition of spatially coherent but mutually uncorrelated modes. For the spatially incoherent light, the modal distribution can be expressed as

$$E_n(\boldsymbol{\rho}) = \sqrt{S(\boldsymbol{\rho})}\exp[i\phi_n(\boldsymbol{\rho})], \tag{4}$$

where $\phi_n(\boldsymbol{\rho})$ is a random phase. For a random scatterer obeying Gaussian statistics [52], we have $\langle \exp[i\phi_n(\boldsymbol{\rho})]\rangle = 0$ and $\langle \exp[i\phi_n(\boldsymbol{\rho}_1) - i\phi_n(\boldsymbol{\rho}_2)]\rangle = \delta(\boldsymbol{\rho}_1 - \boldsymbol{\rho}_2)$, where $\langle\cdot\rangle$ denotes the ensemble average.

Based on the van Cittert–Zernike theorem, when the incoherent light from the random scattering medium passes through a linear optical system with an impulse response function $H(\boldsymbol{\rho}, \mathbf{r})$, the spatial coherence of the light will be improved. The modal function in the observation plane turns out to be

$$E_n(\mathbf{r}) = \iint \sqrt{S(\boldsymbol{\rho})}\exp[i\phi_n(\boldsymbol{\rho})]H(\boldsymbol{\rho}, \mathbf{r})\mathrm{d}^2\boldsymbol{\rho}. \tag{5}$$

Taking all the field realizations into account, i.e., by using $W(\mathbf{r}_1, \mathbf{r}_2) = \langle E_n^*(\mathbf{r}_1)E_n(\mathbf{r}_2)\rangle$, we obtain the cross-spectral density of the random field in the observation plane

$$W(\mathbf{r}_1, \mathbf{r}_2) = \iint \sqrt{S(\boldsymbol{\rho}_1)S(\boldsymbol{\rho}_2)}\langle\exp[-i\phi_n(\boldsymbol{\rho}_1) + i\phi_n(\boldsymbol{\rho}_2)]\rangle H^*(\boldsymbol{\rho}_1, \mathbf{r}_1)H(\boldsymbol{\rho}_2, \mathbf{r}_2)\mathrm{d}^2\boldsymbol{\rho}_1\mathrm{d}^2\boldsymbol{\rho}_2. \tag{6}$$

Using the Gaussian statistics condition for the random phase $\phi_n(\boldsymbol{\rho})$, the above integral is reduced to

$$W(\mathbf{r}_1, \mathbf{r}_2) = \iint |E(\boldsymbol{\rho})|^2 H^*(\boldsymbol{\rho}, \mathbf{r}_1)H(\boldsymbol{\rho}, \mathbf{r}_2)\mathrm{d}^2\boldsymbol{\rho}. \tag{7}$$

It follows from **Eqs. 1, 7** that the object information $O(\mathbf{v})$ hidden a distance behind the random scattering medium is encoded in the spatial coherence function of a random light generated after the scattering medium, which indicates that once the complex spatial coherence structure $W(\mathbf{r}_1, \mathbf{r}_2)$ is fully measured, the object information may be recovered. In the previous studies, it is showed that only the intensity $S(\boldsymbol{\rho})$ on the front surface of the random scatterer can be measured [24–26] (see **Figure 1B**).

In this work, we find that the iterative phase retrieval algorithm [42–56] can be applied to recover the object information. We discuss the detail of the algorithm in this section. The algorithm will be verified experimentally in **Section 3**. The flowchart of the algorithm is shown in **Figure 1C**. The first step in the iterative phase retrieval algorithm is that we guess a initiatory amplitude for the object, e.g., $O_1(\mathbf{v}) = \sqrt{S(\mathbf{v})}$. We note other functions, e.g., a random function can also be used as the initiatory amplitude. In the second step, we take $O_1(\mathbf{v})$ into **Eq. 1** and obtain the corresponding complex field on the front surface of the scattering medium, which can be expressed as

$$E_1(\boldsymbol{\rho}) = -\frac{\mathrm{i}}{\lambda z}\exp(\mathrm{i}kz)\iint O_1(\mathbf{v})\exp\left[\frac{\mathrm{i}k}{2z}(\boldsymbol{\rho} - \mathbf{v})^2\right]\mathrm{d}^2\mathbf{v}. \tag{8}$$

The third step is extracting the phase $\theta_1(\boldsymbol{\rho})$ from $E_1(\boldsymbol{\rho})$. We then combine $\theta_1(\boldsymbol{\rho})$ with $\sqrt{S(\mathbf{v})}$ to form a new function for the field located on the front surface of the scattering medium, i.e., $E_1'(\boldsymbol{\rho}) = \sqrt{S(\mathbf{v})}\exp[\mathrm{i}\theta_1(\boldsymbol{\rho})]$. To obtain the object information, the new field $E_1'(\boldsymbol{\rho})$ then transmit backwards, i.e., in $-z$ direction. The field in the plane where the optical image located can be obtained by

$$O_1'(\mathbf{v}) = \frac{\mathrm{i}}{\lambda z}\exp(-\mathrm{i}kz)\iint E_1'(\boldsymbol{\rho})\exp\left[-\frac{\mathrm{i}k}{2z}(\boldsymbol{\rho} - \mathbf{v})^2\right]\mathrm{d}^2\boldsymbol{\rho}. \tag{9}$$

We assume that the original image is an amplitude image (i.e. with no phase information). Thus, $O(\mathbf{v})$ is a real and positive function. With the restriction of such condition, we first take out the real part of $O_1'(\mathbf{v})$ and then let the negative values in the real part become 0. The new obtained function is then used as the second prediction, $O_2(\mathbf{v})$, for the image information hidden a distance behind the random scatterer. The function $O_2(\mathbf{v})$ is then taken into the above algorithm and the third prediction image $O_3(\mathbf{v})$ will be obtained. It is found in our experiment that by ~ 70 iterations of the above phase retrieval algorithm, the image information can be well reconstructed.

3 EXPERIMENTAL VERIFICATION

In this section, we carry out the experiment to verify the feasibility of the principle and the iterative algorithm. The schematic of our experimental setup is shown in **Figure 2**. In our experiment, the image is an English letter 'S', which is generated with a spatial light modulator (SLM). The random scattering medium is a rotating ground-glass disk (RGGD). The surface roughness of the RGGD used in our experiment is 400 mesh number and the rotating speed can be controlled by the controller of an optical chopper system. In the experiment, the rotating speed is fixed at 3,000 r/min. The distance between the image (SLM) and the random scatterer (RGGD) can be adjusted from 35 to 70 cm. The image is illuminated with a fully coherent beam generated by passing a He-Ne laser (with wavelength $\lambda = 632$ nm) through a linear polarizer (LP) and a beam expander (BE). The optical system between the RGGD and the observation plane is formed by a thin lens L1 of focal distance 250 mm and a thin lens L2 of focal distance 300 mm. The distances between RGGD and L1, L1 and L2, L2 and the observation plane are 250 mm, 600 mm, and 600 mm, respectively. The second thin lens L2 is used to project the optical field immediately after L1 into the observation plane. Thus, the response function of the optical system becomes

$$H(\boldsymbol{\rho}, \mathbf{r}) = -\frac{\mathrm{i}}{\lambda f_1}\exp\left[\frac{\mathrm{i}\pi}{\lambda f_1}(\boldsymbol{\rho}^2 - 2\mathbf{r}\cdot\boldsymbol{\rho})\right], \tag{10}$$

where f_1 denotes the focal length of the thin lens L1. Taking **Eq. 10** into **Eq. 7**, we obtain that the cross-spectral density function of the random light in the observation plane yields

$$W(\mathbf{r}_1, \mathbf{r}_2) = \frac{1}{\lambda^2 f^2}\iint |E(\boldsymbol{\rho})|^2\exp\left[\frac{\mathrm{i}2\pi}{\lambda f}\boldsymbol{\rho}\cdot(\mathbf{r}_1 - \mathbf{r}_2)\right]\mathrm{d}^2\boldsymbol{\rho}. \tag{11}$$

It is found from **Eq. 11** that the generated partially coherent beam in the observation place is of Schell-model type, i.e., its spatial coherence distribution depends only on the position difference $\mathbf{r}_1$—$\mathbf{r}_2$. Moreover, we find that the spatial coherence

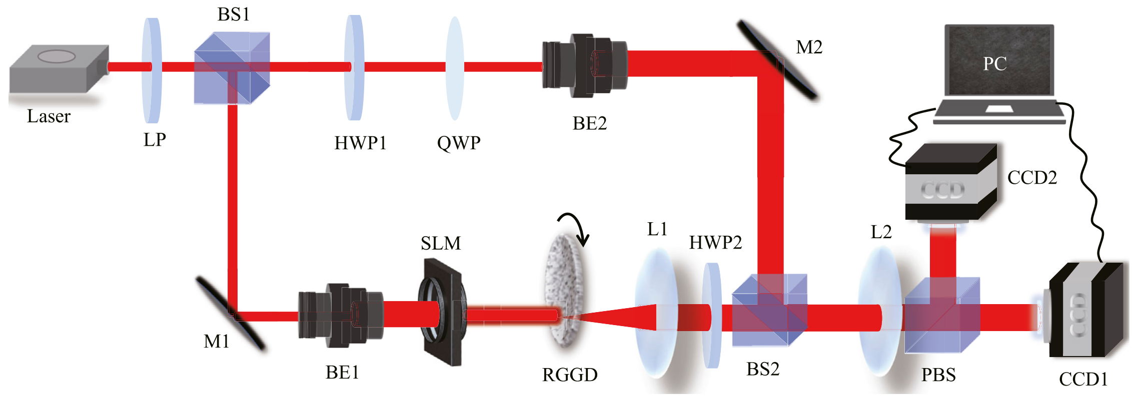

FIGURE 2 | Experimental setup for optical imaging through a random scattering medium via the complex spatial coherence measurement. LP: linear polarizer; BS1 and BS2: beam splitters; HWP1 and HWP2: half-wave plates; QWP: quarter-wave plate; BE1 and BE2: beam expanders; M1 and M2: mirrors; SLM: spatial light modulator; RGGD: rotating ground-glass disk; L1 and L2, thin lenses; PBS: polarization beam splitter; CCD1 and CCD2: charge-coupled devices; PC: personal computer.

function $W(\mathbf{r}_1, \mathbf{r}_2)$ and the intensity $|E(\boldsymbol{\rho})|^2$ on the front surface of the random scatterer form a Fourier transform pair. Thus, $|E(\boldsymbol{\rho})|^2$ can be recovered by

$$|E(\boldsymbol{\rho})|^2 = \frac{1}{\lambda^2 f^2} \iint W(\mathbf{r}_1, \mathbf{r}_2) \exp\left[-\frac{i2\pi}{\lambda f} \boldsymbol{\rho} \cdot (\mathbf{r}_1 - \mathbf{r}_2)\right] d^2\mathbf{r}_1 d^2\mathbf{r}_2. \tag{12}$$

Once $|E(\boldsymbol{\rho})|^2$ is recovery, we take the result into the iterative phase retrieval algorithm and run 66 loops.

Before discussing the experiment results, we present the details of the method for measuring the complex spatial coherence of the generated partially coherent light. The method is based on the generalized Hanbury Brown and Twiss experiment [24], in which we introduce a pair of reference waves having a constant phase difference either 0 or $\pi/2$. In our experiment, the reference waves with the stable phase difference are generated from a circularly polarized beam. In the top reference arm of **Figure 2**, the x-polarized light beam is transmitted through a half-wave plate (HWP) and a quarter-wave plate (QWP). The fast axis of the HWP is set to be $\pi/8$ with respect to the x-polarization direction, while the fast axis of the QWP is set to be parallel to the x-polarization direction. Therefore, a right-handed circularly polarized beam is produced immediately after the QWP. The beam expander (BE2) after QWP is used to produce a beam of the effectively uniform intensity distribution. The x- and y-components of the generated circularly polarized beam are viewed as the pair of reference waves required for our protocol.

Before combining the reference waves with the partially coherent light, we place a HWP after the thin lens L1 to transfer the x-polarized partially coherent light into $\pi/4$-linearly polarized. The x- and y-components of the field realization after the beam splitter (BS2) is then expressed as

$$E_{nx}^{\text{add}}(\mathbf{r}) = E_{nx}(\mathbf{r}) + E_x^{\text{circ}}(\mathbf{r}), \tag{13}$$
$$E_{ny}^{\text{add}}(\mathbf{r}) = E_{ny}(\mathbf{r}) + E_y^{\text{circ}}(\mathbf{r}), \tag{14}$$

where $E_{nx}(\mathbf{r})$ and $E_{ny}(\mathbf{r})$ denote the x- and y-components of one random field realization of the partially coherent light, and $E_x^{\text{circ}}(\mathbf{r})$ and $E_y^{\text{circ}}(\mathbf{r})$ are the x- and y-components of the generated circularly polarized reference wave, respectively. The x- and y-components of the composite field are then split by a polarization beam splitter (PBS) and imaged, respectively, onto CCD1 and CCD2 by a $2f$ imaging system formed by the thin lens L2. The direct-digital-synthesis signal generator is used as external trigger for controlling the two CCDs, to simultaneously capture the random intensities $I_{nx}^{\text{add}}(\mathbf{r})$ and $I_{ny}^{\text{add}}(\mathbf{r})$ of the x- and y-component fields.

We now calculate the cross-correlation of the two composite field intensities, i.e.,

$$G_{xy}^{\text{add}}(\mathbf{r}_1, \mathbf{r}_2) = \langle I_{nx}^{\text{add}}(\mathbf{r}_1) I_{ny}^{\text{add}}(\mathbf{r}_2) \rangle, \tag{15}$$

where the angle brackets denote the ensemble averaging. Taking **Eqs. 13, 14** into **Eq. 15**, we obtain

$$G_{xy}^{\text{add}}(\mathbf{r}_1, \mathbf{r}_2) = \langle I_{nx}^{\text{uncor}}(\mathbf{r}_1) \rangle \langle I_{ny}^{\text{uncor}}(\mathbf{r}_2) \rangle + |W(\mathbf{r}_1, \mathbf{r}_2)|^2 + 2\sqrt{I_x^{\text{circ}}(\mathbf{r}_1) I_y^{\text{circ}}(\mathbf{r}_2)} \operatorname{Im}[W(\mathbf{r}_1, \mathbf{r}_2)]. \tag{16}$$

Above, $I_{nx}^{\text{uncor}}(\mathbf{r}) = I_{nx}(\mathbf{r}) + I_x^{\text{circ}}(\mathbf{r})$, $I_{ny}^{\text{uncor}}(\mathbf{r}) = I_{ny}(\mathbf{r}) + I_y^{\text{circ}}(\mathbf{r})$, $I_{nx}(\mathbf{r})$ and $I_{ny}(\mathbf{r})$ denote the intensities of the x- and y-components of the random field realization, and $I_x^{\text{circ}}(\mathbf{r})$ and $I_y^{\text{circ}}(\mathbf{r})$ denote the intensities of the x- and y-components of the circularly polarized light, respectively. It is found from **Eq. 16** that the imaginary part of $W(\mathbf{r}_1, \mathbf{r}_2)$ is encoded in the intensity cross-correlation function. The undesired background terms, i.e., $\langle I_{nx}^{\text{uncor}}(\mathbf{r}_1) \rangle \langle I_{ny}^{\text{uncor}}(\mathbf{r}_2) \rangle + |W(\mathbf{r}_1, \mathbf{r}_2)|^2$ are removed by doing the intensity cross-correlation $G_{xy}^{\text{uncor}}(\mathbf{r}_1, \mathbf{r}_2) = \langle I_{nx}^{\text{uncor}}(\mathbf{r}_1) I_{ny}^{\text{uncor}}(\mathbf{r}_2) \rangle$. Finally, the imaginary part of the spatial coherence function is obtained as

$$\operatorname{Im}[W(\mathbf{r}_1, \mathbf{r}_2)] = \frac{G_{xy}^{\text{add}}(\mathbf{r}_1, \mathbf{r}_2) - G_{xy}^{\text{uncor}}(\mathbf{r}_1, \mathbf{r}_2)}{2\sqrt{I_x^{\text{circ}}(\mathbf{r}_1) I_y^{\text{circ}}(\mathbf{r}_2)}}. \tag{17}$$

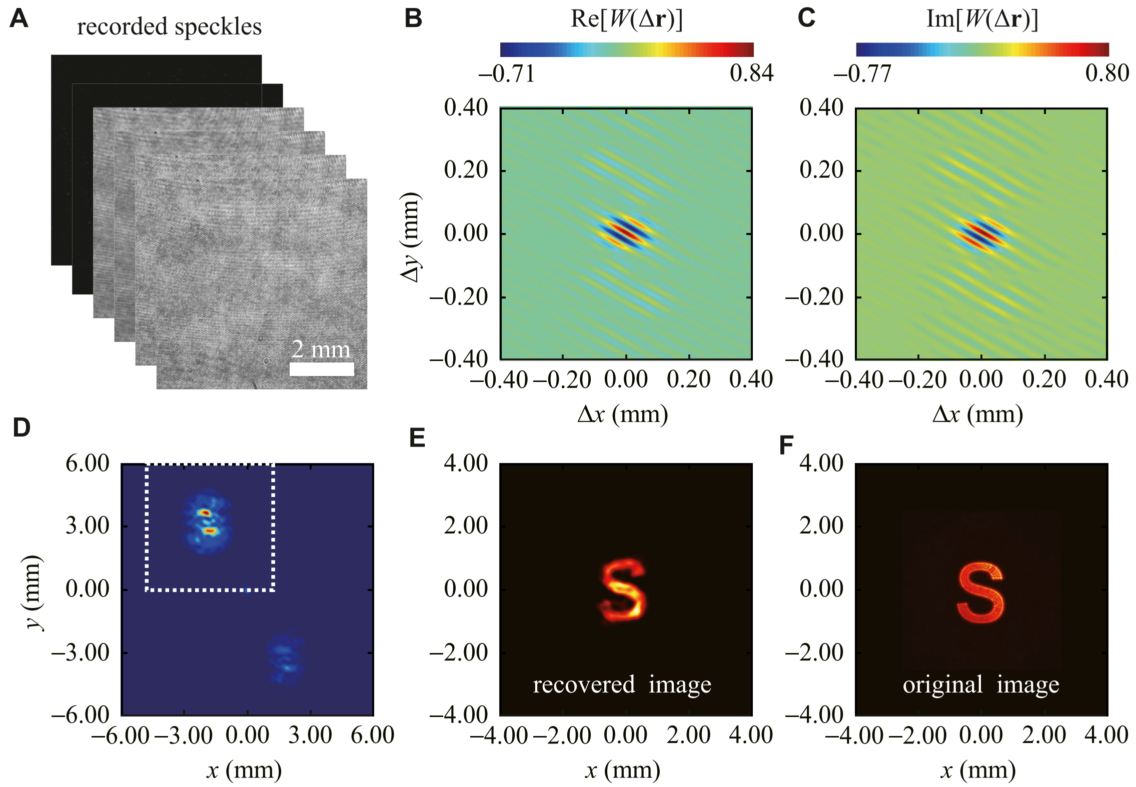

FIGURE 3 | Experimental results of optical imaging through a RGGD with complex spatial coherence measurement. The optical image is placed 57.5 cm in front of the random scatterer. **(A)** The recorded speckles $I_{nx}(\mathbf{r})$, $I_{ny}(\mathbf{r})$, $I_x^{circ}(\mathbf{r})$, $I_y^{circ}(\mathbf{r})$, $I_{nx}^{add}(\mathbf{r})$, and $I_{ny}^{add}(\mathbf{r})$. **(B)** and **(C)** The recovered real and imaginary parts of the spatial coherence function from the speckles shown in (a). **(D)** The recovery intensity on the front surface of the RGGD. **(E)** The recovery image information with the iterative phase retrieval algorithm. **(F)** The original image displayed in the SLM.

The real part of the spatial coherence function, on the other hand, can be obtained by

$$\mathrm{Re}[W(\mathbf{r}_1,\mathbf{r}_2)] = \frac{G_{xx}^{add}(\mathbf{r}_1,\mathbf{r}_2) - G_{xx}^{uncor}(\mathbf{r}_1,\mathbf{r}_2)}{2\sqrt{I_x^{circ}(\mathbf{r}_1)I_x^{circ}(\mathbf{r}_2)}}, \tag{18}$$

where $G_{xx}^{add}(\mathbf{r}_1,\mathbf{r}_2) = \langle I_{nx}^{add}(\mathbf{r}_1)I_{nx}^{add}(\mathbf{r}_2)\rangle$ and $G_{xx}^{uncor}(\mathbf{r}_1,\mathbf{r}_2) = \langle I_{nx}^{uncor}(\mathbf{r}_1)I_{nx}^{uncor}(\mathbf{r}_2)\rangle$ are the intensity-intensity autocorrelation functions. In the experiment, the ensemble average in the intensity cross-correlation and autocorrelation can be replaced with the spatial average of the speckle field since the partially coherent random field is generated with the Fourier transformation optical system [57]. Thus, the real and imaginary parts of the spatial coherence function can be recovered conveniently through recording six realizations of intensity distributions, i.e., $I_{nx}(\mathbf{r})$, $I_{ny}(\mathbf{r})$, $I_x^{circ}(\mathbf{r})$, $I_y^{circ}(\mathbf{r})$, $I_{nx}^{add}(\mathbf{r})$, and $I_{ny}^{add}(\mathbf{r})$.

4 RESULTS AND DISCUSSION

To show the feasibility of our method, we first place the image (SLM) 57.5 cm in front of the RGGD and record the six intensity distributions with CCD1 and CCD2, respectively. **Figure 3A** shows the spatial speckles of the six intensities. By using **Eqs. 17, 18**, the complex spatial coherence structure can be recovered. We show in **Figures 3B,C** the experimental results of the real and imaginary parts of the spatial coherence function of the partially coherent light in the observation plane after the random scatterer. Taking the measured $W(\mathbf{r}_1, \mathbf{r}_2)$ into **Eq. 12** and performing the fast Fourier transform, we obtain the intensity distribution $S(\boldsymbol{\rho})$ on the front surface of the random scatterer, which is shown in **Figure 3D**. We find from **Figure 3D** that the image information cannot be identified from the diffraction pattern. We now apply the iterative phase retrieval algorithm introduced in **Section 2** for the image information recovery. The initiatory intensity for the image is assumed to be the pattern displayed in the dotted box of **Figure 3D**. The algorithm is iterated 66 times. **Figure 3E** shows the result of the recovered image. For a better comparison, the original object loaded in the SLM is also recorded (see in **Figure 3F**]. We find in the experiment that the image information hidden a distance behind the random scattering medium can be well reconstructed with the help of the spatial coherence structure measurement and the iterative phase retrieval algorithm. The experimental results are consistent with our predictions.

Next, we show the ability of our method to retrieve both the lateral position and the shape of the moving object hidden behind the RGGD. The object image is created again by the SLM and

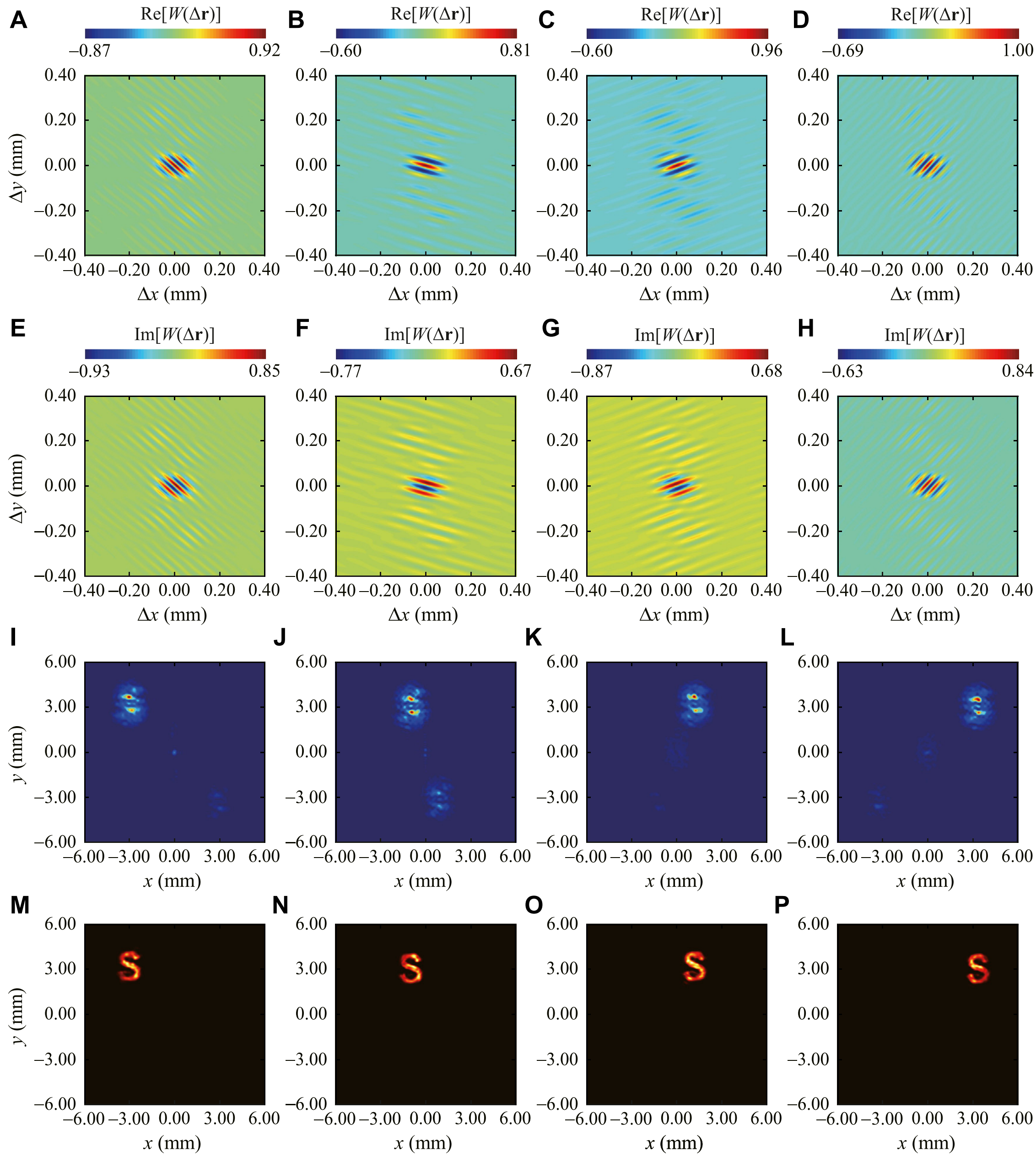

FIGURE 4 | Experimental results for the recovery of a moving image hidden behind the RGGD with complex spatial coherence structure measurement. The image moves in the transverse plane where z = 57.5 cm. **(A)–(D)** and **(E)–(H)** The measured real and imaginary parts of the complex spatial coherence function for the cases when the image is located at different lateral positions. **(I)–(L)** The recovered intensities on the front surface of the RGGD. **(M)–(P)** The recovery images with the iterative phase retrieval algorithm.

placed in the plane having a distance 57.5 cm in front of the RGGD. However, the image can now move freely in the transverse plane. In the top two panels of **Figure 4**, the experimental results of the measured real and imaginary parts of the spatial coherence functions are presented when the image is located at different transverse positions. We find with the change of the image position, the distribution of the complex spatial coherence for the partially coherent light beam in the observation plane changes as well. The corresponding recovered intensities on the front surface of the RGGD obtained by the fast Fourier transform of measured $W(\mathbf{r}_1, \mathbf{r}_2)$ are shown in the third row of **Figure 4**. We now assume these intensity distributions as the initiatory inputs for the iterative phase retrieval algorithm. After 66 times loops, the recovered image intensities are displayed in the bottom row of **Figure 4**. It is found from the experimental results that the image at different transverse positions is well recovered, which indicates that the iterative phase retrieval algorithm shown in **Section 2** can preserve well the lateral position information of the image.

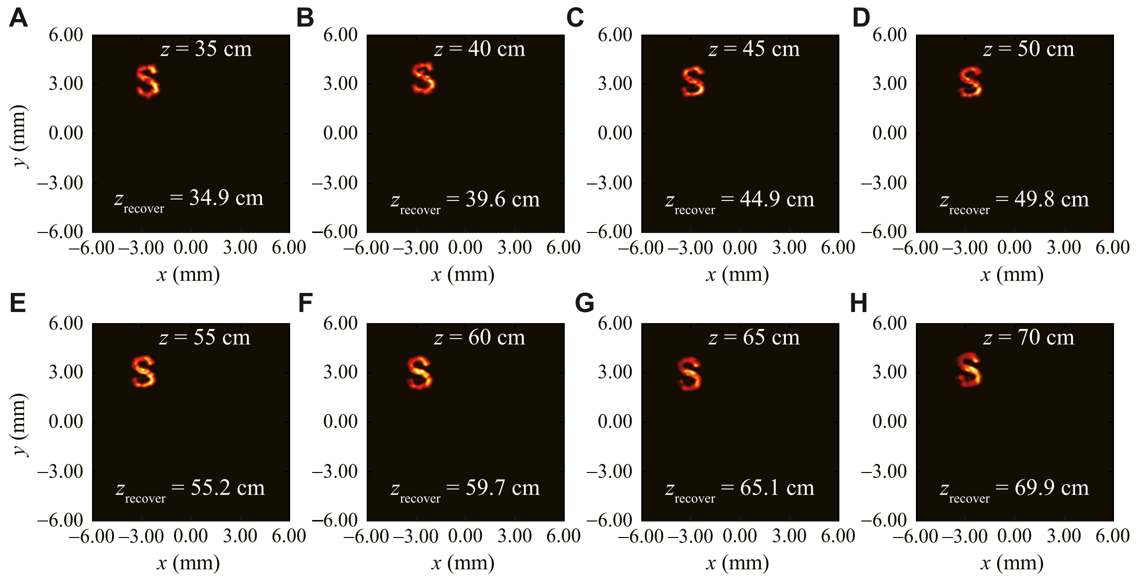

FIGURE 5 | Experimental results of the recovered images with the spatial coherence measurement and the iterative phase retrieval for the case when the image moves along the longitudinal direction. The real distance z and the recovered distance $z_{recover}$ from the RGGD are marked in the figures.

Finally, we carry out the experiment to show the feasibility of our method in recovering the longitudinal position of the image hidden behind the random scattering medium. The image created by the SLM now moves freely in the longitudinal direction. In our experiment, the distance between the SLM and the RGGD can be controlled from 35 to 70 cm. Once the complex spatial coherence structure is measured in the observation plane, the intensity on the front surface of the RGGD can be recovered. After that, we take the recovery intensity as the initial input for the iterative phase retrieval algorithm and modify the value of the distance z in the algorithm. The output results for different values of input z after 66 times iterations are compared with the original image as shown in **Figure 3F**. When the recovered and the original images are matched, the input value of z is recorded as the longitudinal distance for the image. **Figure 5** shows our experimental results of the reconstructed images at different longitudinal positions. The recovered longitudinal distances $z_{recover}$ and the real longitudinal positions z are also shown in the figures. It is found from the experimental results that the image hidden behind the RGGD with different longitudinal distances can be well reconstructed with the spatial coherence measurement and the iterative phase retrieval algorithm. The experimentally recovered longitudinal distances agree well with the real distances between the image and the RGGD.

5 CONCLUSION

In this work, we studied the role of the spatial coherence structure measurement for the partially coherent scattered light on the recovery of the image information (especially the image's longitudinal position) hidden behind a random scattering medium. We showed experimentally that the image information, including its spatial shape, lateral shift, and longitudinal position, encoded in the spatial coherence structure can be fully reconstructed with the spatial coherence measurement and the iterative phase retrieval algorithm in the Fresnel domain. Our experimental results indicate that a 2D spatial coherence measurement can find applications in the 3D optical imaging through the random scattering medium and 3D object position tracking in complex medium. We remark that the scattering from randomly inhomogeneous media (stronger than the rotating ground glass disk used here) does not completely destroy the spatial coherence of radiation [58], which indicates that the multiple-scattering media can still act as an imperfect mirror or lens for coherence-based 3D optical imaging.

DATA AVAILABILITY STATEMENT

The raw data supporting the conclusions of this article will be made available by the authors, without undue reservation.

AUTHOR CONTRIBUTIONS

YC, FW, and YC proposed the idea. DP, XZ, YZ, YL, and YC performed the experiment. All authors analyzed the experiment. YC and DP wrote the original manuscript. YC, FW, and YC supervised the project.

FUNDING

National Key Research and Development Program of China (2019YFA0705000); National Natural Science Foundation of

China (91 750 201, 11 874 046, 11 974 218, 11 904 247, and 12 192 254); Innovation Group of Jinan (2018GXRC010); Local Science and Technology Development Project of the Central Government (YDZX20203700001766).

REFERENCES

1. Mandel L, Wolf E. *Optical Coherence and Quantum Optics*. Cambridge: Cambridge University Press (1995).
2. Friberg AT, Setälä T Electromagnetic Theory of Optical Coherence [Invited]. *J Opt Soc Am A* (2016) 33:2431–42. doi:10.1364/josaa.33.002431
3. Chen Y, Norrman A, Ponomarenko SA, Friberg AT Optical Coherence and Electromagnetic Surface Waves. *Prog Opt* (2020) 65:105–72. doi:10.1016/bs.po.2019.11.001
4. Cai Y, Chen Y, Yu J, Liu X, Liu L Generation of Partially Coherent Beams. *Prog Opt* (2017) 62:157–223. doi:10.1016/bs.po.2016.11.001
5. Ricklin JC, Davidson FM Atmospheric Optical Communication with a Gaussian Schell Beam. *J Opt Soc Am A* (2003) 20:856–66. doi:10.1364/josaa.20.000856
6. Gbur G Partially Coherent Beam Propagation in Atmospheric Turbulence [Invited]. *J Opt Soc Am A* (2014) 31:2038–45. doi:10.1364/josaa.31.002038
7. Redding B, Choma MA, Cao H Speckle-free Laser Imaging Using Random Laser Illumination. *Nat Photon* (2012) 6:355–9. doi:10.1038/nphoton.2012.90
8. Wang F, Chen Y, Liu X, Cai Y, Ponomarenko SA Self-reconstruction of Partially Coherent Light Beams Scattered by Opaque Obstacles. *Opt Express* (2016) 24:23735–46. doi:10.1364/oe.24.023735
9. Gori F, Santarsiero M Devising Genuine Spatial Correlation Functions. *Opt Lett* (2007) 32:3531–3. doi:10.1364/ol.32.003531
10. Martínez-Herrero R, Mejías PM, Gori F. Genuine Cross-Spectral Densities and Pseudo-modal Expansions. *Opt Lett* (2009) 34:1399–401.
11. Gori F, Ramírez-Sánchez V, Santarsiero M, Shirai T On Genuine Cross-Spectral Density Matrices. *J Opt A: Pure Appl Opt* (2009) 11:085706. doi:10.1088/1464-4258/11/8/085706
12. Cai Y, Chen Y, Wang F Generation and Propagation of Partially Coherent Beams with Nonconventional Correlation Functions: a Review [Invited]. *J Opt Soc Am A* (2014) 31:2083–96. doi:10.1364/josaa.31.002083
13. Liang C, Wu G, Wang F, Li W, Cai Y, Ponomarenko SA Overcoming the Classical Rayleigh Diffraction Limit by Controlling Two-point Correlations of Partially Coherent Light Sources. *Opt Express* (2017) 25:28352–62. doi:10.1364/oe.25.028352
14. Shen Y, Sun H, Peng D, Chen Y, Cai Q, Wu D, et al. Optical Image Reconstruction in 4f Imaging System: Role of Spatial Coherence Structure Engineering. *Appl Phys Lett* (2021) 118:181102. doi:10.1063/5.0046288
15. Liu Y, Chen Y, Chen Y, Wang F, Cai Y, Liang C, et al. Robust Far-Field Imaging by Spatial Coherence Engineering. *Opto-Electron Adv* (2021) 4:210027. doi:10.29026/oea.2021.210027
16. Hyde MW, Basu S, Voelz DG, Xiao X Experimentally Generating Any Desired Partially Coherent Schell-Model Source Using Phase-Only Control. *J Appl Phys* (2015) 118:093102. doi:10.1063/1.4929811
17. Hyde MW, Bose-Pillai SR, Wood RA Synthesis of Non-uniformly Correlated Partially Coherent Sources Using a Deformable Mirror. *Appl Phys Lett* (2017) 111:101106. doi:10.1063/1.4994669
18. Chen X, Li J, Rafsanjani SMH, Korotkova O Synthesis of Im-Bessel Correlated Beams via Coherent Modes. *Opt Lett* (2018) 43:3590–3. doi:10.1364/ol.43.003590
19. Bhattacharjee A, Sahu R, Jha AK Generation of a Gaussian Schell-Model Field as a Mixture of its Coherent Modes. *J Opt* (2019) 21:105601. doi:10.1088/2040-8986/ab3b24
20. Zhu X, Yu J, Chen Y, Wang F, Korotkova O, Cai Y Experimental Synthesis of Random Light Sources with Circular Coherence by Digital Micro-mirror Device. *Appl Phys Lett* (2020) 117:121102. doi:10.1063/5.0024283
21. Zhu X, Yu J, Wang F, Chen Y, Cai Y, Korotkova O. Synthesis of Vector Nonuniformly Correlated Light Beams by a Single Digital Mirror Device. *Opt Lett* (2021) 46:2996–9. doi:10.1364/OL.428508
22. Wolf E. *Introduction to the Theory of Coherence and Polarization of Light*. Cambridge: Cambridge University Press (2007).
23. Wang F, Liu X, Yuan Y, Cai Y Experimental Generation of Partially Coherent Beams with Different Complex Degrees of Coherence. *Opt Lett* (2013) 38: 1814–6. doi:10.1364/ol.38.001814
24. Huang Z, Chen Y, Wang F, Ponomarenko SA, Cai Y. Measuring Complex Degree of Coherence of Random Light fields with Generalized Hanbury Brown–Twiss experiment. *Phys Rev Appl* (2020) 13:044042. doi:10.1103/physrevapplied.13.044042
25. Dong Z, Huang Z, Chen Y, Wang F, Cai Y Measuring Complex Correlation Matrix of Partially Coherent Vector Light via a Generalized Hanbury Brown-Twiss experiment. *Opt Express* (2020) 28:20634–44. doi:10.1364/oe.398185
26. Peng D, Huang Z, Liu Y, Chen Y, Wang F, Ponomarenko SA, et al. Optical Coherence Encryption with Structured Random Light. *PhotoniX* (2021) 2: 6–15. doi:10.1186/s43074-021-00027-z
27. Goodman JW, Huntley WH, Jr, Jackson DW, Lehmann M Wavefront-reconstruction Imaging through Random Media. *Appl Phys Lett* (1966) 8: 311–3. doi:10.1063/1.1754453
28. Leith EN, Upatnieks J Holographic Imagery through Diffusing media. *J Opt Soc Am* (1966) 56:523. doi:10.1364/josa.56.000523
29. Rotter S, Gigan S. Light fields in Complex media: Mesoscopic Scattering Meets Wave Control. *Rev Mod Phys* (2017) 89:015005. doi:10.1103/revmodphys.89.015005
30. Yoon S, Kim M, Jang M, Choi Y, Choi W, Kang S, et al. Deep Optical Imaging within Complex Scattering media. *Nat Rev Phys* (2020) 2:141–58. doi:10.1038/s42254-019-0143-2
31. Denk W, Strickler JH, Webb WW Two-photon Laser Scanning Fluorescence Microscopy. *Science* (1990) 248:73–6. doi:10.1126/science.2321027
32. Huang D, Swanson EA, Lin CP, Schuman JS, Stinson WG, Chang W, et al. Optical Coherence Tomography. *Science* (1991) 254:1178–81. doi:10.1126/science.1957169
33. Hoover EE, Squier JA Advances in Multiphoton Microscopy Technology. *Nat Photon* (2013) 7:93–101. doi:10.1038/nphoton.2012.361
34. Mosk AP, Lagendijk A, Lerosey G, Fink M Controlling Waves in Space and Time for Imaging and Focusing in Complex media. *Nat Photon* (2012) 6: 283–92. doi:10.1038/nphoton.2012.88
35. Horstmeyer R, Ruan H, Yang C Guidestar-assisted Wavefront-Shaping Methods for Focusing Light into Biological Tissue. *Nat Photon* (2015) 9: 563–71. doi:10.1038/nphoton.2015.140
36. Del Hougne P, Yeo KB, Besnier P, Davy M Coherent Wave Control in Complex media with Arbitrary Wavefronts. *Phys Rev Lett* (2021) 126: 193903. doi:10.1103/physrevlett.126.193903
37. Yeminy T, Katz O. Guidestar-free Image-Guided Wavefront Shaping. *Sci Adv* (2021) 7:eabf5364. doi:10.1126/sciadv.abf5364
38. Popoff SM, Lerosey G, Carminati R, Fink M, Boccara AC, Gigan S Measuring the Transmission Matrix in Optics: an Approach to the Study and Control of Light Propagation in Disordered media. *Phys Rev Lett* (2010) 104:100601. doi:10.1103/physrevlett.104.100601
39. Boniface A, Dong J, Gigan S. Non-invasive Focusing and Imaging in Scattering media with a Fluorescence-Based Transmission Matrix. *Nat Commun* (2020) 11:6154–7. doi:10.1038/s41467-020-19696-8
40. Freund I, Rosenbluh M, Feng S Memory Effects in Propagation of Optical Waves through Disordered media. *Phys Rev Lett* (1988) 61:2328–31. doi:10.1103/physrevlett.61.2328
41. Osnabrugge G, Horstmeyer R, Papadopoulos IN, Judkewitz B, Vellekoop IM Generalized Optical Memory Effect. *Optica* (2017) 4:886–92. doi:10.1364/optica.4.000886
42. Bertolotti J, Van Putten EG, Blum C, Lagendijk A, Vos WL, Mosk AP Non-invasive Imaging through Opaque Scattering Layers. *Nature* (2012) 491:232–4. doi:10.1038/nature11578
43. Katz O, Small E, Silberberg Y Looking Around Corners and through Thin Turbid Layers in Real Time with Scattered Incoherent Light. *Nat Photon* (2012) 6:549–53. doi:10.1038/nphoton.2012.150
44. Katz O, Heidmann P, Fink M, Gigan S Non-invasive Single-Shot Imaging through Scattering Layers and Around Corners via Speckle Correlations. *Nat Photon* (2014) 8:784–90. doi:10.1038/nphoton.2014.189
45. Okamoto Y, Horisaki R, Tanida J Noninvasive Three-Dimensional Imaging through Scattering media by Three-Dimensional Speckle Correlation. *Opt Lett* (2019) 44:2526–9. doi:10.1364/ol.44.002526

46. Yuan Y, Chen H Dynamic Noninvasive Imaging through Turbid media under Low Signal-Noise-Ratio. *New J Phys* (2020) 22:093046. doi:10.1088/1367-2630/abb16a
47. Edrei E, Scarcelli G. Memory-effect Based Deconvolution Microscopy for Super-resolution Imaging through Scattering media. *Sci Rep* (2016) 6:33558–8. doi:10.1038/srep33558
48. Li D, Kelly DP, Sheridan JT Three-dimensional Static Speckle fields Part I Theory and Numerical Investigation. *J Opt Soc Am A* (2011) 28:1896–903. doi:10.1364/josaa.28.001896
49. Li D, Kelly DP, Sheridan JT. Three-dimensional Static Speckle fields. Part Ii. Experimental Investigation. *J Opt Soc Am A* (2011) 28:1904–8. doi:10.1364/josaa.28.001904
50. Ruan H, Liu Y, Xu J, Huang Y, Yang C Fluorescence Imaging through Dynamic Scattering media with Speckle-Encoded Ultrasound-Modulated Light Correlation. *Nat Photon* (2020) 14:511–6. doi:10.1038/s41566-020-0630-0
51. Wang D, Sahoo SK, Zhu X, Adamo G, Dang C. Non-invasive Super-resolution Imaging through Dynamic Scattering media. *Nat Commun* (2021) 12:3150–9. doi:10.1038/s41467-021-23421-4
52. Goodman JW. *Statistical Optics*. Hoboken, NJ, USA: John Wiley & Sons (2015).
53. Andrews LC, Phillips RL. *Laser Beam Propagation through Tandom Media*. Bellingham, Washington, USA: SPIE (2005).
54. Ostrovsky AS. *Coherent-mode Representations in Optics, Vol. 164*. Bellingham, Washington, USA: SPIE Press (2006).
55. Fienup JR Reconstruction of an Object from the Modulus of its Fourier Transform. *Opt Lett* (1978) 3:27–9. doi:10.1364/ol.3.000027
56. Fienup JR Phase Retrieval Algorithms: a Comparison. *Appl Opt* (1982) 21: 2758–69. doi:10.1364/ao.21.002758
57. Takeda M, Wang W, Naik DN, Singh RK Spatial Statistical Optics and Spatial Correlation Holography: a Review. *Opt Rev* (2014) 21:849–61. doi:10.1007/s10043-014-0138-2
58. Batarseh M, Sukhov S, Shen Z, Gemar H, Rezvani R, Dogariu A. Passive Sensing Around the Corner Using Spatial Coherence. *Nat Commun* (2018) 9: 3629–6. doi:10.1038/s41467-018-05985-w

Conflict of Interest: The authors declare that the research was conducted in the absence of any commercial or financial relationships that could be construed as a potential conflict of interest.

Publisher's Note: All claims expressed in this article are solely those of the authors and do not necessarily represent those of their affiliated organizations, or those of the publisher, the editors, and the reviewers. Any product that may be evaluated in this article, or claim that may be made by its manufacturer, is not guaranteed or endorsed by the publisher.

frontiers in Physics

ORIGINAL RESEARCH
published: 17 January 2022
doi: 10.3389/fphy.2021.828825

An Augmented-Reality Holographic Stereogram Based on 3D Optical Field Information Manipulation and Reconstruction

Yunpeng Liu[1†], Tao Jing[1†], Qiang Qu[1], Ping Zhang[2], Pei Li[3], Qian Yang[4], Xiaoyu Jiang[1] and Xingpeng Yan[1]**

[1]Department of Information Communication, Army Academy of Armored Forces, Beijing, China, [2]Center of Vocational Education, Army Academy of Armored Forces, Beijing, China, [3]R and D Center for Intelligent Control and Advanced Manufacturing, Research Institute of Tsinghua University in Shen Zhen, Shen Zhen, China, [4]Troops of PLA, Beijing, China

OPEN ACCESS

Edited by:
Xing Fu,
Tsinghua University, China

Reviewed by:
Binbin Yan,
Beijing University of Posts and Telecommunications (BUPT), China
Ping Su,
Tsinghua University, China

****Correspondence:***
Xiaoyu Jiang
jiangxiaoyu2007@gmail.com
Xingpeng Yan
yanxp02@gmail.com

†These authors have contributed equally to this work

Specialty section:
This article was submitted to Optics and Photonics, a section of the journal Frontiers in Physics

Received: *04 December 2021*
Accepted: *09 December 2021*
Published: *17 January 2022*

Citation:
Liu Y, Jing T, Qu Q, Zhang P, Li P, Yang Q, Jiang X and Yan X (2022) An Augmented-Reality Holographic Stereogram Based on 3D Optical Field Information Manipulation and Reconstruction. Front. Phys. 9:828825. doi: 10.3389/fphy.2021.828825

Holographic stereogram comprises a hotspot in the field of three-dimensional (3D) display. It can reconstruct the light field information of real and virtual scenes at the same time, further improving the comprehensibility of the scene and achieving the "augmentation" of the scene. In this paper, an augmented reality-holographic stereogram based on 3D reconstruction is proposed. First, the point cloud data is generated by VisualSFM software, and then the 3D mesh model is reconstructed by MeshLab software. The obtained scene model and virtual scene are rendered simultaneously to obtain the real and virtual fusion scene. Analysis of experimental results shows that the proposed method can effectively realize augmented reality-holographic stereogram.

Keywords: holography, holographic stereogram, optical field information manipulation, augmented reality, 3D display

INTRODUCTION

Holographic stereogram (HS) [1–3] comprises a research hotspot in the field of three-dimensional (3D) display, providing a flexible and efficient means of 3D display. HS is widely used in the military, publicity, commerce, and other fields [4, 5]. Using discrete 2D images with parallax information as the input, the 3D reconstruction of a scene can be obtained after image processing, stereoscopic exposure, and development and fixing. An HS cannot show all the information of the scene but is limited to a certain angle (less than 180°). Moreover, HS does not have the depth information in the scene space, but people can still perceive 3D clues, which depends on the binocular parallax effect [6]. HS discretizes and approximates the continuous 3D light field, which greatly reduces the amount of data. In addition, the scene is not limited to real-world objects, but can also be a 3D model rendered by computer. The diversified scene selection of HS not only enriches its expression ability, but also makes the realization of augmented reality-holographic stereogram (ARHS) possible.

ARHS reconstructs the light field information of real and virtual scenes at the same time [7]. The real-scene data are sampled by the camera, and the virtual scene is rendered by computer software or a program. The organic combination of both can further improve the comprehensibility of the scene and achieve the "augmentation" of the scene. The key to realizing ARHS is the effective fusion of real and virtual scenes. There are three methods in AR to prove the realizability of scene fusion. One is the model-based method, which reconstructs the 3D model of a real scene through a computer, exports the model data to the virtual scene rendering software, and renders the virtual scene at the same time to achieve the fusion effect. This method was first proposed by Breen in 1996 [8], but it was difficult to realize due to technical limitations at that time. The second method of proving the realizability of scene fusion is the depth-based method, which determines the occlusion relationship according to the depth value of the target point, and usually only displays the information near the target point. Wloka *et al.* proposed a video transparent AR system that can solve the problem of occlusion between a real scene and computer-generated objects [9]. The system calculates the pixel depth value through the stereo matching algorithm and compares the depth value to determine the position relationship between real and virtual scenes. The third method used to prove the realizability of scene fusion is the image-analysis-based method. First, the edge of the real scene-image is detected, the accurate contour is drawn, and then the occlusion relationship between the real and virtual scenes are manually marked and completed. This method makes use of the advantages of an edge detection algorithm to mark each image manually. After the continuous development of algorithms, especially the rise of neural networks, contour extraction has gradually acquired intelligence, and manual marking has been automated, which greatly im-proves the practicability of this third method. Roxas *et al.* used a semantic segmentation algorithm based on a convolutional neural network (CNN) to obtain more accurate fore-ground segmentation results. In addition, according to the complexity of object boundaries and textures, labels are assigned to real scenes to improve the automation performance [10].

In other fields, research on the display of real- and virtual-scene fusion is also underway. Deng *et al.* used a reflective polarizer (RP) to realize AR 3D display, which has potential applications in stomatology and vehicle AR display [11]. Shi *et al.* demonstrated a CNN–based computer-generated holographic (CGH) pipeline capable of synthesizing a photorealistic color 3D hologram from a single RGBD image in real time [12]. Yang *et al.* proposed a fast CGH method with multiple projection images for a near-eye virtual-reality (VR) and AR 3D display by convoluting the projection images with the corresponding point spread function (PSF) [13].

Recently, using depth-based and image-analysis-based method, we proposed a scene fusion coding method based on instance segmentation and pseudo depth to realize ARHS [14]. However, the scope of application of this method is limited, and the display of a few examples is required; otherwise, a large amount of calculation is required.

In the present work, referring to the model-based method in the AR field, we used VisualSFM and MeshLab software to realize the 3D reconstruction of the scene, import the model into 3D Studio Max software, render the virtual scene at the same time, and then realize the scene fusion. Holographic printing is carried out using our proposed effective perspective image segmentation and mosaicking (EPISM) method [15], and the reconstructed light field is analyzed and discussed, which verifies the effectiveness of the proposed method.

BASIC PRINCIPLES

In our work, the basic steps of ARHS based on 3D reconstruction are as follows. First, the 3D model of a real scene was established by 3D reconstruction. Then, the model was imported into the computer, the virtual scene information was rendered and added, and the effective fusion between the virtual and real scenes was completed according to the preset perspective and occlusion relationship. Finally, it is processed according to the steps of sampling, coding, printing, and display of HS, to realize ARHS.

The core of our method is 3D reconstruction. To verify the effectiveness of the method, we used the 3D reconstruction technology based on multi-view map, which mainly depends on two software packages, i.e., VisualSFM and MeshLab. The fusion of real and virtual scenes depends on 3D Studio Max.

VisualSFM uses a stereo-matching algorithm to detect and match the image feature points, then uses a structure-from-motion (SFM) algorithm to calculate the pose of the camera in space according to the matching data and reconstructs the 3D point-cloud model of the 3D scene. However, the point-cloud model is sparse and in-sufficient for 3D reconstruction. VisualSFM provides the function of calculating dense point clouds, which can store dense point clouds in the computer in the form of data. MeshLab is based on the Poisson surface reconstruction (PSR) algorithm, which can convert dense point-cloud data into a mesh model of a scene. 3D Studio Max can import the previous scene model and render the virtual information at the same time.

Stereo Matching and SFM

Stereo matching refers to the matching of pixel pairs with identical points on multiple perspectives of the same scene, estimating parallax and calculating object-depth information, and preparing for SFM. Before matching, it is necessary to detect the feature points of the image. The Scale invariant feature transform (SIFT) operator is used as a feature point detection tool in VisualSFM.

SIFT has scale and rotation invariance. When the image is rotated and scaled, it still has good detection effect [16, 17]. In addition, it has strong robustness, is suitable for extracting feature point information of scale transformation and various images with angular rotation and has strong accuracy.

SFM determines the spatial and geometric relationship of object points by estimating the changes of the camera's spatial pose. When the spatial positions of more object points are determined, a sparse 3D point cloud can be obtained. To better represent the mapping relationship between pixels and object points in the SFM process, several coordinate systems must be considered.

- World coordinate system. A 3D coordinate system, which represents the actual coordinates of any object point in space.
- Camera coordinate system. A 3D coordinate system, which represents the spatial pose transformation of the camera to facilitate the expression of its motion process.

- Image-plane coordinate system**.** A 2D coordinate system with its origin located at the intersection of the camera optical axis and the image, which can represent the coordinates of any pixel point.

• Pixel-plane coordinate system. A 2D coordinate system with its origin in the upper left-hand corner of the image, which can represent the coordinates of any pixel point.

SFM process is the process of projecting the pixels in the pixel plane coordinate system to the world coordinate system. The projection relation is given directly here. For details, please refer to Refs. [18, 19].

$$Z_c \begin{bmatrix} u \\ v \\ 1 \end{bmatrix} = \begin{bmatrix} f_x & s & c_x \\ 0 & f_y & c_y \\ 0 & 0 & 1 \end{bmatrix} \begin{bmatrix} R & t \\ 0 & 1 \end{bmatrix} \begin{bmatrix} X_w \\ Y_w \\ Z_w \\ 1 \end{bmatrix} = KT \begin{bmatrix} X_w \\ Y_w \\ Z_w \\ 1 \end{bmatrix} \tag{1}$$

where (u, v) represents the coordinates of the image pixel in the pixel-plane coordinate system, (X_w, Y_w, Z_w) the coordinates of the object point in the world coordinate system, and K the camera internal parameter matrix, which is determined by the structural properties of the camera itself. f_x and f_y are the normalized focal lengths, s is the tilt factor, and c_x and c_y are the coordinates of the main point in the image plane coordinate system, both in pixels and known parameters. T is the external parameter matrix, which is determined by the position relationship between the camera and the world coordinate system. R and t represent rotation and translation, respectively, which are unknown parameters. Therefore, the solution of R and t becomes the key to SFM.

The calculation of relative pose R and t between adjacent cameras can be given by singular value decomposition of eigenmatrix E. **Eq. 2** gives the calculation method of E

$$x'Ex = 0 \tag{2}$$

where x' is the 3D point coordinate in the right-hand camera coordinate system and x the 3D point coordinate in the left-hand camera coordinate system. However, the values of their coordinates are unknown. The second calculation method of E is given as follows:

$$E = K_r^T F K_l \tag{3}$$

where K_r^T is the transpose of the internal parameter matrix of the right-hand camera, K_l the internal parameter matrix of the left-hand camera, and F the basic matrix. Here, K is known, and the solution method of the basic matrix is

$$q_r^T F q_l = 0 \tag{4}$$

where q_r^T is the transpose of the image-plane coordinates of the right-hand camera and q_l those of the left-hand camera. They can be calculated directly from the pixel-plane coordinates (u, v).

Thus, the transformation relationship of camera spatial pose can be calculated, and the spatial position of pixels reconstructed.

Computing Dense Point Cloud—Multi-View Stereo

The 3D point cloud obtained by SFM is composed of feature points, so it is sparse. To better reconstruct the 3D scene, it is necessary to densify the sparse point cloud. VisualSFM software can additionally configure the PMVS/CMVS resource package to realize the generation of a dense point cloud. The photos are clustered by CMVS to reduce the amount of dense reconstruction data, and then PMVS is used to generate dense point clouds with real colors through matching, diffusion, and filtering under the constraints of local photometric consistency and global visibility. The basic principle is multi-view stereo (MVS).

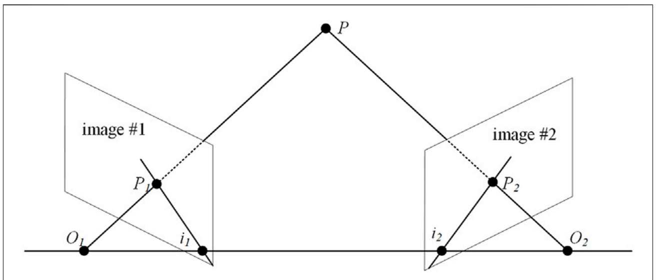

FIGURE 1 | Principle of epipolar constraints.

The main difference between MVS and SFM in obtaining a sparse point cloud is that MVS matches all pixels in the image and reconstructs the corresponding spatial position of each pixel to achieve the effect of high-definition reconstruction. To simplify the process of finding homonymous points in two images, epipolar constraints must be introduced. The epipolar constraint describes the constraint formed by the image point and camera optical center under the projection model when the same point is projected on two images from different perspectives, which can reduce the search range when feature point matching.

Referring to **Figure 1**, the line O_1O_2 connecting the optical centers of the two cameras is called the baseline, and the intersection of the baseline and the plane of images #1 and #2 is called the base point i_1 and i_2. The plane O_1O_2P is called the polar plane, and the intersections i_1P_1 and i_2P_2 of the polar and image planes are called the polar lines. If the image point of an object points in space on image #1 is P_1, then the image point on image #2 must be P_2. The epipolar constraint simplifies the detection and matching of all pixels of the image to the matching of a certain line, which can narrow the search range of feature-point matching and has a more accurate matching effect.

The consistency judgment function $c_{ij}(p)$ is used to judge the similarity of the points on the epipolar constraint to complete the feature matching of all pixels, and then the dense point cloud data are generated according to these registered feature points.

$$c_{ij}(p) = \rho\Big(I_i(\Omega(\pi_i(p))), I_j\big(\Omega\big(\pi_j(p)\big)\big)\Big) \tag{5}$$

where $\pi(p)$ is a function that makes object point p project to a point on the photograph, $\Omega(x)$ defines the area around a point x, and $I(x)$ represent the intensity characteristics of the photo area; ρ (f, g) is used to compare the similarity between two vectors. VisualSFM does not display the dense point cloud on the operation interface but records it in the computer in the form of a data list.

Poisson Surface Reconstruction

Poisson Surface Reconstruction (PSR) is a mesh reconstruction method proposed by Kazhdan *et al.* in 2006 [20]. It uses the input

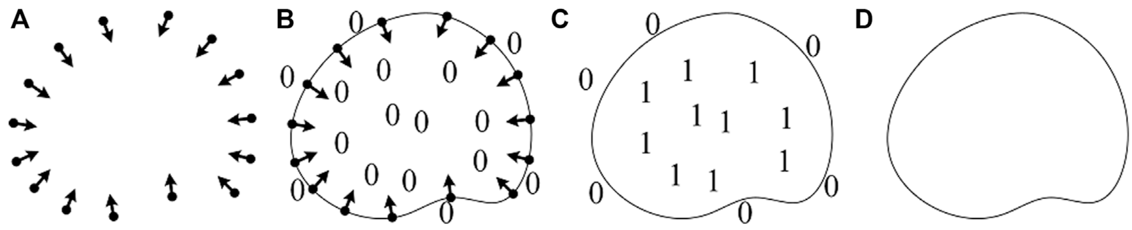

FIGURE 2 | Intuitive illustration of Poisson reconstruction in 2D **(A)** vector field $\vec{V}$ **(B)** gradient field $\nabla\chi_M(x)$ **(C)** indication function $\chi_M(x)$, and **(D)** surface ∂M.

FIGURE 3 | Three images in "old school gate of Tsinghua University" dataset.

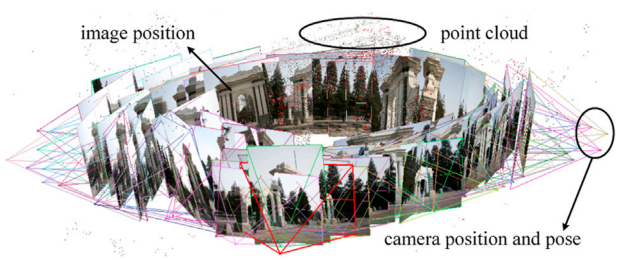

FIGURE 4 | Point cloud model and camera spatial pose.

point-cloud data to build a triangular mesh model and represents the surface reconstruction problem as finding the solution of a Poisson equation. Its core is that the point cloud represents the position of the object surface, and its normal vector represents the internal and external directions. PSR considers all data at the same time without heuristic segmentation and merging. It is a global algorithm, which is conducive to generating smooth surfaces.

By implicitly fitting an indicator function derived from an object, an estimate of a smooth object surface can be given. Letting M represent an area and ∂M be the surface of the area, the indicator function is

$$\chi_M(x) = \begin{cases} 1, x \in M \\ 0, x \notin M \end{cases} \tag{6}$$

where x represents the sampling point. The indicator function can be approximated to ∂M by estimating the indicator function and extracting the isosurface. Therefore, the key to the problem is to calculate the indicator function according to the samples. Here, the gradient $\nabla\chi_M(x)$ of the indicator function must be introduced. The relationship between sample point set X and ∂M can be established through gradient field $\nabla\chi_M(x)$ [20], as shown in **Figure 2**. First, a vector field $\vec{V}$ of the X is created from the period cloud data, as shown in **Figure 2A**. Then in **Figure 2B**, the corresponding $\nabla\chi_M(x)$ is generated according to $\vec{V}$, and in **Figure 2C** the indication function is assigned according to the distribution of the gradient field. Finally, the surface ∂M is created according to the assignment of the point set, as shown in **Figure 2D**.

First, the smoothing filter function $\tilde{F}$ is used to smooth $\chi_M(x)$. Through the divergence theorem, it can be proved that the gradient field of the smoothed indicator function is equal to the smoothed surface normal vector field:

$$\nabla\left(\chi_M \otimes \tilde{F}\right)(x) = \int_{\partial M} \tilde{F}(x-p)\vec{N}_{\partial M}(p)dp \tag{7}$$

where $\otimes$ is the convolution symbol for smoothing, $\vec{N}_{\partial M}$ is the normal vector at the surface (pointing to the inside), and p is the point corresponding to $\vec{N}_{\partial M}$. Due to the discreteness of sample points, $\vec{N}_{\partial M}$ is not known for every x near the surface, so it must be approximated piecewise:

$$\nabla\left(\chi_M \otimes \tilde{F}\right)(x) \approx \sum_{x\in X} |\mho_X| \tilde{F}(x - x\cdot p)x\cdot\vec{N} \equiv \vec{V} \tag{8}$$

where $x.\,p$ and $x\,\vec{N}$ represent the position and normal vector of x, respectively, $\mho_X\square\ \partial M$ is the surface area near x divided according to space, and $\vec{V}$ represents the vector field composed of the sample set. Assuming that the sample points

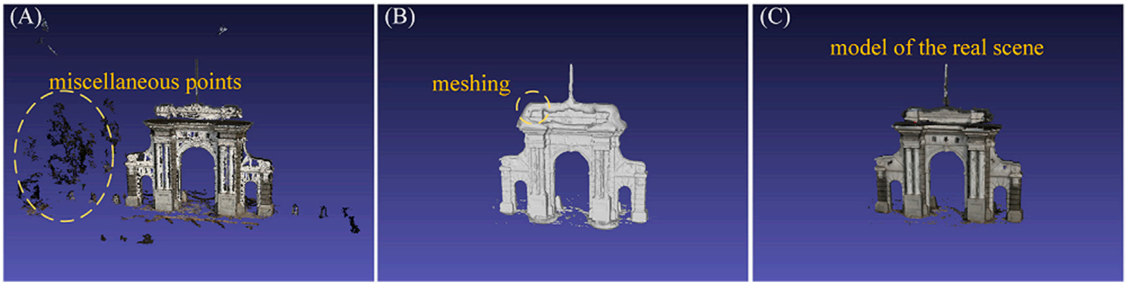

FIGURE 5 | Model generation process **(A)** Point cloud with miscellaneous points **(B)** meshing, and **(C)** reconstruction result.

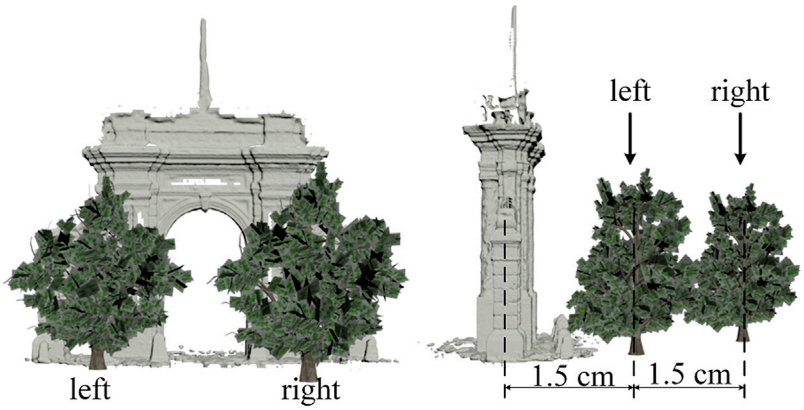

FIGURE 6 | Sampling image.

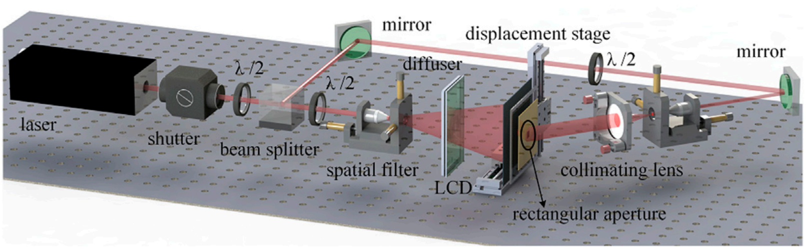

FIGURE 7 | Holographic printing optical scheme.

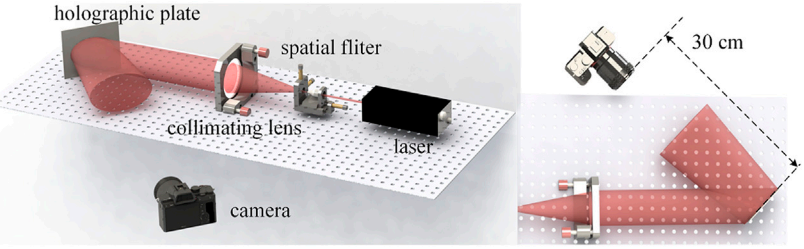

FIGURE 8 | Holographic optical reconstruction scheme.

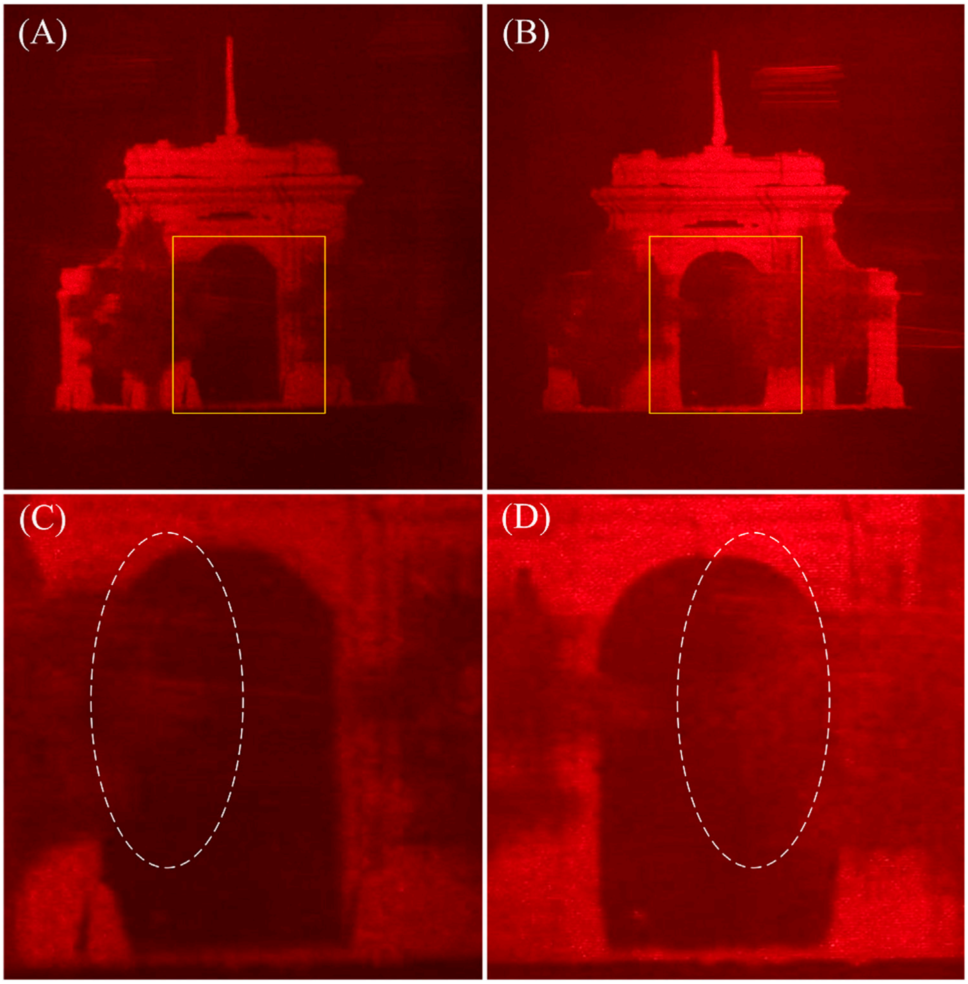

FIGURE 9 | Horizontal parallax information of reconstructed image **(A)** Left-hand perspective **(B)** right-hand perspective **(C)** detail of **(A)**, and **(D)** detail of **(B)**.

are evenly distributed, $\mho_X$ in the above formula can be omitted. **Equations 7** and **8** are simultaneous, and $\tilde{x}$ represents the smoothed $\chi_M(x)$; then,

$$\nabla\tilde{\chi} = \vec{V} \tag{9}$$

Using the divergence operator, **Eq. 9** can be transformed into a Poisson equation,

$$\Delta\tilde{\chi} = \nabla\cdot\vec{V} \tag{10}$$

The indicator function can be calculated by solving the Poisson equation. The solution of **Eq. 10** is obtained by Laplace matrix iteration, which will not be repeated here.

EXPERIMENT AND ANALYSIS

3D Reconstruction and Data Processing

The dataset "old school gate of Tsinghua University" was used in our experiment [21]. The data were from the State Key Laboratory of pattern recognition, Institute of Automation, Chinese Academy of Sciences, who used a Riegl-LMS-Z420i laser scanner to obtain the data of buildings and take image data at the same time. The accuracy of the laser scanner within 50 m is 10 mm and the scanning-angle interval 0.0057°. The experiment only used 68 images in the dataset, with dimensions of 4,368 × 2,912 pixel. Three images are shown in **Figure 3**.

The images were batch-imported into VisualSFM. Stereo matching took 143 s, and 2,278 matches were completed. Matching uses a SIFT operator to form a new intermediate file, which records the matching information in the form of a data list. The file is read, and the sparse 3D point cloud calculated. The point-cloud model and camera spatial pose appear on the software display interface, which takes 196 s, and is shown in **Figure 4**. The dense point-cloud data are calculated and stored in the computer in the form of a model file and a list file, which takes 10.367 min.

The dense point cloud data were imported into MeshLab for operations such as removing miscellaneous points, meshing, repairing manifold edges, parameterization, and texturing, to

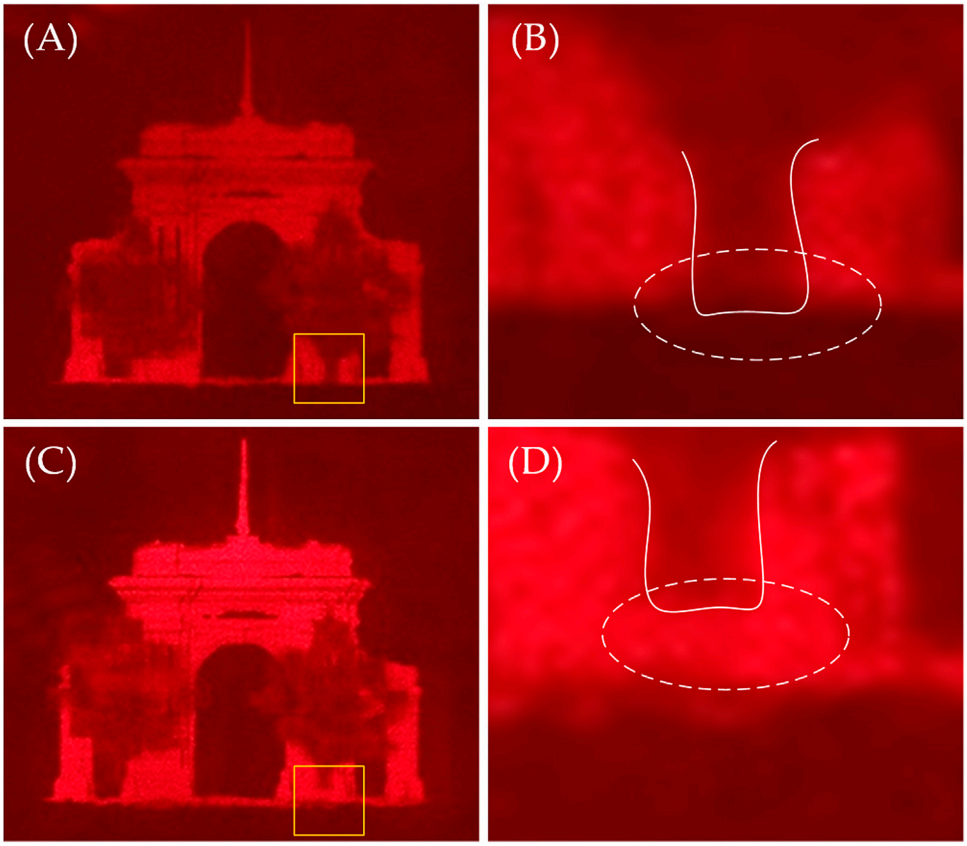

FIGURE 10 | Vertical parallax information of the reconstructed image **(A)** Head up view **(B)** detail of **(A)** **(C)** bottom view, and **(D)** detail of **(C)**.

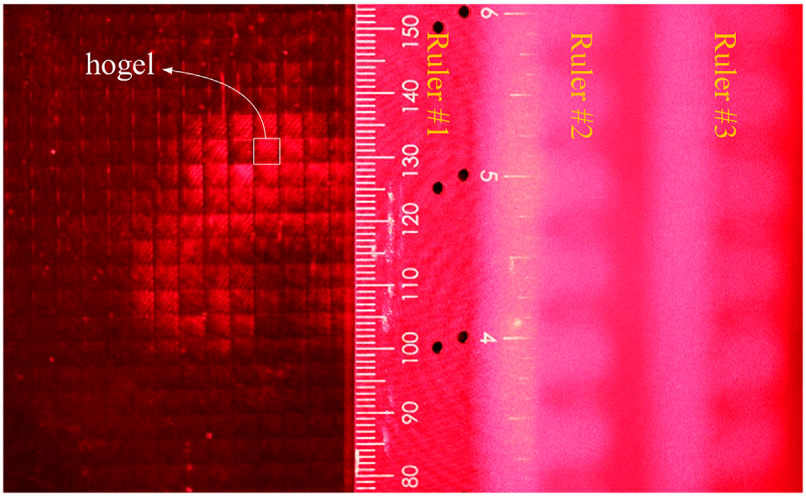

FIGURE 11 | Camera focused on Ruler #1.

obtain the model of the real scene, export the model file and store it in the computer. The model generation process is shown in **Figure 5**.

The model file was imported into 3D Studio Max software (texture is usually lost in this process) and the spatial pose of the model adjusted. The tree model (virtual scene) was merged and

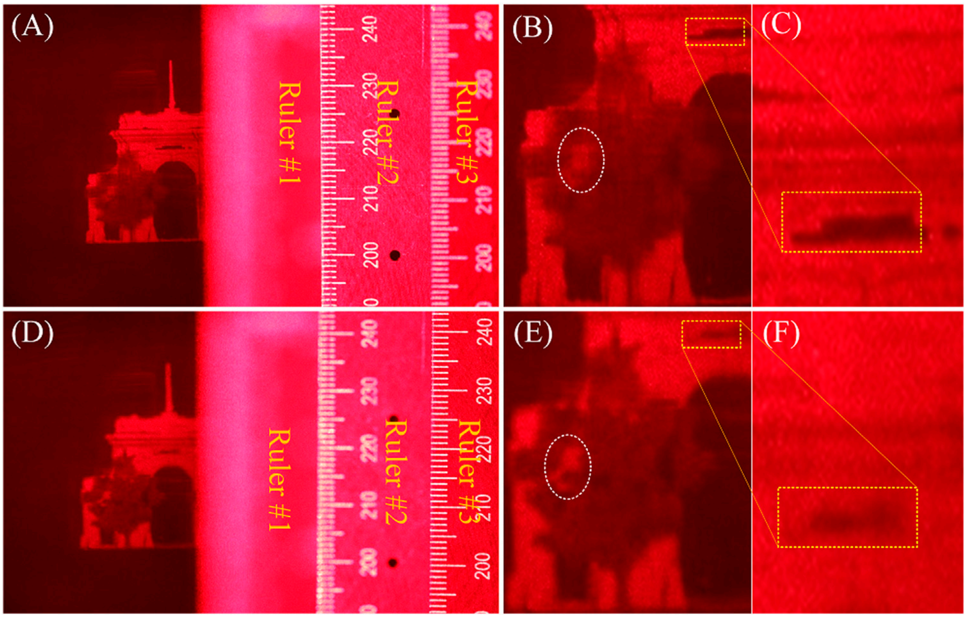

FIGURE 12 | Comparation of depth information **(A)** Camera focused on Ruler #2 **(B)** detail of **(A)**, and **(C)** detail of **(B)** **(D)** Camera focused on Ruler #3 **(E)** detail of **(D)**, and **(F)** detail of **(E)**.

imported to obtain the fusion scene. The scene position relationship was adjusted, and the geometric center of the school gate placed at the origin, with the left- and right-hand trees in front of the gate approximately 1.5 and 3 cm away from the gate, respectively. The camera was located 13.8 cm from the origin for shooting and sampling, and the sampling images are shown in **Figure 6**. The EPISM method proposed in this paper was used for sampling and coding. In this experiment, the hogel size is 4 mm × 4 mm and the printing area is 8 cm × 8 cm. (For specific details and methods, please refer to Ref. [15].)

Holographic Printing and Reconstruction

The optical experimental scheme was set up as shown in **Figure 7**. A 400-MW/639-nm single longitudinal mode linearly polarized solid-state laser (CNI MSL-FN-639) was used as the light source, and an electronic shutter (Sigma Koki SSH-C2B) was used to control the exposure time. After passing through a λ/2-wave plate and a polarizing beam splitter (PBS), the laser beam was divided into two beams, namely the object beam and the reference beam. The polarization state of the object beam was adjusted by a λ/2-wave plate to be consistent with the reference beam. The attenuator of the reference beam was adjusted to attain an object reference energy ratio of 1:20. The object beam irradiated the LCD screen after being expanded and reached the holographic plane after being diffused by the scattering film. After filtering and collimating, the uniform plane-wave reference beam was obtained. The object and reference beams interfered with each other after being incident from both sides, and the exposure image information was written. The holographic plate was fixed on a KSA300 X-Y linear displacement platform; the positioning accuracy of the platform in the horizontal and vertical directions was 1 μm. The displacement platform was controlled by an MC600 programmable controller.

Holographic plate is a silver salt dry plate. After holographic printing, it is developed, fixed, and bleached. The holographic plate can reconstruct 3D images in the conjugate of original reference light after developing and bleaching. As shown in **Figure 8**, the reconstructed image was taken with a Canon camera and a macro lens with a focal length of 100 mm, which was placed approximately 30 cm in front of the holographic plate.

Results and Analysis

In this subsection, we show and analyze the 3D information of the obtained hologram, including horizontal parallax, vertical parallax, and depth information. It should be noted that although our experimental system can display ±19.8° horizontal and vertical field angles, the actual displayed field angle cannot meet this standard to display the main part of the fusion scene.

Figure 9 shows the horizontal parallax information of the reconstructed image at the same vertical position, in which (C) and (D) show some details in the yellow rectangles of (A) and (B), respectively. As can be seen from the information in the white elliptical curves in (C) and (D), the tree in (D) on the left-hand side of the middle door blocks most of the doorway, and the tree on the right-hand side fails to block the doorway, while (D) depicts the opposite. This shows that the perspective of (A) is on the left and that of (B) is on the right. The angle between them is approximately 10°.

Figure 10 shows the vertical parallax information of the reconstructed image in the same horizontal position, where (B) and (D) show some of the details in the yellow rectangles of (A) and (C), respectively. For ease of observation, the edge contour at the logarithmic root is depicted in the figures. From information in the white elliptical curves in (B) and (D), the bottom of the tree root in (B) is nearly parallel to the bottom of the school gate, while the bottom of the tree root in (D) is higher. This shows that (A) is a head's-up view and (C) is a bottom view. The angle between them is approximately 5°.

Figures 11,12 show the depth information of the reconstructed image. Here, only the left-hand side of the fusion scene is of importance. To facilitate analysis, three rulers are placed in the reconstructed light field, one is in the hologram plate, one is 13.8 cm away from the hologram, and the other is 15.3 cm away from the hologram. When the camera focuses on Ruler #1, as shown in **Figure 11**, the grid shape of the hogel is clearly visible, and the reconstructed image cannot be observed.

When the camera focuses on Ruler #2, as shown in **Figure 12** (A-C), the details of the tree circled by the white elliptical curve are blurred, but an incomplete part of the school gate in the yellow box is clearly displayed. When the camera focuses on Ruler #3, as shown in **Figure 12** (D-F), the opposite is true. This shows that the scene protrudes from the holographic plate display, and that the distance is equal to the sampling distance; in addition, the depth information between the scenes also conforms to the preset relationship during sampling. The depth information of the scene can be expressed effectively.

CONCLUSION

In this paper, an augmented reality–holographic stereogram based on 3D reconstruction is proposed that provides an effective means for augmented holographic 3D display of a scene. The relevant research results can be applied to medical, military, and other fields. In the 3D reconstruction, two software programs were used—VisualSFM and MeshLab. The basic principle of the 3D reconstruction algorithm employed in the software is introduced, and the 3D reconstruction completed by using an image dataset depicting the "old school gate of Tsinghua University." We rendered, sampled, and encoded the 3D model and the virtual scene at the same time, and then holographic printing was carried out to obtain the holographic stereogram with full parallax. Results and analysis verified the effectiveness of the proposed method. Since we were concerned about the effectiveness of the method, we selectively ignored the poor effect of the 3D reconstruction approach used, especially the loss of texture information when the model was imported into the 3D modeling software. The 3D model obtained from 68 images has obvious holes. To obtain better results, we must increase the number of images or use other methods to complete 3D reconstruction, which is also our next planned research direction.

DATA AVAILABILITY STATEMENT

The original contributions presented in the study are included in the article/supplementary material further inquiries can be directed to the corresponding authors.

AUTHOR CONTRIBUTIONS

Conceptualization, YL and XY; methodology, YL, TJ, and XY; software, QQ, PZ, and TJ; validation, PL, X.J, and QY; formal analysis, YL and TJ; resources, XY and PZ; data curation, PZ and XJ; writing—original draft preparation, YL, QQ, and QY; writing—review and editing, YL and QZ; visualization, PZ and QQ; supervision, XJ and XY; project administration, XY; funding acquisition, XY All authors have read and agreed to the published version of the manuscript.

FUNDING

This research was funded by the National Key Research and Development Program of China (Grant No. 2017YFB1104500), National Natural Science Foundation of China (Grant No. 61775240), and Foundation for the Author of National Excellent Doctoral Dissertation of the People's Republic of China (Grant No. 201432).

REFERENCES

1. Su J, Yan X, Huang Y, Jiang X, Chen Y, Zhang T. Progress in the Synthetic Holographic Stereogram Printing Technique. *Appl Sci* (2018) 8(6):851. doi:10.3390/app8060851
2. Yamaguchi M. Light-field and Holographic Three-Dimensional Displays [Invited]. *J Opt Soc Am A* (2016) 33(12):2348–64. doi:10.1364/JOSAA.33.002348
3. Choi YS, Lee S, Jung JY, Jeong KY, Park HG, Seo MK. Optical Metasurface-Based Holographic Stereogram. *Adv Opt Mater.* (2020) 8(8):1901970. doi:10.1002/adom.201901970
4. Liu P, Sun X, Zhao Y, Li Z. Ultrafast Volume Holographic Recording with Exposure Reciprocity Matching for TI/PMMAs Application. *Opt Express* (2019) 27(14):19583–95. doi:10.1364/OE.27.019583
5. Jiang Q, Jin G, Cao L. When Metasurface Meets Hologram: Principle and Advances. *Adv Opt Photon* (2019) 11(3):518–76. doi:10.1364/AOP.11.000518
6. Ning Q. Binocular Disparity and the Perception of Depth. *Neuron* (1997) 18(3):359–68. doi:10.1016/S0896-6273(00)81238-6
7. He Z, Sui X, Jin G, Cao L. Progress in Virtual Reality and Augmented Reality Based on Holographic Display. *Appl Opt* (2019) 58(5):A74–A81. doi:10.1364/AO.58.000A74
8. Breen DE, Whitaker RT, Rose E, Tuceryan M. Interactive Occlusion and Automatic Object Placement for Augmented Reality. *Computer Graphics Forum* (1996) 15(3):11–22. doi:10.1111/1467-8659.1530011
9. Wloka MM, Anderson BG. Resolving Occlusion in Augmented Reality. In: Proceedings of the 1995 symposium on Interactive 3D graphics, April 9–12, 1995, Monterey, CA. New York, NY, USA (1995). p. 5–12. doi:10.1145/199404.199405
10. Roxas M, Hori T, Fukiage T, Okamoto Y, Oishi T. Occlusion Handling Using Semantic Segmentation and Visibility-Based Rendering for Mixed Reality. In: Proceedings of the 24th ACM Symposium on Virtual Reality Software and Technology, November 28, 2018–December 1, 2018, Tokyo, Japan. New York, NY, USA (2018). doi:10.1145/3281505.3281546

11. Li Q, He W, Deng H, Zhong F-Y, Chen Y. High-performance Reflection-type Augmented Reality 3D Display Using a Reflective Polarizer. *Opt Express* (2021) 29(6):9446–53. doi:10.1364/OE.421879
12. Shi L, Li B, Kim C, Kellnhofer P, Matusik W. Author Correction: Towards Real-Time Photorealistic 3D Holography with Deep Neural Networks. *Nature* (2021) 593(7849):E13. doi:10.1038/s41586-021-03476-5
13. Yang X, Zhang H, Wang Q-H. A Fast Computer-Generated Holographic Method for VR and AR Near-Eye 3D Display. *Appl Sci* (2019) 9(19):4164. doi:10.3390/app9194164
14. Liu Y, Yan X, Liu X, Wang X, Jing T, Lin M, et al. Fusion Coding of 3D Real and Virtual Scenes Information for Augmented Reality-Based Holographic Stereogram. *Front Phys* (2021) 9:736268. doi:10.3389/fphy.2021.736268
15. Su J, Yuan Q, Huang Y, Jiang X, Yan X. Method of Single-step Full Parallax Synthetic Holographic Stereogram Printing Based on Effective Perspective Images' Segmentation and Mosaicking. *Opt Express* (2017) 25(19):23523–44. doi:10.1364/OE.25.023523
16. Lowe DG. Distinctive Image Features from Scale-Invariant Keypoints. *Int J Computer Vis* (2004) 60:91–110. doi:10.1023/B:VISI.0000029664.99615.94
17. Lowe DG. Object Recognition from Local Scale-Invariant Features. In: Proceedings of the seventh IEEE international conference on computer vision; 20-27 Sept.1999; Kerkyra, Greece. IEEE (1999). p. 1150–7. doi:10.1109/ICCV.1999.790410
18. Lucieer A, Jong SMd., Turner D. Mapping Landslide Displacements Using Structure from Motion (SfM) and Image Correlation of Multi-Temporal UAV Photography. *Prog Phys Geogr Earth Environ* (2014) 38(1):97–116. doi:10.1177/0309133313515293
19. Wallace L, Lucieer A, Malenovský Z, Turner D, Vopěnka P. Assessment of forest Structure Using Two UAV Techniques: A Comparison of Airborne Laser Scanning and Structure from Motion (SfM) point Clouds. *Forests* (2016) 7(3):62. doi:10.3390/f7030062
20. Kazhdan M, Bolitho M, Hoppe H. Poisson Surface Reconstruction. In: *Proceedings of the Fourth Eurographics Symposium on Geometry Processing*. Sardinia, Italy: Cagliari (2006). June 26-28. doi:10.5555/1281957.1281965
21. Robot Vision Group. 3D Reconstruction Dataset (nd). Available at: http://vision.ia.ac.cn/data.

Conflict of Interest: The authors declare that the research was conducted in the absence of any commercial or financial relationships that could be construed as a potential conflict of interest.

Publisher's Note: All claims expressed in this article are solely those of the authors and do not necessarily represent those of their affiliated organizations, or those of the publisher, the editors and the reviewers. Any product that may be evaluated in this article, or claim that may be made by its manufacturer, is not guaranteed or endorsed by the publisher.

frontiers in Physics

ORIGINAL RESEARCH
published: 16 February 2022
doi: 10.3389/fphy.2022.847649

Propagation Properties of a Twisted Hermite-Gaussian Correlated Schell-Model Beam in Free Space

Leixin Liu[1], Haiyun Wang[1], Lin Liu[1], Yiming Dong[2], Fei Wang[1], Bernhard J. Hoenders[3], Yahong Chen[1], Yangjian Cai[1,4,5]* and Xiaofeng Peng[4,5]*

[1]School of Physical Science and Technology, Soochow University, Suzhou, China, [2]Department of Physics, Shaoxing University, Shaoxing, China, [3]Zernike Institute for Advanced Materials, University of Groningen, Groningen, Netherlands, [4]School of Physics and Electronics, Shandong Normal University, Jinan, China, [5]Shandong Provincial Engineering and Technical Center of Light Manipulation and Shandong Provincial, Key Laboratory of Optics and Photonic Devices, School of Physics and Electronics, Shandong Normal University, Jinan, China

OPEN ACCESS

Edited by:
Shangran Xie, Beijing Institute of Technology, China

Reviewed by:
Xinglin Zeng, Max Planck Institute for the Science of Light, Germany
Yang Chen, Paul Scherrer Institut (PSI), Switzerland

***Correspondence:**
Yangjian Cai
yangjiancai@suda.edu.cn
Xiaofeng Peng
xfpeng888@163.com

Specialty section:
This article was submitted to Optics and Photonics, a section of the journal Frontiers in Physics

Received: 03 January 2022
Accepted: 18 January 2022
Published: 16 February 2022

Citation:
Liu L, Wang H, Liu L, Dong Y, Wang F, Hoenders BJ, Chen Y, Cai Y and Peng X (2022) Propagation Properties of a Twisted Hermite-Gaussian Correlated Schell-Model Beam in Free Space. Front. Phys. 10:847649. doi: 10.3389/fphy.2022.847649

We introduce a novel type of twisted partially coherent beams with a nonconventional correlation function, named the twisted Hermite-Gaussian correlated Schell-model (THGCSM) beam. The condition that a twist phase can be imposed on a partially coherent beam is addressed for Schell-model fields endowed with rectangular symmetry. Further, the analytical formula for the THGCSM beam propagating in free space has been derived with the help of the generalized Collins formula. The propagation properties, such as the spectral density and the spectral degree of coherence (SDOC) of the THGCSM beam, also have been studied in detail by some numerical examples. The numerical results show that the twist phase plays a role in resisting beam splitting, caused by the correlation structure, and induces the rotation of the distribution of the SDOC on propagation. Moreover, it is interesting to find that when the beam carries a twist phase, this will endow the beam the ability to maintain its distribution of the SDOC on propagation and enhance the self -reconstruction capability of the SDOC. Our results may provide new insights into nonconventional partially coherent beams with twisted phase and may be useful in some applications, such as optical communications and information recovery.

Keywords: self-reconstruction, spectral degree of coherence, twist phase, propagation properties, partially coherent

INTRODUCTION

Coherence is one of the most notable features of a laser beam. These light beams (i.e., partially coherent beam) have attracted intensive attentions due to their wide applications in inertial confinement fusion, ghost imaging, sub-Rayleigh imaging, particle trapping, free space optical communications and optical scattering [1–8]. Furthermore, Gori et al. [9, 10] proposed the sufficient conditions for designing a real genuine cross-spectral density function or matrix of a partially coherent beam. Based on the above works, a variety of partially coherent beams with nonconventional correlation functions (i.e., the correlation function doesn't satisfy the Gaussian distribution) have been introduced theoretically and generated experimentally [11–27]. It is found that beams with nonconventional correlation functions will exhibit unique properties on propagation, such as self-splitting, self-reconstruction, locally sharpened and laterally shifted intensity maxima [13, 22, 27], which are useful in multi-particles trapping, atoms guiding, image transfer and recovery. Moreover, the beam profiles in the focal plane (or far fields) can be controlled by endowing the beam with a specific correlation function [15–19, 26], for example, dark-hollow beam profiles (or an optical cage) can be formed near the focal plane when the correlation function satisfies a Laguerre–Gaussian distribution [18]. A Multi-Gaussian correlated Schell-model beam would generate a rectangular intensity profile in the focal plane, and a ring-shaped beam and controllable intensity lattices also can be achieved with the help of the correlation functions [15, 26]. In addition, partially coherent beams with prescribed correlation functions can be applied to reduce scintillation in turbulence [28], overcome the classical Rayleigh diffraction limit [29], coherence-based optical encryption [30], robust microscopy imaging [31], robust far-field imaging [32], and optical beam shaping [33].

On the other hand, partially coherent beams with a twist phase (i.e., twisted partially coherent beam) carry orbital angular momentum (OAM) [34]. Twist phase as a "genuinely two-dimensional" phase can't exist in a coherent beam and its value is bounded in strength. Twist phase was introduced by Simon et al. in 1993 and has been demonstrated in an experiment by Friberg [35, 36]. Due to the intrinsic chiral property of the twist phase the rotation of the beam spot on propagation is induced, and both the distribution of the SDOC, the degree of polarization and the state of polarization of the beam on propagation are affected [37, 38]. Besides, light beams with a twist phase have advantages in resisting coherence (or turbulence)-induced degeneration, depolarization and overcoming the classical Rayleigh limit [37, 39]. It is shown in [40, 41] that using a twist phase can greatly increase the amount of OAM of a partially coherent vortex beam and enhance its self-reconstruction capability.

Recently, some new ways have been introduced to generate twisted Gaussian Schell-model beams and measure their orbital angular momentum [42, 43]. The problem of when a twist phase can be imposed on a partially coherent beam, generated from a Schell-model source with axial symmetries, was explored in [44, 45]. Two approaches have been proposed to devise genuine twist beams with and without symmetry [46, 47]. In this paper, we devised a newly twisted partially coherent beam named the twisted Hermite-Gaussian correlated Schell-model (THGCSM) beam. The condition that the THGCSM beam will be bona fide is met, and the propagation properties of the THGCSM beam have been investigated in detail. Our results show that the twist phase plays a role of preventing deterioration of the intensity distribution and induces rotation of the distribution of the SDOC around the axis on propagation. Furthermore, the twist phase also will enhance the ability of the beam to maintain the distribution of the SDOC and its self-reconstruction capability, which will be useful for optical information processing and recovery.

THEORY OF THE TWISTED HERMITE-GAUSSIAN CORRELATED SCHELL-MODEL BEAM

Twisted Schell-Model Beams With Rectangular Symmetry

Based on the unified theory of coherence and polarization, the statistical properties of a partially coherent beam can be characterized by the cross-spectral density (CSD) [48]. For Schell-model fields, endowed with rectangular symmetry, the cross-spectral density (CSD) of the beam can be expressed as

$$W_0\ (\boldsymbol{r_1}, \boldsymbol{r_2}) = \tau^*(\boldsymbol{r_1})\tau(\boldsymbol{r_2})\, u(|x_1 - x_2|)\, u(|y_1 - y_2|), \quad (1)$$

where $\boldsymbol{r_1} = (x_1, y_1)$, $\boldsymbol{r_2} = (x_2, y_2)$ are two arbitrary transverse position vectors, τ (r_i) denotes the transmission function of an arbitrary (complex) amplitude filter and u ($|x_1$-$x_2|$)u ($|y_1$-$y_2|$) is the spectral degree of coherence. When the beam carries a twist phase, the CSD is defined as

$$W_{0u}\ (\boldsymbol{r_1}, \boldsymbol{r_2}) = \tau^*(\boldsymbol{r_1})\tau(\boldsymbol{r_2})\, u(|x_1 - x_2|)\, u(|y_1 - y_2|)\ exp(-ik\mu_0 \boldsymbol{r_1} \times \boldsymbol{r_2}), \quad (2)$$

where the last exponential term represents the twist phase, with μ_0 being the twist factor. According to the Refs. [44, 45], the CSD will be bona fide, if and only if the corresponding uniform source, defined as

$$W_u\ (\boldsymbol{r_1}, \boldsymbol{r_2}) = u(|x_1 - x_2|)\, u(|y_1 - y_2|)\, exp(-ik\mu_0 \boldsymbol{r_1} \times \boldsymbol{r_2}), \quad (3)$$

is bona fide too. Then, we find that the uniform source satisfies the following formal integral relationship

$$\int d^2\rho W_u(\boldsymbol{r_1}, \boldsymbol{\rho}) T_u(\boldsymbol{\rho}, \boldsymbol{r_2}) = \int d^2\rho T_u(\boldsymbol{r_1}, \boldsymbol{\rho}) W_u(\boldsymbol{\rho}, \boldsymbol{r_2}), \quad (4)$$

for any pair (r_1, r_2), $\boldsymbol{\rho} = (\rho_x, \rho_y)$ is an arbitrary transverse position vector, and $T_u = exp(-ik\mu_0 \boldsymbol{r}_1 \times \boldsymbol{r}_2)$ denotes the twist phase. To prove this, on substituting **Eq. 3** into **Equation 4**, the l. h. s of **Eq. 4** reads as follows

$$\int d^2\rho W_u(\boldsymbol{r_1}, \boldsymbol{\rho}) T_u(\boldsymbol{\rho}, \boldsymbol{r_2}) = \int d^2\rho\, u(|x_1 - \rho_x|)\, u(|y_1 - \rho_y|)\ exp(-ik\mu_0(\boldsymbol{r_1} - \boldsymbol{r_2}) \times \boldsymbol{\rho}), \quad (5)$$

For the r. h. s of **Eq. 4** we obtain:

$$\int d^2\rho T_u(\boldsymbol{r_1}, \boldsymbol{\rho}) W_u(\boldsymbol{\rho}, \boldsymbol{r_2}) = \int d^2\rho\, u(|\rho_x - x_2|)\, u(|\rho_y - y_2|)\ exp(-ik\mu_0(\boldsymbol{r_1} - \boldsymbol{r_2}) \times \boldsymbol{\rho}), \quad (6)$$

Then, taking into account that $\exp[-ik\mu_0(\boldsymbol{r_1} - \boldsymbol{r_2}) \times \boldsymbol{\rho}] = \exp[-ik\mu_0(\boldsymbol{r_1} - \boldsymbol{r_2}) \times (\boldsymbol{\rho} - (\boldsymbol{r_2} - \boldsymbol{r_1}))]$,

Eq. 6 can be expressed as follows

$$\int d^2\rho T_u(\boldsymbol{r_1}, \boldsymbol{\rho}) W_u(\boldsymbol{\rho}, \boldsymbol{r_2}) = \int d^2\rho\, u(|\rho_x - (x_2 - x_1) - x_1|)\, u(|\rho_y - (y_2 - y_1) - y_1|) \times exp[-ik\mu_0(\boldsymbol{r_1} - \boldsymbol{r_2}) \times (\boldsymbol{\rho} - (\boldsymbol{r_2} - \boldsymbol{r_1}))]. \quad (7)$$

On letting $\boldsymbol{\rho} = \boldsymbol{\rho} - (\boldsymbol{r}_2 - \boldsymbol{r}_1)$, **Eq. 7** can be recast as

$$\int d^2\rho T_u(\boldsymbol{r_1},\boldsymbol{\rho}) W_u(\boldsymbol{\rho},\boldsymbol{r_2}) = \int d^2\rho\, u(|\rho_x - x_1|)\, u(|\rho_y - y_1|) \; exp[-ik\mu_0 (\boldsymbol{r_1} - \boldsymbol{r_2}) \times \boldsymbol{\rho}]. \quad (8)$$

Thus, the **Equation 4** has been proved. Moreover, it has been mentioned in [45], when the **Equation 4** is satisfied, the uniform source W_u defined by **Eq. 3** and the twist phase T_u share the same coherent modes, defined as

$$\Phi_{j,m}(r) = \sqrt{\frac{u}{\pi}}\left[\frac{(j-|m|)!}{(j+|m|)!}\right]^{1/2} (r\sqrt{u})^{2|m|} exp(i2m\varphi) L_{j-|m|}^{2|m|}(ur^2)\; exp\left(-\frac{ur^2}{2}\right), \quad (9)$$

with $u = k\mu_0$, $k = 2\pi/\lambda$ is the wavenumber with wavelength λ, and $j = 0, 1/2, 1, \ldots, m = -j, j+1, \ldots, j$. Here, $L_{j-|m|}^{2|m|}$ is the Laguerre polynomials with the radial index j-$|m|$ and the angular index $2|m|$, while exp $(i2m\varphi)$ represents the vortex phase.

If the uniform source W_u is bona fide, the sufficient condition is that the eigenvalue sequence $\{\lambda_{j,m}\}$ should be nonnegative. These eigenvalues are defined as

$$\lambda_{j,m} = \iint d^2\boldsymbol{r_1}\boldsymbol{r_2} W_u(\boldsymbol{r_1},\boldsymbol{r_2}) \Phi_{j,m}(\boldsymbol{r_1}) \Phi_{j,m}^*(\boldsymbol{r_2}). \quad (10)$$

On substituting **equations 3** and **(9)** into **Equation 10**, and on letting $\boldsymbol{r}_1 - \boldsymbol{r}_2 = \boldsymbol{r}$, we have

$$\lambda_{j,m} = \int d^2 r u(x) u(y) \int d^2 r_2 \; exp(-ik\mu_0 \boldsymbol{r} \times \boldsymbol{r_2}) \Phi_{j,m}(\boldsymbol{r}+\boldsymbol{r_2}) \Phi_{j,m}^*(\boldsymbol{r_2}). \quad (11)$$

Use the Following Expression [45]

$$\int d^2 r_2\, exp(-ik\mu_0 \boldsymbol{r} \times \boldsymbol{r_2}) \Phi_{j,m}(\boldsymbol{r}+\boldsymbol{r_2}) \Phi_{j,m}^*(\boldsymbol{r_2}) = \mathcal{L}_{j+m}(ur^2), \quad (12)$$

with $\mathcal{L}_n(x) = L_n(x)\, exp(-x/2)$, and $\lambda_{j,m} = \lambda_{j+m} = \Lambda_b$. After some operation, we have

$$\Lambda_b = \sum_{k0=0}^{b} \int u(x) L_{k0}^{-1/2}(ux^2)\, exp\left(-\frac{ux^2}{2}\right) dx \times \int u(y) L_{b-k0}^{-1/2}(uy^2)\, exp\left(-\frac{uy^2}{2}\right) dy. \quad (13)$$

Eq. 13 is one of the main results of this paper, which can be used to assess the conditions when the Schell-model beams with rectangular symmetry can carry the twist phase.

Analytical Formula for a Twisted Hermite-Gaussian Correlated Schell-Model Beam

In this section, we introduce a new kind of twisted partially coherent beam with nonconventional correlation function, named the twisted Hermite-Gaussian correlated Schell-model (THGCSM) beam. As a natural extension of the Hermite-Gaussian correlated Schell-model (HGCSM) beam [22], the CSD in the source plane ($z = 0$) is defined as

$$W(\boldsymbol{r_1},\boldsymbol{r_2}) = \exp\left(\frac{\boldsymbol{r_1}^2 + \boldsymbol{r_2}^2}{4\sigma_0^2}\right) \frac{H_{2m}[(x_2 - x_1)/\sqrt{2}\delta_0]}{H_{2m}[0]} \exp\left[-\frac{(x_2-x_1)^2}{2\delta_0^2}\right] \times \frac{H_{2n}\left[\frac{(y_2-y_1)}{\sqrt{2}\delta_0}\right]}{H_{2n}[0]} \exp\left[-\frac{(y_2-y_1)^2}{2\delta_0^2}\right] \exp(-ik\mu_0 \boldsymbol{r_1} \times \boldsymbol{r_2}), \quad (14)$$

where $\boldsymbol{r_1} = (x_1, y_1)$, $\boldsymbol{r_2} = (x_2, y_2)$ are two arbitrary transverse position vectors in the source plane, σ_0 and δ_0 represent the beam width and the spatial coherence width, respectively. H_{2m} and H_{2n} are the Hermite polynomial of order 2m and 2n, respectively. After some algebra, **Equation 14** can be expressed in the following alternative form

$$W(\boldsymbol{r_1},\boldsymbol{r_2}) = \frac{m!\sqrt{\pi}}{\Gamma(m+1/2)} \frac{n!\sqrt{\pi}}{\Gamma(n+1/2)} exp\left(\frac{r_1^2 + r_2^2}{4\sigma_0^2}\right) L_m^{-1/2}\left[-\frac{(x_2-x_1)^2}{2\delta_0^2}\right] exp\left[-\frac{(x_2-x_1)^2}{2\delta_0^2}\right] \times L_n^{-1/2}\left[-\frac{(y_2-y_1)^2}{2\delta_0^2}\right] exp\left[-\frac{(y_2-y_1)^2}{2\delta_0^2}\right] exp(-ik\mu_0 \boldsymbol{r_1} \times \boldsymbol{r_2}). \quad (15)$$

As mentioned in **section 2.1**, the THGCSM beam will be bona fide, if and only if the corresponding uniform source, defined as

$$W_{u0}(\boldsymbol{r_1},\boldsymbol{r_2}) = L_m^{-1/2}\left[-\frac{(x_2-x_1)^2}{2\delta_0^2}\right] exp\left[-\frac{(x_2-x_1)^2}{2\delta_0^2}\right] \times L_n^{-1/2}\left[-\frac{(y_2-y_1)^2}{2\delta_0^2}\right] exp\left[-\frac{(y_2-y_1)^2}{2\delta_0^2}\right] exp(-ik\mu_0 \boldsymbol{r_1} \times \boldsymbol{r_2}). \quad (16)$$

is bona fide too. On substituting **Equation 15** into **Equation 10**, and after some tedious integrations and algebraic manipulations, we have

$$\Lambda_b = \sum_{k0=0}^{b} \frac{2\delta_0^2}{1+u\delta_0^2} \frac{\Gamma(m+k0+1/2)\Gamma(n+b-k0+1/2)}{m!k!n!(b-k0)!} \left(\frac{u\delta_0^2}{1+u\delta_0^2}\right)^{m+n} \left(\frac{1-u\delta_0^2}{1+u\delta_0^2}\right)^{b} \times {}_2F_1\left[-m, -k0; -m-k0+\frac{1}{2}; -\frac{(1+u\delta_0^2)}{(1-u\delta_0^2)}\right] \times {}_2F_1\left[-n, k0-b; k0-b-n+\frac{1}{2}, -\frac{(1+u\delta_0^2)}{1-u\delta_0^2}\right], \quad (17)$$

where ${}_2F_1$ is a hypergeometric function. So, in order for W_u to be bona fide (i.e., $\lambda_{j,m}$ should be nonnegative), the parameter $u = k\mu_0$ in **Eq. 17** must be bounded by the following inequality:

$$u\delta_0^2 \leq 1. \quad (18)$$

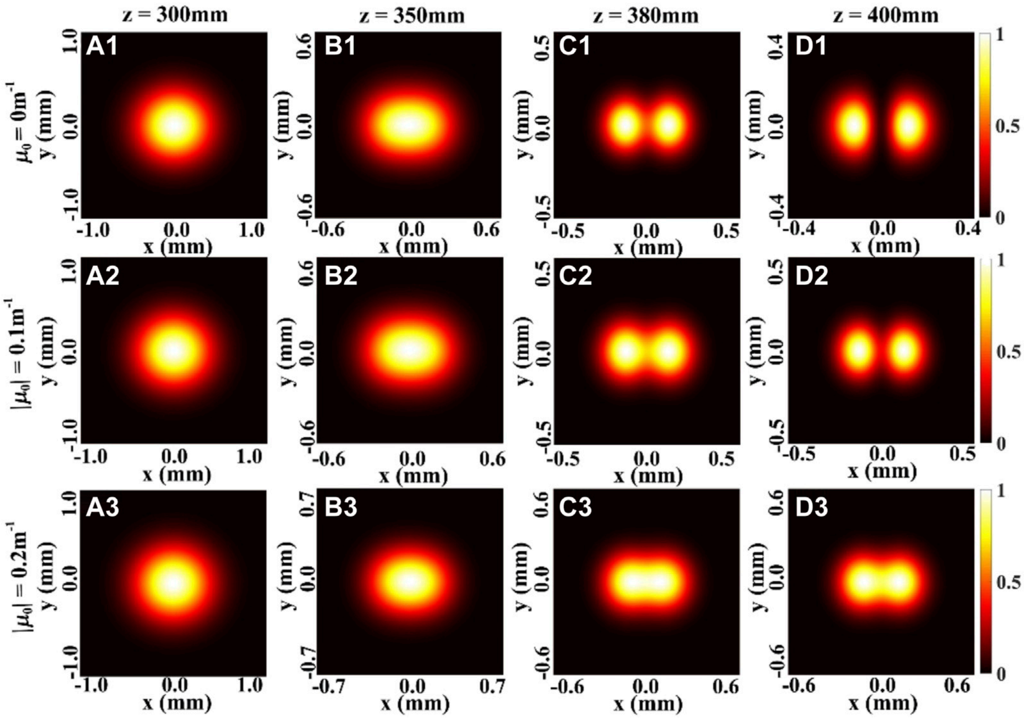

FIGURE 1 | Density plot of the normalized spectral density of a focused THGCSM beam with m = 1, n = 0 for different values of the twist factor μ_0 at several propagation distances.

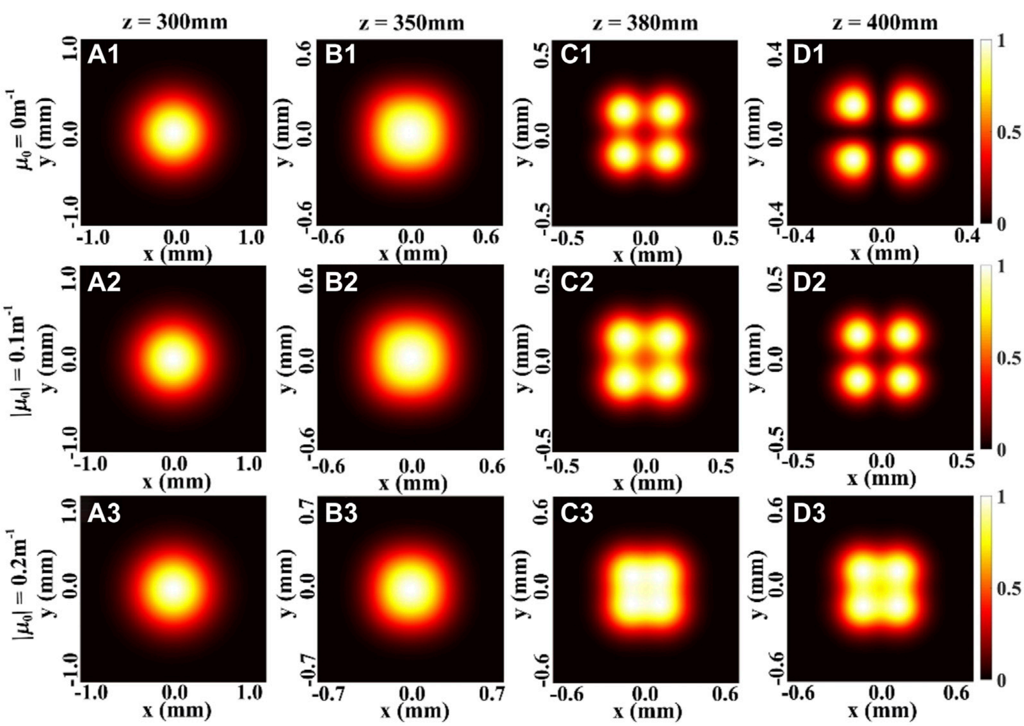

FIGURE 2 | Density plot of the normalized spectral density of a focused THGCSM beam with m = 1, n = 1 for different values of the twist factor μ_0 at several propagation distances.

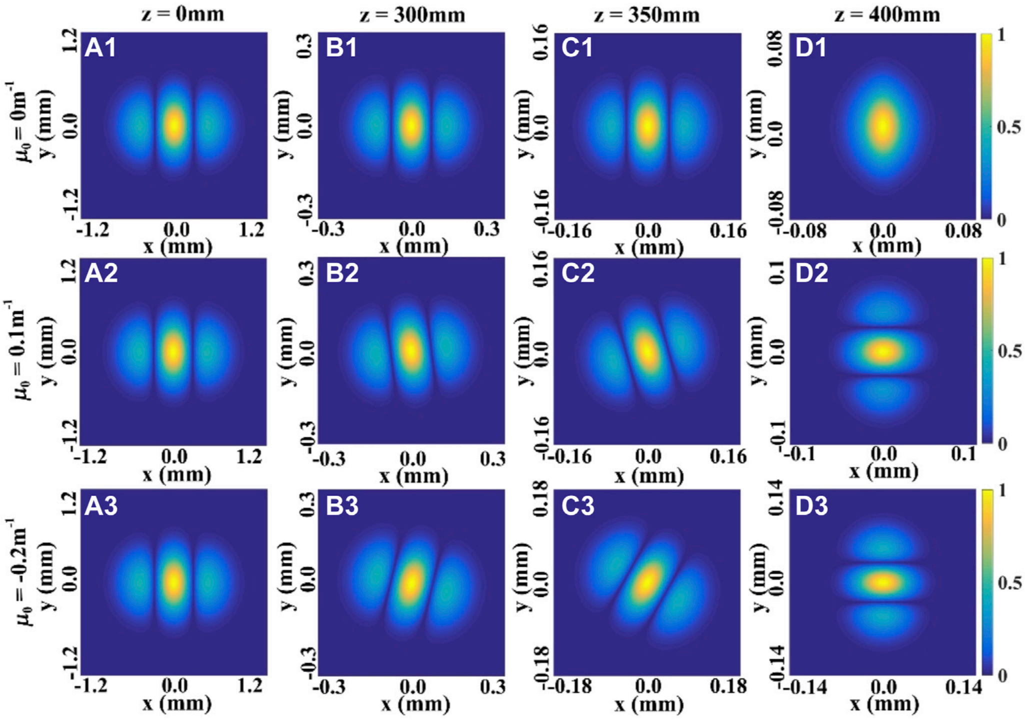

FIGURE 3 | Modulus of the SDOC between two points $\boldsymbol{\rho}$ and$-\boldsymbol{\rho}$ of the THGCSM beam with m = 1, n = 0 for different values of the twist factor μ_0 at several propagation distances.

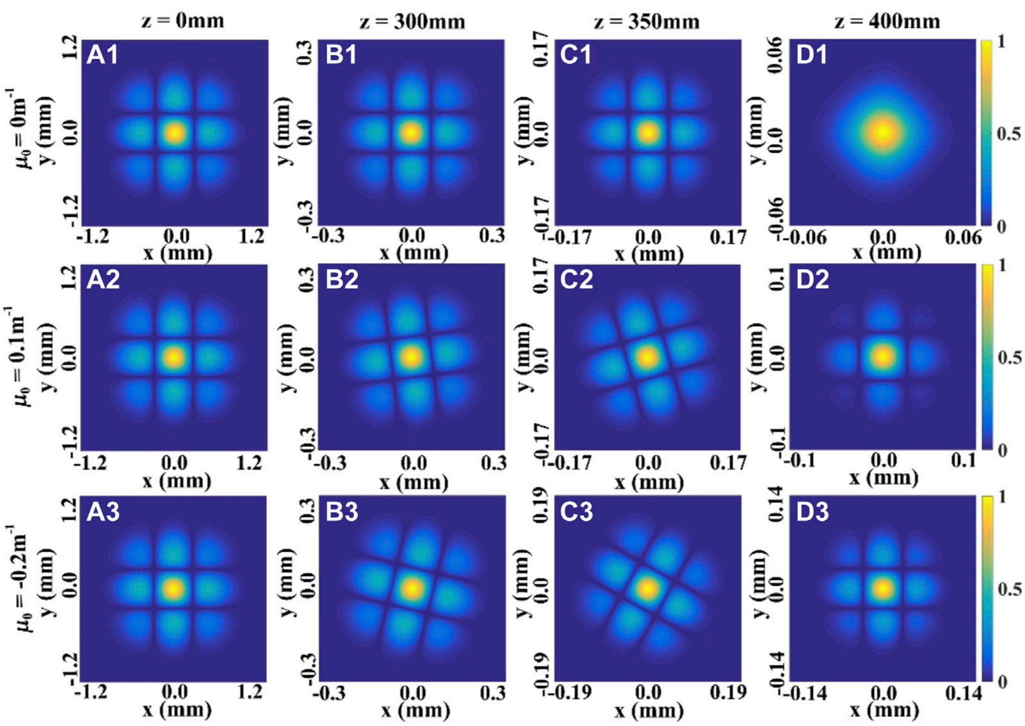

FIGURE 4 | Modulus of the SDOC between two points $\boldsymbol{\rho}$ and $-\boldsymbol{\rho}$ of the THGCSM beam with m = 1, n = 1 for different values of the twist factor μ_0 at several propagation distances.

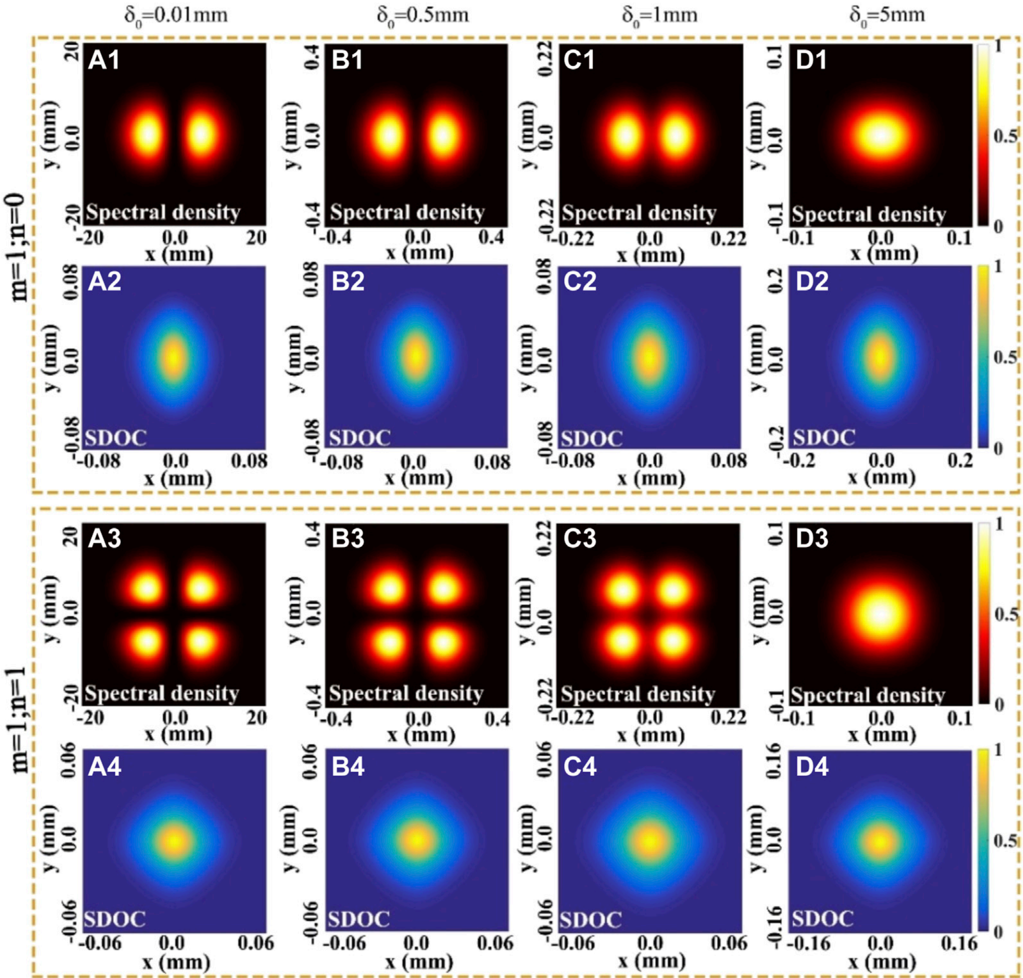

FIGURE 5 | Density plots of the normalized spectral density and the modulus of the SDOC ($|\eta(\boldsymbol{\rho},-\boldsymbol{\rho})|$) of a focused HGCSM beam for different values of the spatial coherence width δ_0 in the focal plane.

Thus, the THGCSM beam will be bona fide, if and only if the **Equation 18** is satisfied. Then, the propagation of the THGCSM beam through an ABCD optical system can be investigated with the help of the generalized Collins formula [38, 40].

$$W(\boldsymbol{\rho}_1,\boldsymbol{\rho}_2;z)=\frac{1}{(\lambda B)^2}exp\left[-\frac{ikD}{2B}(\rho_1^2-\rho_2^2)\right]\int_{-\infty}^{\infty}\int_{-\infty}^{\infty}W(\boldsymbol{r}_1,\boldsymbol{r}_2)\times exp\left[-\frac{ikA}{2B}(\boldsymbol{r}_1^2-\boldsymbol{r}_2^2)\right]exp\left[\frac{ik}{B}(\boldsymbol{r}_1\cdot\boldsymbol{\rho}_1-\boldsymbol{r}_2\cdot\boldsymbol{\rho}_2)\right]d^2\boldsymbol{r}_1d^2\boldsymbol{r}_2, \tag{19}$$

where $\boldsymbol{\rho}_1=(\boldsymbol{\rho}_{x1},\boldsymbol{\rho}_{y1})$ and $\boldsymbol{\rho}_2=(\boldsymbol{\rho}_{x2},\boldsymbol{\rho}_{y2})$ are two arbitrary transverse position vectors in the observation plane, and A, B, C, D are the transfer matrix elements of an optical system. On substituting **Equation 14** into **Equation 19**, we obtain the analytical formulae for the CSD of a THGCSM beam in the output plane as follows:

$$W(\rho_1,\rho_2;z)=\frac{\pi^2}{\lambda^2B^2\alpha_1\alpha_2}\exp\left[-\frac{\beta_x^2+\beta_y^2}{4\alpha_2}\right]\exp\left[-\frac{ikD}{2B}(\rho_1^2-\rho_2^2)\right]\exp\left[-\frac{k^2}{4\alpha_1B^2}(\rho_1-\rho_2)^2\right]$$
$$\times\sum_{k_1=0}^{m}\sum_{k_2=0}^{n}\sum_{p_1=0}^{k_1}\sum_{p_2=0}^{k_2}\frac{m!\sqrt{\pi}}{\Gamma(m+1/2)}\frac{n!\sqrt{\pi}}{\Gamma(n+1/2)}\frac{(2k_1)}{(2k_1-2p_1)!p_1!}\frac{(2k_2)}{(2k_2-2p_2)!p_2!}\frac{(-1)^{k_1+k_2}}{k_1!k_2!}$$
$$\times\begin{pmatrix}n-\frac{1}{2}\\ n-k_2\end{pmatrix}\begin{pmatrix}m-\frac{1}{2}\\ m-k_1\end{pmatrix}\left(\frac{1}{2\delta_0^2}\right)^{k_1+k_2}\left(\frac{\beta_x}{2\alpha_2}\right)^{2k_1}\left(\frac{\beta_y}{2\alpha_2}\right)^{2k_2}\left(\frac{\alpha_2}{\beta_x^2}\right)^{p_1}\left(\frac{\alpha_2}{\beta_y^2}\right)^{p_2}, \tag{20}$$

with

$$\alpha_1=\frac{1}{2\sigma_0^2};\alpha_2=\frac{1}{8\sigma_0^2}+\frac{1}{2\delta_0^2}+\frac{k^2\mu_0^2}{4\alpha_1}+\frac{k^2A^2}{4\alpha_1B^2}, \tag{21}$$

$$\beta_x=\frac{ik(\rho_{x1}+\rho_{x2})}{2B}+\frac{k^2\mu_0(\rho_{y1}-\rho_{y2})}{2\alpha_1B}+\frac{k^2A(\rho_{x1}-\rho_{x2})}{2\alpha_1B^2}, \tag{22}$$

$$\beta_y=\frac{ik(\rho_{y1}+\rho_{y2})}{2B}-\frac{k^2\mu_0(\rho_{x1}-\rho_{x2})}{2\alpha_1B}+\frac{k^2A(\rho_{y1}-\rho_{y2})}{2\alpha_1B^2} \tag{23}$$

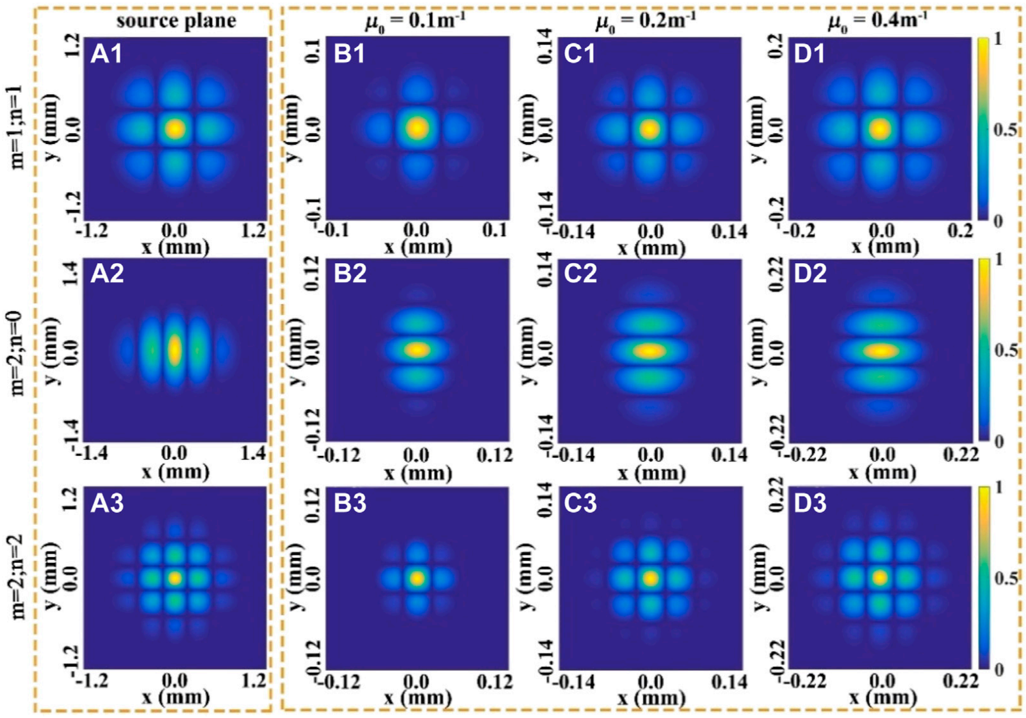

FIGURE 6 | Modulus of the SDOC ($|\eta(\boldsymbol{\rho},-\boldsymbol{\rho})|$) of the THGCSM beam for different values of the twist factor μ_0 in the source and focal plane, respectively.

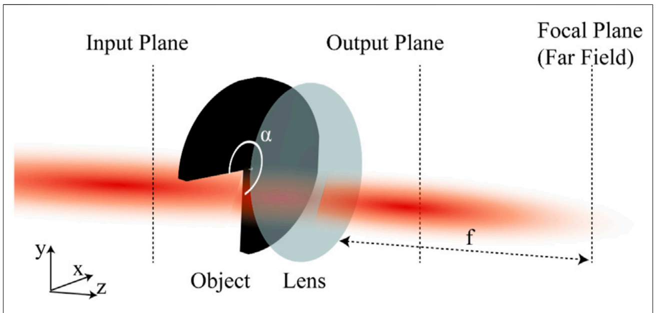

FIGURE 7 | Illustration of a THGCSM beam self-healing process.

The spectral density of the THGCSM beam at point $\boldsymbol{\rho}$ in the receiver plane is defined as

$$S(\boldsymbol{\rho}, z) = W(\boldsymbol{\rho}, \boldsymbol{\rho}, z). \tag{24}$$

The spectral degree of coherence (SDOC) of the THGCSM beam at a pair of transverse points with position vectors $\boldsymbol{\rho_1}$ and $\boldsymbol{\rho_2}$ in the output plane can be expressed by the formula

$$\eta(\boldsymbol{\rho}_1, \boldsymbol{\rho}_2; z) = \frac{W(\boldsymbol{\rho}_1, \boldsymbol{\rho}_2; z)}{\sqrt{W(\boldsymbol{\rho}_1, \boldsymbol{\rho}_1; z) W(\boldsymbol{\rho}_2, \boldsymbol{\rho}_2; z)}} \tag{25}$$

Based on the obtained formulae above, we can study the propagation properties of a THGCSM beam in a convenient way.

NUMERICAL SIMULATION OF A THGCSM BEAM

Paraxial Propagation of the THGCSM Beam Through an ABCD Optical System.

In this section, we study the paraxial propagation of the THGCSM beam through an ABCD optical system by applying the formulae derived in **section 2**. In the following examples, we consider the beam propagating in free space after passing through a lens with focal length f = 400mm, which is located at $z = 0$. The parameters of the beam and the transfer matrix are defined as $\lambda = 632.8\ nm$, $\sigma_0 = 1$ mm, $\delta_0 = 0.5$ mm, $A = 1 - z/f$, $B = z$, $C = -1/f$, and $D = 1$. According to **Equation 24**, we calculate the normalized spectral density of a focused THGCSM beam at several propagation distances with different values of the twist factor μ_0, as shown in **Figures 1**, **2**. One can find that when $\mu_0 = 0\,\mathrm{m}^{-1}$ (see the first row), the THGCSM beam reduces to a HGCSM beam, and with the increase of the propagation distance, the intensity distributions of the HGCSM beam gradually change from one beam spot into two spots or four beam spots as expected [22]. From the second and third rows of **Figures 1**, **2,** it is interesting to find that a twist phase does not seem to cause the beam to rotate during the transmission, no matter what the value of the parameters m n is. This result is quite different from that obtained in former works [37, 38], where it was shown that the twist phase would induce the beam to rotate on propagation. This phenomenon will be explained in **Figure 8**, by investigating the self-reconstruction characteristics of the beam spectral density. In addition, the

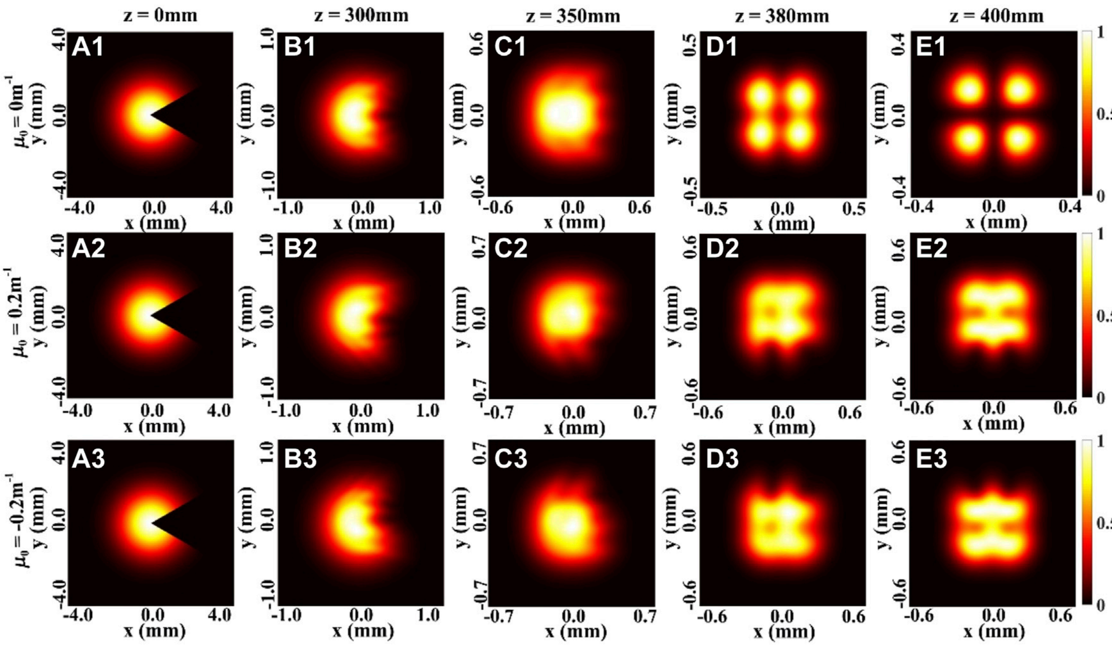

FIGURE 8 | Density plot of the normalized spectral density of a focused THGCSM beam with $m = 1$, $n = 1$ obstructed by a SSOO with center angle $\alpha = \pi/3$ for different values of the twist factor μ_0 at several propagation distances.

twist phase has the effect of hindering the beam spot to split on propagation, and the larger the value of the twist factor is, the beam spot will split more difficult. This means that the twist phase plays a role preventing deterioration of the intensity distribution. Thus, the twist phase can be used to control the intensity distribution of a THGCSM beam on propagation in free space.

Then, the evolution properties the SDOC of a focused THGCSM beam on propagation also have been investigated. **Figures 3**, **4** show the modulus of the SDOC between two points **ρ** and -**ρ** (i.e., $|\eta(\boldsymbol{\rho},-\boldsymbol{\rho})|$), at several propagation distances with different values of the twist factor μ_0. The first row of the **Figures 3**, **4** show the variation of the SDOC of a focused HGCSM beam versus the propagation distances z. It is found that the distribution of the SDOC of the HGCSM beam exhibits an array distribution in the source plane (i.e., $z = 0$ mm), and the number of the beamlets increase as the values of the beam order m or n increase.

When the propagation distance z increases, the profile of the SDOC firstly remains invariant, and then becomes one beam spot in the focal plane. This means that the information regarding the SDOC is increasingly lacking with increasing propagation distance. The second and the third rows of the **Figures 3**, **4** show the influence of the twist phase on the evolution properties of the SDOC. We find that the twist phase induces a rotation of the SDOC on propagation, such that when $\mu_0 > 0$, the distribution of the SDOC rotates anti-clockwise, and when $\mu_0 < 0$, the distribution of the SDOC rotates clockwise. The SDOC rotates faster with increasing twist factor μ_0, and the rotation angle varies between $-\pi/2$ or $\pi/2$ in the focal plane. These phenomena can be explained by the fact that the twist phase imposes angular momentum on the beam. Further, one can still determine the structure of the SDOC even in the focal plane. Thus, the twist phase can be used to maintain the beam's information of the correlation function.

In order to investigate the influence of the spatial coherence width and the twist phase on the beam propagation properties, the density plots of the normalized spectral density and the modulus of the SDOC have been studied, as shown in **Figures 5**, **6**. In **Figure 5**, we calculated the density plots of the normalized spectral density and the modulus of the SDOC ($|\eta(\boldsymbol{\rho},-\boldsymbol{\rho})|$) of a focused HGCSM beam (i.e., THGCSM beam with $\mu_0 = 0$) for different values of the spatial coherence width δ_0 in the focal plane. One can find that with the increase of the spatial coherence width, the beam profile of the HGCSM beam will evolve from the original array beam shape to a Gaussian beam profile (i.e., the self-splitting properties of the HGCSM beam on propagation gradually disappear) as expected in [22].

Moreover, regardless of the value of the spatial coherence width, the distribution of the SDOC is always maintained as a beam spot. Therefore, the ability to obtain information about the correlation function of the beam in the far field (or focal plane) cannot be improved by changing the coherence length or the order m n of the beam.

Further, we calculated the modulus of the SDOC ($|\mu(\boldsymbol{\rho},-\boldsymbol{\rho})|$) of the THGCSM beam in the source and focal plane, respectively. It is interesting to find that with the increase of the twist factor, the strength of the sidelobes of the SDOC are

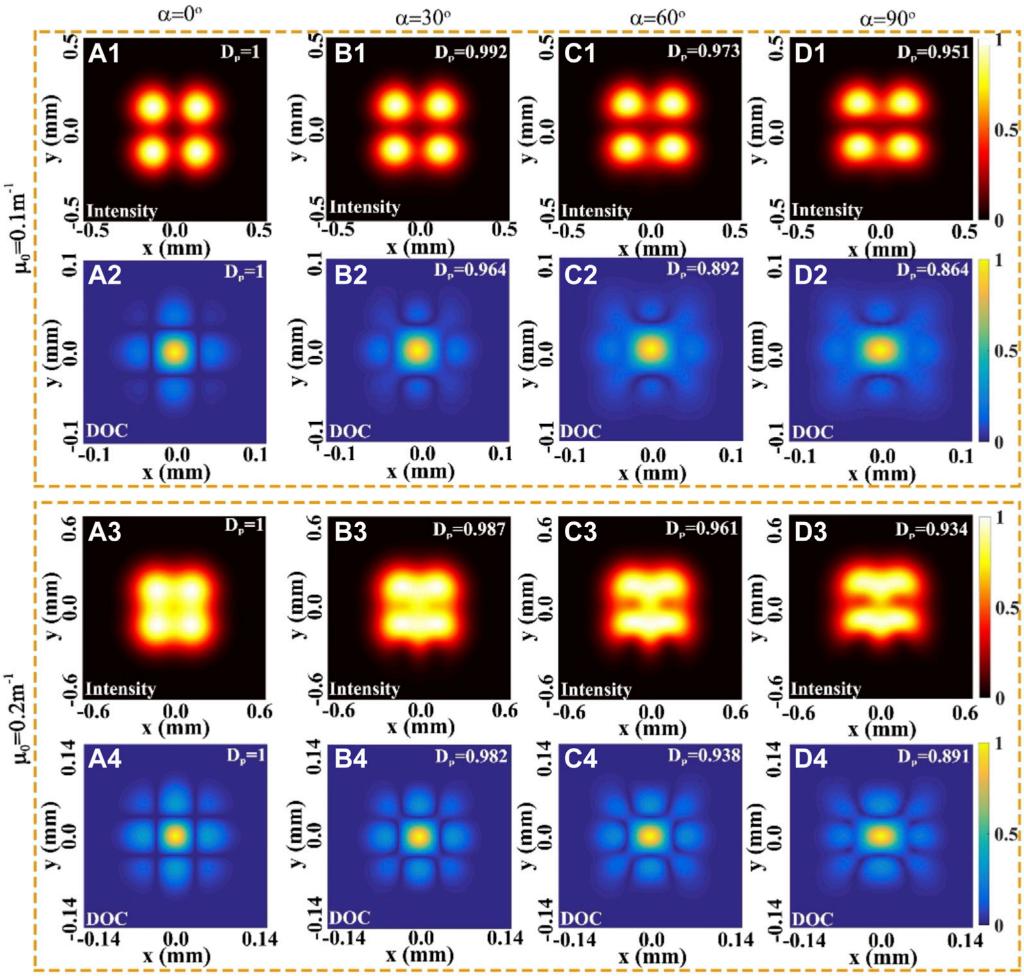

FIGURE 9 | Density plot of the normalized spectral density and the modulus of the SDOC ($|\eta(\boldsymbol{\rho},-\boldsymbol{\rho})|$) of a focused THGCSM beam with $m = 1$, $n = 1$ obstructed by a SSOO for different values of twist factor μ_0 and center angle α in the focal plane.

enhanced. This exciting new finding may help us to find a new way to improve the reliability of the correlation function.

Self-Reconstruction Characteristics of the THGCSM Beam

In this section, we focus on the Self-reconstruction behavior of the THGCSM beam when the THGCSM beam is partially blocked by a sector-shaped opaque obstacle (SSOO) in the source plane. **Figure 7** shows the illustration of a THGCSM beam self-healing process. A beam in the input plane ($z = 0$) is disturbed by a partially opaque obstacle in the input plane and is propagating through an ABCD optical system consisting of a lens and the free space behind the lens.

Figure 8 shows the changes of the density plot of the normalized spectral density of a focused THGCSM beam obstructed by a SSOO for different values of the twist factor at several propagation distances. From the first row of the **Figure 8**, one can see that with the increase of the propagation distance z, due to the effect of the correlation function, the beam splits into four beamlets as expected in [22]. The second and third row of the **Figure 8** show the effect of the twist phase on the normalized spectral density. By comparing the condition $\mu_0 = 0.2\,\mathrm{m}^{-1}$ and the condition $\mu_0 = -0.2\,\mathrm{m}^{-1}$, we can find that the twist phase would induce the rotation of the beam on propagation: the distribution of the spectral density rotates clockwise when $\mu_0 > 0$, the distribution of the spectral density rotates anti-clockwise when $\mu_0 < 0$. This phenomenon is consistent with former results [37, 38]. Therefore, the twist phase actually still causes the beam to rotate during propagation, but it is not noticeable when the beam is intact (**Figures 1**, **2**).

Moreover, **Figure 9** shows the Self-reconstruction characteristics of the normalized spectral density and the modulus of the SDOC ($|\eta\boldsymbol{\rho},-\boldsymbol{\rho})|$) when the beam is obstructed by a SSOO for different values of the center angle α in the focal plane. To assess the influences of the twist parameter on the self-reconstruction capability quantitatively, a parameter named the degree of self-reconstruction D_P (i.e., $D_p = \frac{\left[\iint \langle I_{wt}(\boldsymbol{\rho})\rangle\langle I_{ob}(\boldsymbol{\rho})\rangle d^2\boldsymbol{\rho}\right]^2}{\iint \langle I_{wt}(\boldsymbol{\rho})^2\rangle d^2\boldsymbol{\rho} \iint \langle I_{ob}(\boldsymbol{\rho})^2\rangle d^2\boldsymbol{\rho}}$, with I_{wt} and I_{ob} stand for the beam intensities without and with obstruction, respectively) is used to characterize it [41]. It is interesting to find that even if the beam has been obstructed by a SSOO, one still can determine the information of the correlation function of an obstructed THGCSM from its SDOC distribution in the focal plane. In addition, with the increase of the center angle, the self-reconstruction capability also decreased (see the evolution of the quantity D_P in the left upper corner of the figure). Our results can find application in information transmission and recovery.

CONCLUSION

In summary, we have introduced a new class of partially coherent twisted beam, named twisted Hermite-Gaussian correlated Schell-model (THGCSM) beam, and investigated its propagation properties through an ABCD optical system. The problem of when a twist phase can be imposed on Schell-model source fields with rectangular symmetries was solved. Based on the derived assessment condition, the condition that the THGCSM beam will be a bona fide one, also has been explored. The analytical expression for the CSD function of the THGCSM propagation through an ABCD optical system has been derived with the help of the generalized Collins integral formula. Based on the derived formula we have examined the evolution properties of the THGCSM beam. Our simulation results indicate that the evolution properties of the beam are closely related to the twist phase, e.g., with an increasing twist phase, the self-splitting properties of the beam gradually weaken on propagation. Further, the evolution of the SDOC also has been studied. Apart from inducing the rotation of the SDOC on propagation, the twist phase can greatly enhance the ability of the SDOC to maintain its profile on propagation, even in the focal plane. This provides a way to improve the reliability of the correlation function. Moreover, the self-reconstruction characteristics of the THGCSM beam have been explored in detail, and one can find that even if the beam has been obstructed by an opaque obstacle, one still can determine the information relating to the correlation function of an obstructed THGCSM from its SDOC distribution in the focal plane. Our results are anticipated to find applications in optical communications and information recovery.

DATA AVAILABILITY STATEMENT

The original contributions presented in the study are included in the article/Supplementary Material, further inquiries can be directed to the corresponding authors.

AUTHOR CONTRIBUTIONS

LeL and XP proposed the idea. LeL wrote the original manuscript. HW, LiL, YD, and FW gave suggestions in numerical simulation. XP, YC, and BH supervised the project. All authors contributed to the revision of the manuscript and approved the final version.

FUNDING

This work was supported by the National Natural Science Foundation of China (Nos 12192254, 11774251, 11874046, 11904247, 11974218, 12104263, 12174279); National Key Research and Development Program of China (2019YFA0705000); Natural Science Foundation of Shandong Province (ZR2021QA093); Local Science and Technology Development Project of the Central Government (Grant No. YDZX20203700001766); Innovation Group of Jinan (2018GXRC010).

REFERENCES

1. Kato Y, Mima K, Miyanaga N, Arinaga S, Kitagawa Y, Nakatsuka M, et al. Random Phasing of High-Power Lasers for Uniform Target Acceleration and Plasma-Instability Suppression. *Phys Rev Lett* (1984) 53:1057–60. doi:10.1103/PhysRevLett.53.1057
2. Ferri F, Magatti D, Gatti A, Bache M, Brambilla E, Lugiato LA. High-resolution Ghost Image and Ghost Diffraction Experiments with thermal Light. *Phys Rev Lett* (2005) 94:183602. doi:10.1103/PhysRevLett.94.183602
3. Oh J-E, Cho Y-W, Scarcelli G, Kim Y-H. Sub-Rayleigh Imaging via Speckle Illumination. *Opt Lett* (2013) 38:682–4. doi:10.1364/OL.38.000682
4. Auñón JM, Nieto-Vesperinas M. Partially Coherent Fluctuating Sources that Produce the Same Optical Force as a Laser Beam. *Opt Lett* (2013) 38:2869–72. doi:10.1364/OL.38.002869
5. Zhao C, Cai Y. Trapping Two Types of Particles Using a Focused Partially Coherent Elegant Laguerre-Gaussian Beam. *Opt Lett* (2011) 36:2251–3. doi:10.1364/OL.36.002251
6. Ricklin JC, Davidson FM. Atmospheric Optical Communication with a Gaussian Schell Beam. *J Opt Soc Am A* (2003) 20:856–66. doi:10.1364/josaa.20.000856
7. Beams R, Cançado LG, Oh S-H, Jorio A, Novotny L. Spatial Coherence in Near-Field Raman Scattering. *Phys Rev Lett* (2014) 113:186101. doi:10.1103/PhysRevLett.113.186101
8. van Dijk T, Fischer DG, Visser TD, Wolf E. Effects of Spatial Coherence on the Angular Distribution of Radiant Intensity Generated by Scattering on a Sphere. *Phys Rev Lett* (2010) 104:173902. doi:10.1103/PhysRevLett.104.173902
9. Gori F, Santarsiero M. Devising Genuine Spatial Correlation Functions. *Opt Lett* (2007) 32:3531–3. doi:10.1364/ol.32.003531
10. Gori F, Ramírez-Sánchez V, Santarsiero M, Shirai T. On Genuine Cross-Spectral Density Matrices. *J Opt A: Pure Appl Opt* (2009) 11:085706. doi:10.1088/1464-4258/11/8/085706
11. Cai Y, Chen Y, Yu J, Liu X, Liu L. Generation of Partially Coherent Beams. *Prog Opt* (2017) 62:157–223. doi:10.1016/bs.po.2016.11.001
12. Cai Y, Chen Y, Wang F. Generation and Propagation of Partially Coherent Beams with Nonconventional Correlation Functions: A Review [invited]. *J Opt Soc Am A* (2014) 31:2083–96. doi:10.1364/JOSAA.31.002083

13. Lajunen H, Saastamoinen T. Propagation Characteristics of Partially Coherent Beams with Spatially Varying Correlations. *Opt Lett* (2011) 36:4104–6. doi:10.1364/OL.36.004104
14. Wang F, Liu X, Yuan Y, Cai Y. Experimental Generation of Partially Coherent Beams with Different Complex Degrees of Coherence. *Opt Lett* (2013) 38:1814–6. doi:10.1364/OL.38.001814
15. Mei Z, Korotkova O. Random Sources Generating Ring-Shaped Beams. *Opt Lett* (2013) 38:91–3. doi:10.1364/OL.38.000091
16. Mei Z, Korotkova O. Cosine-Gaussian Schell-Model Sources. *Opt Lett* (2013) 38:2578–80. doi:10.1364/OL.38.002578
17. Liang C, Wang F, Liu X, Cai Y, Korotkova O. Experimental Generation of Cosine-Gaussian-Correlated Schell-Model Beams with Rectangular Symmetry. *Opt Lett* (2014) 39:769–72. doi:10.1364/OL.39.000769
18. Chen Y, Cai Y. Generation of a Controllable Optical Cage by Focusing a Laguerre-Gaussian Correlated Schell-Model Beam. *Opt Lett* (2014) 39:2549–52. doi:10.1364/OL.39.002549
19. Korotkova O. Random Sources for Rectangular Far fields. *Opt Lett* (2014) 39:64–7. doi:10.1364/OL.39.000064
20. Chen Y, Wang F, Liu L, Zhao C, Cai Y, Korotkova O. Generation and Propagation of a Partially Coherent Vector Beam with Special Correlation Functions. *Phys Rev A* (2014) 89:13801. doi:10.1103/PhysRevA.89.013801
21. Ma L, Ponomarenko SA. Free-space Propagation of Optical Coherence Lattices and Periodicity Reciprocity. *Opt Express* (2015) 23:1848–56. doi:10.1364/OE.23.001848
22. Chen Y, Gu J, Wang F, Cai Y. Self-splitting Properties of a Hermite-Gaussian Correlated Schell-Model Beam. *Phys Rev A* (2015) 91:13823. doi:10.1103/PhysRevA.91.013823
23. Zhu S, Chen Y, Wang J, Wang H, Li Z, Cai Y. Generation and Propagation of a Vector Cosine-Gaussian Correlated Beam with Radial Polarization. *Opt Express* (2015) 23:33099–155. doi:10.1364/OE.23.033099
24. Chen Y, Ponomarenko SA, Cai Y. Experimental Generation of Optical Coherence Lattices. *Appl Phys Lett* (2016) 109:061107. doi:10.1063/1.4960966
25. Liu X, Yu J, Cai Y, Ponomarenko SA. Propagation of Optical Coherence Lattices in the Turbulent Atmosphere. *Opt Lett* (2016) 41:4182–5. doi:10.1364/OL.41.004182
26. Liang C, Mi C, Wang F, Zhao C, Cai Y, Ponomarenko SA. Vector Optical Coherence Lattices Generating Controllable Far-Field Beam Profiles. *Opt Express* (2017) 25:9872–85. doi:10.1364/OE.25.009872
27. Xu Z, Liu X, Chen Y, Wang F, Liu L, Monfared YE, et al. Self-healing Properties of Hermite-Gaussian Correlated Schell-Model Beams. *Opt Express* (2020) 28:2828–37. doi:10.1364/OE.383805
28. Gu Y, Gbur G. Scintillation of Nonuniformly Correlated Beams in Atmospheric Turbulence. *Opt Lett* (2013) 38:1395–7. doi:10.1364/OL.38.001395
29. Liang C, Wu G, Wang F, Li W, Cai Y, Ponomarenko SA. Overcoming the Classical Rayleigh Diffraction Limit by Controlling Two-point Correlations of Partially Coherent Light Sources. *Opt Express* (2017) 25:28352–62. doi:10.1364/OE.25.028352
30. Peng D, Huang Z, Liu Y, Chen Y, Wang F, Ponomarenko SA, et al. Optical Coherence Encryption with Structured Random Light. *PhotoniX* (2021) 2:6–15. doi:10.1186/s43074-021-00027-z
31. Shen Y, Sun H, Peng D, Chen Y, Cai Q, Wu D, et al. Optical Image Reconstruction in 4f Imaging System: Role of Spatial Coherence Structure Engineering. *Appl Phys Lett* (2021) 118:181102. doi:10.1063/5.0046288
32. Liu Y, Chen Y, Chen Y, Wang F, Cai Y, Liang C, et al. Robust Far-Field Imaging by Spatial Coherence Engineering. *Opto-Electron Adv* (2021) 4:210027. doi:10.29026/oea.2021.210027
33. Chen Y, Wang F, Cai Y. Partially Coherent Light Beam Shaping via Complex Spatial Coherence Structure Engineering. *Adv Phys X* (2022) 7:2009742. doi:10.1080/23746149.2021.2009742
34. Serna J, Movilla JM. Orbital Angular Momentum of Partially Coherent Beams. *Opt Lett* (2001) 26:405–7. doi:10.1364/OL.26.000405
35. Simon R, Mukunda N. Twisted Gaussian Schell-Model Beams. *J Opt Soc Am A* (1993) 10:95. doi:10.1364/JOSAA.10.000095
36. Friberg AT, Tervonen E, Turunen J. Interpretation and Experimental Demonstration of Twisted Gaussian Schell-Model Beams. *J Opt Soc Am A* (1994) 11:1818–26. doi:10.1364/JOSAA.11.001818
37. Peng X, Liu L, Yu J, Liu X, Cai Y, Baykal Y, et al. Propagation of a Radially Polarized Twisted Gaussian Schell-Model Beam in Turbulent Atmosphere. *J Opt* (2016) 18:125601. doi:10.1088/2040-8978/18/12/125601
38. Wu G. Propagation Properties of a Radially Polarized Partially Coherent Twisted Beam in Free Space. *J Opt Soc Am A* (2016) 33:345–50. doi:10.1364/JOSAA.33.000345
39. Tong Z, Korotkova O. Beyond the Classical Rayleigh Limit with Twisted Light. *Opt Lett* (2012) 37:2595–7. doi:10.1364/OL.37.002595
40. Peng X, Liu L, Wang F, Popov S, Cai Y. Twisted Laguerre-Gaussian Schell-Model Beam and its Orbital Angular Moment. *Opt Express* (2018) 26:33956–69. doi:10.1364/OE.26.033956
41. Peng X, Wang H, Liu L, Wang F, Popov S, Cai Y. Self-reconstruction of Twisted Laguerre-Gaussian Schell-Model Beams Partially Blocked by an Opaque Obstacle. *Opt Express* (2020) 28:31510–23. doi:10.1364/OE.408357
42. Wang H, Peng X, Liu L, Wang F, Cai Y, Ponomarenko SA. Generating Bona Fide Twisted Gaussian Schell-Model Beams. *Opt Lett* (2019) 44:3709–12. doi:10.1364/OL.44.003709
43. Wang H, Peng X, Zhang H, Liu L, Chen Y, Wang F, et al. Experimental Synthesis of Partially Coherent Beam with Controllable Twist Phase and Measuring its Orbital Angular Momentum. *Nanophotonics* (2021). doi:10.1515/nanoph-2021-0432
44. Borghi R. Twisting Partially Coherent Light. *Opt Lett* (2018) 43:1627–30. doi:10.1364/OL.43.001627
45. Borghi R, Gori F, Guattari G, Santarsiero M. Twisted Schell-Model Beams with Axial Symmetry. *Opt Lett* (2015) 40:4504. doi:10.1364/OL.40.004504
46. Mei Z, Korotkova O. Random Sources for Rotating Spectral Densities. *Opt Lett* (2017) 42:255–8. doi:10.1364/OL.42.000255
47. Gori F, Santarsiero M. Devising Genuine Twisted Cross-Spectral Densities. *Opt Lett* (2018) 43:595–8. doi:10.1364/OL.43.000595
48. Wolf E. *Introduction to the Theory of Coherence and Polarization of Light [M]*. Cambridge: Cambridge University Press (2007).

Conflict of Interest: The authors declare that the research was conducted in the absence of any commercial or financial relationships that could be construed as a potential conflict of interest.

ORIGINAL RESEARCH
published: 25 March 2022
doi: 10.3389/fphy.2022.862605

Large-Scale Black Silicon Induced by Femtosecond Laser Assisted With Laser Cleaning

Zhidong Wen[1,2], Haiyan Shi[1], Song Yue[1], Man Li[1], Zhe Zhang[1,2], Ran Wang[1], Qi Song[3], Ziye Xu[3], Zichen Zhang[1] and Yu Hou[1]**

[1]Microelectronics Instruments and Equipment R&D Center, Institute of Microelectronics, Chinese Academy of Sciences, Beijing, China, [2]School of Microelectronics, University of Chinese Academy of Sciences, Beijing, China, [3]International Research Centre for Nano Handling and Manufacturing of China, Changchun University of Science and Technology, Changchun, China

Black silicon is a promising and effective candidate in the field of photoelectric devices due to the high absorptance and broad-spectrum absorption property. The deposition around the processing area induced by the pressure of SF_6, gravity, and the block of the processing chamber interferes the adjacent laser ablation and hampers uniform large-scale black silicon fabrication. To solve the problem, femtosecond laser- induced black silicon assisted with laser plasma shockwave cleaning is creatively proposed in our study. The results showed that higher, denser, and more uniform microstructures can be obtained than the conventional laser-induced method without laser cleaning. The average absorptance is 99.15% in the wavelength range of 0.3–2.5 μm, while it is more than 90% in the range of 2.5–20 μm. In addition, the scanning pitch dependence of surface morphology is discussed, and the better result is obtained in the range of 25–35 μm with 40-μm laser spot. Finally, a large-scale 50-mm × 50-mm black silicon with uniform microstructures was prepared by our method. It has been demonstrated that the deposition is effectively eliminated *via* our method, and the optical absorption is also enhanced significantly. It is of great significance for realizing large-scale preparation of photoelectric devices based on black silicon and lays the foundation for the development of laser-inducing equipment and industrial application.

Keywords: large scale, laser cleaning, deposition, black silicon, laser inducing

OPEN ACCESS

Edited by:
Shangran Xie,
Beijing Institute of Technology, China

Reviewed by:
Pan Wang,
Nankai University, China
Alpan Bek,
Middle East Technical University, Turkey
Qing Wang,
Beijing Institute of Technology, China

****Correspondence:***
Zichen Zhang
zz241@ime.ac.cn
Yu Hou
houyu@ime.ac.cn

Specialty section:
This article was submitted to Optics and Photonics, a section of the journal Frontiers in Physics

Received: *26 January 2022*
Accepted: *04 March 2022*
Published: *25 March 2022*

Citation:
Wen Z, Shi H, Yue S, Li M, Zhang Z, Wang R, Song Q, Xu Z, Zhang Z and Hou Y (2022) Large-Scale Black Silicon Induced by Femtosecond Laser Assisted With Laser Cleaning. Front. Phys. 10:862605. doi: 10.3389/fphy.2022.862605

INTRODUCTION

Light-trapping structures can improve the local resonance modes of light and the propagating light wavelength range in the material, which not only enhances absorption of light from near-ultraviolet to the near-infrared and improves photocurrent but also reduces materials used. Currently, various nanoscale light-capturing methods, including photonic crystals, plasmonic nanostructures, and nanoscale lines and gratings [1–3], have been investigated. Black silicon is fabricated with micro-, nano-, or micro–nano-scale structures [4, 5]. While the absorption of silicon is reduced abruptly due to the forbidden bandwidth when the light wavelength is more than 1,100 nm [6], a better optical absorption property is showed on the black silicon due to the multiple reflections between the microstructures and impurity doping, especially in the near-infrared band ranging from 1,100 nm to 2,500 nm [7, 8]. Since the first research about black silicon was reported from Harvard University in 1998 [9], extensive research has been conducted on this promising material. Consequently, black silicon is an effective and low-cost candidate compared with the other photoelectric materials.

Due to the high absorptance and broad-spectrum absorption property, black silicon is applied in many fields. About photocatalysis and photo-electrocatalysis [10, 11], B. Wang et al. [12] fabricated a plasmon-enhanced black silicon material to synthesize ammonia using photo-electrocatalysis in 2020. About photodetection [13, 14], Z. Qi et al. [15] fabricated a gold nanoparticle-modified silicon pyramid-shaped material that was able to enhance thermal electron NIR light detection in 2017. About solar cell [16–19], I. Putra et al. [20] made a B-Si solar cell by performing a silver-assisted chemical etching of the micro-pyramid on a silicon wafer to form a finer nanocolumn structure on the micro-pyramid in 2019. In short, black silicon has great potential in the field of optoelectronic devices.

Furthermore, how to fabricate the micro-nano structures to get a good optical property is a great challenge in the field of photoelectric devices. In the past several decades, there were many methods reported about the preparation of black silicon, including metal-assisted chemical etching (MACE) [21, 22], wet chemical etching [23], reactive ion etching (RIE) [24, 25], and laser processing [26–29]. The absorption result of samples treated with femtosecond laser in SF_6 was superior to the results of samples using other methods [30]. Sulfur-hyperdoped silicon processed by ultrafast laser led to a wide continuous impurity band, which has a wide contribution of energy levels and gives rise to infrared absorptance. In addition, the laser technology was compatible with the CMOS processing and has the advantages of flexibility, simplicity, and precision. However, there was a problem in the processing industrially that a large amount of powder deposited on the processing area after the laser irradiation [31]. The particles splashed from the surface due to the laser energy deposit mostly on the sides of the processing row. It deteriorated microstructure morphology on the next row, leading to a worse optical property of the whole large-scale black silicon.

Currently, research related to black silicon mainly centers on a small point. It is attributed to the difficulty to realize large-scale uniformity of microstructures by femtosecond laser and the high cost of the laser-processing equipment. Laser cleaning is a novel surface cleaning technology, with the advantages [32] of environmental protection, non-contact, wide range of applications, high cleaning accuracy, etc. The laser cleaning technology is applied in many fields, including the removal of paint [33], rust, compounds [34], particles [35], and the protection of artifacts [36]. In our study, laser cleaning was used to remove the deposit and enhance the uniformity of large-scale black silicon.

In our study, to solve the problem of deposition and prepare large-scale black silicon, a method of laser induction assisted with laser plasma shockwave cleaning was investigated. Compared with the conventional process method, the addition of the laser cleaning technology was helpful to remove the deposition so that a better optical property of the microstructures was achieved. A series of experiment were conducted. Then the morphology and the absorption property were obtained. The results indicated that laser induction assisted with laser cleaning was an effective and low-cost method which could be applied to the preparation of large-scale black silicon industrially, especially for the application of solar energy sells and optoelectronic devices.

MATERIALS AND METHODS

The N-type silicon wafers (111) with a thickness of 200 μm were used as samples in our experiments. The wafers were polished before laser processing. A 25-W, 515-nm femtosecond laser system with a duration of 400 fs and a repetition rate of 200 kHz was used to fabricate black silicon. In addition, the processing position of the samples was controlled precisely by an xyz motion platform and affiliated software.

Figure 1A shows the schematic diagram of the whole processing system used in our study. The laser beam was focused through the lens (with a focal length of 75 mm), and the laser spot with a diameter of 40 μm was irradiated on the silicon wafer. The sample was set in SF_6 with a pressure of 67 kPa. The scanning speed was 20 mm/s, with a laser fluence of 7.96 J/cm^2 during the inducing process, while it was 100 mm/s with a laser fluence of 3.98 J/cm^2 in the laser cleaning process. In order to fabricate large-scale black silicon, several fixed spacing rows were designed via affiliated software first as shown in **Figure 1A**. The laser-inducing process and laser-cleaning process were conducted alternatively. The detailed process was as follows: 1) first, laser scans in a certain direction forming one laser-induced black silicon; 2) second, the adjacent scanning by laser cleaning with the same spacing row was conducted; 3) third, the laser-inducing process was repeated along the same path as the second step; and 4) finally, large-scale uniform black silicon was formed by repeating the aforementioned steps. **Figures 1B,C** show the difference between our method and the conventional laser induction method. In our experiments, different distances between the processing rows were tried to find better performances of the large-scale black silicon.

The morphology of the microstructures was characterized by the scanning electron microscope (SEM) and the laser-scanning confocal microscope. The 3D optical image was obtained from the laser-scanning confocal microscope to observe the whole morphology and calculate the RMS value. The color bar corresponded to the height of the model built in the 3D images. Furthermore, the absorptance of the treated samples in our study was analyzed using an ultraviolet spectrophotometer (for the wavelength range from 0.3 to 2.5 μm) and a Bruker Tensor–Fourier transform infrared (FTIR) spectrometer (for the wavelength range from 2.5 to 20 μm), both equipped with integrating spheres.

RESULTS AND DISCUSSION

It was verified that the conical microstructures can be formed on the silicon material after pulsed laser processing in the gas of SF_6. The powder splashed from the surface deposited on the sides of the processing line subsequently because of gravity, gas pressure, and the block of the glass cover. **Figure 2** indicates the schematic

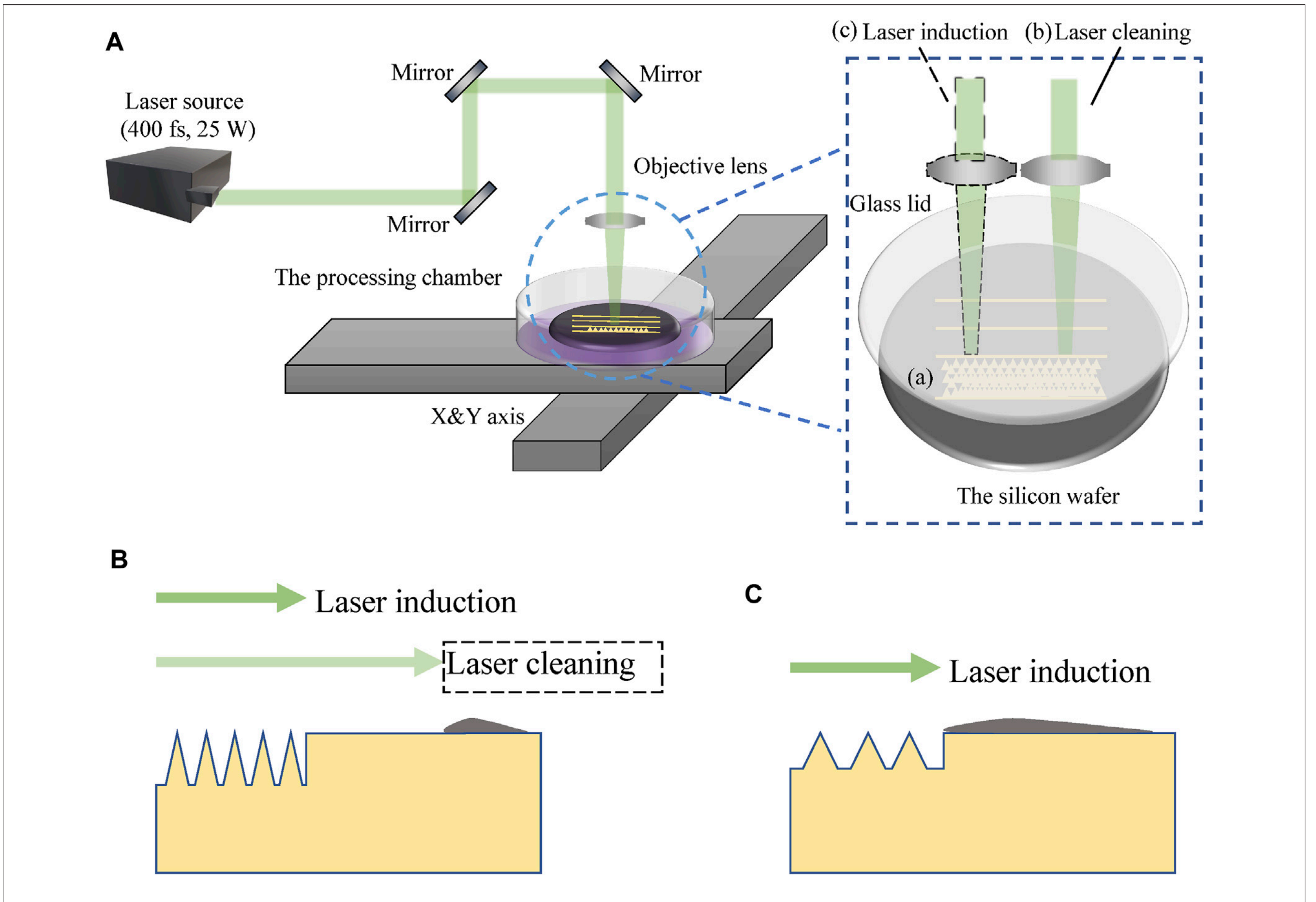

FIGURE 1 | (A) Schematic diagram of the femtosecond laser processing system. **(B)** Laser induction assisted with laser cleaning and **(C)** conventional laser induction.

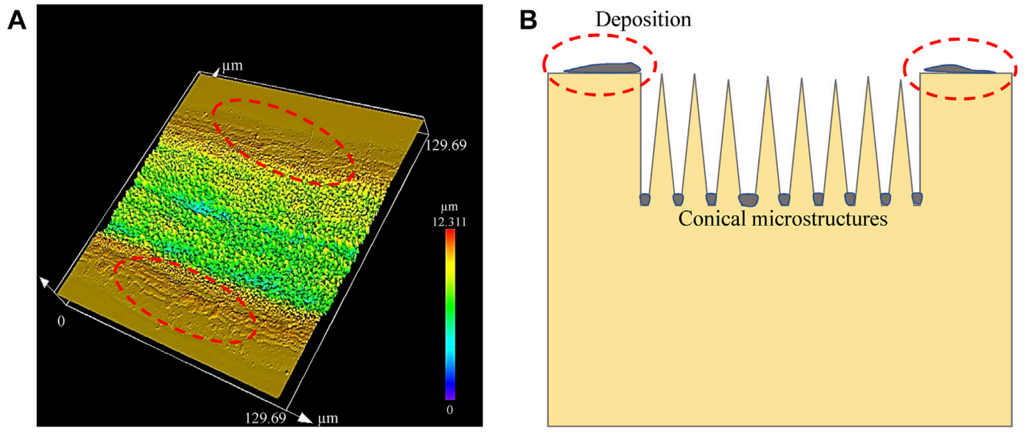

FIGURE 2 | Deposition on the single row fabricated with laser inducing process. **(A)** 3D image of the processing row and **(B)** schematic of the deposition laterally.

diagram of the deposition laterally and the 3D image of a single row after the conventional laser-inducing process. The optical property and the microstructure of the fabricated black silicon were influenced. In order to remove the deposition, laser cleaning was conducted. The laser plasma shockwave cleaning has been an advanced and effective method to remove particles in recent

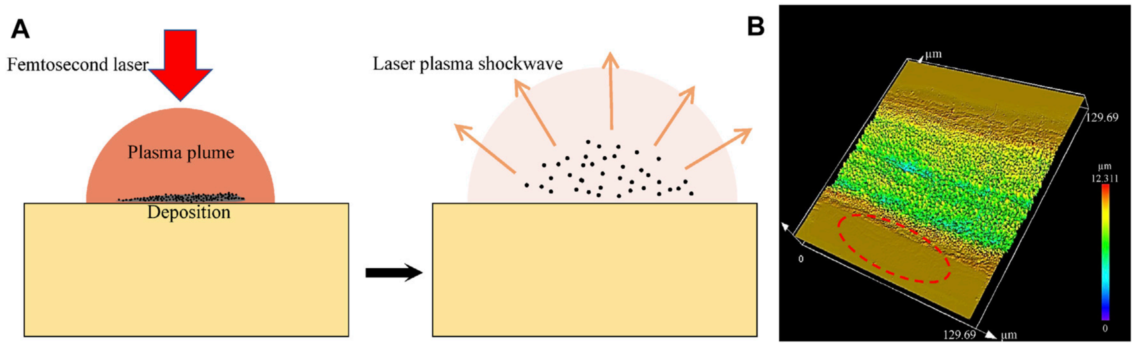

FIGURE 3 | **(A)** Schematic diagram of the laser plasma shockwave cleaning and **(B)** result of **Figure 2A** processed with laser cleaning.

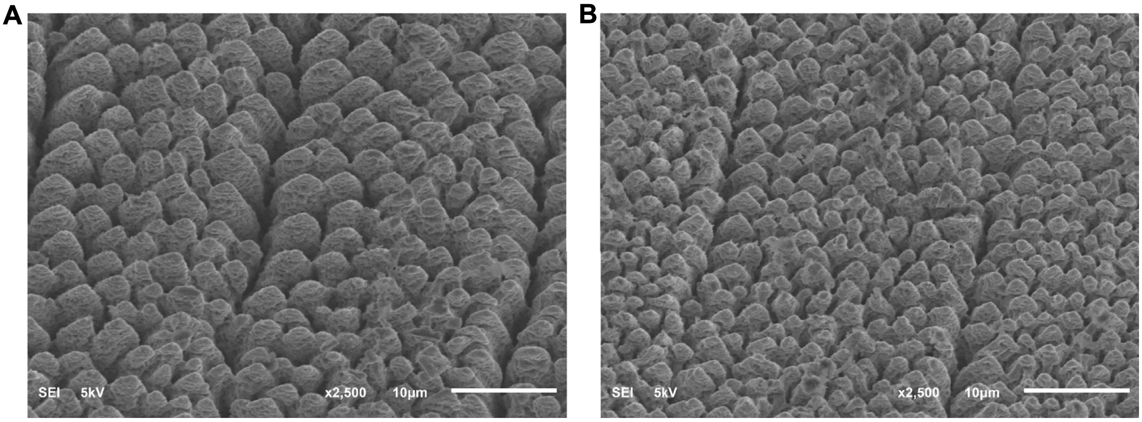

FIGURE 4 | Surface morphology processed **(A)** without laser cleaning and **(B)** with laser cleaning.

years. Under the irradiation of the intense pulsed laser, the powder and the plasma plume were created [37]. The phenomena of gasification and ionization occurred in the plasma plume. Then, the plasma plume expanded rapidly with high temperature (>104 K) and high pressure (>1 GPa). Finally, the laser-heated plasma exploded and led to the formation of laser-supported detonation waves [38] to remove nanoparticles. The schematic diagram of the laser plasma shockwave cleaning is shown in **Figure 3A**. The detailed mechanism of laser cleaning is still a major research point. **Figure 3B** shows the result of **Figure 2A** processed after laser cleaning. The RMS value obtained from the laser scanning confocal microscope, which was the root mean square height for the evaluation area, was widely used to characterize the surface roughness. The RMS value for the non-cleaned region marked in red line in **Figure 2A** was 0.114 μm, while it was 0.054 μm for the cleaned area marked in **Figure 3B**. It is obvious that the deposition was eliminated effectively.

Figure 4 demonstrates the processed morphology prepared by laser-inducing process without laser cleaning and assisted with laser cleaning. The conical structures were formed in both processing methods. The microstructures in **Figure 4B** were denser and higher than the structures in **Figure 4A**. The RMS value for the area processed without laser cleaning was 1.71 μm,

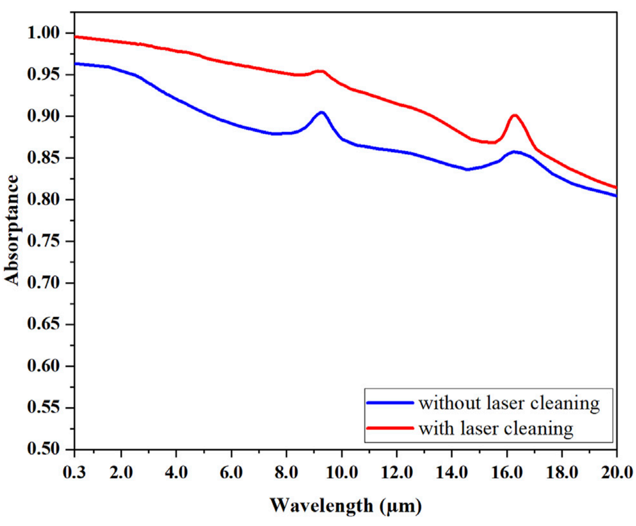

FIGURE 5 | Absorption curves of samples processed without laser cleaning and with laser cleaning.

while it was 1.95 μm for the sample processed with laser cleaning. It is known that the better absorption property was attributed to the larger deep-to-width ratio and the multiple reflections

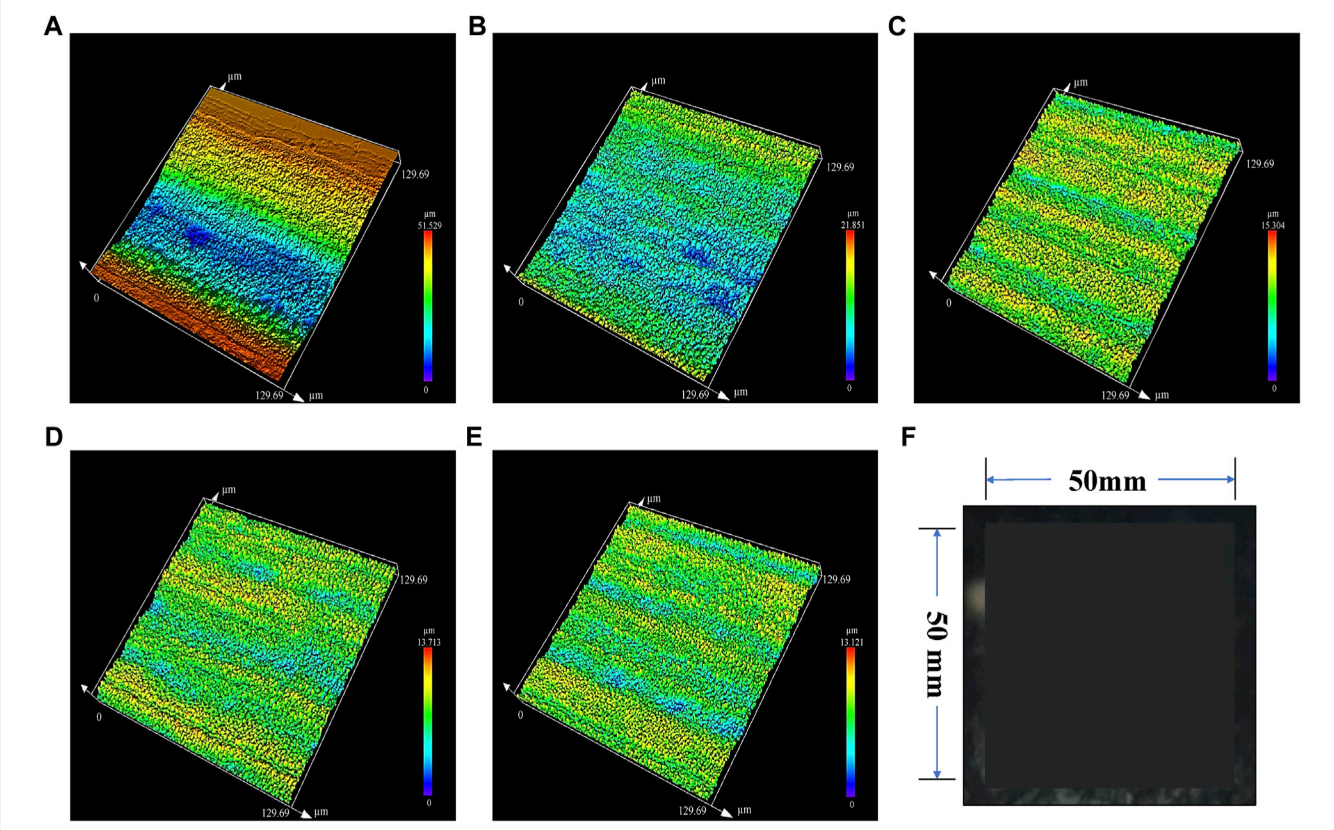

FIGURE 6 | 3D images of samples with different pitches between rows, including **(A)** 5 μm, **(B)** 15 μm, **(C)** 25 μm, **(D)** 35 μm, and **(E)** 45 μm. **(F)** Image of 50-mm × 50-mm black silicon.

between the conical structures [39]. The absorption curves of the processing area over the wavelength ranged from 300 nm to 20 μm and are illustrated in **Figure 5**. It is obvious that the absorptance of the samples prepared with laser cleaning was enhanced experimentally in the regions of ultraviolet, visible, near-infrared, and mid-infrared. In the wavelength range of 0.3–2.5 μm, the average absorption of the samples treated with laser cleaning was improved from 95.72 to 99.15%, while in the range of 2.5–20 μm, an average absorption of more than 90% was achieved in our experiments using the laser cleaning technology, which is the highest absorptance achieved on silicon by laser technology as far as we know.

In order to realize the industrial application of optoelectronic devices, it is necessary to improve the processing performance of large-scale black silicon prepared by the laser-inducing process assisted with laser cleaning. In our experiment, the different distances (5, 15, 25, 35, 45 μm) between adjacent rows were analyzed to improve the whole processing morphology. The 3D optical images of the samples are shown in **Figure 6**. The surfaces were ablated obviously, while the distance between rows was 5 μm or 15 μm because of the large overlapping laser energy, as shown in **Figures 6A,B**. **Figure 6E** shows that the energy deposited on the side of the rows was too little to induce the microstructures somewhere. As shown in **Figures 6C,D**, the 3D optical images show that the better microstructure morphology was obtained when the distance of rows was between 25 and 35 μm. The laser spot used in our study was 40 μm. In the fabrication of large-scale black silicon, different scanning pitches led to different overlapping rates of the laser spot and different energy irradiated on the silicon surface. An extremely small scanning pitch causes excessive laser energy on the irradiation area, while an extremely large pitch contributes too little energy to get the undesirable surface microstructure and worse optical properties. Therefore, an appropriate scanning pitch, which is related to the diameter of the laser spot and the laser fluence, should be selected in the laser processing of large-scale black silicon. Finally, the image of 50-mm × 50-mm black silicon prepared by femtosecond laser-inducing process assisted with laser cleaning is shown in **Figure 6F**. The scanning pitch between the adjacent rows was 25 μm. The processed area is shown in black completely due to its perfect light trapping.

The method of the laser-inducing process assisted with laser plasma shockwave cleaning was certified previously to improve the optical property of large-scale black silicon. The laser cleaning technology was effective in removing the deposition beside the processing line and enhancing the density and uniformity of microstructures. In addition, the method assisted with laser cleaning was helpful in promoting the widespread application of photoelectric devices based on black silicon, especially in the field of mid-infrared. It also laid the foundation on the development and industrial application of laser-inducing equipment. However, the powder generated from the laser-cleaning and laser-inducing processes may redeposit on the previous processed area. The processing chamber prevents the powder from splashing out of the processing area. Further investigation is needed to reduce the influence of redeposition on the laser-induced surface and absorption property of black silicon.

CONCLUSION

In our study, the method of laser induction assisted with laser plasma shockwave cleaning in ambient SF_6 to fabricate large-scale black silicon has been put forward. About this method, the femtosecond laser plasma shockwave cleaning technology was used to remove the deposition on the sides of processing rows before the next laser inducing.

In the laser-induced large-scale preparation of black silicon industrially, the particles deposit around the processing area induced by the gas pressure, gravity, and the block of the processing chamber. A set of experiments has been carried out to confirm the effectiveness of our method. In our experiments, the analysis of the SEM images and the 3D optical images indicated that the microstructures prepared by our method were denser and more uniform than the traditional laser-inducing process. The RMS value of the microstructures with this method was approximately 0.2 μm higher than the result without laser cleaning. Furthermore, great enhancement of the absorptance over a broad range was achieved significantly. In the wavelength range of 0.3–2.5 μm, the average absorption was 99.15%, and in the range of 2.5–20 μm, an absorptance of more than 90% has been realized experimentally. The absorptance is the highest compared with the results reported in other research as far as we know. Different scanning distances including 5, 15, 25, 35, and 45 μm with a 40-μm laser spot were conducted to get better microstructures. The best morphology was obtained with the processing pitches of 25 and 35 μm. Excessive overlapping laser energy led to the ablation of the surface of silicon, while too little overlapping laser energy induced to an undesirable morphology between the adjacent rows. Moreover, high-performance black silicon with a size of 50 mm × 50 mm was fabricated in our experiments.

The laser-inducing process assisted with laser plasma shockwave cleaning provides an effective and low-cost solution to eliminate the deposition in laser-induced large-scale black silicon. It is helpful to the development of optoelectronic devices, especially in the field of photocatalysis and photo-electrocatalysis, near-infrared and visible light photodetection, solar cell, sensing, antibacterial materials, and so on. Also, the method promotes the development and widespread application of femtosecond laser equipment.

DATA AVAILABILITY STATEMENT

The original contributions presented in the study are included in the article/Supplementary Material, further inquiries can be directed to the corresponding authors.

AUTHOR CONTRIBUTIONS

ZW, YH, and ZZ proposed the idea. ZW, YH, and ZZ performed the experiments. ZW, HS, ML, RW, QS, and ZX investigated the research progress. ZW, HS, SY, and YH wrote the original manuscript. YH, ZZ, ML, RW, and SY supervised the project.

FUNDING

This research was supported by the Beijing Municipal Science and Technology Commission (no. Z211100004821002).

REFERENCES

1. Ferry VE, Polman A, Atwater HA. Modeling Light Trapping in Nanostructured Solar Cells. *Acs Nano* (2011) 5(12):10055–64. doi:10.1021/nn203906t
2. Hsu C-M, Battaglia C, Pahud C, Ruan Z, Haug F-J, Fan S, et al. High-Efficiency Amorphous Silicon Solar Cell on a Periodic Nanocone Back Reflector. *Adv Energ Mater.* (2012) 2(6):628–33. doi:10.1002/aenm.201100514
3. Kim Y, Bicanic K, Tan H, Ouellette O, Sutherland BR, García de Arquer FP, et al. Nanoimprint-Transfer-Patterned Solids Enhance Light Absorption in Colloidal Quantum Dot Solar Cells. *Nano Lett* (2017) 17(4):2349–53. doi:10.1021/acs.nanolett.6b05241
4. Lv J, Zhang T, Zhang P, Zhao Y, Li S. Review Application of Nanostructured Black Silicon. *Nanoscale Res Lett* (2018) 13:13. doi:10.1186/s11671-018-2523-4
5. Juzeliūnas E, Fray DJ. Silicon Electrochemistry in Molten Salts. *Chem Rev* (2020) 120(3):1690–709. doi:10.1021/acs.chemrev.9b00428
6. Casalino M, Coppola G, Iodice M, Rendina I, Sirleto L. Near-Infrared Sub-bandgap All-Silicon Photodetectors: State of the Art and Perspectives. *Sensors* (2010) 10(12):10571–600. doi:10.3390/s101210571
7. Loudon AY, Hiskett PA, Buller GS, Carline RT, Herbert DC, Leong WY, et al. Enhancement of the Infrared Detection Efficiency of Silicon Photon-Counting Avalanche Photodiodes by Use of Silicon Germanium Absorbing Layers. *Opt Lett* (2002) 27(4):219–21. doi:10.1364/ol.27.000219
8. Younkin R, Carey JE, Mazur E, Levinson JA, Friend CM. Infrared Absorption by Conical Silicon Microstructures Made in a Variety of Background Gases Using Femtosecond-Laser Pulses. *J Appl Phys* (2003) 93(5):2626–9. doi:10.1063/1.1545159
9. Her T-H, Finlay RJ, Wu C, Deliwala S, Mazur E. Microstructuring of Silicon with Femtosecond Laser Pulses. *Appl Phys Lett* (1998) 73(12):1673–5. doi:10.1063/1.122241
10. Alexander F, AlMheiri M, Dahal P, Abed J, Rajput NS, Aubry C, et al. Water Splitting TiO2 Composite Material Based on Black Silicon as an Efficient Photocatalyst. *Solar Energ Mater Solar Cell* (2018) 180:236–42. doi:10.1016/j.solmat.2017.05.024
11. Zhao S, Yuan G, Wang Q, Liu W, Wang R, Yang S. Quasi-hydrophilic Black Silicon Photocathodes with Inverted Pyramid Arrays for Enhanced Hydrogen Generation. *Nanoscale* (2020) 12(1):316–25. doi:10.1039/c9nr06635g
12. Wang B, Yao L, Xu G, Zhang X, Wang D, Shu X, et al. Highly Efficient Photoelectrochemical Synthesis of Ammonia Using Plasmon-Enhanced Black Silicon under Ambient Conditions. *ACS Appl Mater Inter* (2020) 12(18):20376–82. doi:10.1021/acsami.0c00881
13. Juntunen MA, Heinonen J, Laine HS, Vahanissi V, Repo P, Vaskuri A, et al. N-type Induced junction Black Silicon Photodiode for UV Detection. In:

Conference on Integrated Photonics - Materials, Devices, and Applications IV; 2017 May 09-10; Barcelona, SPAIN (2017).

14. Meng Y, An L, Han X, Li Y, Hou C, Zhang Q, et al. Controllable (Ga1−xZnx)(N1−xOx) Nanorods Grown on Black Silicon as Anodes for Water Splitting. *Appl Surf Sci* (2020) 502:144174. doi:10.1016/j.apsusc.2019.144174
15. Zhou Z-Q, Wang L-X, Shi W, Sun S-L, Lu M. A Synergetic Application of Surface Plasmon and Field Effect to Improve Si Solar Cell Performance. *Nanotechnology* (2016) 27(14):145203. doi:10.1088/0957-4484/27/14/145203
16. Guenther KM, Baumann AL, Gimpel T, Kontermann S, Schade W. Yyyy Tandem Solar Cell Concept Using Black Silicon for Enhanced Infrared Absorption. In: 2nd International Conference on Crystalline Silicon Photovoltaics (SiliconPV); 2012 Apr 03-05; Leuven, BELGIUM. IMEC (2012).
17. Zhong S, Liu B, Xia Y, Liu J, Liu J, Shen Z, et al. Influence of the Texturing Structure on the Properties of Black Silicon Solar Cell. *Solar Energ Mater Solar Cell* (2013) 108:200–4. doi:10.1016/j.solmat.2012.10.001
18. Li P, Wei Y, Zhao Z, Tan X, Bian J, Wang Y, et al. Highly Efficient Industrial Large-Area Black Silicon Solar Cells Achieved by Surface Nanostructured Modification. *Appl Surf Sci* (2015) 357:1830–5. doi:10.1016/j.apsusc.2015.10.035
19. Abdullah MF, Alghoul MA, Naser H, Asim N, Ahmadi S, Yatim B, et al. Research and Development Efforts on Texturization to Reduce the Optical Losses at Front Surface of Silicon Solar Cell. *Renew Sustain Energ Rev* (2016) 66:380–98. doi:10.1016/j.rser.2016.07.065
20. Putra IR, Li J-Y, Chen C-Y. 18.78% Hierarchical Black Silicon Solar Cells Achieved with the Balance of Light-Trapping and Interfacial Contact. *Appl Surf Sci* (2019) 478:725–32. doi:10.1016/j.apsusc.2019.02.001
21. Cheng S-Q, Cai B, Zhu Y-M. Black Silicon as Absorber for Near-Infrared Photo-Thermal Conversion. In: Opto Electronics Communications Conference (OECC); 2015 Jun 28-Jul 02; Shanghai, PEOPLES R CHINA. IEEE (2015).
22. Phan TL, Yu WJ. CVD-grown Carbon Nanotube Branches on Black Silicon Stems for Ultrahigh Absorbance in Wide Wavelength Range. *Sci Rep* (2020) 10(1):10. doi:10.1038/s41598-020-60580-8
23. Tan Q, Tang L, Mao H, Chen Y, Ren Y, Lei C, et al. Nanoforest of Black Silicon Fabricated by AIC and RIE Method. *Mater Lett* (2016) 164:613–7. doi:10.1016/j.matlet.2015.11.062
24. Hildebrandt M, Hildebrandt M, Lu M. Self-organized Antireflecting Nano-Cone Arrays on Si (100) Induced by Ion Bombardment. *J Appl Phys* (2011) 109(5):053513. PubMed PMID: WOS:000288387900036. doi:10.1063/1.3560539
25. Qiu Y, Hao H-C, Zhou J, Lu M. A Close to unity and All-Solar-Spectrum Absorption by Ion-Sputtering Induced Si Nanocone Arrays. *Opt Express* (2012) 20(20):22087–94. doi:10.1364/oe.20.022087
26. Vorobyev AY, Guo C. Direct Creation of Black Silicon Using Femtosecond Laser Pulses. *Appl Surf Sci* (2011) 257(16):7291–4. doi:10.1016/j.apsusc.2011.03.106
27. Huang Z-M, Huang W-Q, Jiang Z-M, Liu S-R, Wu X-K, Qin C-J. Electronic States of Defect with Impurity and Infrared Emission on Black Silicon Prepared by an Ns-Laser. *Opt Lett* (2017) 42(2):358–61. doi:10.1364/ol.42.000358
28. Zhao J-H, Lv Z-H, Li C-H, Yu X-Y, Li X-B. The Infrared Photodiode of Textured Silicon Irradiated under Mixed Gas by Femtosecond Laser. *IEEE Sensors J* (2016) 17(4):1. doi:10.1109/jsen.2016.2638434
29. Su Y, Zhan X, Zang H, Fu Y, Li A, Xu H, et al. Direct and Stand-Off Fabrication of Black Silicon with Enhanced Absorbance in the Short-Wavelength Infrared Region Using Femtosecond Laser Filament. *Appl Phys B* (2018) 124(11). doi:10.1007/s00340-018-7092-9
30. Fan Z, Cui D, Zhang Z, Zhao Z, Chen H, Fan Y, et al. Recent Progress of Black Silicon: From Fabrications to Applications. *Nanomaterials* (2021) 11(1):41. doi:10.3390/nano11010041
31. Chen T, Wang W, Tao T, Mei X, Pan A. Deposition and Melting Behaviors for Formation of Micro/nano Structures from Nanostructures with Femtosecond Pulses. *Opt Mater* (2018) 78:380–7. doi:10.1016/j.optmat.2018.02.051
32. Gradini R, Chen F, Tan R, Newlin L. A Summary on Cutting Edge Advancements in Sterilization and Cleaning Technologies in Medical, Food, and Drug Industries, and its Applicability to Spacecraft Hardware. *Life Sci Space Res* (2019) 23:31–49. doi:10.1016/j.lssr.2019.05.002
33. Madhukar YK, Mullick S, Nath AK. Development of a Water-Jet Assisted Laser Paint Removal Process. *Appl Surf Sci* (2013) 286:192–205. doi:10.1016/j.apsusc.2013.09.046
34. Xie X, Huang Q, Long J, Ren Q, Hu W, Liu S. A New Monitoring Method for Metal Rust Removal States in Pulsed Laser Derusting via Acoustic Emission Techniques. *J Mater Process Tech* (2020) 275:116321. doi:10.1016/j.jmatprotec.2019.116321
35. Jia B, Miao X, Jiang Y, Tang H, Yao C. Cleaning of Graphite Particles Embedded in the Surface of Ductile Iron by Using a Novel Method. *Math Probl Eng* (2021) 2021:1–9. doi:10.1155/2021/6664916
36. Rivas T, Pozo-Antonio JS, López de Silanes ME, Ramil A, López AJ. Laser versus Scalpel Cleaning of Crustose Lichens on Granite. *Appl Surf Sci* (2018) 440:467–76. doi:10.1016/j.apsusc.2018.01.167
37. Wu J, Zhao J, Qiao H, Hu X, Yang Y. The New Technologies Developed from Laser Shock Processing. *Materials* (2020) 13(6):1453. doi:10.3390/ma13061453
38. Harilal SS, Miloshevsky GV, Diwakar PK, LaHaye NL, Hassanein A. Experimental and Computational Study of Complex Shockwave Dynamics in Laser Ablation Plumes in Argon Atmosphere. *Phys Plasmas* (2012) 19(8):083504. doi:10.1063/1.4745867
39. Bett AJ, Eisenlohr J, Höhn O, Repo P, Savin H, Bläsi B, et al. Wave Optical Simulation of the Light Trapping Properties of Black Silicon Surface Textures. *Opt Express* (2016) 24(6):A434–A45. doi:10.1364/oe.24.00a434

Conflict of Interest: The authors declare that the research was conducted in the absence of any commercial or financial relationships that could be construed as a potential conflict of interest.

ORIGINAL RESEARCH
published: 28 March 2022
doi: 10.3389/fphy.2022.870339

Simulations and Experiments Toward Continuous Wave 167 nm Laser Generation for ARPES With High Energy Resolution

Ziyue Zhang[1,2], *Hainian Han*[1,3]*, *Guodong Zhao*[1], *Guodong Liu*[1], *Xingjiang Zhou*[1] *and Zhiyi Wei*[1,3]

[1]*Beijing National Laboratory for Condensed Matter Physics, Institute of Physics, Chinese Academy of Sciences, Beijing, China,* [2]*Qian Xuesen Laboratory of Space Technology, China Academy of Space Technology, Beijing, China,* [3]*Songshan Lake Materials Laboratory, Dongguan, China*

Continuous wave (CW) laser at a vacuum ultraviolet (VUV) range with the narrow-linewidth is an ideal optical source in angle-resolved photoemission spectroscopy (ARPES) for the research of superconductors with a narrow band gap. In this study, we present an eighth-harmonic-generation (EHG) laser scheme for CW laser generation at the VUV range, in particular at 167.75 nm, based on the cascaded power enhancement cavities. An intracavity second-harmonic generation (ICSHG) 671 nm laser with the narrow-linewidth and active frequency stabilization is built as the first stage, delivering the 2.55 W output power. A resonant cavity for fourth-harmonic-generation (FHG) constitutes the second stage, which generates the 335.5 nm laser with the output power of up to 1.25 W. The third stage is designed for the EHG of 167.75 nm based on the KBBF crystal. To realize the efficient CW laser generation at 167.75 nm, a theoretical analysis concerning the enhancement factor and the conversion efficiency of the KBBF-based EHG is carried out. The results show that it is possible for mW-level 167.75 nm generation if the transmittance of the KBBF prism-coupled device is increased to 97%. A 59 W circular intracavity power is observed in the 335.5 nm enhanced cavity experiments, corresponding to the peak power density of up to 20.86 MW/cm^2. This work paves a solid way for CW VUV laser generation with the narrow-linewidth, which would be an ideal tool for the extremely high resolution ARPES.

Keywords: vacuum ultraviolet, resonant enhancement, second-harmonic generation, narrow-linewidth, KBBF, ARPES

OPEN ACCESS

Edited by:
Xing Fu,
Tsinghua University, China

Reviewed by:
Zhigang Zhao,
Shandong University, China
Chaitanya Kumar Suddapalli,
The Institute of Photonic Sciences (ICFO), Spain

Correspondence:
Hainian Han
hnhan@iphy.ac.cn

Specialty section:
This article was submitted to Optics and Photonics, a section of the journal Frontiers in Physics

Received: *06 February 2022*
Accepted: *25 February 2022*
Published: *28 March 2022*

Citation:
Zhang Z, Han H, Zhao G, Liu G, Zhou X and Wei Z (2022) Simulations and Experiments Toward Continuous Wave 167 nm Laser Generation for ARPES With High Energy Resolution. Front. Phys. 10:870339. doi: 10.3389/fphy.2022.870339

INTRODUCTION

Angle-resolved photoemission spectroscopy (ARPES) is the most direct and powerful method to study the electronic structure of materials and plays an important role in the fields of advanced materials including high temperature superconductors, topological materials, and quantum materials. The higher the photon energy of the drive sources is, the larger the Brillouin zone can be measured, which is preferred for the research of superconductors with a narrow band gap. With the traditional vacuum ultraviolet (VUV) pulsed lasers as the drive sources, the energy resolution of the ARPES is limited to meV and the space charge effect affects the reliability of the obtained spectroscopy. The narrow-linewidth continuous wave (CW) VUV lasers can be utilized as an alternative drive source to improve the energy resolution to neV and eliminate the space charge effect [1–6]. The narrow-linewidth continuous wave lasers have also revolutionized the fields of precision metrology through atomic and molecular spectroscopy. The 167.079 nm narrow-linewidth CW laser corresponds to the transition from $^1S_0$ to $^3P_0$ of $^{27}Al^+$, used for achieving the Doppler cooling of the aluminum ions optical clocks [7]. So it is important to develop > 7 eV VUV narrow-linewidth CW laser sources.

There are several methods to generate VUV lasers such as free electron lasers, high harmonic generation and synchrotron radiation, and so on, which are all pulsed lasers and very expensive scientific facilities [8–10]. The excimer lasers are the most common deep ultraviolet lasers, which are key elements in the fields of lithography. However, they are mostly pulsed lasers with a single repetition frequency and have a poor beam quality, which brings inconvenience to the scientific application [11]. The VUV generation based on nonlinear frequency conversion has attracted great attention because of the good beam quality, high compactness, high robustness, and the flexible parameter adjustability [12]. Several reports have classified the ultraviolet nonlinear crystals through the generated photon energy limit and absorption edge, showing that the $KBe_2BO_3F_2$ (KBBF) crystal is the only transparent medium supporting the > 7 eV second-harmonic generation (SHG) [13]. A number of ultraviolet laser results based on the KBBF nonlinear crystal have been reported including femtosecond, picosecond to quasi-CW microsecond pulse durations generation, joule to microjoule pulse energies generation, 170–210 nm tuning wavelengths generation, which have also been used to drive the ARPES, photoemission electron microscopy, and revolutionized many frontier research studies [14–18]. In 2015, S. B. Dai et al. demonstrated a 65 μW 167.75 nm picosecond pulse laser generation based on the eighth-harmonic generation (EHG) of the 1,342 nm picosecond fundamental frequency laser [19]. In 2018, J. J. Li et al. present the 1.5 μJ 167.79 nm laser output with the linewidth of 0.025 pm, which was also generated from EHG of a 5 Hz 1,336 nm fundamental frequency quasi-CW laser [20].

When it comes to VUV narrow-linewidth CW laser generation, the conversion efficiency of the single-pass nonlinear process such as SHG and sum-frequency generation is extremely low as the focused power density hardly reaches MW/cm^2. The resonant enhanced cavity is generally used to improve the SHG efficiency of the CW lasers. However, it is still difficult to generate VUV through cavity-enhanced SHG based on the KBBF nonlinear medium. There are three main obstacles: first, the loss of the ultraviolet resonant cavity is hard to control, which mainly comes from the unmature ultraviolet coating technology and the complex structure of the KBBF prism-coupled device (KBBF-PCD) [21]. The former limits the reflectivity and adds the transmission loss of the cavity mirrors. Every time passing through the KBBF-PCD, the laser beam suffers the Fresnel reflection loss, unpredictable scattering, and absorption losses due to the uneven optical-contact interface, making it difficult to enhance the fundamental laser. Second, the fundamental ultraviolet output power is also much lower than the common visible and near-infrared wavelength and there are few commercial products. Third, cascading resonant cavities with the Pound–Drever–Hall (PDH) techniques make it challenging to keep the compactness and long-term operation [22]. In 2012, M. Scholz et al. reported a 1.3 mW 191 nm VUV laser generated from the fourth-harmonic generation (FHG) of a commercial 764 nm semiconductor laser with the power of 1.6 W and the line width of 50 kHz [23]. In 2013, they utilized 3 W 772 nm semiconductor lasers as the fundamental source and generated the 193 nm CW VUV laser with the stable output power of 4 mW [24].

In this report, we present the theoretical and experimental results ready for the 167.75 nm VUV CW laser generation. A narrow-linewidth Nd: YVO_4 single-frequency CW laser based on the intracavity second-harmonic generation (ICSHG) is utilized as the fundamental source with the output power of 2.55 W at 671 nm. The active frequency stabilization is built to suppress the frequency jitter. The second cavity-enhanced FHG stage is based on a BBO crystal, delivering a 1.25 W 335.5 nm laser. The third SHG stage is designed to employ the KBBF crystal. A theoretical analysis is carried out, showing that the prerequisite of the mW-level 167.75 nm VUV CW laser generation is the transmittance of the KBBF-PCD increased to more than 97%. A 59 W circular intracavity power of the 335.5 nm is experimentally observed in the resonant EHG cavity, laying a good foundation for the 167.75 nm VUV CW laser generation.

LASER SYSTEMS FOR 335.5 NM GENERATION

A high power all-solid-state single-frequency CW laser with the active frequency stabilization system is used as the fundamental source, as shown in **Figure 1**. An 880 nm laser diode is used to pump the Nd: YVO_4 gain medium, and a TGG device is inserted to keep the direction of optical beam. An LBO nonlinear crystal is placed between the concave mirrors to convert the 1,342 nm radiation to the 671 nm laser, synchronously choosing the resonant wavelength and maintaining the sing-frequency operation [25]. The output power of the 671 nm laser is 2.55 W with a peak-to-peak variation of 0.69%, as shown in **Figure 2A**. The M^2 factor is measured to be 1.14 in the x direction and 1.09 in the y direction respectively, exhibiting a good beam quality.

To further suppress the short-term and long-term frequency drift, an active frequency stabilization system based on the Pound–Drever–Hall (PDH) method is built as shown in **Figure 1**. A 10 cm-long Fabry–Perot cavity made of indium steel material is chosen as the reference for the pre-stabilization stage. The leakage of the 1,342 nm single-frequency laser, the line width of which is measured to be 115 kHz, is led to the Fabry–Perot cavity after frequency was modulated using an electro-optic modulator (EOM). A photodetector is placed at the end of the Fabry–Perot cavity to get the transmitted signal, which is then demodulated in the phase detector and processed using a PID controller. The control

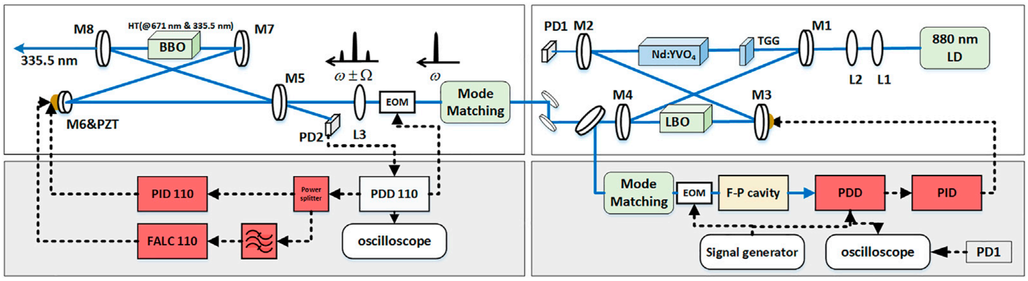

FIGURE 1 | Fourth harmonic laser system. M1–M8: cavity mirrors. L1-L3: focused lens. LD: Laser diode. EOM: Electro-optic modulator. PD: Photodiode.

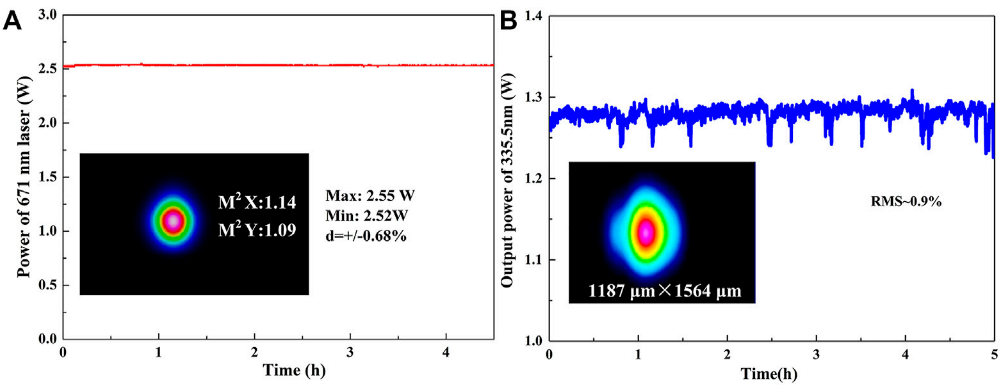

FIGURE 2 | (A) Stability of the output power of the 671 nm laser, the inset: beam quality. **(B)**The stability of the 335.5 nm single-frequency laser, the inset: the beam profile.

signal of the PID output is added to the piezo transducer (PZT) glued on the cavity mirror. The short-term frequency drift is suppressed from 100 MHz/2 min to less than 17.5 MHz/2 min, and the long-term frequency drift is suppressed by a factor of 2. The pre-stabilization cavity helped control the high frequency noise of the 671 nm single-frequency laser, benefiting the locking state of the cascading resonant cavity stages.

The second stage is designed to generate the fourth harmonic of the 1,342 nm single-frequency radiation. A 671 nm resonant cavity based on the nonlinear BBO crystal is built with the PDH locking system. After proper mode matching, the 2.55 W 671 nm laser is injected into the bow-tie resonant cavity with a conversion efficiency of 49%. The output power of the 335.5 nm ultraviolet laser is 1.25 W with a rms variation of 0.9% within 5 h because of the environmental disturbances, as shown in **Figure 2B**. Due to the walk-off effect, the beam spot of the 335.5 nm laser is elliptical even after being shaped by the cylindrical mirror, as shown in **Figure 2B**, bringing trouble to the mode matching of the next resonant stage. We estimate the line width of the second-harmonic at 671 nm to be < 163 kHz and the linewidth of the fourth-harmonic at 335.5 nm to be 230 kHz, as the SHG process increase the spectral linewidth with a factor of $\sqrt{2}$ [23].

VUV LASER GENERATION

Theoretical Background

According to the theory of G. D. Boyd, D. A. Kleiman, and A. Ashikin, when the fundamental frequency laser passes through a nonlinear crystal in a phase-matched direction, the output power P_2 of the SHG is as follows:

$$P_2 = E_{SHG} \cdot P_1^2, \tag{1}$$

where P_1 is the power of the fundamental frequency laser [26–28]. The nonlinear efficiency E_{SHG} is written as follows:

$$E_{SHG} = \frac{2\omega_1^2 d_{eff}^2}{\pi\varepsilon_0 c^3 n_1^2 n_2} \cdot lk_1 e^{-\alpha' l} \cdot h, \tag{2}$$

where ω_1 and k_1 are the angular frequency and wave vector of the fundamental frequency respectively, n_1 and n_2 are the indices of refraction of the fundamental frequency and the second harmonic respectively, d_{eff} is the effective nonlinear coefficient at the fundamental frequency, and l is the optical path in the nonlinear medium. $\alpha' = \alpha^1 + 1/2\alpha^2$, where α^1 and α^2 are the absorption coefficient for the fundamental and second harmonic respectively. The function h is expressed as follows:

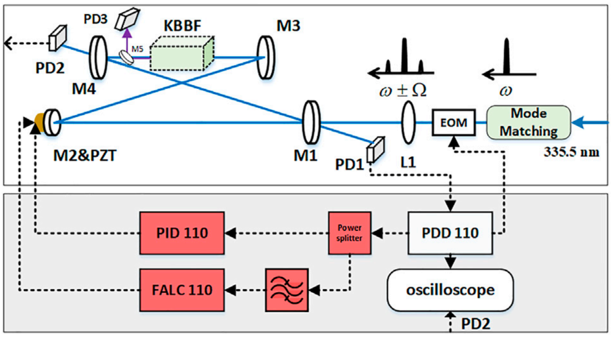

FIGURE 3 | Experimental setup of the resonant cavity based on the KBBF crystal. M1-M5: cavity mirror, PD: Photodetector, PZT: Piezo electric transducer, EOM: electronic-optical modulator.

$$h = \frac{\pi^2}{\xi_x} exp(\mu\alpha l)\left[\frac{2}{\sqrt{\pi}} e \int_{-\infty}^{\infty} exp(-4s^2)|H|^2 ds\right]. \tag{3}$$

According to Ref. [28], where $\xi_x = \frac{l}{b_x} = \frac{l}{k_1\omega_x^2}$ is the focusing parameter and

$$H = \frac{1}{2\pi}\int_{-\xi_x(1-\mu)}^{\xi_x(1+\mu)} \frac{exp(-\kappa\tau_x')\, exp(i\sigma'\tau_x')}{(1+i\tau_x')^{\frac{1}{2}}[1+i(e^2\tau_x'+\Delta)]^{\frac{1}{2}}} d\tau_x'. \tag{4}$$

The focus position is $\mu = \frac{l-2f_x}{l}$, and the astigmatic distance beam waists are $\Delta = \frac{2(f_x-f_y)}{k_1\omega_y^2}$. The ellipticity of the Gaussian beam is $e = \frac{\omega_x}{\omega_y}$, and the phase mismatch is $\sigma' = 1/2\, k_1\omega_y^2\Delta k + 4s\rho\omega_x k_1/2$. $\kappa = 1/2(\alpha^1 - 1/2\alpha^2)k_1\omega_x^2$.

Since the nonlinear efficiency of a type-I phase-matched crystal is low and the fundamental power of a CW laser is not comparable with high-peak-power narrow-duration pulsed lasers, the output power of the single-pass nonlinear process is usually at less than μW-level. A bow-tie resonant cavity is designed to enhance the fundamental power and improve the SHG conversion efficiency, as shown in **Figure 3**. Mirror M1 and M2 are plane. The former is the input coupler with the reflectivity of r_1 and the transmission of t_1 corresponding to the fundamental frequency, and the latter is mounted on two PZTs to stabilize the cavity length to the resonant wavelength. The mirror M3 and M4 are concave and the nonlinear crystal is placed at the focus between them. The reflectivity of the mirror M2–M4 is assumed as r_2, r_3, and r_4. The mirror M4 is usually chosen as the output coupler of the second harmonic, but for the > 7 eV VUV lasers present coating technology can hardly maintain the high reflectivity of the fundamental frequency and high transmission of the second harmonic synchronously. As a result, a reflective output coupler is inserted with high transmission of fundamental laser and high reflection for the harmonic generation with a transmission of t_5. The KBBF-PCD is the nonlinear medium as mentioned before with a transmission of t_{PCD}.

When the fundamental laser is coupled into the cavity and circling around, the main losses it suffered are the transmission and scattering loss of cavity mirrors r_i, the transmission loss of the KBBF-PCD (1-t_{PCD}), and the nonlinear conversion loss ($1-t_{SHG}$). Therefore, the equivalent reflectivity of resonator cavity can be expressed as $r = r_2r_3r_4t_5\cdot t_{PCD}\cdot t_{SHG}$, and $t_{SHG} = 1 - E_{SHG}\cdot P_c$. As the resonant cavity enters a steady state, the incident fundamental power P_1, the reflected power of the input coupler P_r, and the total circulating power P_c in the cavity have the following relationship

TABLE 1 | Parameters related to the KBBF crystal.

Crystal length	1 mm
Phase-matching angle (335.5–167.75 nm)	73.2°
n_1 (335.5 nm in the KBBF)	1.5007
n_2 (167.75 nm in the KBBF)	1.4993
d_{eff} (335.5 nm in the KBBF)	0.14 pm/V
α_1	0.1 cm^{-1}
α_2	10 cm^{-1}
Walk-off angle	38.83 mrad

$$\frac{P_r}{P_1} = \frac{\left(\sqrt{r_1}-\sqrt{r}\right)^2}{\left(1-\sqrt{r_1 r}\right)^2}, \tag{5}$$

$$\frac{P_c}{P_1} = \frac{t_1}{\left[1-\sqrt{r_1 r}\right]^2} = \frac{t_1}{\left[1-\sqrt{r_1\cdot r_2r_3r_4t_5\cdot t_{PCD}\cdot(1-E_{nl}\cdot P_c}\right]^2}, \tag{6}$$

when the reflectivity of the input coupler is consistent with the equivalent reflectivity of the cavity, $r_1 = r$, the impedance matching is fulfilled, which means the most efficient input coupling of the fundamental laser.

Simulation Results

The cavity is designed as shown in **Figure 3**. The reflectivity of the cavity mirrors M2–M4 is designed as $r_2 = r_3 = r_4 > 99.8\%$ at 335.5 nm, which is the highest reflectivity present coating technology can get. The output coupler M5 is designed as $t_5 > 99.5\%$ at 335.5 nm and $r_5 > 94\%$ at 167.75 nm. The parameters related to the KBBF device are listed in **Table 1**. The conversion efficiency is E_{SHG} calculated to be 1.41×10^{-6}/W.

Assuming that the mirrors are ideal and the input beam of the fundamental laser is circular and optimal mode matching, the input power of the fundamental laser is about 1.1 W. According to **Eqs 1–6**, simulations of the resonant cavity is carried out and the results are shown in **Figure 4**.

First, when the transmittance of the KBBF device is determined, the intracavity circulating power varies with the reflectivity of the input coupler and there is an optimum corresponding to the impedance matching state. For instance, when $t_{PCD} = 99\%$, the impedance matching appears at $r_1 = 97.9\%$. In this condition, the intracavity power P_c of the fundamental 335.5 nm laser is 52.58 W and the generated harmonic 167.75 nm is 3.89 mW theoretically, the nonlinear efficiency of which is only 0.35%.

Second, as the transmittance of the KBBF-PCD decreases from 99% to 97%, the optimal intracavity circulating power also decreases significantly from 52.58 W to 25.06 W and the impedance matching reflectance of the input coupler drops from 97.9% to 95.9%. The theoretically generated harmonic laser drops from 3.89 mW to 1.03 mW and the nonlinear

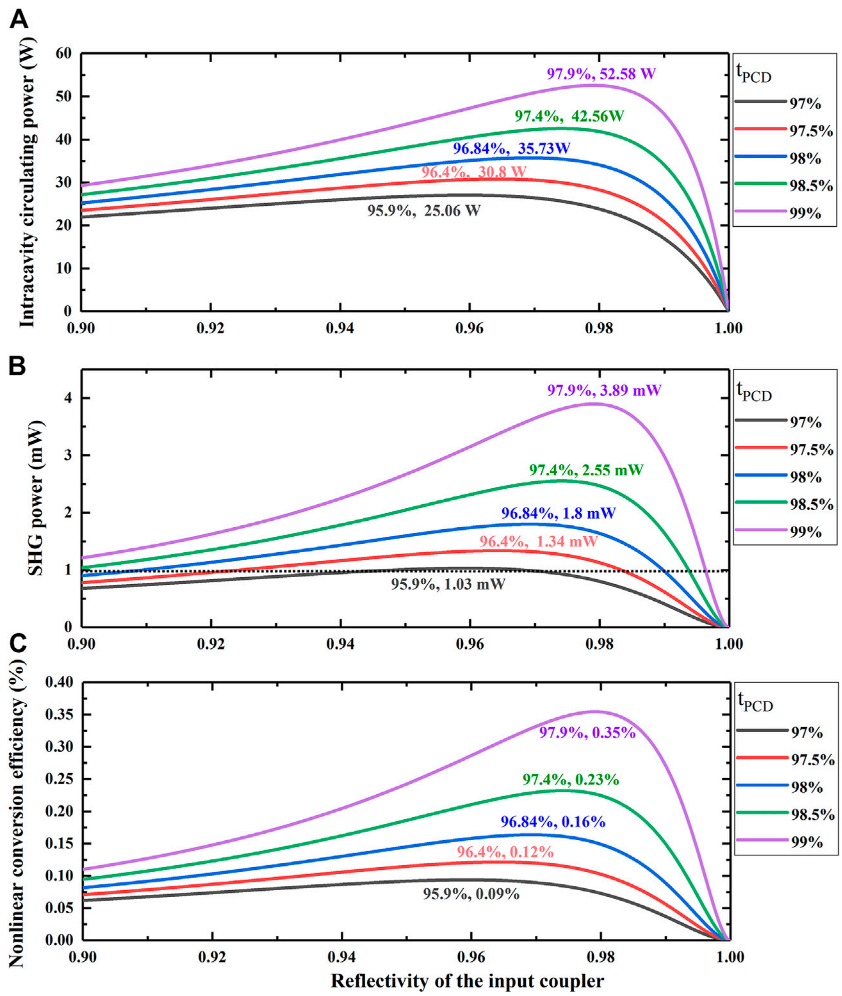

FIGURE 4 | (A) Intracavity circular power, **(B)**second-harmonic generation output power, and **(C)** nonlinear conversion efficiency versus input coupler.

conversion efficiency reduces from 0.35% to less than 0.09%, indicating that the transmittance of the KBBF-PCD is the key factor for the generation of the 167.75 nm harmonic laser. As the KBBF crystal is difficult to grow in the z-direction and cannot be cut along the phase-matching angle, a PCD structure was invented by C. T. Chen et al. to fix the crystal between prisms. The inhomogeneous optical contact introduces scattering loss at the interfaces of the KBBF medium and prims. The large phase-matched angle 73.2° makes the Fresnel reflection loss larger than 12%. These technical problems make it very challenging to control the transmission loss of 335.5 nm fundamental laser passing through a phase-matched KBBF-PCD less than 3%, which is predicted as the prerequisite for the generation of mW-level of the 167.75 nm VUV CW single-frequency laser.

Experimental Results

A bow-tie resonant EHG cavity is built according to the previous calculations and designs as shown in **Figure 3**. Since the VUV laser is absorbed seriously by the oxygen in the air, the whole cavity is built in a large vacuum chamber.

The distance S1 between plane mirror M1 and M2 is about 120 mm, and the beam waist between the plane mirror M1 and M2 is calculated to be 185 μm. The radius of the concave mirrors is 100 mm and the distance between them is adjusted to be 115 mm. The total length of the cavity is 493 mm. The reflectivity of the input coupler is designed to be 97%, and the others are 99.8% reflective. In order to efficiently couple the fundamental laser into the EHG resonant cavity, mode matching of the fundamental laser with the resonant mode is of great importance. As a result, after changing different groups of lenses, we chose a lens with the focal length of 1-m to shape the fundamental laser to $173 \times 207\, \mu m^2$, which is the optimal mode-matching conditions as the walk-off effect leading to an elliptical beam spot.

In order to achieve the PDH stabilization, two PZTs with the displacement of 2 μm and 10 μm were used for the fast-loop and slow-loop stabilization respectively. The size of the plane mirror M2 is $\phi 6 \times 2\, mm^2$ to reduce the load of the PZTs. A photodetector PD1 is placed behind the input coupler M1 to detect the reflective signal. Another photodetector PD2 is placed

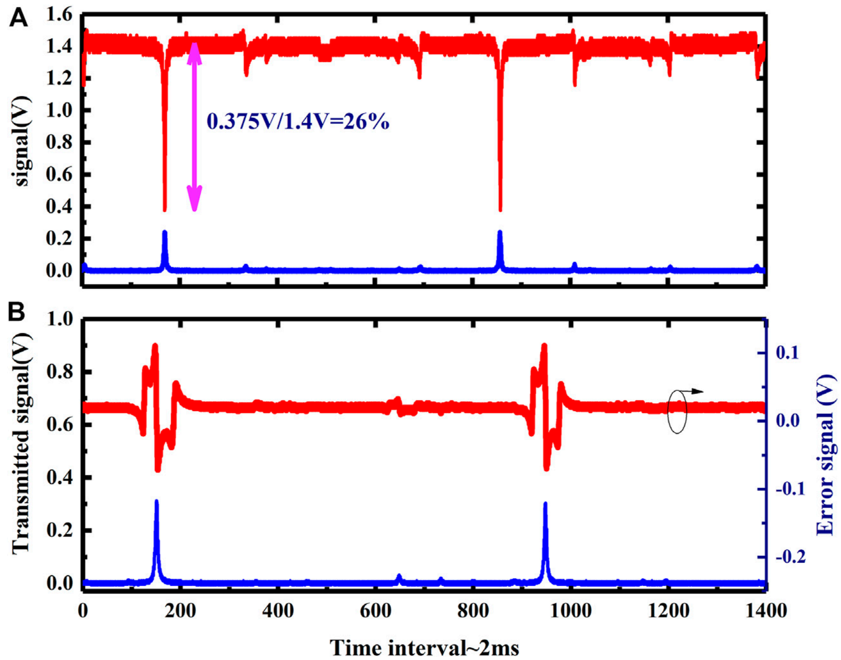

FIGURE 5 | (A) Reflection peaks (red) and transmission peaks (blue) of the 335.5 nm resonant cavity; **(B)** error signals (red).

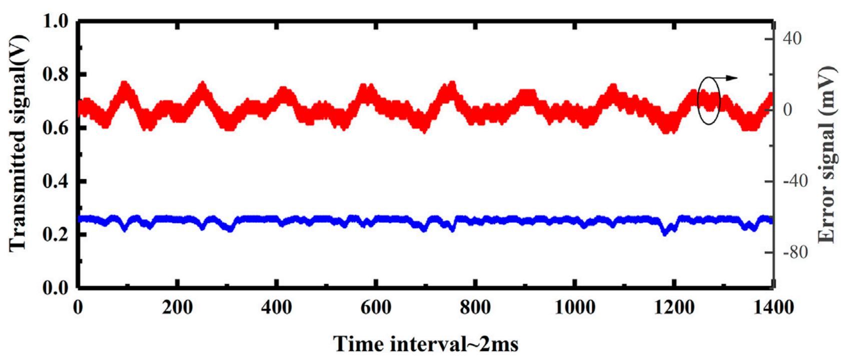

FIGURE 6 | Transmitted signal (blue) and error signal (red) of the PDH locked resonant cavity.

behind the concave mirror to detect the leakage. The locking electronics are from Toptica electronics.

The laser is first phase modulated using an EOM with the modulation frequency of 20 MHz, the detected reflected signal and transmitted signal are shown in **Figure 5A**. The positions of the focusing lens and the cavity mirrors are carefully adjusted according to the detected signals to suppress the high-order modes and improve the amplitude of the circulating power. The reflected signal is optimized as shown in **Figure 5A**, about 26% power was reflected at the resonant position, which is attributed to the mode mismatching and the impedance mismatching.

The reflected signal is then demodulated by the phase detector and the error signal is shown in **Figure 5B**. Two PID modules also from Toptica electronics are used to stabilize the cavity to the resonant wavelength. Once the locking state is activated, the error signal becomes zero and the transmitted signal stays at the high level, as shown in **Figure 6**. The leakage power of the concave mirror with a transmittance of 0.206% is measured to be 121 mW, and the circulating intracavity power is inferred to be 59 W. According to **Eq. 6**, under certain conditions the reflectivity of the input coupling is 97%, then the enhanced factor would be 90. The difference is attributed to the unperfect mode mismatching and the other scattering losses.

CONCLUSION

We have demonstrated the generation of the 335.5 nm laser with a high-peak-power density ready for the generation of the narrow-linewidth 167.75 nm VUV single-frequency CW laser, based on a home-built resonant cavity. The cascading resonant harmonic generation systems are designed, delivering the 671 nm single-frequency CW laser with the output power of the 2.55 W and the 335.5 nm single-frequency of 1.25 W. The EHG resonant cavity is preliminarily verified with the circulating power of 59 W and the peak power density of 20.86 MW/cm^2. A theoretical analysis is carried out, indicating that improving the transmittance of the KBBF-PCD to larger than 97% is the prerequisite for the mW-level generation of the 167.75 nm VUV narrow-line width single-frequency CW laser.

DATA AVAILABILITY STATEMENT

The raw data supporting the conclusion of this article will be made available by the authors, without undue reservation.

AUTHOR CONTRIBUTIONS

GL and XZ contributed to the ARPES application requirements. ZZ, HH and ZW contributed to the design and experimental schemes. ZZ and HH performed the experiments and are responsible for the data processing. ZZ, GZ, HH, and ZW contributed to write and edit the manuscript.

FUNDING

This work was supported by the Strategic Priority Research Program of the Chinese Academy of Sciences (Grant Nos. XDA1502040404 and XDB25000000) and the National Natural Science Foundation of China (Grant Nos. 91850209, 11888101 and 11974404).

REFERENCES

1. Zhou XJ, Wannberg B, Yang WL, Brouet V, Sun Z, Douglas JF, et al. Space Charge Effect and Mirror Charge Effect in Photoemission Spectroscopy. *J Electron Spectrosc Relat Phenomena* (2005) 142(Issue 1):27–38. ISSN 0368-2048. doi:10.1016/j.elspec.2004.08.004
2. Zhou XJ, Cuk T, Devereaux T, Nagaosa N, Shen Z-X. Angle-Resolved Photoemission Spectroscopy on Electronic Structure and Lectron-Phonon Coupling in Cuprate Superconductors. In: JR Schrieffer JS Brooks, editors. *Handbook of High-Temperature Superconductivity*. New York, NY: Springer (2007). p. 87–144. doi:10.1007/978-0-387-68734-6_3
3. Damascelli A, Hussain Z, Shen Z-X. Angle-resolved Photoemission Studies of the Cuprate Superconductors. *Rev Mod Phys* (2003) 75:473–541. doi:10.1103/RevModPhys.75.473
4. Tamai A, Meevasana W, King PDC, Nicholson CW, de la Torre A, Rozbicki E, et al. Spin-orbit Splitting of the Shockley Surface State on Cu(111). *Phys Rev B* (2013) 87:075113. doi:10.1103/PhysRevB.87.075113
5. Taniuchi T, Kotani Y, Shin S. Ultrahigh-spatial-resolution Chemical and Magnetic Imaging by Laser-Based Photoemission Electron Microscopy. *Rev Scientific Instr* (2015) 86:023701. doi:10.1063/1.4906755
6. Tamai A, Wu QS, Cucchi I, Bruno FY, Riccò S, Kim TK, et al. Fermi Arcs and Their Topological Character in the Candidate Type-II Weyl SemimetalMoTe2. *Phys Rev X* (2016) 6:031021. doi:10.1103/PhysRevX.6.031021
7. Chou CW, Hume DB, Koelemeij JC, Wineland DJ, Rosenband T. Frequency Comparison of Two High-Accuracy Al+ Optical Clocks. *Phys Rev Lett* (2010) 104:070802. doi:10.1103/PhysRevLett.104.070802
8. O'Shea P, Freund H Free-Electron Lasers: Status and Applications. *Science* (2001) 292:1853–8. doi:10.1126/science.1055718
9. Paul PM, Toma ES, Breger P, Mullot G, Auge´ F, Balcou P, et al. Observation of a Train of Attosecond Pulses from High Harmonic Generation. *Science* (2001) 292:1689–92. doi:10.1126/science.1059413
10. Moser HO, Wilhelmi O, Yang P Synchrotron Radiation Research At Singapore Synchrotron Light Source. *Accel. Phys. Technol. App.* (2004):601–627.
11. Basting D, Marowsky G. *Excimer Laser Technology*. Berlin, Heidelberg: Springer Berlin Heidelberg (2005). Imprint: Springer.
12. Peng Q-J, Zong N, Zhang S-J, Wang Z-M, Yang F, Zhang F-F, et al. DUV/VUV All-Solid-State Lasers: Twenty Years of Progress and the Future. *IEEE J Select Top Quan Electron.* (2018) 24(5):1–12. Art no. 1602312. doi:10.1109/JSTQE.2018.2829665
13. Liu G, Wang G, Zhu Y, Zhang H, Zhang G, Wang X, et al. Development of a Vacuum Ultraviolet Laser-Based Angle-Resolved Photoemission System with a Superhigh Energy Resolution Better Than 1 meV. *Rev Sci Instrum* (2008) 79:023105. doi:10.1063/1.2835901
14. Yang F, Wang Z, Zhou Y, Li F, Xu J, Xu Y, et al. Theoretical and Experimental Investigations of Nanosecond 177.3 Nm Deep-Ultraviolet Light by Second Harmonic Generation in KBBF. *Appl Phys B* (2009) 96:415–22. doi:10.1007/s00340-009-3506-z
15. Yang F, Wang Z, Zhou Y, Cheng X, Xie S, Peng Q, et al. 41mW High Average Power Picosecond 177.3nm Laser by Second-Harmonic Generation in KBBF. *Opt Commun* (2010) 283:142–5. doi:10.1016/j.optcom.2009.09.051
16. Wang G, Wang X, Zhou Y, Li C, Zhu Y, Xu Z, et al. High-efficiency Frequency Conversion in Deep Ultraviolet with a KBe_2BO_3F_2 Prism-Coupled Device. *Appl Opt* (2008) 47:486–8. doi:10.1364/ao.47.000486
17. Zhang H, Wang G, Guo L, Geng A, Bo Y, Cui D, et al. 175 to 210 Nm Widely Tunable Deep-Ultraviolet Light Generation Based on KBBF crystal. *Appl Phys B* (2008) 93:323–6. doi:10.1007/s00340-008-3198-9
18. Zhang X, Wang L, Wang X, Wang G, Zhu Y, Chen C. High-Power Sixth-Harmonic Generation of an Nd:YAG Laser with KBe2BO3F2 Prism-Coupled Devices. *Opt Commun* (2012) 285:4519–22. doi:10.1016/j.optcom.2012.06.080
19. Dai SB, Zong N, Yang F, Zhang SJ, Wang ZM, Zhang FF, et al. 167.75-nm Vacuum-Ultraviolet Ps Laser by Eighth-Harmonic Generation of a 1342-nm Nd:YVO_4 Amplifier in KBBF. *Opt Lett* (2015) 40:3268–71. doi:10.1364/OL.40.003268
20. Dai S-B, Chen M, Zhang S-J, Wang Z-M, Zhang F-F, Yang F, et al. 2.14 mW Deep-Ultraviolet Laser at 165 Nm by Eighth-Harmonic Generation of a 1319 Nm Nd:YAG Laser in KBBF. *Laser Phys Lett* (2016) 13:035401. doi:10.1088/1612-2011/13/3/035401
21. Chen CT, Wang GL, Wang XY, Xu ZY. Deep-UV Nonlinear Optical crystal KBe2BO3F2-Discovery, Growth, Optical Properties and Applications. *Appl Phys B* (2009) 97:9–25. doi:10.1007/s00340-009-3554-4
22. Black ED. An Introduction to Pound-Drever-Hall Laser Frequency Stabilization. *Am J Phys* (2001) 69:79–87. doi:10.1119/1.1286663
23. Scholz M, Opalevs D, Leisching P, Kaenders W, Wang G, Wang X, et al. 13-mW Tunable and Narrow-Band Continuous-Wave Light Source at 191 Nm. *Opt Express* (2012) 20:18659–64. doi:10.1364/oe.20.018659
24. Scholz M, Opalevs D, Leisching P, Kaenders W, Wang G, Wang X, et al. A Bright Continuous-Wave Laser Source at 193 Nm. *Appl.Phys Lett* (2013) 103:051114. doi:10.1063/1.4817786

25. Ma Y, Li Y, Feng J, Zhang K. High-power Stable Continuous-Wave Single-Longitudinal-Mode Nd:YVO_4 Laser at 1342 Nm. *Opt Express* (2018) 26: 1538–46. doi:10.1364/oe.26.001538
26. Ashkin A, Boyd G, Dziedzic J. Resonant Optical Second Harmonic Generation and Mixing. *IEEE J Quan Electron.* (1966) 2:109–24. doi:10.1109/jqe.1966.1074007
27. Boyd GD, Kleinman DA. Parametric Interaction of Focused Gaussian Light Beams. *J Appl Phys* (1968) 39:3597–639. doi:10.1063/1.1656831
28. Freegarde T, Coutts J, Walz J, Leibfried D, Hänsch TW. General Analysis of Type I Second-Harmonic Generation with Elliptical Gaussian Beams. *J Opt Soc Am B* (1997) 14:2010. doi:10.1364/josab.14.002010

Conflict of Interest: The authors declare that the research was conducted in the absence of any commercial or financial relationships that could be construed as a potential conflict of interest.

frontiers | Frontiers in Physics

ORIGINAL RESEARCH
published: 06 April 2022
doi: 10.3389/fphy.2022.880436

Effect of Thermal Blooming on the Higher-Order Mode Fiber Laser Array Propagation Through the Atmosphere

*Yuqiu Zhang, Tianyue Hou, Yu Deng, Pengfei Ma, Rongtao Su and Pu Zhou**

College of Advanced Interdisciplinary Studies, National University of Defense Technology, Changsha, China

The influence of thermal blooming on the propagation properties of higher-order mode (HOM) fiber laser array is studied by using the algorithm for simulating the laser beam propagation in the atmosphere. Based on the multiphase screen method and finite-difference method, the four-dimensional (4D) computer code of time-dependent propagation is designed to simulate the propagation of HOM fiber laser array through the atmosphere. In this study, the laser energy focusability of the LP_{11} mode beam array is investigated in detail for different beamlet arrangements, transverse wind speed, and the content of LP_{01} mode under the conditions of thermal blooming. In free space, the focal shape of the LP_{11} mode beam array depends on the arrangement of the second circle of the initial beam array, whereas the influence of the central beamlets is weak. The number of side lobes can be tailored by changing the arrangement of the beamlets. In contrast, under the conditions of thermal blooming, the central beamlet has a significant effect on focal beam shape. It is demonstrated that the laser energy focusability can be improved by rotating the central beamlet or increasing the transverse wind speed. As the content of the LP_{01} mode increases, the energy is gradually concentrated from the side lobes to the center lobe. Furthermore, the effects of initial beam array arrangements on the energy focus and focal shape are investigated. The optimal arrangement for obtaining high energy focusability is discussed in detail. These results could provide useful references for applications of the HOM beam array.

Keywords: thermal blooming, atmospheric propagation, higher-order modes, coherent beam combining, wave optics simulation

Edited by:
Xing Fu,
Tsinghua University, China

Reviewed by:
Dong Mao,
Northwestern Polytechnical University, China
Hua Shen,
Nanjing University of Science and Technology, China

****Correspondence:***
Pu Zhou
zhoupu203@163.com

Specialty section:
This article was submitted to Optics and Photonics, a section of the journal Frontiers in Physics

Received: *21 February 2022*
Accepted: *11 March 2022*
Published: *06 April 2022*

Citation:
Zhang Y, Hou T, Deng Y, Ma P, Su R and Zhou P (2022) Effect of Thermal Blooming on the Higher-Order Mode Fiber Laser Array Propagation Through the Atmosphere. Front. Phys. 10:880436. doi: 10.3389/fphy.2022.880436

INTRODUCTION

The large mode area (LMA) fiber is remarkable for its advantages in suppressing a number of nonlinear effects [1–3]. In recent years, higher-order modes (HOMs) with specific spatial intensity, phase, and polarized distributions have been widely applied in many practical applications, such as optical tweezers, optical communication, micro-machining, and material processing [4–8]. Driven by these demanding applications, the methods of generating HOMs in fiber lasers have been demonstrated widely [9–12]. HOMs can be generated based on the active mode control system, and various methods have been successfully demonstrated, including spatial light modulator (SLM) [13], long-period fiber gratings [14, 15], fiber Bragg grating [16], random fiber lasers [17], polarization control [18, 19], and mode-selective couplers (MSCs) [20, 21]. Notably, You et al. demonstrated a kilowatt (kW)-level HOM laser beam based on the master oscillator power amplifier (MOPA) configuration [22]. These advancements of HOMs can be beneficial for further power scaling.

The power scaling of the output laser beyond the kilowatt (kW) level can be achieved by the coherent beam combining (CBC) technology as well [23–25]. In last decades, the coherent combining of laser beams has been widely used in high-power systems and inertial confinement fusion due to the advantages such as efficiency, compactness, and reliability [26–28]. Recently, high output power [29–31] and a large number of channels [32, 33] based on the coherent combining of the fiber amplifier array have been reported. In addition, the structured light beams can also be generated from the beam array [34]. Until now, various structured light beams based on CBC technology have been demonstrated theoretically and experimentally [35–38].

When a high-power laser beam propagates through the atmosphere, the propagation characteristics of the laser beam could be affected by nonlinear effects such as thermal blooming, self-focusing, stimulated Raman scattering, and etc. The thermal blooming effect is one of the most important nonlinear effects, which is caused by the energy of the laser beam absorbed by molecules and aerosols in the atmosphere [39]. Thermal blooming leads to decreasing of the peak irradiance, and the presence of a transverse wind will further cause the shift of the peak irradiance, which will result in the degradation of beam quality and limit the use of high-power laser delivery [40, 41]. Over the last decades, the study of the effect of thermal blooming on high-power laser beams propagating in the atmosphere has gained considerable attention. For example, Gebhardt and Smith developed a theoretical model to predict thermal blooming distortion in the atmosphere [42]. Fleck et al. proposed a four-dimensional (4D) computer code of the time-dependent propagation of high-power laser beams to investigate the thermal blooming effect [43]. Moreover, the effect of thermal blooming on annular beams, airy beams, Hermite–Gaussian beams, and vortex beams has been studied in detail [44–47]. With the development of the CBC technology, the studies of the effect of thermal blooming on the beam array have also been carried out in recent years [48–51]. To the best of our knowledge, the effect of thermal blooming on the HOM beam array has not been investigated yet.

The aim of the study is to study the influence of thermal blooming on the propagation properties of a coherent beam combined with the high-power continuous wave HOM beam array in the atmosphere. The mathematical model of the HOM beam array and 4D computer algorithms are presented in the *Theoretical Model* section. The LP_{11} mode beam array is considered in this study. In the *Numerical Simulations Results and Analysis* section, the changes of focal shape in free space for different beamlet arrangements are studied. In addition, the influence of the beamlet arrangement and content of the LP_{01} mode on the energy focusability under the conditions of thermal blooming is investigated in detail. In the *Conclusion* section, the main results obtained in this study are summarized.

Theoretical Model

At present, the step-index fiber is taken as the gain medium for most high-power fiber laser systems. Without loss of generality,

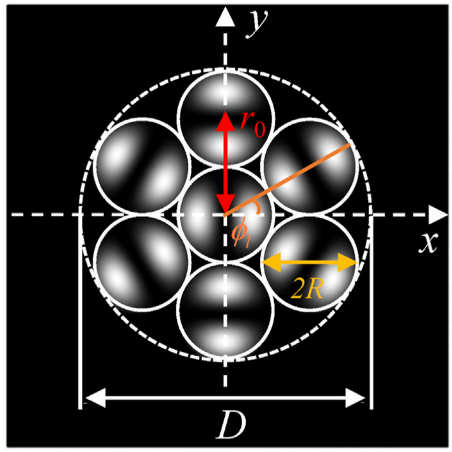

FIGURE 1 | Schematic diagram of a HOM beam array.

the HOMs excited from a step-index fiber is investigated in this study. It is considered that the coordinate z-axis is parallel to the geometrical axis of the fiber with the core radius a. In the weakly guiding approximation, the field distribution of the LP_{nm}-mode can be expressed as [52].

$$E_{nm}(r,\phi) = R_{nm}(r)\cos(n\phi), \tag{1}$$

where (r,ϕ) are the polar coordinates. The radial dependence of the approximately transverse field amplitude in **Eq. 1** is defined as follows

$$R_{nm}(r) = \begin{cases} k_1 J_n\left(U_m \frac{r}{a}\right) & 0 \le r \le a \\ k_2 K_n\left(W_m \frac{r}{a}\right) & r > a \end{cases}, \tag{2}$$

where $k_1 J_n(U_m) = k_2 K_n(W_m)$ and J_n and K_n are the n-order Bessel function of the first kind and the modified Bessel function of the first kind, respectively. U_m and W_m are the solutions of the characteristic equations (53).

$$\frac{J_n(U_m)}{U J_{n+1}(U_m)} = \frac{K_n(W_m)}{W K_{n+1}(W_m)} \tag{3}$$

and

$$U^2 + W^2 = V \tag{4}$$

The normalized frequency V is defined as

$$V = \frac{2\pi a}{\lambda}\sqrt{n_{\text{core}}^2 - n_{\text{clad}}^2}, \tag{5}$$

where n_{core} and n_{clad} are the core refractive index and cladding refractive index, respectively. The numerical aperture (NA) can be written as $NA = \sqrt{n_{core}^2 - n_{clad}^2}$. The exemplary fiber that will be considered here has an ideal step-index profile with a core/inner-cladding diameter of 20/400 μm and an NA of 0.06.

The HOMs excited in the fiber are magnified 200 times by a large diameter collimator and then combined in the beam combiner system. It is assumed that a HOM beam array consists of seven beamlets located as $z = 0$, which are arranged in a tiled hexagonal architecture by coherent beam combining, as shown in **Figure 1**. The distance between the centers of neighboring sub-aperture is r_0 and the diameter of the whole beam array is D. The optical field of each beamlet is E_{nm}^{l}. The electric field distribution of the HOM beam array with a hard aperture is expressed as

$$E = A_{\mathrm{coe}} \sum_{l=1}^{N} E_{nm}^{l} \left[r^2 + r_0^2 + 2 r r_0 \cos(\phi - \phi_l) \right] \times circ\left[r^2 + R^2 + 2 r R \cos(\phi - \phi_l) \right], \tag{6}$$

where $\phi_l = \pi l/3$. The $circ(\bullet)$ denotes the hard aperture truncated function with a diameter of R. The coefficient A_{coe} can be obtained according to the well-known relationship between power P and the electric field E_{nm}^{l} [54].

$$P = \int_0^{2\pi} \mathrm{d}\phi \int_0^{\infty} |E|^2 r \mathrm{d}r, \tag{7}$$

In the parabolic approximation, the electric field E satisfies the Maxwell wave equation (43).

$$2\mathrm{i}k \frac{\partial E}{\partial z} = \nabla_{\perp}^2 E + k^2 \left(\frac{n^2}{n_0^2} - 1 \right) E, \tag{8}$$

where $\nabla_{\perp}^2 = \partial^2/\partial x^2 + \partial^2/\partial y^2$ and n, and n_0 are the refractive indices of the atmosphere with and without disturbance, respectively. $k = 2\pi/\lambda$ is the wave number related to the wavelength λ. According to the hydrodynamic equation, the atmospheric density ρ_1 with disturbance caused by thermal blooming can be obtained [43].

$$\frac{\partial \rho_1}{\partial t} + v \cdot \nabla \rho_1 = -\frac{\gamma - 1}{c_s^2} \alpha I, \tag{9}$$

where v, γ, c_s, and α are the wind speed, specific heat, sound speed capacity ratio, and absorption coefficient in the atmosphere, respectively. The intensity I is given by $I = |E|^2 \exp(\alpha z)$.

Based on **Eqs 1–9**, we designed a 4D computer code to simulate the time-dependent propagation of a HOM beam array propagating through the atmosphere by using the multiphase screen method and finite-difference method [43]. A lens with focus $z_f = 5$ km located at $z = 0$ is considered in this study. In the following calculations, the parameters are taken as $a = 50$ μm, $R = 4.5$ cm, $\lambda = 1.064$μm, $n_0 = 1.00031$, $v = 2$ m/s along x-axis, $\rho_0 = 1.30246$ kg/m^3, $c_s = 340$ m/s, $\alpha = 0.07$/km, $P = 1$ kw, and $N = 7$, $z = 5$ km.

NUMERICAL SIMULATION RESULTS AND ANALYSIS

Linear Propagation of the HOM Beam Array

In this section, the propagation properties of the LP_{11} mode beam array propagating in free space are demonstrated. As we all know, the intensity distribution of the LP_{01} mode is circular symmetry, and the far field intensity distribution of the LP_{01} mode coherent beam array is comprises a central lobe with a number of side lobes. But for the LP_{11} mode, the intensity distribution is axial symmetry, and therefore, the arrangement of the LP_{11} mode has a significant impact on the focal intensity distributions.

The intensity distributions of the LP_{11} mode beam array with centrosymmetric arrangement are shown in **Figure 2**. It is assumed that the angle of the LP_{11} mode around the central beamlet in **Figure 2A** is set as $\theta = 0$, and the different rotation angles for the initial beamlet arrangement are shown in **Figures 2B–D**. It can be seen that the beam shapes of the LP_{11} mode beam array at the receiver plane are quite different from those of the LP_{01} mode beam array. The beam shapes of the LP_{11} mode beam array are a radial spot beam array without a central lobe. As θ changes from 0 to 90°, the number of side lobes gradually changes from 6 to 12. By comparing the beam shapes at the initial plane, it is clearly seen that the focal intensity distributions are consistent with the first ring of the hexagonal mesh of the fiber laser array (see the red circle highlight in **Figures 2A–D**). These observations indicate that the desired beam shape of the focusing spots can be obtained by simply rotating the surrounding beamlets.

Effect of Thermal Blooming on the HOM Beam Array

It can be clearly seen that different focal spots can be obtained by changing the initial arrangement of the LP_{11} mode beam array as mentioned in the *Linear propagation of HOMs beam array* section. Therefore, the impact of thermal blooming on the LP_{11} mode beam array can be quite different for different arrangements. In this section, based on the results in the *Linear propagation of HOMs beam array* section, the effects of thermal blooming on the special arrangements of the LP_{11} mode beam array are investigated in detail.

The intensity distributions of the LP_{11} mode beam array for centrosymmetric arrangement under the conditions of thermal blooming are shown in **Figures 3**, **4**. From **Figures 4I–L**, it can be observed that the influence of thermal blooming on the LP_{11} mode beam array can be quite different for different rotation angles. In addition, the focal beam shapes are not symmetrical except for the arrangement of **Figure 3A**. The difference between **Figure 3** and **Figure 4** is that the initial central beamlets in **Figure 4** are rotated by 90 degrees. It can be seen that the focal beam shapes under thermal blooming are quite different, although the focal beam shapes in free space are the same. The phenomena illustrates that the arrangement of the central beamlet has little influence on the focal beam shapes in free space but has a significant effect on the focal beam shapes under thermal blooming.

It is assumed that the directions of the central beamlet in **Figures 3A–D** are parallel to that of the wind and that in **Figures 4A–D** are vertical to that of the wind. Generally, the power of the bucket-based beam width is used to describe beam spreading and energy focusability, which is expressed as [55]

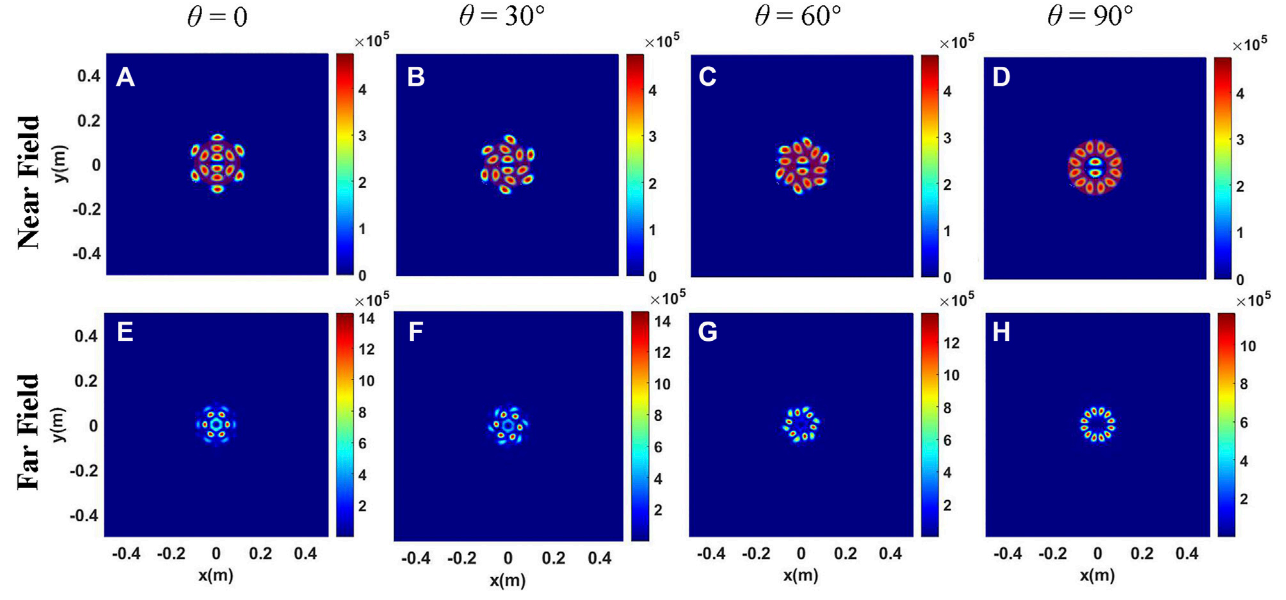

FIGURE 2 | Intensity distributions of the LP_{11} mode beam array for different rotation angles of beamlets. **(A–D)** Intensity distributions at the initial plane. **(E–H)** Intensity distributions at the receiver plane in free space.

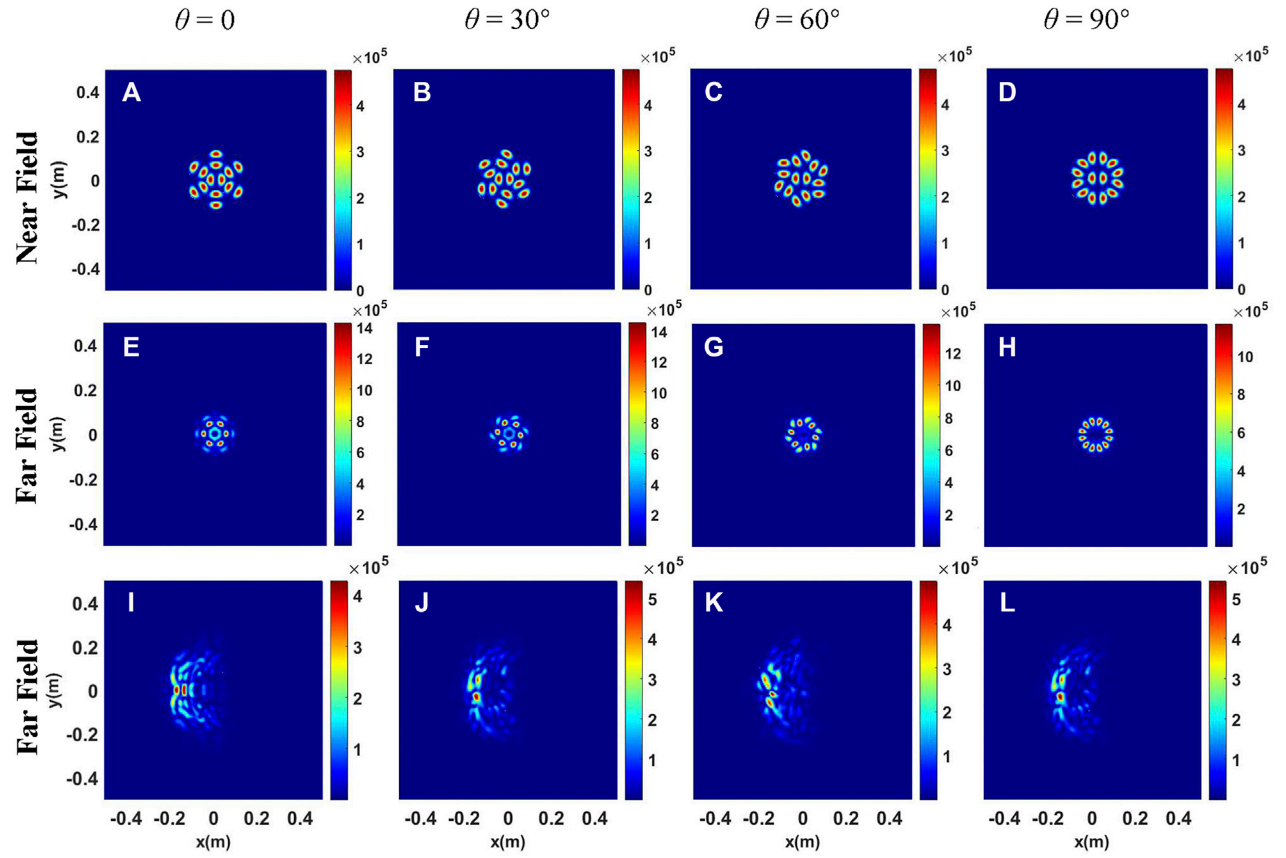

FIGURE 3 | Intensity distributions of the LP_{11} mode beam array for different rotation angles of beamlets. **(A–D)** Intensity distributions at the initial plane; **(E–H)** Intensity distributions at the receiver plane in free space; **(I–L)** Intensity distributions at the receiver plane under thermal blooming.

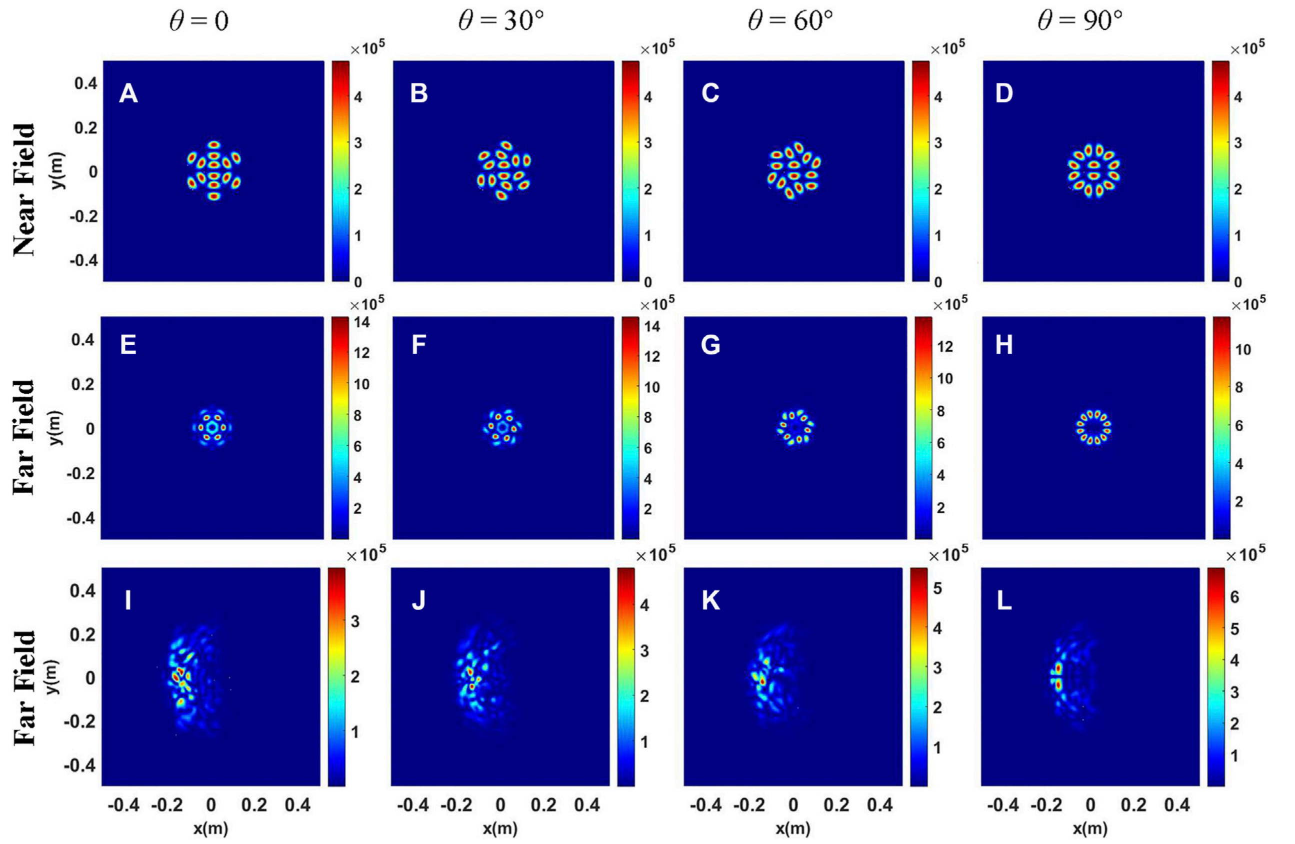

FIGURE 4 | Intensity distributions of the LP_{11} mode beam array with different rotation angles of beamlets. **(A–D)** Intensity distributions at the initial plane; **(E–H)** Intensity distributions at the receiver plane in free space; **(I–L)** Intensity distributions at the receiver plane under thermal blooming.

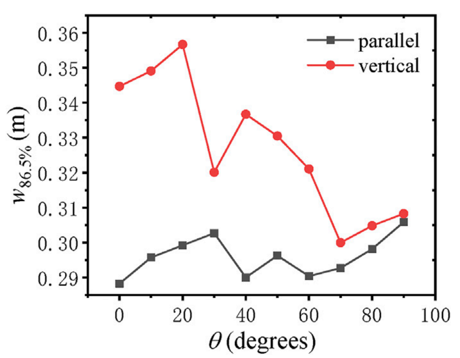

FIGURE 5 | Variation of beam width $w_{86.5\%}$ with rotating angle θ for different arrangements of the central beamlet.

$\int_0^{w_\eta} I r dr = \eta \int_0^{+\infty} I r dr$, where w_η is the bucket half-width chosen. The beam width $w_{86.5\%}$ is adopted in this study. On the other hand, the beam centroid position is changed due to the effect of thermal blooming, which is defined as [55] $\bar{j} = \iint jI\mathrm{d}x\mathrm{d}y / \iint I\mathrm{d}x\mathrm{d}y$, where $j = x$ and y. The center of the bucket is taken as $(\bar{x}, \bar{y})$ in the following calculations. The changes of the beam width at the target for different values of rotation angles are shown in **Figure 5**. It can be seen that the value of beam width $w_{86.5\%}$ of the parallel direction is lower than that of the vertical direction. Thus, the beam focusability of the parallel direction is higher than that of the vertical direction. That means the thermal blooming becomes more severe for the vertical central beamlet arrangement, especially when $\theta = 20°$. As the θ increases, the difference of the beam width $w_{86.5\%}$ between parallel and vertical directions decreases. Thus, the laser energy focusability can be controlled simply by rotating the central beam.

Here, we choose four arrangement types of initial beamlets (see **Figures 6A–D**) to investigate the influence of transverse wind speed on the energy focusability. As can be seen from **Figure 6E**, the beam width decreases and becomes closer as the wind speed increases. The physical reason is that the absorbed energy in the propagation path is carried away more quickly as the wind speed increases. That is to say, increasing the transverse wind speed can help increase the energy focusability. In addition, the beam width of **Figure 6A** is the largest for different values of wind speed. Thus, the arrangement of **Figure 6A** should be avoided in order to improve the energy focusability.

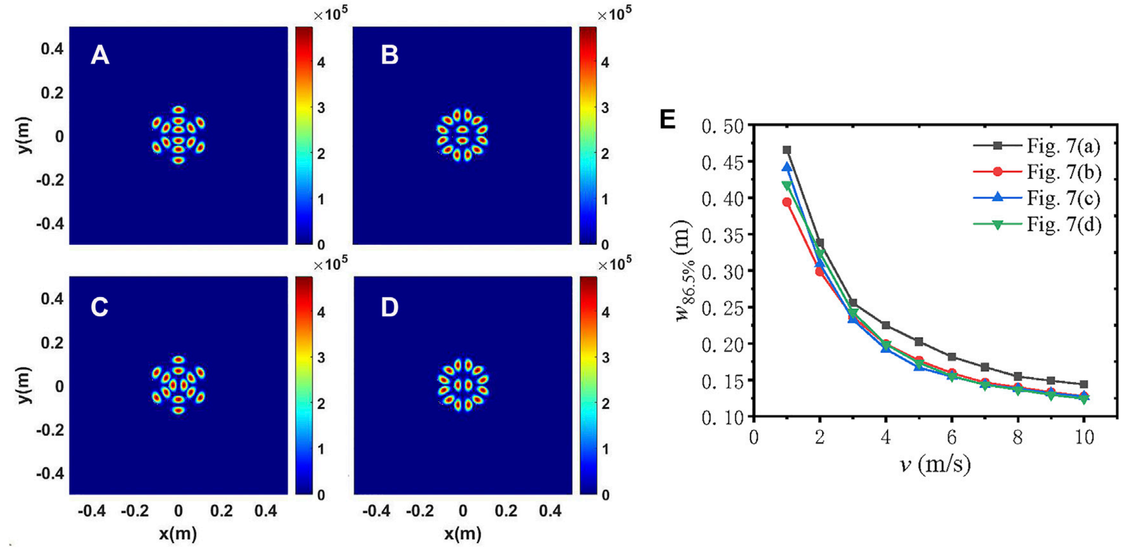

FIGURE 6 | (A–D) Intensity distributions of the LP_{11} mode beam array with different arrangement of beamlets; **(E)** variation of beam width $w_{86.5\%}$ with wind speed v.

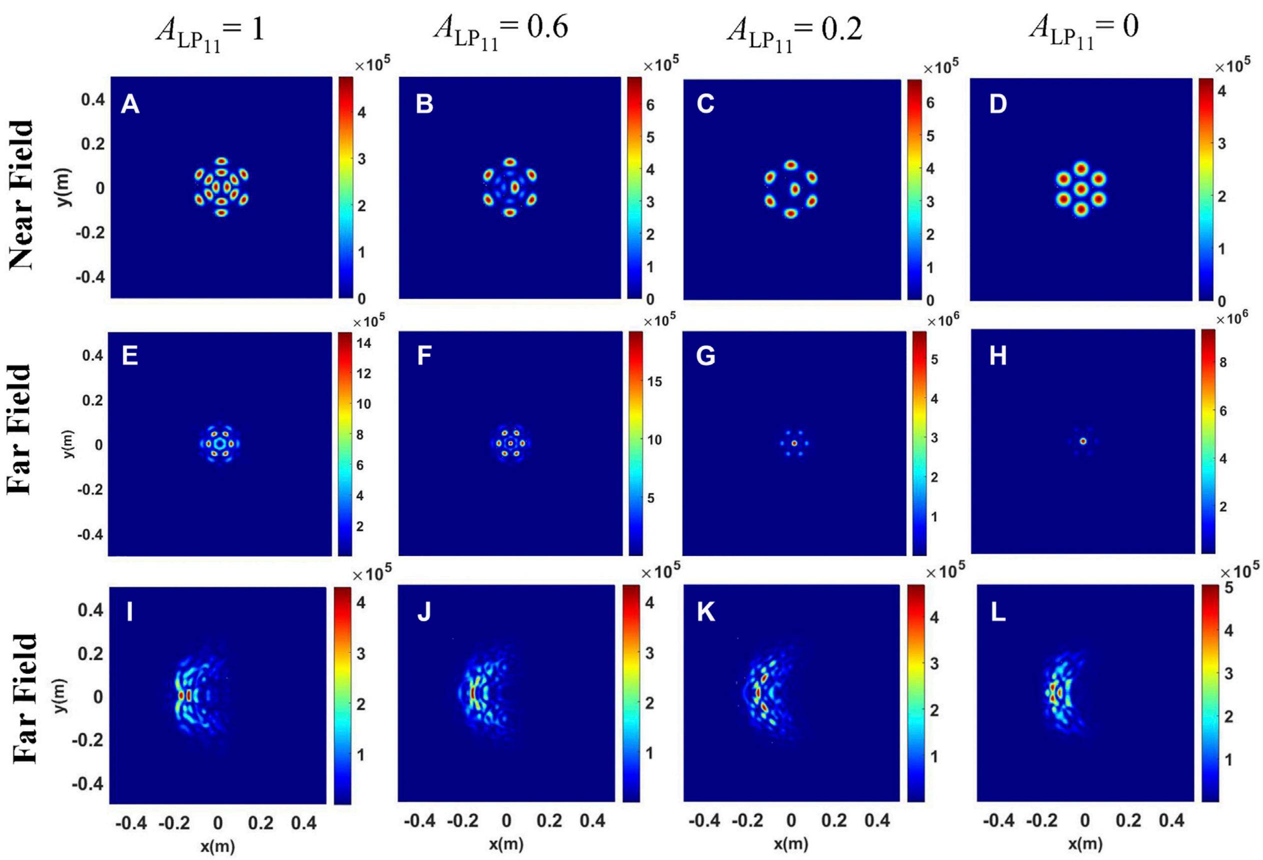

FIGURE 7 | Intensity distributions of the mixed-mode beam array for different content of the LP_{01} mode. **(A–D)** Intensity distributions at the initial plane; **(E–H)** Intensity distributions at the receiver plane in free space; **(I–L)** Intensity distributions at the receiver plane under the conditions of thermal blooming.

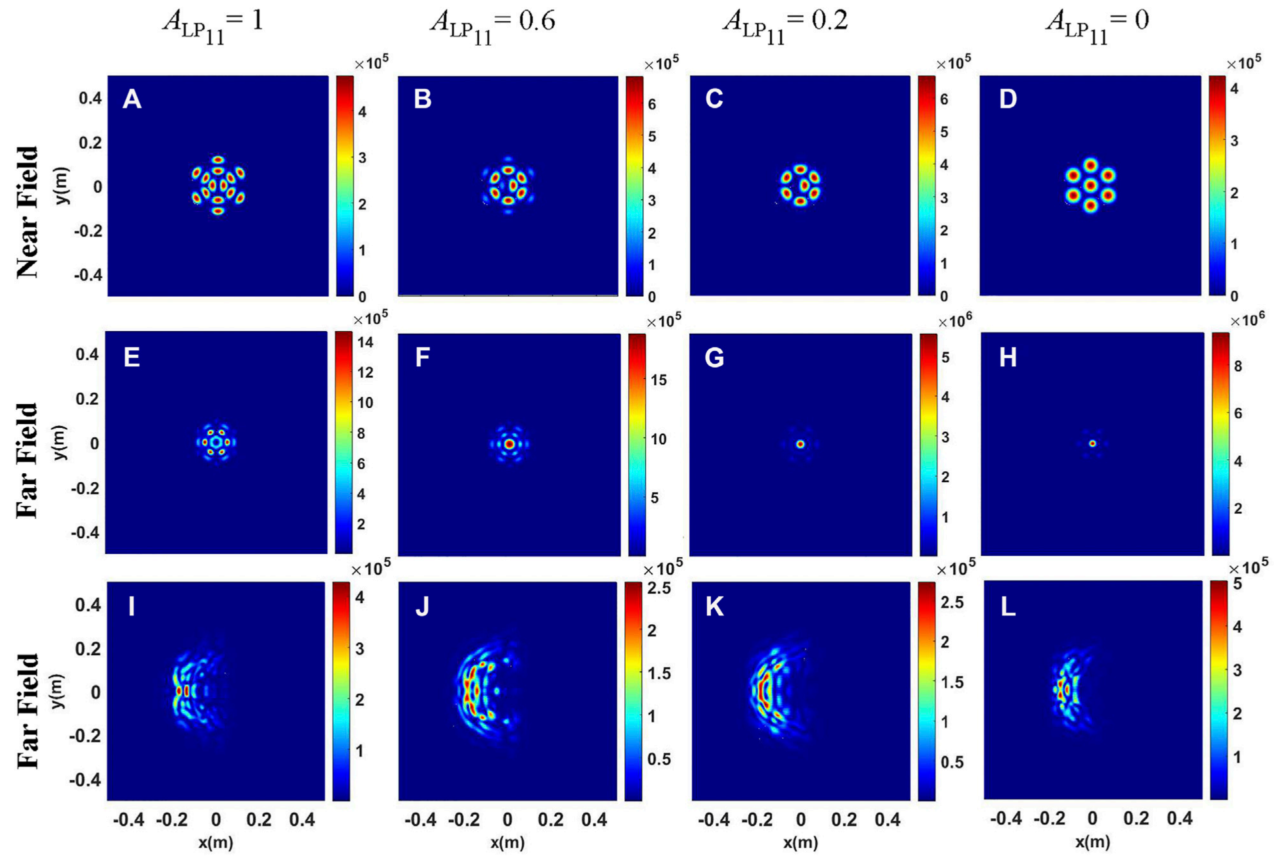

FIGURE 8 | Intensity distributions of the mixed-mode beam array for different content of the LP_{01} mode. **(A–D)** Intensity distributions at the initial plane; **(E–H)** Intensity distributions at the receiver plane in free space; **(I–L)** Intensity distributions at the receiver plane under the conditions of thermal blooming.

Impact of Fundamental Mode Content on the HOM Beam Array

In practical applications, it is difficult to obtain the pure LP_{01} mode even at relatively high conversion efficiency. Therefore, the case of the mixture of LP_{01} and LP_{11} modes is worth studying. Considering that the model superposition states comprise different admixtures of the LP_{01} and LP_{11} modes, the initial field can be expressed as

$$E_{\text{mix}} = \sum_{l=1}^{N}\left\{\sqrt{A_{LP_{11}}}\,E_{11}^{l}\left[r^2 + r_0^2 + 2rr_0\cos\left(\phi-\phi_l\right)\right] + \sqrt{1-A_{LP_{11}}}\,E_{01}^{l}\left[r^2 + r_0^2 + 2rr_0\cos\left(\phi-\phi_l\right)\right]\right\}, \tag{10}$$

where $A_{LP_{11}}$ is the power fraction of the LP_{11} mode and the value of $A_{LP_{11}}$ is $0 \le A_{LP_{11}} \le 1$.

The intensity distributions of the mixed-mode beam array are shown in **Figures 7–9**. It can be seen from **Figures 7–9** that in free space, as the content of the LP_{01} mode increases, the energy is gradually concentrated from the side lobes to the center lobe. That is to say, the energy distribution between the central lobe and side lobes can be controlled by changing the content of the LP_{01} mode. The difference in **Figures 7–9** is that the initial arrangement of the outer-ring beamlets is different. As can be seen from **Figure 7**, the focal beam shape of the pure LP_{11} mode beam array comprises six radial spots, and the energy is concentrated in the central lobe for the pure LP_{01} mode beam array.

As we rotate the outer-ring beamlets 180 degrees on the basis of **Figure 7**, the intensity distributions of the mixed mode beam array under different conditions are shown in **Figure 8**. It can be clearly seen that when the mixed-mode beam array propagates in free space, the energy of the central lobe in **Figure 8** is more concentrated than that in **Figure 7**. The physical reason is that the beam distribution at the initial plane is more compact in **Figure 8**. However, the intensity distributions under thermal blooming in **Figure 8** are more dispersive than those in **Figure 7**. Thus, the arrangements of beamlets at the initial plane in **Figure 7** are more resistant to the degrading effect of thermal blooming.

As we rotate the outer-ring beamlets 90 degrees on the basis of **Figure 8**, the intensity distributions of the mixed-mode beam array under different conditions are shown in **Figure 9**. As mentioned previously, the focal intensity distribution comprises 12 radial spots when the initial intensity distribution is shown in **Figure 9A**. However, the number of side lobes decreases as the content of the LP_{01} mode increases, that is, the side lobes are six when the content of

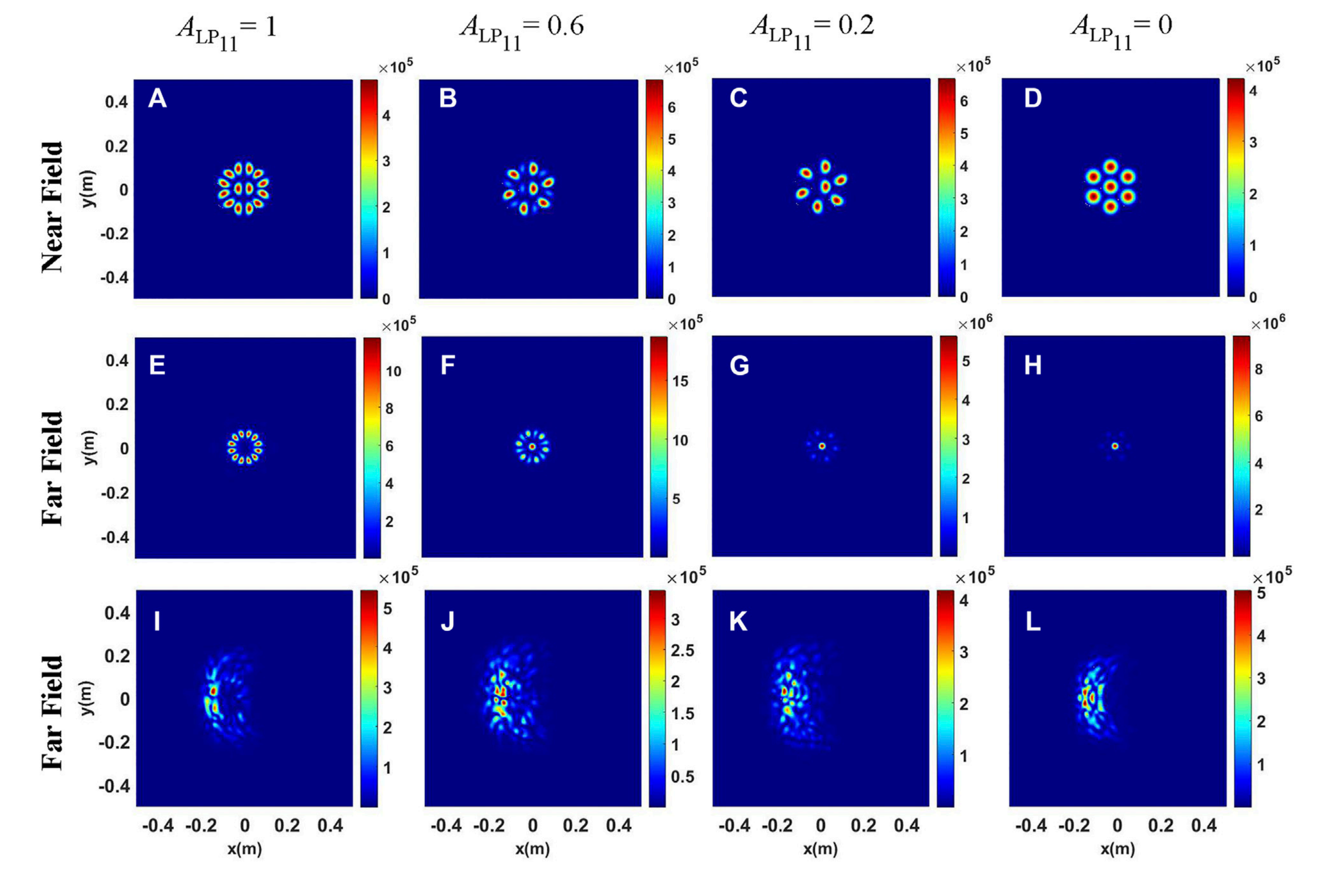

FIGURE 9 | Intensity distributions of the mixed-mode beam array for different content of the LP_{01} mode. **(A–D)** Intensity distributions at the initial plane; **(E–H)** Intensity distributions at the receiver plane in free space; **(I–L)** Intensity distributions at the receiver plane under the conditions of thermal blooming.

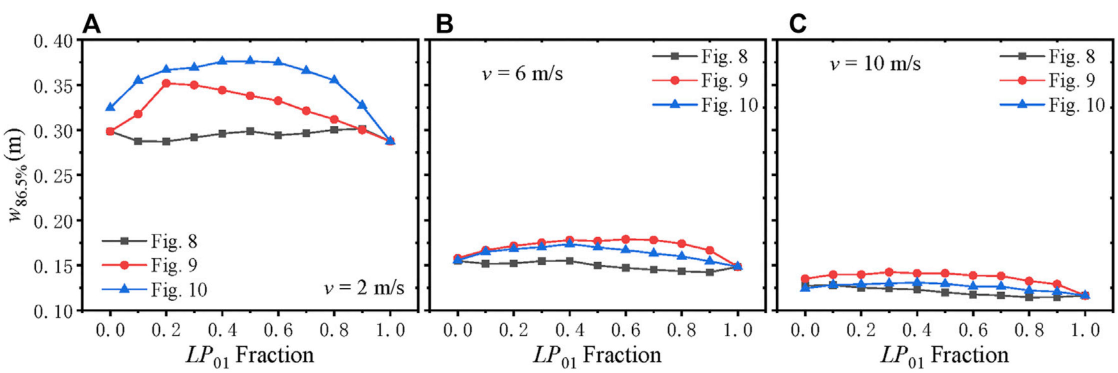

FIGURE 10 | Variation of beam width $w_{86.5\%}$ with LP_{01} fraction for different values of wind speeds.

the LP_{01} mode is 0.6. In order to compare the energy focusability under the three conditions more intuitively, the beam width $w_{86.5\%}$ versus the LP_{01} fraction for different initial beamlet arrangements is investigated in **Figure 10**. It can be seen from **Figures 10A–C** that the beam width decreases as the wind speed increases. Thus, increasing the value of wind speed can be helpful in increasing energy focusability. On the other hand, the beam width in **Figure 8** is the smallest under the same wind speed. Thus, the initial beamlet arrangements in **Figure 8** can also be helpful in increasing energy focusability. In addition, the beam width in **Figure 9** is smaller than that in **Figure 10** when the wind speed is small. However, when the wind speed increases, the beam width in **Figure 9** is larger than that in **Figure 10**. It indicates that compared with **Figure 9**, the effect of wind speed has a greater impact on the focusability of **Figure 10**.

CONCLUSION

In this study, the propagation properties of high-power HOM beam arrays propagating in the atmosphere are studied in detail. Based on the multiphase screen method and finite-difference method, a 4D computer code of the HOM beam array propagating through the atmosphere under the conditions of thermal blooming is designed. In particular, the LP_{11} mode is considered in this study. The propagation characteristics of the pure LP_{11} mode beam array in free space and in the atmosphere are investigated. It has been found that the focal intensity distributions in free space are consistent with the arrangement of the second circle of the initial beam array. The desired beam shape of focusing spots can be obtained by rotating the surrounding beamlets. In addition, the arrangement of the central beamlet has little influence on the focal beam shapes in free space but has a significant effect on the focal beam shapes under the conditions of thermal blooming. Thus, the energy focusability can be improved by rotating the central beamlet. When the transverse wind speed increases, the thermal blooming effect decreases and the energy focusability increases. Moreover, the influence of the content of the LP_{01} mode is investigated in this study, and three kinds of arrangement of the initial beam array are considered. The results show that as the content of the LP_{01} mode increases, the energy is gradually concentrated from the side lobes to the center lobe. The energy ratio of the side lobes to the central lobe is related to the initial arrangement. Meanwhile, the energy distribution between the central lobe and side lobes can be controlled by changing the content of the LP_{01} mode. The condition for obtaining high energy focusability has been discussed in detail. These results obtained in this study are useful for directed-energy applications in the atmosphere.

DATA AVAILABILITY STATEMENT

The original contributions presented in the study are included in the article/Supplementary Material, further inquiries can be directed to the corresponding author.

AUTHOR CONTRIBUTIONS

All authors listed have made a substantial, direct, and intellectual contribution to the study and approved it for publication.

FUNDING

National Natural Science Foundation of China (61705265), and Natural Science Foundation of Hunan province, China (2019JJ10005).

REFERENCES

1. Dong L, Kong F, Gu G, Hawkins TW, Jones M, Parsons J, et al. Large-Mode-Area All-Solid Photonic Bandgap Fibers for the Mitigation of Optical Nonlinearities. *IEEE J Select Top Quan Electron.* (2016) 22(2):316–22. doi:10.1109/jstqe.2015.2451012
2. Wang L, He D, Yu C, Feng S, Hu L, Chen D. Very Large-Mode-Area, Symmetry-Reduced, Neodymium-Doped Silicate Glass All-Solid Large-Pitch Fiber. *IEEE J Select Top Quan Electron.* (2016) 22(2):108–12. doi:10.1109/jstqe.2015.2427746
3. Jeong Y, Sahu JK, Payne DN, Nilsson J. Ytterbium-doped Large-Core Fiber Laser with 1.36 kW Continuous-Wave Output Power. *Opt Express* (2004) 12(25):6088–92. doi:10.1364/opex.12.006088
4. Venkatakrishnan K, Tan B. Generation of Radially Polarized Beam for Laser Micromachining. *jlmn* (2012) 7(3):274–8. doi:10.2961/jlmn.2012.03.0008
5. Richardson DJ, Fini JM, Nelson LE. Space-division Multiplexing in Optical Fibres. *Nat Photon* (2013) 7(5):354–62. doi:10.1038/nphoton.2013.94
6. Meier M, Romano V, Feurer T. Material Processing with Pulsed Radially and Azimuthally Polarized Laser Radiation. *Appl Phys A* (2007) 86(3):329–34. doi:10.1007/s00339-006-3784-9
7. Liu Z, Wang L, Liang P, Zhang Y, Yang J, Yuan L. Mode Division Multiplexing Technology for Single-Fiber Optical Trapping Axial-Position Adjustment. *Opt Lett* (2013) 38(14):2617–20. doi:10.1364/ol.38.002617
8. Wang J. Advances in Communications Using Optical Vortices. *Photon Res* (2016) 4(5):B14–B28. doi:10.1364/prj.4.000b14
9. Ramachandran S, Kristensen P, Yan MF. Generation and Propagation of Radially Polarized Beams in Optical Fibers. *Opt Lett* (2009) 34(16):2525–7. doi:10.1364/OL.34.002525
10. Mao D, Li M, He Z, Cui X, Lu H, Zhang W, et al. Optical Vortex Fiber Laser Based on Modulation of Transverse Modes in Two Mode Fiber. *APL Photon* (2019) 4(6):060801. doi:10.1063/1.5094599
11. Lin D, Daniel JMO, Gecevičius M, Beresna M, Kazansky PG, Clarkson WA. Cladding-pumped Ytterbium-Doped Fiber Laser with Radially Polarized Output. *Opt Lett* (2014) 39(18):5359–61. doi:10.1364/OL.39.005359
12. Mao D, Zheng Y, Zeng C, Lu H, Wang C, Zhang H, et al. Generation of Polarization and Phase Singular Beams in Fibers and Fiber Lasers. *Adv Photon* (2021) 3(1):014002. doi:10.1117/1.Ap.3.1.014002
13. Lin D, Carpenter J, Feng Y, Jain S, Jung Y, Feng Y, et al. Reconfigurable Structured Light Generation in a Multicore Fibre Amplifier. *Nat Commun* (2020) 11(1):3986. doi:10.1038/s41467-020-17809-x
14. Liu T, Chen S, Qi X, Hou J. High-power Transverse-Mode-Switchable All-Fiber Picosecond MOPA. *Opt Express* (2016) 24(24):27821–7. doi:10.1364/oe.24.027821
15. Wang S, Zhang M, Wang H, Hu G. Single- and Dual-Wavelength Fiber Laser with Multi-Transverse Modes. *Opt Express* (2021) 29(13):20299–306. doi:10.1364/oe.430258
16. Li H, Zhang Y, Dong Z, Lv J, Gu C, Yao P, et al. A High-Efficiency All-Fiber Laser Operated in High-Order Mode Using Ring-Core Yb-Doped Fiber. *Annalen Der Physik* (2019) 531(10):1900079. doi:10.1002/andp.201900079
17. Lv J, Li H, Zhang Y, Tao R, Dong Z, Gu C, et al. Few-mode Random Fiber Laser with a Switchable Oscillating Spatial Mode. *Opt Express* (2020) 28(26):38973. doi:10.1364/oe.412234
18. Su R, Yang B, Xi X, Zhou P, Wang X, Ma Y, et al. 500 W Level MOPA Laser with Switchable Output Modes Based on Active Control. *Opt Express* (2017) 25(19):23275–81. doi:10.1364/oe.25.023275
19. Sun B, Wang A, Xu L, Gu C, Lin Z, Ming H, et al. Low-threshold Single-Wavelength All-Fiber Laser Generating Cylindrical Vector Beams Using a Few-Mode Fiber Bragg Grating. *Opt Lett* (2012) 37(4):464–6. doi:10.1364/OL.37.000464

20. Huang Y, Shi F, Wang T, Liu X, Zeng X, Pang F, et al. High-order Mode Yb-Doped Fiber Lasers Based on Mode-Selective Couplers. *Opt Express* (2018) 26(15):19171–81. doi:10.1364/oe.26.019171
21. Huang P, Cai Y, Wang J, Wan H, Zhang Z, Zhang L. Multiwavelength Mode-Locked Cylindrical Vector Beam Fiber Laser Based on Mode Selective Coupler. *Laser Phys Lett* (2017) 14(10):105103. doi:10.1088/1612-202X/aa82cd
22. You Y, Bai G, Zou X, Li X, Su M, Wang H, et al. A 1.4-kW Mode-Controllable Fiber Laser System. *J Lightwave Technol* (2021) 39(8):2536–41. doi:10.1109/jlt.2021.3049603
23. Zhou P, Liu Z, Wang X, Ma Y, Ma H, Xu X, et al. Coherent Beam Combining of Fiber Amplifiers Using Stochastic Parallel Gradient Descent Algorithm and its Application. *IEEE J Select Top Quan Electron.* (2009) 15(2):248–56. doi:10.1109/jstqe.2008.2010231
24. Fan TY. Laser Beam Combining for High-Power, High-Radiance Sources. *IEEE J Select Top Quan Electron.* (2005) 11(3):567–77. doi:10.1109/jstqe.2005.850241
25. Brignon A. *Coherent Laser Beam Combining*. Weinheim, Germany: Wiley VCH (2013).
26. Goodno GD, Asman CP, Anderegg J, Brosnan S, Cheung EC, Hammons D, et al. Brightness-scaling Potential of Actively Phase-Locked Solid-State Laser Arrays. *IEEE J Select Top Quan Electron.* (2007) 13(3):460–72. doi:10.1109/jstqe.2007.896618
27. Hou T, Zhang Y, Chang Q, Ma P, Su R, Wu J, et al. High-power Vortex Beam Generation Enabled by a Phased Beam Array Fed at the Nonfocal-Plane. *Opt Express* (2019) 27(4):4046–59. doi:10.1364/oe.27.004046
28. Yu CX, Augst SJ, Redmond SM, Goldizen KC, Murphy DV, Sanchez A, et al. Coherent Combining of a 4 kW, Eight-Element Fiber Amplifier Array. *Opt Lett* (2011) 36(14):2686–8. doi:10.1364/ol.36.002686
29. Ma P, Chang H, Ma Y, Su R, Qi Y, Wu J, et al. 7.1 kW Coherent Beam Combining System Based on a Seven-Channel Fiber Amplifier Array. *Opt Laser Technology* (2021) 140:107016. doi:10.1016/j.optlastec.2021.107016
30. Müller M, Aleshire C, Klenke A, Haddad E, Légaré F, Tünnermann A, et al. 104 kW Coherently Combined Ultrafast Fiber Laser. *Opt Lett* (2020) 45(11):3083–6. doi:10.1364/ol.392843
31. Shekel E, Vidne Y, Urbach B. 16kW Single Mode CW Laser with Dynamic Beam for Material Processing. In: Proc. SPIE. L Dong, editor. San Diego, CA: SPIE (2020). doi:10.1117/12.2545900
32. Fsaifes I, Daniault L, Bellanger S, Veinhard M, Bourderionnet J, Larat C, et al. Coherent Beam Combining of 61 Femtosecond Fiber Amplifiers. *Opt Express* (2020) 28(14):20152–61. doi:10.1364/oe.394031
33. Chang H, Chang Q, Xi J, Hou T, Su R, Ma P, et al. First Experimental Demonstration of Coherent Beam Combining of More Than 100 Beams. *Photon Res* (2020) 8(12):1943–8. doi:10.1364/PRJ.409788
34. Zhan Q. Cylindrical Vector Beams: from Mathematical Concepts to Applications. *Adv Opt Photon* (2009) 1(1):1–57. doi:10.1364/aop.1.000001
35. Hou T, An Y, Chang Q, Ma P, Li J, Huang L, et al. Deep-learning-assisted, Two-Stage Phase Control Method for High-Power Mode-Programmable Orbital Angular Momentum Beam Generation. *Photon Res* (2020) 8(5):715–22. doi:10.1364/prj.388551
36. Kurti RS, Halterman K, Shori RK, Wardlaw MJ. Discrete Cylindrical Vector Beam Generation from an Array of Optical Fibers. *Opt Express* (2009) 17(16):13982–8. doi:10.1364/oe.17.013982
37. Yu T, Xia H, Xie W, Xiao G, Li H. The Generation and Verification of Bessel-Gaussian Beam Based on Coherent Beam Combining. *Results Phys* (2020) 16:102872. doi:10.1016/j.rinp.2019.102872
38. Chu X, Liu Z, Zhou P. Generation of a High-Power Airy Beam by Coherent Combining Technology. *Laser Phys Lett* (2013) 10(12):125102. doi:10.1088/1612-2011/10/12/125102
39. Spencer MF. Wave-optics Investigation of Turbulence thermal Blooming Interaction: I. Using Steady-State Simulations. *Opt Eng* (2020) 59(8):1. doi:10.1117/1.Oe.59.8.081804
40. Gebhardt FG. High Power Laser Propagation. *Appl Opt* (1976) 15(6):1479–93. doi:10.1364/ao.15.001479
41. Schoen NC, Novoseller DE. Multiple Aperture Laser Systems for thermal Blooming Environments. *Appl Opt* (1983) 22(21):3366–70. doi:10.1364/AO.22.003366
42. Gebhardt FG. Twenty-five Years of thermal Blooming: an Overview. In: Proc. SPIE (1990). doi:10.1117/12.18326
43. Fleck JA, Morris JR, Feit MD. Time-dependent Propagation of High Energy Laser Beams through the Atmosphere. *Appl Phys* (1976) 10(2):129–60. doi:10.1007/BF00896333
44. Ji X, Eyyuboğlu HT, Ji G, Jia X. Propagation of an Airy Beam through the Atmosphere. *Opt Express* (2013) 21(2):2154–64. doi:10.1364/oe.21.002154
45. Vorob'ev VV, Murav'ev NI, Sorokin YM, Shemetov VV. Thermal Self-Interaction of Annular Laser Beams in a Moving Medium. *Sov J Quan Electron.* (1977) 7(11):1333–6. doi:10.1070/qe1977v007n11abeh004119
46. Ding Z, Li X, Cao J, Ji X. Influence of thermal Blooming on the Beam Quality of an Array of Hermite-Gaussian Beams Propagating in the Atmosphere. *Appl Opt* (2020) 59(34):10944–52. doi:10.1364/ao.405980
47. Zhao L, Wang J, Guo M, Xu X, Qian X, Zhu W, et al. Steady-state thermal Blooming Effect of Vortex Beam Propagation through the Atmosphere. *Opt Laser Technology* (2021) 139:106982. doi:10.1016/j.optlastec.2021.106982
48. Zhang Y, Hou T, Chang H, Su R, Ma P, Zhou P. Thermal Blooming Effect and the Scaling Laws of Partial Spatially Coherent Beam Array Propagating through the Atmosphere. *Results Phys* (2021) 26:104444. doi:10.1016/j.rinp.2021.104444
49. Spencer MF, Hyde MW. Phased Beam Projection from Tiled Apertures in the Presence of Turbulence and thermal Blooming. In Proc. SPIE (2013). doi:10.1117/12.2022666
50. Li X, Cao J, Ding Z, Ji X. Influence of Fill Factors on the thermal Blooming of Array Laser Beams in the Air. *Optik* (2019) 182:314–23. doi:10.1016/j.ijleo.2018.12.161
51. Banakh VA, Falits AV. Numerical Simulation of Propagation of Laser Beams Formed by Multielement Apertures in a Turbulent Atmosphere under thermal Blooming. *Atmos Ocean Opt* (2013) 26(6):455–65. doi:10.1134/S102485601306002X
52. Yoda H, Polynkin P, Mansuripur M. Beam Quality Factor of Higher Order Modes in a Step-index Fiber. *J Lightwave Technol* (2006) 24(3):1350–5. doi:10.1109/jlt.2005.863337
53. Snyder AW, Love JD. *Optical Waveguide Theory*. London, New York: Boston: Springer MA Press (1983).
54. Zhang Y, Ji X, Li X, Li Q, Yu H. Self-focusing Effect of Annular Beams Propagating in the Atmosphere. *Opt Express* (2017) 25(18):21329–41. doi:10.1364/oe.25.021329
55. Sean Ross T. *Laser Beam Quality Metrics*. Bellingham: SPIE Press (2013).

Conflict of Interest: The authors declare that the research was conducted in the absence of any commercial or financial relationships that could be construed as a potential conflict of interest.

Publisher's Note: All claims expressed in this article are solely those of the authors and do not necessarily represent those of their affiliated organizations, or those of the publisher, the editors, and the reviewers. Any product that may be evaluated in this article, or claim that may be made by its manufacturer, is not guaranteed or endorsed by the publisher.

frontiers | Frontiers in Physics

ORIGINAL RESEARCH
published: 20 May 2022
doi: 10.3389/fphy.2022.912196

Wavelength-Tunable Kerr-Lens Mode-Locked Femtosecond Cr:ZnS Laser With a ~300-nm Tuning Range From 2.2 to 2.5μm

Qing Wang[1,2,3], Runyu Wang[1,2,3], Fan Yang[1,2,3] and Yan Li[1,2,3]*

[1]School of Optics and Photonics, Beijing Institute of Technology, Beijing, China, [2]Key Laboratory of Photoelectronic Imaging Technology and System, Ministry of Education, Beijing, China, [3]Key Laboratory of Photonics Information Technology, Ministry of Industry and Information Technology, Beijing, China

Tunable 2~3-μm femtosecond lasers are of high interest in various applications, such as medical diagnostics and molecular spectroscopy. Cr:ZnSe/ZnS is extremely suited for broadband tunable femtosecond lasers due to its excellent emission bands. In this article, we demonstrate a wavelength-tunable Kerr-lens mode-locked Cr:ZnS laser by utilizing a birefringent filter. The group delay dispersion of the operation and the thickness of the birefringent are finely optimized. With the rotation of the birefringent filter, the scheme offers a tuning bandwidth of over 300 nm from 2,220 nm to 2,520 nm. To the best of our knowledge, it is the broadest tuning range among the reported femtosecond Cr:ZnS lasers.

Keywords: Kerr-lens mode-locking, mid-infrared, femtosecond laser, tunability, Cr:ZnS

OPEN ACCESS

Edited by:
Xing Fu,
Tsinghua University, China

Reviewed by:
Ümit Demirbaş,
Antalya Bilim University, Turkey
Wenlong Tian,
Xidian University, China

****Correspondence:***
Qing Wang
qingwang@bit.edu.cn

Specialty section:
This article was submitted to Optics and Photonics, a section of the journal Frontiers in Physics

Received: *04 April 2022*
Accepted: *19 April 2022*
Published: *20 May 2022*

Citation:
Wang Q, Wang R, Yang F and Li Y (2022) Wavelength-Tunable Kerr-Lens Mode-Locked Femtosecond Cr:ZnS Laser With a ~300-nm Tuning Range From 2.2 to 2.5 μm. Front. Phys. 10:912196. doi: 10.3389/fphy.2022.912196

INTRODUCTION

Broadband mid-infrared (MIR) laser sources are in great demand for a plethora of applications, including biological identification, medical diagnostics, and molecular spectroscopy, due to the presence of strong fundamental and overtone vibrational absorption lines of different gases [1, 2]. To be more specific, the range between 2 and 3 μm covers the absorption lines of NH_2, CO, CO_2, and water related to typical biological tissue absorption [3]. Femtosecond laser sources covering 2–3 μm could be used for time-resolved spectroscopy of such molecules [4]. Besides, such sources can be also used for remote sensing and driving various nonlinear processes, such as MIR supercontinuum generation [5] and high-harmonic generation [6]. Compared to untunable broadband MIR sources, wavelength-tunable femtosecond lasers are more attractive due to the better matching of their wavelength range with detected molecules or various nonlinear processes.

Cr:ZnSe/ZnS is an ideal material for generating tunable femtosecond mode-locked lasers in 2–3 μm. Cr:ZnSe/ZnS with ultrabroad emission bands provides the accessibility of broadband femtosecond lasers and a large range of tunability. The broad absorption bands of the gain media cover some sufficient and reliable pump sources, such as commercial fiber lasers or laser diodes. Furthermore, Cr:ZnSe/ZnS provides no excited state absorption, provides room temperature operation, and is close to a four-level energy structure. Hence, with their favorable physical characteristics, these materials have been considered as "Ti:sapphire" in the MIR [7].

Femtosecond oscillators are commonly achieved by Kerr-lens passively mode-locked schemes or saturable absorber passively mode-locked schemes based on semiconductors or graphenes [8–11]. The first mode-locked Cr:ZnSe/ZnS laser was based on a semiconductor saturable absorber

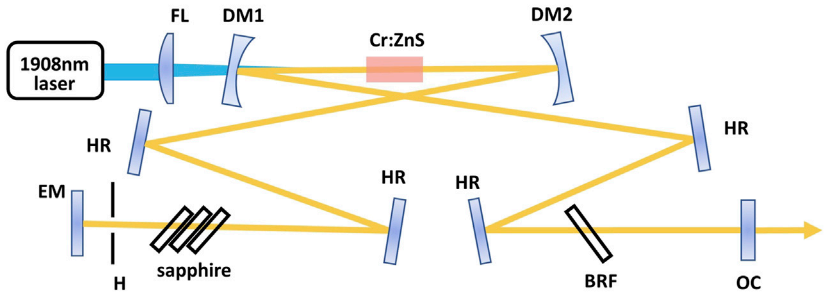

FIGURE 1 | Kerr-lens mode-locked Cr:ZnS oscillator. FL, focusing lens (*f* = 100 mm); DM, curved dichroic mirror (ROC = 100 mm); EM, end mirror (the same as HR, high reflection, at 2,150–2,700 nm); OC, output coupler, *T* = 10% at 1,700–2,700 nm; H, hard aperture; BRF, birefringent filter.

mirror (SESAM) reported in 2005 [12]. Several advantages, such as enabling self-starting and low-noises, offered by SESAM mode-locking schemes are appealing. However, the bandwidth of the SESAM restricts the realization of few-cycle pulses and the range of tunability. Compared to saturable absorber passive mode-locking, Kerr-lens mode-locked oscillators break through these restrictions and become more attractive to fulfill broadband femtosecond lasers with a large tunable bandwidth.

Cr:ZnSe/ZnS has been demonstrated as an excellent material for tunable continuous wave laser, which could be tuned from 1880 to 3,350 nm [13, 14]. Meanwhile, some tunable femtosecond oscillators based on Cr:ZnSe/ZnS are reported, in which a birefringent filter (BRF) or a pair of prisms is used [15–17]. Although the first tunable femtosecond Cr:ZnSe laser is achieved by adjusting a slit working with a prism pair [16], the space chirp induced by the prism pair has a severe negative influence on beam quality. In Ref. [17], the tunable range is expended to 180 nm achieved by the BRF. Until now, the broadest tunable range in femtosecond Cr:ZnSe/ZnS laser has been from 2,120 nm to 2,408 nm [15]. All these works only offer pulses with the wavelength below 2,400 nm and tunable bandwidth below 300 nm.

In this letter, a widely tunable femtosecond Cr:ZnS oscillator is reported. The KML Cr:ZnS laser operating at 2347 nm allows the generation of stable126-fs pulses with an average output power of 344 mW at a repetition rate of 72.6 MHz. A BRF offers less loss, a broadband tunable range, and better beam quality. By utilizing a 0.5-mm-thick BRF with a broad free spectral range, we achieved more than 300 nm tuning bandwidth from 2,220 to 2,520 nm. Large negative dispersion compensation was set for ideal soliton mode-locking operation and a broad tunable bandwidth. To the best of our knowledge, it is the broadest tuning range in femtosecond Cr:ZnSe/ZnS oscillators and fills the gap in the long-wave range beyond 2,400 nm. This tunable wavelength range not only contains the absorption lines of NH_2 and CO (below 2,400 nm) but also contains the absorption lines of HF and COS (beyond 2,400 nm) [18]. This work has unique potential applications in molecular spectroscopy and nonlinear processes.

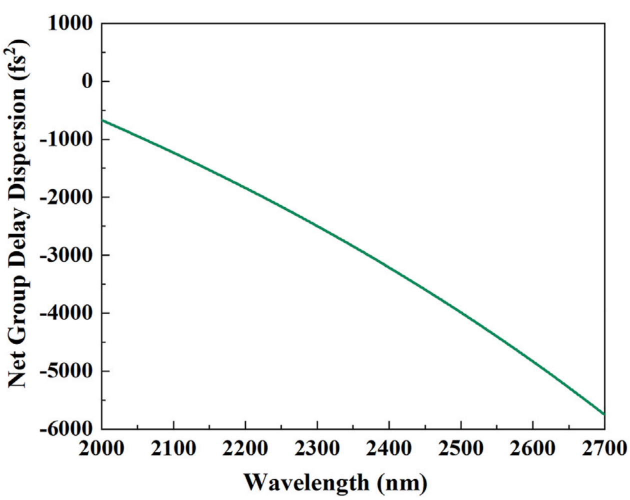

FIGURE 2 | Round-trip net group delay dispersion curve in Kerr-lens mode-locked Cr:ZnS laser.

EXPERIMENTAL SETUP

The experimental setup is depicted in **Figure 1**. The 2 × 2 × 9-mm^3 polycrystalline Cr:ZnS was used as the gain medium of the oscillator, which is AR-coated at both 1908 nm and 2,100–2,600 nm, with 10% low-signal transmission ratios at a wavelength of 1908 nm. The gain element is mounted in a copper heat sink, and its temperature is maintained by thermal electric coolers (TECs) to 20°C. A 1908-nm linear polarized Tm-doped fiber laser system with an output power of 5.4 W is used to pump the Cr:ZnS. The Cr:ZnS is placed in the middle of the first stability zone of an X-folded cavity. The two dichroic mirrors (DMs) are coated with high reflection over 2.1–2.7 μm and high transmission around 1.91 μm with a radius of curvature (ROC) of −100 mm. All the plane mirrors are high reflection coated from 2,100 to 2,700 nm. The output coupler (OC) is a plane mirror based on 6-mm-thick fused-silica (IR) with a transmission of 10% from 1700 to 2,700 nm. A hard aperture arranged close to the end mirror was used to stabilize Kerr-lens mode-locking operation. The whole cavity

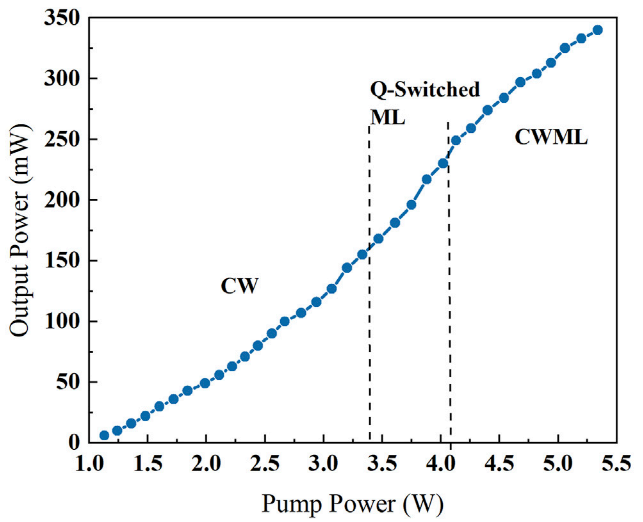

FIGURE 3 | Measured output power and operation mode versus incident pump power at 2,347 nm center wavelength. CW, continuous wave; Q-switched ML, Q-switched mode-locking; CWML, continuous wave mode-locking.

length is 2066 mm, corresponding to a pulse repetition rate of 72.6 MHz.

In order to optimize the group delay dispersion (GDD) in the cavity, three 5-mm-thick sapphires were placed near the end of the short arm at Brewster's angle (59.95°), providing $-4{,}250\ fs^2$ negative GDD at 2,400 nm. The 9-mm-thick Cr:ZnS leads to $1{,}080\ fs^2$ positive GDD at 2,400 nm. The round-trip net GDD curve of the asymmetric cavity shown in **Figure 2** indicates that the anomalous dispersion condition is provided from 2,000 to 2,700 nm. A MgF_2 BRF inserted in the cavity at Brewster's angle (53.77°) allowed a tunable output center wavelength from 2,220 nm to 2,520 nm under anomalous dispersion conditions in the soliton KLM regime. The thickness of the BRF was selected as 0.5 mm, corresponding to the transmission range (FWHM, full width at half maximum) of 740 nm for a central wavelength of 2.4 μm.

RESULTS AND DISCUSSION

The resonator was at first adjusted for maximizing the CW output power. Then fine alignment of the position of DM2 and the EM is needed to realize Kerr-lens mode-locking operation, which was initiated by shaking the EM. The operation mode of the oscillator varied with pump power. It is under CW operation at low pump power (3 W), transferred to Q-switched ML when further increasing pump power, and converted to continuous wave mode-locking (CWML) with sufficient pump power (over 4.26 W). The output power versus incident pump power under varied operations is shown in **Figure 3** when the center wavelength is at 2,347 nm.

The laser routinely produced pulses of 126 fs, whose center wavelength is 2,347 nm, at the highest pump power of 5.4 W. The average output power is 344 mW, corresponding to a pulse energy of 4.7 nJ with a peak power of 38 kW. The optical spectrum is measured by an APE waveScan spectrometer. As shown in **Figure 4A**, the sidebands distributed at both sides of the center wavelength are called Kelly sidebands. Kelly sidebands are often observed at soliton mode-locked schemes with large abnormal dispersion. The sidebands are induced by dispersion and nonlinearities when pulses produce energy beyond the restriction of soliton area [19, 20]. The center wavelength of the left sideband is at around 2,236 nm, and the right one is at around 2,459 nm with a similar

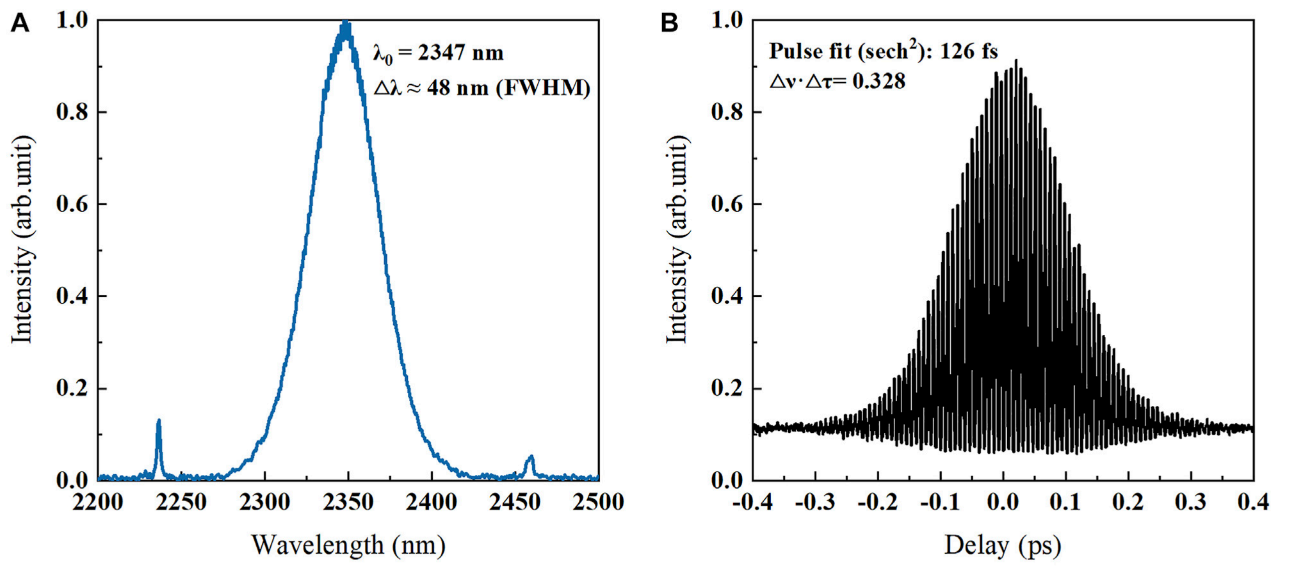

FIGURE 4 | Measured spectrum and autocorrelation trace at 2,347 nm center wavelength. **(A)** Optical spectrum. **(B)** Interferometric autocorrelation trace.

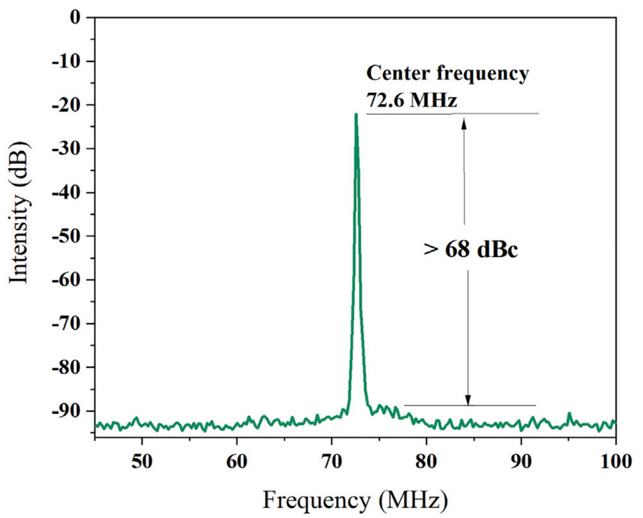

FIGURE 5 | Radio frequency spectrum of the mode-locked pulses at 2,347 nm center wavelength.

frequency shift. As shown in **Figure 4B**, the interferometric autocorrelation trace is measured with an APE. pulseCheck. By assuming a sech^2-pulse shape, a spectral bandwidth of 48 nm (FWHM) and a pulse duration of 126 fs demonstrated a time-bandwidth product of 0.328, near the Fourier transform limitation of 0.315. **Figure 5** shows the radio frequency spectrum of the fundamental frequency at 72.6 MHz, measured by a frequency spectrum analyzer with a resolution bandwidth of 1 kHz. The mode-locking stability is confirmed by the clear single peak with a high extinction down to 68 dBc without any side lobes at fundamental cavity repetition.

By rotation of the 0.5-mm-thick MgF_2 BRF, the central wavelength of the mode-locked Cr:ZnS laser at a pump power of 5.4 W shifts from 2,220 nm to 2,520 nm, as shown in **Figure 6A**. The tuning range is over 300 nm, and to the best of our knowledge, it is the broadest one in Cr:ZnS/ZnSe mode-locked lasers ever reported. In a similar situation, the CW laser could be tuned from 2,155 nm to 2,623 nm by rotating the BRF, equal to a 500 nm tuning range. The tuning limit of the short wavelength is affected by HR, whose high reflection range is from 2,150 nm to 2,700 nm. At the central wavelength below 2,220 nm, the stable pulses are not accessible. Besides, the experimental setup was operating in the air, so the long-wave tuning range was restricted by absorption lines of vapor (**Figure 6A** with dash lines). The output power of the CW laser reduced sharply, induced by strong absorption of vapor

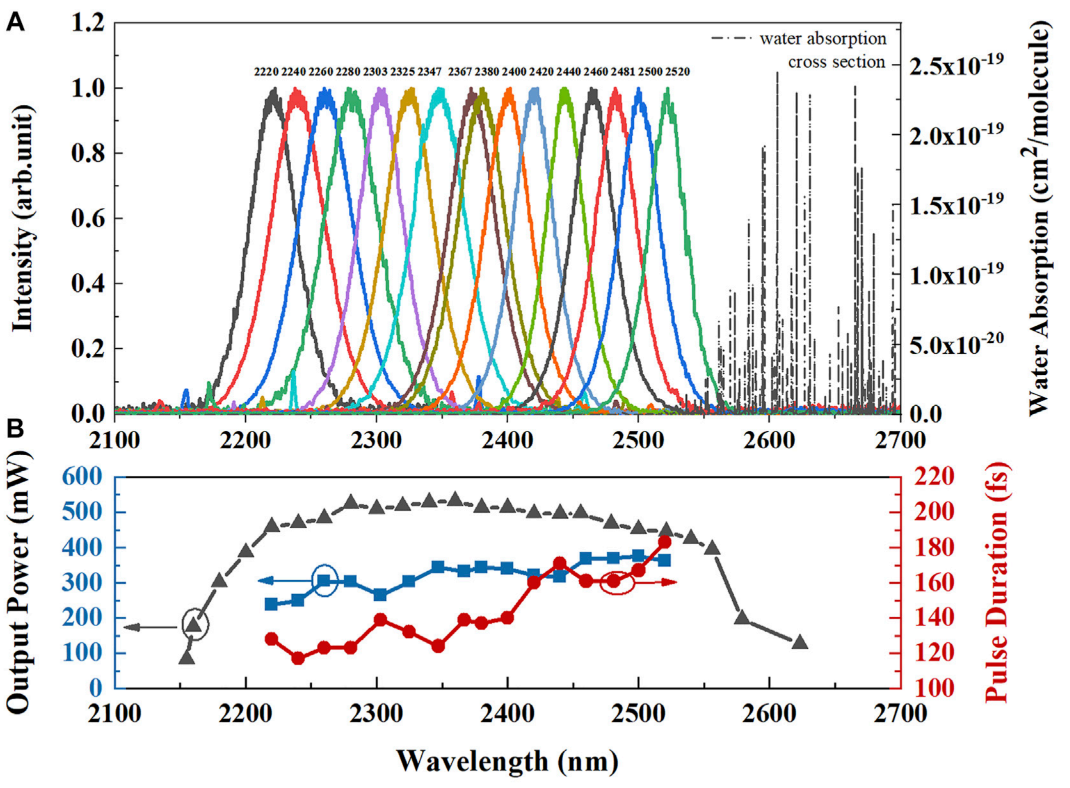

FIGURE 6 | Measured details with the tuning of the central wavelength of KLM laser. **(A)** Various mode-locked optical spectrums at different tuning wavelengths (solid lines) and water absorption lines (dash lines). **(B)** CW output power (gray triangle), CWML output power (blue square), and pulse duration (red circle) versus central wavelength.

(depicted in **Figure 6B** with a gray line). In our experiment, some absorption peaks also appeared at the spectrum curve of 2,520 nm in CWML operation, and mode-locked pulses disappeared when further rotating the BRF to a longer wavelength. Therefore, the tuning range can be expanded if we use mirrors with a broader coating range or operate the scheme in vacuum to avoid strong absorption of vapor.

The various average output powers of CWML operation and duration times of pulses are depicted in **Figure 6B** with blue and red lines. The widening duration of the pulse is attributed to the increasing abnormal dispersion at a long wavelength range (**Figure 2**).

CONCLUSION

In conclusion, we demonstrated a high-performance broadly tunable femtosecond KML Cr:ZnS laser over a 300-nm tuning range. We use three 5-mm-thick sapphires to adjust the GDD of the resonator to realize stable soliton mode-locking in a wide spectral range. Kerr-lens mode-locked operation without the extra restriction of bandwidth allows a short pulse duration (126 fs, 2,347 nm) and a wide tuning range from 2,220 nm to 2,520 nm. We believe a broader tuning range could be achieved in a vapor-free atmosphere. To the best of our knowledge, this operation offered the widest tunable bandwidth among the reported femtosecond Cr:ZnSe/ZnS lasers. It is the first time that the tunable central wavelength is extended beyond 2.5 μm. This wavelength-tunable femtosecond laser source may provide potential applications in time-resolved molecular spectroscopy and MIR generation.

DATA AVAILABILITY STATEMENT

The original contributions presented in the study are included in the article/Supplementary Material, further inquiries can be directed to the corresponding author.

AUTHOR CONTRIBUTIONS

QW designed and supervised the research project. RW contributed to the specific experiment and the first draft of the manuscript. FY and YL measured the experimental data. All authors contributed to manuscript revision and approved the submitted version.

FUNDING

This work was supported by the Beijing Natural Science Foundation (No. 4222074).

REFERENCES

1. Fried NM. Recent Advances in Infrared Laser Lithotripsy [Invited]. *Biomed. Opt. Express* (2018) 9:4552. doi:10.1364/BOE.9.004552
2. Scholle K, Lamrini S, Koopmann P, Fuhrberg P. 2 Mm Laser Sources and Their Possible Applications. In: *Frontiers in Guided Wave Optics and Optoelectronics*. London: IntechOpen (2010). doi:10.5772/39538
3. Sorokina IT. Broadband Mid-infrared Solid-State Lasers. In: M Ebrahim-Zadeh IT Sorokina, editors. *Mid-Infrared Coherent Sources and Applications* (2008). p. 225–60. doi:10.1007/978-1-4020-6463-0_7
4. Pupeza I, Huber M, Trubetskov M, Schweinberger W, Hussain SA, Hofer C, et al.Field-resolved Infrared Spectroscopy of Biological Systems. *Nature* (2020) 577:52–9. doi:10.1038/s41586-019-1850-7
5. Grassani D, Tagkoudi E, Guo H, Herkommer C, Yang F, Kippenberg TJ, et al.Mid Infrared Gas Spectroscopy Using Efficient Fiber Laser Driven Photonic Chip-Based Supercontinuum. *Nat Commun* (2019) 10:1553. doi:10.1038/s41467-019-09590-3
6. Leshchenko VE, Talbert BK, Lai YH, Li S, Tang Y, Hageman SJ, et al.High-power Few-Cycle Cr:ZnSe Mid-infrared Source for Attosecond Soft X-Ray Physics. *OPTICA* (2020) 7:981–8. doi:10.1364/OPTICA.393377
7. Sorokin E, Naumov S, Sorokina IT. Ultrabroadband Infrared Solid-State Lasers. *IEEE J. Sel. Top Quantum Electron.* (2005) 11:690–712. doi:10.1109/JSTQE.2003.850255
8. Nagl N, Grobmeyer S, Potzlberger M, Pervak V, Krausz F, Mak KF (2020). Directly Diode-Pumped Few-Optical-Cycle Cr:ZnS Laser at 800 mW of Average Power. In: *Conference on Lasers and Electro-Optics OSA Technical Digest*. Washington, DC: OSA. doi:10.1364/CLEO_SI.2020.SF3H.5
9. Wang Y, Fernandez TT, Coluccelli N, Gambetta A, Laporta P, Galzerano G. 47-fs Kerr-Lens Mode-Locked Cr:ZnSe Laser with High Spectral Purity. *Opt. Express* (2017) 25:25193. doi:10.1364/OE.25.025193
10. Cizmeciyan MN, Kim JW, Bae S, Hong BH, Rotermund F, Sennaroglu A. Graphene Mode-Locked Femtosecond Cr:ZnSe Laser at 2500 Nm. *Opt. Lett.* (2013) 38:341. doi:10.1364/ol.38.000341
11. Barh A, Heidrich J, Alaydin BO, Gaulke M, Golling M, Phillips CR, et al.Watt-level and Sub-100-fs Self-Starting Mode-Locked 24-μm Cr:ZnS Oscillator Enabled by GaSb-SESAMs. *Opt. Express* (2021) 29:5934. doi:10.1364/oe.416894
12. Pollock CR, Brilliant NA, Gwin D, Carrig TJ, Alford WJ, Heroux JB, et al.Mode Locked and Q-Switched Cr:ZnSe Laser Using a Semiconductor Saturable Absorbing Mirror (SESAM). In: *Advanced Solid-State Photonics*. Washington, D.C: OSA. TuA6. doi:10.1364/ASSP.2005.TuA6
13. Demirbas U, Sennaroglu A. Intracavity-pumped Cr2+:ZnSe Laser with Ultrabroad Tuning Range between 1880 and 3100 Nm. *Opt. Lett.* (2006) 31:2293. doi:10.1364/OL.31.002293
14. Sorokin E, Sorokina IT, Mirov MS, Fedorov VV, Moskalev IS, Mirov SB. Ultrabroad Continuous-Wave Tuning of Ceramic Cr:ZnSe and Cr:ZnS Lasers. In: *Lasers, Sources and Related Photonic Devices*. (Washington, D.C: OSA) (2010). doi:10.1364/ASSP.2010.AMC2
15. Cho WB, Choi SY, Zhu C, Kim MH, Kim JW, Kim JS, et al.Graphene Mode-Locked Femtosecond Cr2+:ZnS Laser with ~300 Nm Tuning Range. *Opt. Express* (2016) 24:20774. doi:10.1364/oe.24.020774
16. Ma J, Xie G, Lv P, Gao W, Yuan P, Qian L, et al.Wavelength-Versatile Graphene-Gold Film Saturable Absorber Mirror for Ultra-broadband Mode-Locking of Bulk Lasers. *Sci Rep* (2014) 4. doi:10.1038/srep05016
17. Mirov SB, Fedorov VV, Martyshkin D, Moskalev IS, Mirov M, Vasilyev S. Progress in Mid-IR Lasers Based on Cr and Fe-Doped II-VI Chalcogenides. *IEEE J. Sel. Top Quantum Electron.* (2015) 21:292–310. doi:10.1109/JSTQE.2014.2346512
18. Sorokina IT, Sorokin E. Femtosecond Cr2+-Based Lasers. *IEEE J. Sel. Top Quantum Electron.* (2015) 21:273–91. doi:10.1109/JSTQE.2014.2341589

19. Smith NJ, Blow KJ, Andonovic I. Sideband Generation through Perturbations to the Average Soliton Model. *J. Light Technol.* (1992) 10:1329–33. doi:10.1109/50.166771
20. Kelly SMJ. Characteristic Sideband Instability of Periodically Amplified Average Soliton. *Electron. Lett.* (1992) 28:806–7. doi:10.1049/el:19920508

Conflict of Interest: The authors declare that the research was conducted in the absence of any commercial or financial relationships that could be construed as a potential conflict of interest.

Publisher's Note: All claims expressed in this article are solely those of the authors and do not necessarily represent those of their affiliated organizations, or those of the publisher, the editors, and the reviewers. Any product that may be evaluated in this article, or claim that may be made by its manufacturer, is not guaranteed or endorsed by the publisher.

frontiers | Frontiers in Physics

ORIGINAL RESEARCH
published: 16 June 2022
doi: 10.3389/fphy.2022.922651

Check for updates

Hybrid Nd:YAG/Nd:LuAG Nanosecond Laser Oscillator and Amplifier

Xinxing Lei [1,2], *Xing Fu* [1,2]* and *Qiang Liu* [1,2]*

[1] Key Laboratory of Photonic Control Technology (Tsinghua University), Ministry of Education, Beijing, China, [2] State Key Laboratory of Precision Measurement Technology and Instruments, Department of Precision Instrument, Tsinghua University, Beijing, China

We demonstrate an active mirror Q-switched laser with Nd:YAG/Nd:LuAG hybrid gain media, achieving a laser output of 1 J, 10 Hz, 8 ns. Using this hybrid oscillator as well as Nd:YAG and Nd:LuAG amplifiers, the difference in extraction efficiency of hybrid amplification was measured and analyzed, which is useful for high-energy hybrid amplification chains.

Keywords: hybrid gain medium, nanosecond laser, active mirror, Nd:LuAG, spectral mismatch

OPEN ACCESS

Edited by:
Ivan Divliansky,
University of Central Florida, United States

Reviewed by:
Kang Zhijun,
Aerospace Information Research Institute (CAS), China
Qi Wang,
China South Industrial Academy, China

***Correspondence:**
Xing Fu
fuxing@tsinghua.edu.cn
Qiang Liu
qiangliu@tsinghua.edu.cn

Specialty section:
This article was submitted to Optics and Photonics, a section of the journal Frontiers in Physics

Received: *18 April 2022*
Accepted: *09 May 2022*
Published: *16 June 2022*

Citation:
Lei X, Fu X and Liu Q (2022) Hybrid Nd:YAG/Nd:LuAG Nanosecond Laser Oscillator and Amplifier. Front. Phys. 10:922651. doi: 10.3389/fphy.2022.922651

INTRODUCTION

The high-energy diode-pumped nanosecond laser is gaining attention because of its excellent performance. In a face-cooled multi-slab configuration based on cryogenic gas-cooled Yb:YAG disks, the DiPOLE100 system has first obtained an output energy of 105 J at 10 Hz [1]. Recently, the output level was raised to 150 J at 10 Hz [2]. Another efficient laser configuration is the active mirror (AM) because of its round-trip extraction structure. In 2013, Lucia achieved 14 J at 2 Hz laser output using a Yb:YAG AM [3]. In 2021, a 9.3 J, 33 Hz output was achieved using the Yb: YAG cryogenically-cooled active-mirror amplifier [4]. Our group obtained room-temperature 10 J level at 10 Hz using Nd:YAG and Nd:LuAG AMs [5, 6]. High-energy AM oscillator configuration has also been studied [7, 8], but few results have been reported for the Q-switched laser.

For laser systems operating at room temperature, one of the most commonly used gain media is Nd:YAG, but its relatively low saturation fluence limits its scaling performance to high energy level. Nd:LuAG has recently been demonstrated with excellent scaling performance [6, 9], as its saturation fluence of 1.93 J/cm^2 is three times that of Nd:YAG [10]. Therefore, a hybrid amplification chain which uses Nd:YAG at low fluence and Nd:LuAG at high fluence is an effective method for high-energy lasers. However, the fluorescence spectrum of Nd:LuAG has a small red shift compared to Nd:YAG, so it is necessary to investigate the gain characteristics in detail in the case of spectral mismatch.

THEORY

When the injected laser is not the center frequency of the gain, the ratio of the emission cross-section of the laser frequency and the center frequency needs to be known in order to perform the calculation of the output energy. The ratio is expressed as follows:

$$k(\nu) = \frac{\sigma_{21}(\nu)}{\sigma_{21}(\nu_0)} \tag{1}$$

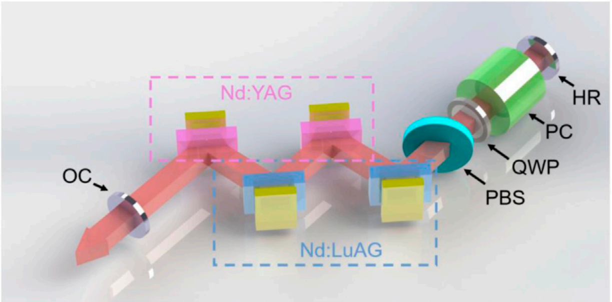

FIGURE 1 | Schematic diagram of the Nd:YAG/Nd:LuAG hybrid Q-switched laser oscillator. OC, output coupler; HR, high reflective mirror; PBS, polarizing beam splitter; PC, Pockels cell; QWP, quarter-wave plate.

Then the saturation fluence can be expressed as follows:

$$E_s(\nu) = \frac{h\nu}{\gamma\sigma_{21}(\nu)} \approx \frac{h\nu_0}{\gamma\sigma_{21}(\nu)} = \frac{E_s(\nu_0)}{k(\nu)} \tag{2}$$

where $E_s(\nu_0)$ is the saturation fluence of the center frequency of gain medium; $h\nu$ is the photon energy; γ is the degeneration factor. The output energy can be calculated from the Frantz–Nodvik equation (11):

$$G(\nu) = \frac{E_s(\nu_0)}{E_{in}k(\nu)} \ln\left\{1 + \left[exp\left(\frac{E_{in}}{E_s(\nu_0)}k(\nu)\right) - 1\right] exp\left(\frac{E_{sto}}{E_s(\nu_0)}k(\nu)l\right)\right\} \tag{3}$$

where E_{in} is the injected energy fluence, E_{sto} is the energy storage per unit volume, and l is the path length of the laser in the gain medium. According to **Eq. 3**, it is known that the enhancing the energy storage of the gain medium leads to higher energy loss due to the spectral mismatch. In this case, increasing the injected energy fluence E_{in} to obtain a high extraction efficiency is an effective way to reduce the loss; thus, the active mirror configuration with round-trip energy extraction has an advantage over the single pass straight-through configuration.

EXPERIMENTAL SETUP

The schematic diagram of the hybrid Nd:YAG/Nd:LuAG Q-switched laser oscillator is shown in **Figure 1**. The gain medium of the hybrid laser consisted of two pieces of Nd:YAG crystal slabs and two pieces of Nd:LuAG crystal slabs with the AM configuration. The Nd:YAG crystal slabs were 0.6 % doped, with dimensions of 30 × 20 × 8 mm^3, while the Nd:LuAG crystal slabs were 0.8 % doped, with dimensions of 30 × 20 × 7 mm^3. The front surface of each slab was anti-reflection (AR) coated at 1,064 nm and high-reflection (HR) coated at 808 nm relative to air, and the back surface was HR coated at 1,064 nm and AR coated at 808 nm relative to water. The laser at the incidence angle of 45° was reflected on the back surface and then passed through the gain medium for the second time. Cooling water flowed through the 1-mm-thick channel on the back of the slabs at a speed of 5 m/s to efficiently take away the heat.

Each slab was pumped from the back surface by a laser diode (LD) array which consists of 30 laser diode bars and can provide a peak output power of 6.4 kW with an emitting area of 12.5 × 10 mm^2. After being collimated using a microlens, each diode bar has the divergence angles of 8 and 5° along the slow and fast axes, respectively. Therefore, without optical coupling optics, a maximum peak intensity of 3.6 kW/cm^2 can be obtained at the pump surface of the slabs. Each LD can be driven independently so that the oscillator can be operating in the hybrid mode with both types of gain media or in the pure mode with a single type.

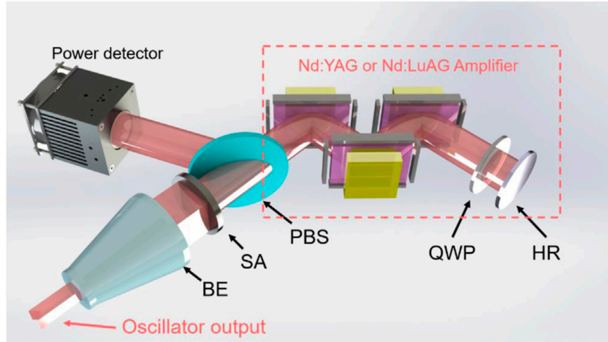

FIGURE 2 | Schematic diagram of the measurement setup for investigating the amplification efficiency. BE, beam expander; SA, serrated aperture; PBS, polarizing beam splitter; QWP, quarter-wave plate; HR, high reflective mirror.

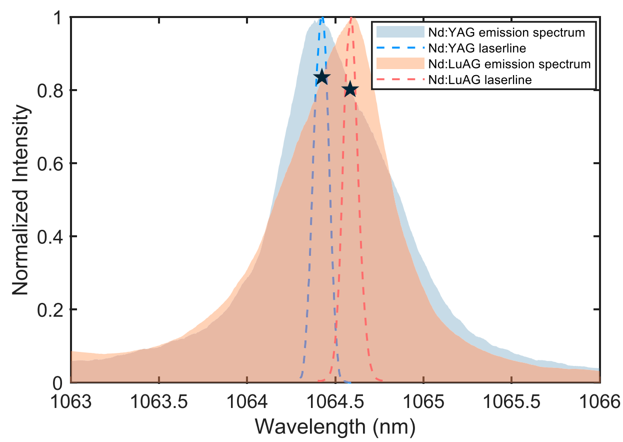

FIGURE 3 | Fluorescence spectra and laser spectra of Nd:YAG and Nd:LuAG.

A KD*P Pockels cell (PC), a polarizing beam splitter (PBS), and a quarter wave plate (QWP) were inserted in the cavity acting as the Q-switcher. A planar–planar cavity was used for the oscillator, and the output coupler (OC) with the transmittance of 60, 70, 80, and 90% was tested. The pump duration of LD was set as 280 μs at the repetition frequency of 10 Hz.

For the subsequent experiments on scaling efficiency, large-size Nd:YAG and Nd:LuAG AMs were used as amplifier modules, as shown in **Figure 2**. The seed laser output from the oscillator was expanded using a telescope and apodized using a serrated aperture (SA) with a diameter of 28 mm to ensure uniform amplification. Then, the laser double passed through three pieces of Nd:YAG AMs or Nd:LuAG AMs for investigation.

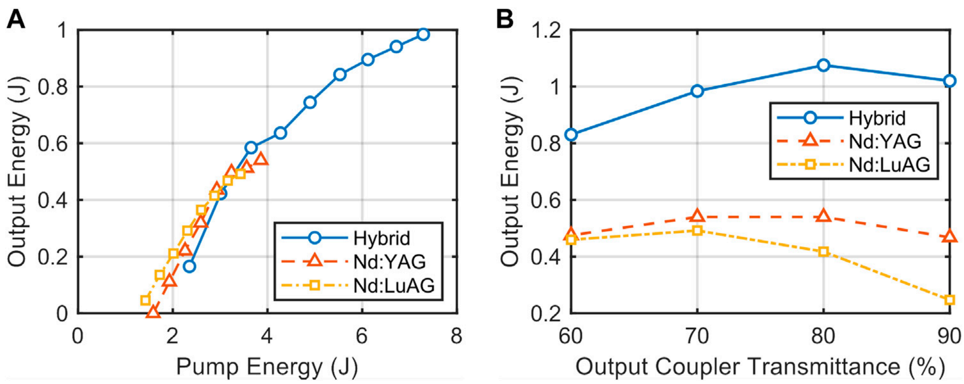

FIGURE 4 | Output performance of the hybrid Nd:YAG/Nd:LuAG Q-switched laser oscillator. **(A)** Output energy versus the pump energy; **(B)** maximum output energy versus the output coupler transmittance.

RESULTS AND DISCUSSIONS

Spectra of Nd:YAG and Nd:LuAG

The measured fluorescence spectra and lasing spectra of Nd:YAG and Nd:LuAG are shown in **Figure 3**. The central wavelengths of Nd:YAG and Nd:LuAG were 1,064.42 nm and 1,064.60 nm, respectively, and both of them have the same laser bandwidth of 0.1 nm (FWHM) and the fluorescence bandwidth of 0.6 nm (FWHM). The fluorescence spectra of the two crystals overlap for most portions, which allows efficient scaling of hybrid master oscillator power amplifier (MOPA) structure combing two types of gain media. Furthermore, when the two crystals are inserted in one oscillator and operate together, their mixing gain remains as single-peaked as the output laser wavelength that was measured as 1,064.46 nm. Since Nd:YAG has a higher gain than Nd:LuAG, the spectrum of the hybrid output is more biased toward Nd:YAG.

The shape of the fluorescence spectrum is consistent with the shape of the emission cross-section of $\sigma_{21}(\nu)$ [12]. Therefore, the ratio of the emission cross-sections of Nd:YAG and Nd:LuAG can be obtained from the measured fluorescence spectra as marked with stars in **Figure 3**:

$$\begin{aligned} k_1 &= \frac{\sigma_{21,\mathrm{Y}}(\nu_{\mathrm{Lu}})}{\sigma_{21,\mathrm{Y}}(\nu_{\mathrm{Y}})} = 0.8, \\ k_2 &= \frac{\sigma_{21,\mathrm{Lu}}(\nu_{\mathrm{Y}})}{\sigma_{21,\mathrm{Lu}}(\nu_{\mathrm{Lu}})} = 0.84 \end{aligned} \tag{4}$$

where $\sigma_{21,\mathrm{Y}}$ and $\sigma_{21,\mathrm{Lu}}$ are the emission cross-sections of Nd:YAG and Nd:LuAG, respectively, and ν_{Y} and ν_{Lu} are central frequencies of Nd:YAG and Nd:LuAG, respectively. It can be seen that the variation in the shape of the fluorescence spectra of Nd:YAG and Nd:LuAG leads to $k_2 > k_1$, which implies that the Nd:LuAG amplifier with a Nd:YAG seed laser has a higher scaling efficiency than the opposite case.

Oscillator Output

The output characteristics were measured with three modes of Nd:YAG slabs pumped only, Nd:LuAG slabs pumped only, and four slabs fully pumped, with the results demonstrated in **Figure 4A**. In addition, the output characteristics under different transmittance (60, 70, 80, and 90%) were compared in **Figure 4B**.

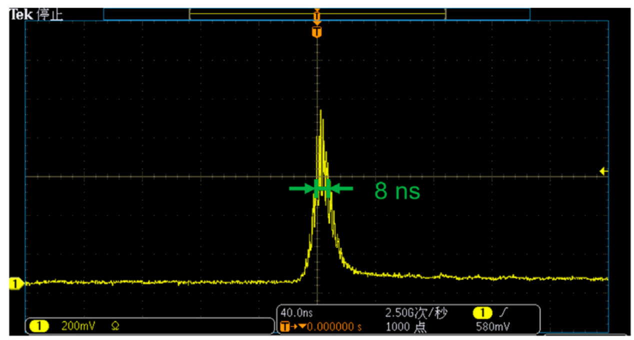

FIGURE 5 | Measured oscilloscope trace of hybrid Q-switched laser pulsed output.

With the optimum OC transmittance of 80%, a maximum output energy of 1.08 J was obtained at the pump energy of 7.3 J, corresponding to an optical-optical efficiency of 14.8%. **Figure 5** shows the measured oscilloscope trace of the Q-switched pulse shape, with the pulse width of 8 ns. The spot size of the output beam is 10 × 11 mm^2. When Nd:YAG and Nd:LuAG slabs were pumped separately, the maximum energy obtained was 540 and 490 mJ, respectively, at the optimum OC transmittance of 70%.

Comparison of Amplification Efficiencies

The laser output from the Q-switched oscillator was expanded using a telescope and then entered the amplifier stage of Nd:YAG or Nd:LuAG. **Figure 6** compares the gain of Nd:YAG amplifier with different seed lasers. By fitting the gain data, k_1 and k_2 were obtained as 0.85 and 0.91, respectively. We claim that the values fitted, which are larger than those obtained by fluorescence spectra as presented in **Section 4.1**, are considered to be closer to the actual values. The measured fluorescence spectrum of the gain medium, which was used to infer the emission cross-section

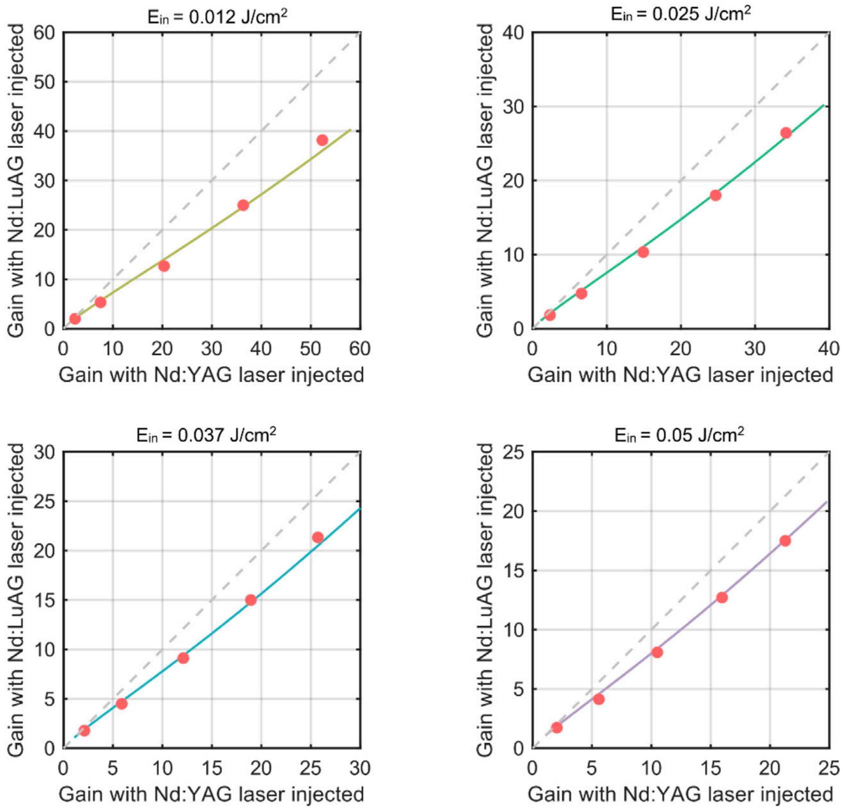

FIGURE 6 | Gain of the Nd:YAG amplifier with different laser injected. solid line, fitted with $k_1 = 0.85$; circle, measured; dashed line, reference line with a slope of 1.

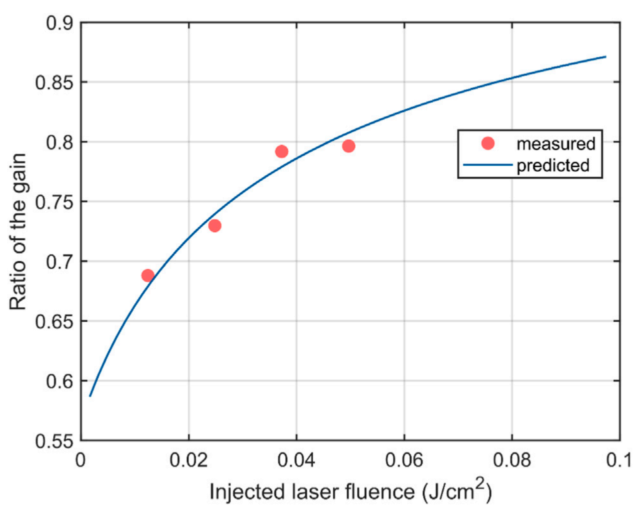

FIGURE 7 | Ratio of the gain with Nd:YAG and Nd:LuAG seed injected versus injected laser fluence.

in **Section 4.1**, was actually narrower than the real fluorescence spectrum due to a gain narrowing effect that the fluorescence near the center of the gain gets amplified more effectively, leading to the underestimate of k_1 and k_2 in **Section 4.1**.

Figure 7 shows the ratio of the gain of the Nd:YAG amplifier with Nd:YAG and Nd:LuAG seed injected, versus injected laser fluence at the same pump energy. When the incident fluence increased, the extraction efficiency increased, and the ratio of the gain increased. Therefore, to reduce the loss due to spectral mismatch, a large incident fluence is required to keep the amplifier operating at a heavily saturated condition.

CONCLUSION

In this study, we reported a Q-switched oscillator with a hybrid gain media of Nd:YAG and Nd:LuAG, producing a laser output of 1.08 J, 10 Hz, 8 ns. Furthermore, the ratios of the emission cross-section for two types of gain medium were obtained *via* a hybrid scaling experiment, which can be used to calculate the amplified output energy in the case of spectral mismatch. The results indicate that the overlapping gain spectra of Nd:YAG and Nd:LuAG makes it possible to obtain high gain even when the spectra are mismatched.

DATA AVAILABILITY STATEMENT

The raw data supporting the conclusion of this article will be made available by the authors, without undue reservation.

AUTHOR CONTRIBUTIONS

XL performed the experiments and made the data analysis. XL, XF, and QL contributed to writing and editing the manuscript.

FUNDING

Supported by the Open-Foundation of Key Laboratory of Laser Device Technology, China North Industries Group Corporation Limited (No. KLLDT202101).

REFERENCES

1. Mason P, Divoký M, Ertel K, Pilař J, Butcher T, Hanuš M, et al.Kilowatt Average Power 100 J-Level Diode Pumped Solid State Laser. *Optica* (2017) 4: 438–9. doi:10.1364/optica.4.000438
2. Martin D, Jan P, Martin H, Navrátil P, Denk O, Severová P, et al.150 J DPSSL Operating at 1.5 kW Level. *Opt Lett* (2021) 46:5771–3. doi:10.1364/OL.444902
3. Gonçalvès-Novo T, Albach D, Vincent B, Arzakantsyan M, Chanteloup J-C. 14 J/2 Hz Yb^{3+}:YAG Diode Pumped Solid State Laser Chain. *Opt Express* (2013) 21:855–66. doi:10.1364/OE.21.000855
4. Ogino J, Tokita S, Kitajima S, Yoshida H, Li Z, Motokoshi S, et al.10 J Operation of a Conductive-Cooled Yb:YAG Active-Mirror Amplifier and Prospects for 100 Hz Operation. *Opt Lett* (2021) 46:621–4. doi:10.1364/ol.414926
5. Liu T, Sui Z, Chen L, Li Z, Liu Q, Gong M, et al.12 J, 10 Hz Diode-Pumped Nd: YAG Distributed Active Mirror Amplifier Chain with ASE Suppression. *Opt Express* (2017) 25:21981–92. doi:10.1364/oe.25.021981
6. Liu T, Feng T, Sui Z, Liu Q, Gong M, Zhang L, et al.50 Mm-Aperture Nd:LuAG Ceramic Nanosecond Laser Amplifier Producing 10 J at 10 Hz. *Opt Express* (2019) 27:15595–603. doi:10.1364/oe.27.015595
7. Fu X, Liu T, Deng X, Li P, Liu Q, Yan X, et al.Ultrahigh-efficiency 4-J, 10-Hz, Nd:YAG Quasi-Continuous-Wave Active Mirror Oscillator. *Appl Phys B* (2015) 121:453–7. doi:10.1007/s00340-015-6252-4
8. Ding J, Wang J, Yu G, Zhou J, Zhu X, Chen W, et al.Theoretical and Experimental Study of Diode-Pumped Nd:LuAG Disk Lasers. In: Proc. SPIE 11849, Fourth International Symposium on High Power Laser Science and Engineering (HPLSE 2021) (2021). p. 1184910. doi:10.1117/12.2599034
9. Liu Q, Gong M, Liu T, Sui Z, Fu X. Efficient Sub-joule Energy Extraction from a Diode-Pumped Nd:LuAG Amplifier Seeded by a Nd:YAG Laser. *Opt Lett* (2016) 41:5322–5. doi:10.1364/ol.41.005322
10. Wang X-D, Xu X-D, Zang T-C, Ma C-L, Zhao Z-W, Xu J. Growth and Spectral Properties of Nd:Lu3Al5O12 Crystal. *J Inorg Mater* (2010) 25(4): 435–40. doi:10.3724/sp.j.1077.2010.00435
11. Frantz LM, Nodvik JS. Theory of Pulse Propagation in a Laser Amplifier. *J Appl Phys* (1963) 34(8):2346–9. doi:10.1063/1.1702744
12. Siegman AE. *Lasers*. California: University Science (1986). p. 286–92p.

Conflict of Interest: The authors declare that the research was conducted in the absence of any commercial or financial relationships that could be construed as a potential conflict of interest.

ORIGINAL RESEARCH
published: 17 June 2022
doi: 10.3389/fphy.2022.923402

Multi-Beam Large Fundamental Mode Neodymium Glass Regenerative Amplifier With Uniform Performance

*Song Gao, Xudong Xie, Jun Tang, Chen Fan, Xuejun Fu, Zhifei Chen and Ke Yao**

Research Center of Laser Fusion, CAEP, Mianyang, China

In this study, the designing method of multi-beam regenerative amplifiers with the repetitive rate was proposed and demonstrated. To obtain multi-beam regenerative amplifiers with uniform performance, the disparities in output energy, energy stability, and mode size were analyzed, and the detailed optimizing method was presented. With the designs, eight-beam regenerative amplifiers were developed. The output performances of eight-beam regenerative amplifiers were uniform. The output energies were in the range of 25.4–28.8 mJ, and the energy stabilities over two hours were in the range of 2.4%–5.1% (PV) and 0.3%–0.9% (RMS).

Keywords: regenerative amplifier, Nd:glass, laser beam characterization, multi-beam uniformity, diode-pumped

Edited by:
Xing Fu,
Tsinghua University, China

Reviewed by:
JiSi Qiu,
Aerospace Information Research Institute (CAS), China
Chengqiang Lu,
South Industry Institute, China

****Correspondence:***
Ke Yao
yyh143@163.com

Specialty section:
This article was submitted to Optics and Photonics, a section of the journal Frontiers in Physics

Received: *19 April 2022*
Accepted: *06 May 2022*
Published: *17 June 2022*

Citation:
Gao S, Xie X, Tang J, Fan C, Fu X, Chen Z and Yao K (2022) Multi-Beam Large Fundamental Mode Neodymium Glass Regenerative Amplifier With Uniform Performance.
Front. Phys. 10:923402.
doi: 10.3389/fphy.2022.923402

1 INTRODUCTION

Neodymium glass (Nd:glass) is the best gain medium so far for inertial confinement fusion (ICF) lasers, such as the SG-series in China, the National Ignition Facility (NIF) in American, and the Megajoule in France [1–4]. The Nd:glass has good optical homogeneity, broad gain bandwidth (more than 20 nm), and the potential for large size and high doping concentration [5–7]. However, as the stimulated emission cross (σ) is small, the single-pass small-signal gain coefficient is small ($g = n\sigma$) at the same stored energy. Thus, in order to achieve sufficient total gain, multi-pass amplifiers are strongly preferable. Among them, the regenerative amplifier is a good candidate. First, the amplification pass can be several tens or more, and the total gain is very large ($>10^9$). Second, gain saturation induced by multi-pass amplification is particularly beneficial to improve the extraction efficiency and pulse-to-pulse energy stability [8–10]. Third, owing to the mode self-reproducing of the regenerative cavity, the beam quality is excellent, typically the fundamental mode. Therefore, the regenerative amplifier is commonly served as a high-gain compact module in the preamplifier of ICF lasers [11].

To date, numerous researches on the regenerative amplifier design have been conducted. In 1983, Magni et al. theoretically derived the general properties of resonators containing a variable lens and investigated the mode spot sizes, the dynamical stability, and the misalignment sensitivity [12]. This method was widely used in the regenerative amplifier design [13, 14]. Afterward, to overcome high misalignment sensitivity of the amplifier, a method was proposed for analyzing the impact of cavity misalignment on the mode drift of the gain media [15]. With these aforementioned methods, the regenerative amplifier can be designed and developed. However, in the situation that multi-beam lasers are required to simultaneously irradiate onto the target (e.g., ICF), in order to obtain the best laser–matter interaction results, the performances of multi-beam are desired to be uniform, including output energy and temporal waveform. This is generally called energy/power balance across multi-beam lasers [16–19]. Therefore, as a part of ICF lasers, the uniformities of multi-beam regenerative amplifiers are strongly desired. Since the laser is amplified many times in the

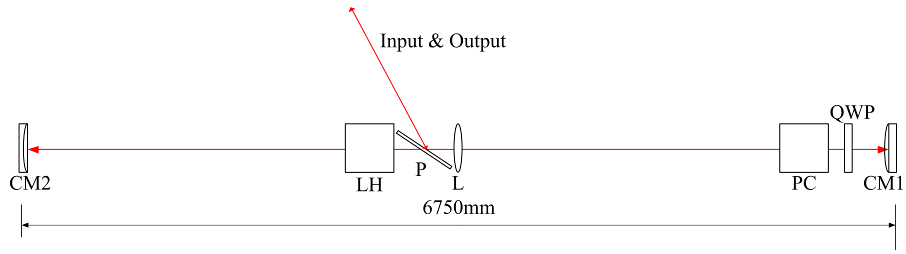

FIGURE 1 | Simplified regenerative amplifier concept. CM1 and CM2: cavity mirrors; LH: laser head; P: thin-film polarizer; L: lens; PC: Pockels cell; QWP: quarter-wave plate.

regenerative amplifier, slight parameter differences of optical components or weak focal lensing can contribute to large changes in mode radius and energy, i.e., disparities across multi-beam lasers. This will influence the power balance of ICF lasers.

In this study, the designing method of multi-beam regenerative amplifiers with the repetitive rate was proposed and demonstrated. The disparities in output energy, energy stability, and mode size were analyzed with the practical optical component parameters and operating conditions. The detailed designing and optimizing method was presented to obtain a multi-beam regenerative amplifier with uniform performance. With the designs, eight-beam regenerative amplifiers were developed. The output performances were measured. The output performances of eight-beam regenerative amplifiers were uniform. The output energies were in the range of 25.4–28.8 mJ, and the energy stabilities over two hours were in the range of 2.4%–5.1% (PV) and 0.3%–0.9% (RMS). The results were in good accordance with the design results.

2 MULTI-BEAM REGENERATIVE AMPLIFIER DESIGN

2.1 Regenerative Amplifier Model

The simplified regenerative amplifier concept is shown in **Figure 1**. The amplifier contains two cavity mirrors (CM1 and CM2), a laser head (LH), a Pockels cell (PC), a quarter-wave plate (QWP), a thin-film polarizer (P), and a lens (L). The L, CM1, and CM2 are used to determine the mode size. The PC and QWP are used to control the amplification pass. The cavity length is 6750mm, which corresponds to 45 ns round trip. Thus, a laser pulse with a maximum of 25 ns temporal width can be amplified, considering the 10 ns rising edge of the PC.

The input laser with *s*-polarization is injected into the amplifier cavity from P. When the input laser first passes through the PC, the PC is powered off. After a round trip, the laser turns to be *p*-polarization with the help of QWP. After the laser passes through the PC for the second time, the PC is powered with a quarter-wave voltage, and the function of the PC and QWP is similar to that of a half-wave plate. The laser polarization state keeps constant during a round trip, and the laser can be amplified successively until the PC is powered off. The output laser with *s*-polarization is outputted from P. The total amplification pass is $fix(t \times c/l)$, where t is the voltage width of PC, c is the speed of light, l is the cavity length, and the function $fix(x)$ is obtaining the maximum integer of x.

2.2 Energy and Energy Stability Design

In practical multi-beam regenerative amplifiers, due to the parameter differences of optical components (e.g., reflectivity and transmission), the total loss of the cavity is different. Moreover, in laser–matter interactions with multi-beam lasers, the moments of multi-beam lasers arriving at the target must be the same. Thus, the amplification pass (or the voltage width of PC) should be identical. In this circumstance, the output energy and energy stability exhibit obvious differences from beam to beam. Here, the typical parameters of optical components are shown in **Table1**. In this table, four configurations of parameters are included. The design baseline is the typical parameter of the optical component. The minimum value, maximum value, and mean value are obtained by actually measuring the minimum, maximum, and mean parameters from over 100 real components.

With these parameters in **Table1**, the energy curves of different configurations are calculated theoretically. In the theoretical calculations, the Avizonis–Grotbeck model is adopted [20]. Compared with the commonly used Frantz–Nodvik model [21], the Avizonis–Grotbeck model involves the loss of gain medium, which is important, especially for rod-shaped gain medium and multi-pass amplification, which makes the theoretical simulations more exact. Here, the static loss and dynamic loss of Nd:glass are 0.12% cm^{-1} and 0.36% cm^{-1}, respectively, which are obtained from the Nd:glass factory. The static loss and dynamic loss are the loss without and with LD pumping, respectively. Combined with the input energy of ~0.1 μJ, the theoretical energy curves are calculated, as shown in **Figure 2**. In the figure, the small-signal gain and the amplification pass are chosen to be 1.269 and 96-pass, respectively, so as to satisfy the output energy of 25 mJ and excellent energy stability at design baseline (black line in **Figure 2**). Due to the different losses, the energy and energy stability of the four configurations show undesirable disparities. For configurations of the minimum value, mean value, and maximum value, the output energy is far larger than 25 mJ before the laser is exported from the regenerative amplifier. The optical damages are probably induced and affect the safe operations. Moreover, the performances of energy stability are

TABLE 1 | Typical parameters of optical components.

Optical component	Design baseline (%)	Minimum value (%)	Maximum value (%)	Mean value (%)
Lens	99.6	99.860	99.930	99.90
Quarter-wave plate	99.6	99.700	99.900	99.80
Pockels cell	97.0	97.020	98.307	97.66
Nd:glass	98.5	98.511	98.906	98.71
Polarizer	99.6	99.730	99.930	99.83
Reflecting mirror	99.8	99.845	99.880	99.86

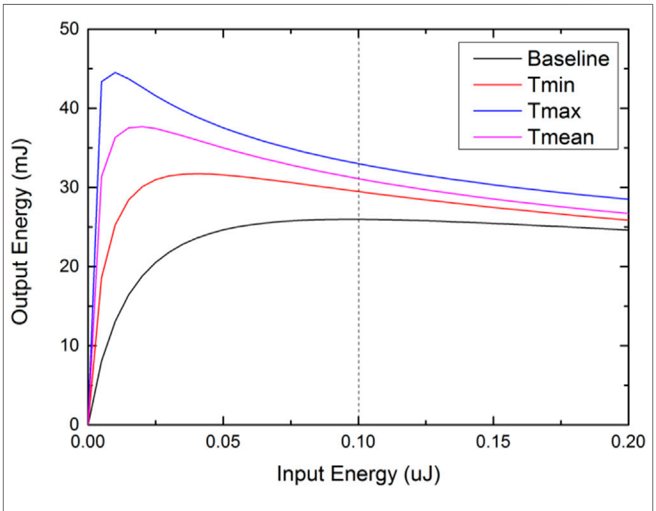

FIGURE 2 | Energy curves of different configurations.

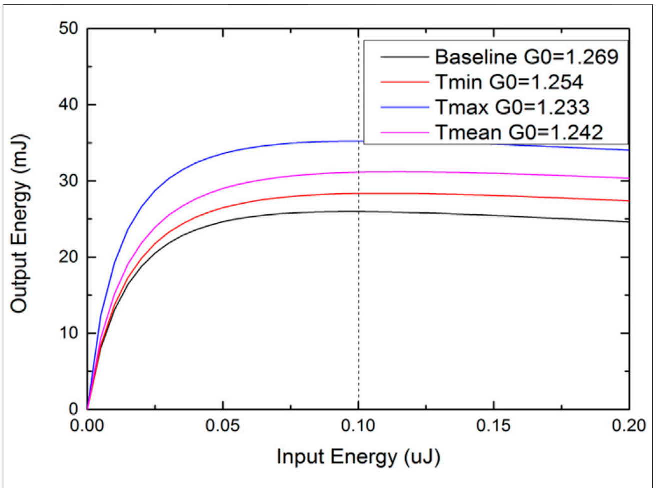

FIGURE 3 | Optimized energy curves of four configurations.

also different. For design baseline, the curve at 0.1 μJ is nearly flat. It means that the output energy is extremely insensitive to the fluctuations of input energy. However, for the minimum value, mean value, and maximum value, the output energy varies with the fluctuations of input energy, which will influence the power balance of multi-beam lasers.

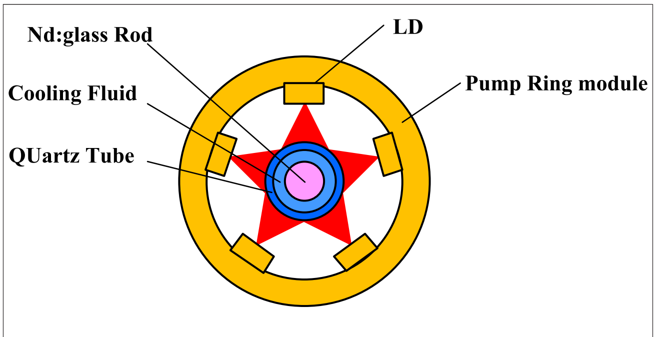

FIGURE 4 | Profile of the laser amplifier.

In order to obtain uniform energy stabilities of multi-beam lasers and avoid optical damage, an active method of controlling the product of gain and loss is adopted. Here, by slightly adjusting the small-signal gain, the products of gain and loss of multi-beam regenerative amplifiers are uniform. With this method, the optimized small-signal gain of four configurations are 1.269, 1.254, 1.233, and 1.242, respectively. The optimized energy curves of four configurations are shown in **Figure 3**. From the figure, the output energies of four configurations are all in the safe operating range of 25–35 mJ. The energy stabilities are nearly uniform and not sensitive to the fluctuations of the input laser.

2.3 Laser Head Design

The laser head is a diode-side-pumped circular Nd:glass rod with a 1 Hz repetition rate. The profile is shown in **Figure 4**. The laser head consists of Nd:glass, cooling fluid, quartz tube, and pump ring module. The geometric size of the rod is Φ5 mm × 100 mm. The gain medium is N31 Nd:glass whose Nd^{3+} concentration is 2.2 wt% [22, 23]. The ends of the rod are tapered to stifle unwanted whispering gallery parasitic modes. The quartz tube is 1 mm thickness, which is used to separate the cooling fluid from the diode. The pumping ring module is a 5-side ring-pumping scheme with a pumping power of 2.5 kW, and two pumping ring modules are incorporated. The center wavelength of the diode is 802 nm.

In order to obtain excellent beam quality, the pumping is required to be uniform[24]. The simulated pumping uniformity with the aforementioned parameters is shown in **Figure 5** using the ray-tracing method. The uniformity in the center 3 mm × 3 mm region is 91.8%.

The small-signal gain is estimated according to the energy-transfer mechanism [25], including the pumping transfer

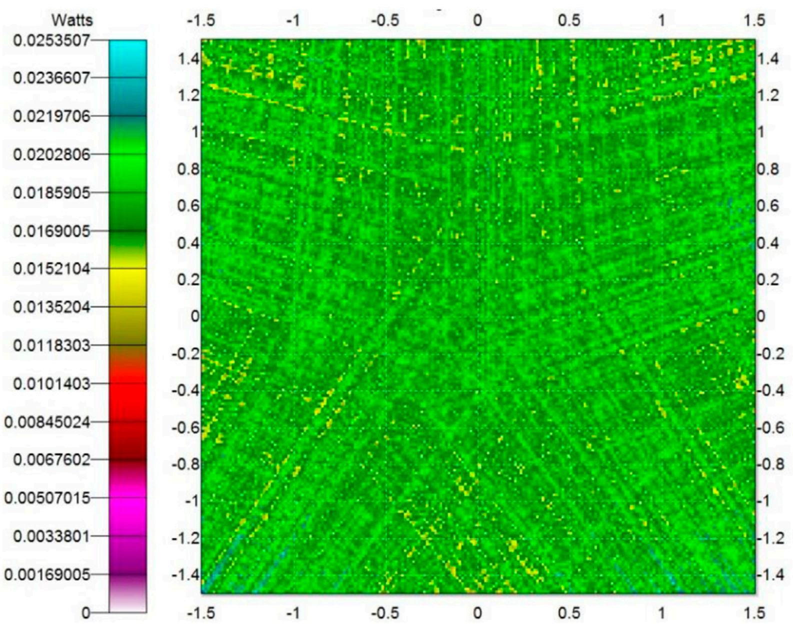

FIGURE 5 | Pumping distribution of LH.

efficiency, absorbing efficiency, quantum efficiency, Stokes efficiency, and storage efficiency. In this case, the total energy transfer efficiency (η_{tot}) is 26%. The maximum small-signal gain is estimated to be 1.95 using **Eq. 1**. It is slightly larger than the aforementioned required small-signal gain.

$$G_0 = \exp\left(\frac{\eta_{tot} P_p t_p}{E_s A}\right) \tag{1}$$

where P_p is the pumping power; t_p is the pumping width, which is 500 μs; E_s is saturated fluence (4.97 J/cm^2 for N31 Nd:glass); and A is the section area of the gain medium.

2.4 Cavity Design of the Regenerative Amplifier

Due to the long cavity length, even weak focal lensing can contribute to large changes in mode radius for non-optimized cavity configurations, i.e., undesired disparities across multi-beam lasers. For multi-beam regenerative amplifiers, on the one hand, as mentioned previously, in order to obtain uniform output energy and energy stability, the small-signal gain of each beam is strongly dependent on the optical loss. This means the pumping power and induced thermal lensing are different. According to the laser head design and thermal analyses, at the small-signal gain of 1.269 (design baseline in **Section 2.2**), the corresponding thermal lensing is about 25 m. Furthermore, one can easily estimate the thermal lensing for the other three cavity loss configurations, which are 23.75 m (minimum value), 22.74 m (mean value), and 21.98 m (maximum value), respectively. On the other hand, the diode pumping fluctuations induced by power supply and the machining errors of optical components such as CM1, CM2, and L will also cause mode radius changing. Thus, the cavity should be stable over a large range of the thermal lens.

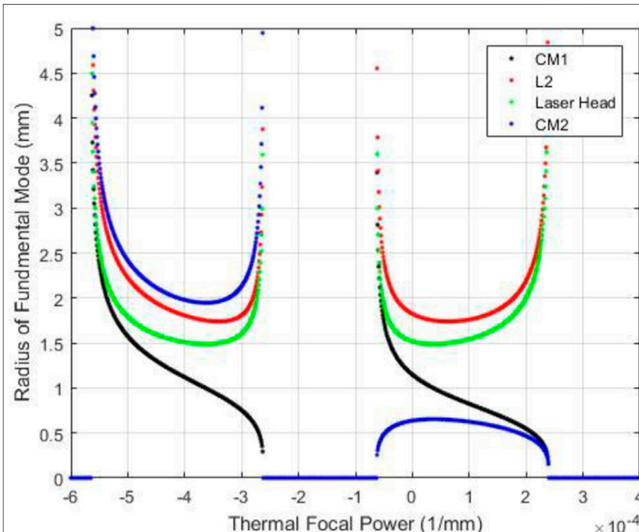

FIGURE 6 | Optimized stability zones of the regenerative cavity.

The cavity design is developed by utilizing an analytic ABCD description [20]. By varying the end mirror and cavity lens radius and the distance of optical components in **Figure 1**, the stability zones for each cavity parameter were evaluated. Only the cavity parameters meeting the following constraints were analyzed: first, the mode radius in the rod is ~1.5 mm, so as to obtain large

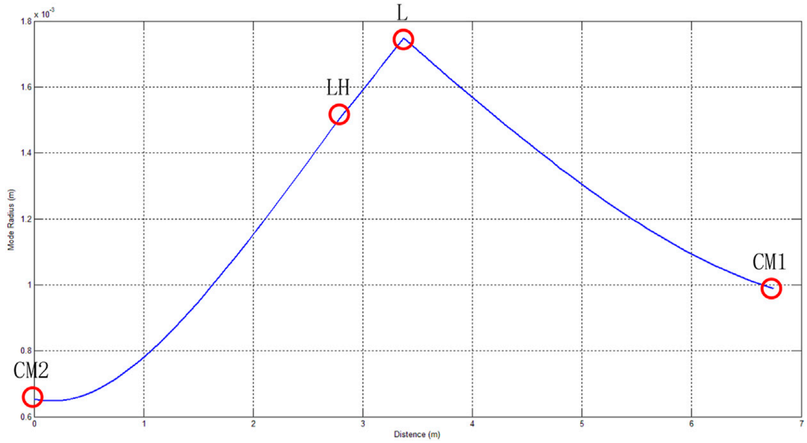

FIGURE 7 | Mode size of the regenerative cavity.

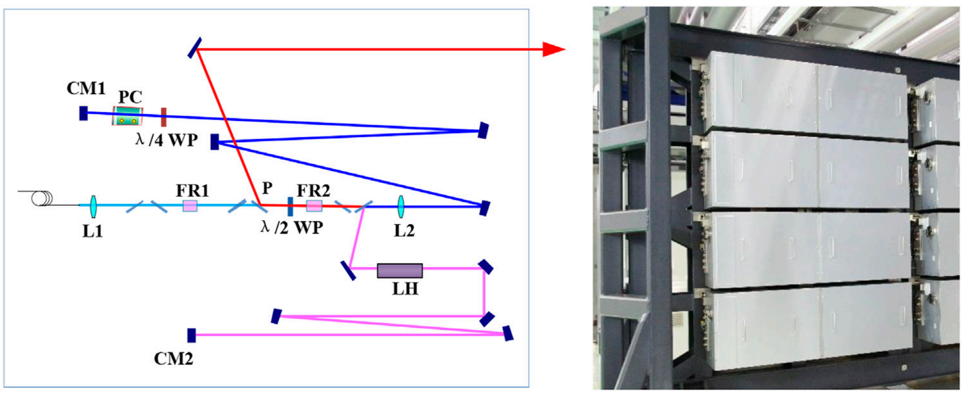

FIGURE 8 | Schematic diagram of the regenerative amplifier.

energy without damage risk. Second, the cavity should be stable with the thermal lensing changing from 21.98 to 25 m or more. This is necessary when changing the small-signal gain for multi-beam lasers. Third, the mode radius on the other optical components is larger than 0.5 mm to avoid optical damages. With these criteria, the optimized cavity parameters are as follows: the radii of the curvature of CM1 and CM2 are −10,000 and 10,000 mm, respectively. The focal length of L is 2,430 mm, and its position is at the center of the cavity. The distance between LH and CM2 is 2,750 mm. The corresponding stability zones are shown in **Figure 6**. In the figure, the x-axis is the thermal focal power, which is reciprocal to thermal lensing, and the y-axis is the mode radius. From the figure, at the thermal focal power of 4×10^{-5} mm^{-1} (i.e., 25 m for thermal lensing), the cavity mode size is insensitive to the thermal lensing variations. When the thermal focal power varies by ±20%, the mode radius at Nd:glass changes to smaller than 0.1%. Considering all the factors that may result in mode size changes including the diode pumping fluctuation, the thermal lensing variations, and machining errors of optical components, the total mode radius changes are small. This is negligible. With the parameters, the mode size of the regenerative cavity is calculated, as shown in **Figure 7**. The mode radii in the laser head (LH), lens (L), and cavity mirrors (CM1 and CM2) are 1.5, 1.75, 0.98, and 0.65 mm, respectively.

TABLE 2 | Output energy and energy stability of eight-beam regenerative amplifiers.

Beam	Output energy (MJ)	Energy stability (two hours)
L1	26.9	PV = 4.2%; RMS = 0.4%
L2	26.8	PV = 4.0%; RMS = 0.8%
L3	27.6	PV = 2.7%; RMS = 0.3%
L4	28.8	PV = 3.1%; RMS = 0.4%
R1	25.4	PV = 4.1%; RMS = 0.7%
R2	28.4	PV = 4.1%; RMS = 0.6%
R3	28.5	PV = 5.1%; RMS = 0.9%
R4	25.8	PV = 2.4%; RMS = 0.3%

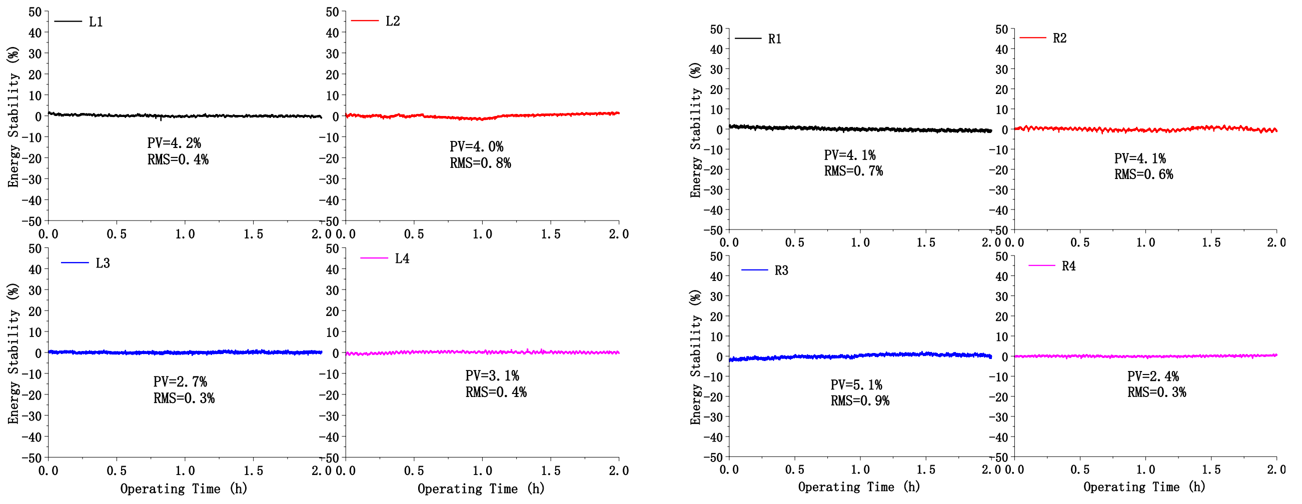

FIGURE 9 | Energy stabilities of eight-beam regenerative amplifiers over two hours.

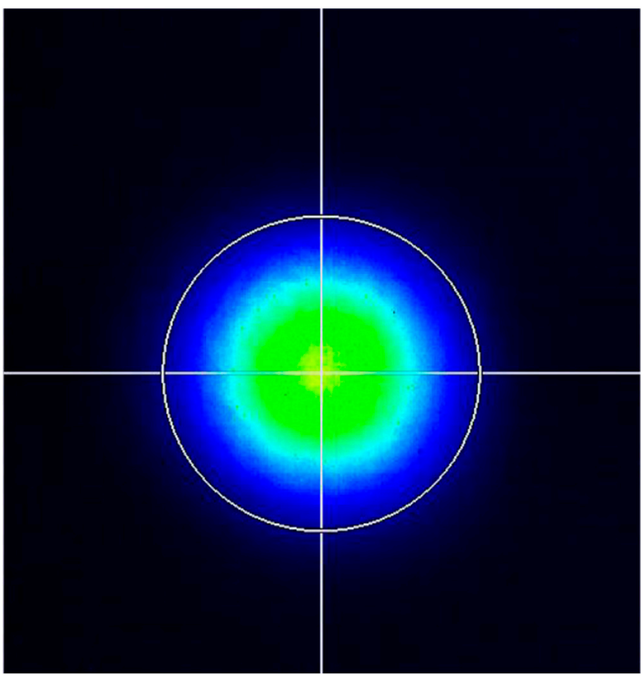

FIGURE 10 | Typical beam of the regenerative amplifier.

3 EXPERIMENTAL RESULTS

Based on the regenerative amplifier design, eight-beam regenerative amplifiers were developed, named L1–L4 and R1–R4. The eight beams were installed on a 4 × 2 truss. The L1–L4 and R1–R4 were image-mirrored. The schematic diagram of the regenerative amplifier is shown in **Figure 8**.

The amplification pass is 112-pass, which is larger than the designed 96-pass. It is mainly due to the imperfect mode matching between the input laser mode and cavity mode. At 112-pass amplification, the output energy and energy stability of eight-beam regenerative amplifiers are shown in **Table 2**. The output energies are in the range of 25.4–28.8 mJ, and the energy stabilities over two hours are 2.4%–5.1% (PV) and 0.3%–0.9% (RMS). This is in good accordance with the designed results. The corresponding energy stability curves are shown in **Figure 9**. From the figure, some slow variations can be seen, which mainly come from the slight misalignment induced by temperature changes of environment and energy fluctuations of the input laser.

The output beam is measured by CCD positioned after the polarizer P. The distance between the CCD and the lens L2 is identical to the distance between the laser head LH and the lens L2. Hence, the measured beam size is equivalent to that on LH. The typical beam is shown in **Figure 10**. The beam quality of eight beam lasers is good and uniform, exhibiting Gauss distribution. The beam size at $1/e^2$ is about 3 mm, which is in good accordance with the designed value.

4 CONCLUSION

In this study, the designing method of multi-beam regenerative amplifiers with the repetitive rate was proposed and demonstrated. To obtain multi-beam regenerative amplifiers with uniform performance, the disparities in output energy, energy stability, and mode size were analyzed, and the detailed optimizing method was presented. With the designs, eight-beam regenerative amplifiers were developed. The output performances are measured including the output energy and energy stability. The output performances of eight-beam regenerative amplifiers are uniform. The output energies are in the range of 25.4–28.8 mJ, and the energy stabilities over two hours are in the range of 2.4%–5.1% (PV) and 0.3%–0.9% (RMS). The results are in good accordance with the design results.

DATA AVAILABILITY STATEMENT

The original contributions presented in the study are included in the article/supplementary material; further inquiries can be directed to the corresponding author.

AUTHOR CONTRIBUTIONS

SG: regenerative amplifier design, demonstration, and manuscript writing. JT: regenerative amplifier demonstration. CF: regenerative amplifier test. KY: regenerative amplifier design.

REFERENCES

1. Miller GH, Moses EI, Wuest CR. The National Ignition Facility. *Opt Eng* (2004) 43(12):2841–53. doi:10.1117/1.1814767
2. André ML. Status of the LMJ Project. In: Solid State Lasers for Application to Inertial Confinement Fusion: Second Annual International Conference; 8 December 1997; Paris, France. Proceeding of SPIE (1997). p. 38–42.
3. Zheng WG, Zhang XM, Wei XF, Jing F, Sui Z, Zheng K, et al. Status of the SG-III Solid-State Laser Facility. *J Phys Conf Ser* (2008) 112:032009. doi:10.1088/1742-6596/112/3/032009
4. Fan W, Jiang YE, Wang JF, Wang X, Huang D, Lu X, et al. Progress of the Injection Laser System of SG-II. *High Power Laser Sci Eng* (2018) 6:e34. doi:10.1017/hpl.2018.31
5. Hogan WJ, Moses EI, Warner BE, Sorem MS, Soures JM. The National Ignition Facility. *Nucl Fusion* (2000) 41:567–73.
6. Boehly TR, Brown DL, Craxton RS, Keck RL, Knauer JP, Kelly JH, et al. Initial Performance Results of the OMEGA Laser System. *Opt Commun* (1997) 133: 495–506. doi:10.1016/s0030-4018(96)00325-2
7. Campbell JH, Suratwala TI. Nd-doped Phosphate Glasses for High-Energy/high-Peak-Power Lasers. *J Non-Crystalline Sol* (2000) 263-264:318–41. doi:10.1016/s0022-3093(99)00645-6
8. Yao K, Gao S, Tang J, Xie X, Fan C, Lu Z, et al. Off-axis Eight-Pass Neodymium Glass Laser Amplifier with High Efficiency and Excellent Energy Stability. *Appl Opt* (2018) 57:8727–32. doi:10.1364/ao.57.008727
9. Yao K, Xie X, Tang J, Fan C, Gao S, Lu Z, et al. Diode-side-pumped Joule-Level Square-Rod Nd:glass Amplifier with 1 Hz Repetition Rate and Ultrahigh Gain. *Opt Express* (2019) 27(23):32912–23. doi:10.1364/oe.27.032912
10. Yao Z, Cheng L, Tang R, Xue J. Wakefield Generation by Chirped Super-gaussian Laser Pulse in Inhomogeneous Plasma. *Plasma Sci Technol* (2018) 20: 115002. doi:10.1088/2058-6272/aacbbf
11. Spaeth ML, Manes KR, Kalantar DH, Heebner JE, Bliss ES, Miller PE, et al. Description of the NIF Laser. *Fusion Sci Technolegy* (2016) 26(1):25–145. doi:10.13182/FST15-144
12. Magni V. Multielement Stable Resonators Containing a Variable Lens. *J Opt Soc Am A* (1987) 4(10):1962–9. doi:10.1364/josaa.4.001962
13. Bowers M, Burkhart S, Cohen S, Erbert G, Heebner J, Herman M, et al. The Injection Laser System on the National Ignition Facility. In: Solid State Lasers XVI: Technology and Devices; 9 March 2007; San Jose, California, United States. International Society for Optics and Photonics (2007). p. 64511M.
14. Huang W, Wang J, Lu X, Fan W, Li X, Zhu J. Design and Demonstration of a Passive-Cooled, Innoslab-Based Nd:glass Regenerative Amplifier with High Beam Quality. *OSA Continuum* (2019) 2(6):1838–43. doi:10.1364/osac.2.001838
15. Shi Y, Zhang P, Jiang Y, Wang J, Zhou L, Lu X, et al. High-stability, High-Energy Nd:glass Rod Regenerative Amplifier with Compensation for Cavity Misalignment. *Appl Opt* (2021) 60(5):1150–8. doi:10.1364/ao.414923
16. Sampat S, Kosc TZ, Bauer KA, Dean RD, Donaldson WR, Kwiatkowski J, et al. Power Balancing the Multibeam OMEGA Laser. *Appl Opt* (2018) 57(32): 9571–82. doi:10.1364/ao.57.009571
17. Jones OS, Speck DR, Haan SW. The NIF Power Balance. In: 3rd International Conference on Solid-state Lasers for Applications to Inertial Confinement Fusion; Jun 1998; Monterey, CA, USA. Proceeding of SPIE (1999). p. 78–104.
18. Kalantar DH, Dixit SN, Haynam CA, Mehta NC, Shaw MJ, Widmayer CC, et al. NIF Power Balance Performance Modeling and Testing. In: Proceeding of the 49th Annual Meeting of the Division of Plasma Physics; November 12-16, 2007; Orlando,florida. American physicl society (2007). p. 52.
19. Garrec BJL, Nicolas O. Laser Performance Operation Model and its Application to LIL Energy and Power Balance. *J Phys Conf Ser* (2008) 112: 032019. doi:10.1088/1742-6596/112/3/032019
20. Avizonis PV, Grotbeck RL. Experimental and Theoretical Ruby Laser Amplifier Dynamics. *J Appl Phys* (1966) 37:687–93. doi:10.1063/1.1708238
21. Frantz LM, Nodvik JS. Theory of Pulse Propagation in a Laser Amplifier. *J Appl Phys* (1963) 34:2346–9. doi:10.1063/1.1702744
22. Hu L, Chen S, Tang J, Wang B, Meng T, Chen W, et al. Large Aperture N31 Neodymium Phosphate Laser Glass for Use in a High Power Laser Facility. *High Power Laser Sci Eng* (2014) 2:1–6. doi:10.1017/hpl.2014.4
23. Hu L, He D, Chen H, Wang X, Meng T, Wen L, et al. Research and Development of Neodymium Phosphate Laser Glass for High Power Laser Application. *Opt Mater* (2017) 63:213–20. doi:10.1016/j.optmat.2016.11.052
24. Clarkson WA. Thermal Effects and Their Mitigation in End-Pumped Solid-State Lasers. *J Phys D: Appl Phys* (2001) 34:2381–95. doi:10.1088/0022-3727/34/16/302
25. Koechner W. *Solid State Laser Engineering*. New York: Springer (2006). p. 112.

Conflict of Interest: The authors declare that the research was conducted in the absence of any commercial or financial relationships that could be construed as a potential conflict of interest.

Publisher's Note: All claims expressed in this article are solely those of the authors and do not necessarily represent those of their affiliated organizations, or those of the publisher, the editors, and the reviewers. Any product that may be evaluated in this article, or claim that may be made by its manufacturer, is not guaranteed or endorsed by the publisher.

frontiers | Frontiers in Physics

ORIGINAL RESEARCH
published: 30 June 2022
doi: 10.3389/fphy.2022.923710

Diode-Pumped 50 Hz–10 J Nano-Second Nd:YAG Laser

Xinying Jiang, Kaibo Xiao, Xiongwei Yan, Zhenguo Wang, Xuejun Jiang, Qiao Xue, Wenlong Wu, Ji Chen, Chuanchao Zhang, Jiangang Zheng, Zhitao Peng, Kuixing Zheng, Ping Li, Dongxia Hu, Qihua Zhu and Wanguo Zheng**

Laser Fusion Research Center, CAEP, Mianyang, China

In this letter, we report a diode-pumped nano-second laser with the output energy 10 J, the repetition rate 50 Hz, and the average power 500 W. The main amplifier was made up of eight amplify modules. Each amplify module was pumped by an 808 nm laser diode and cooled by water from the back end of the Nd:YAG slab. To our knowledge, this represents the highest pulse repetition rate for the 10 J class nano-second single-aperture Nd:YAG laser. The beam quality was controlled by means of mechanical design and adjustment and compensation by a home-made deforming mirror. The beam quality was controlled well with the beam quality of the laser 2.61DL.

Keywords: re-frequency pulse laser, high-energy laser, high conversion efficiency, thermal management, Nd:YAG laser

OPEN ACCESS

Edited by:
Xing Fu,
Tsinghua University, China

Reviewed by:
Yulei Wang,
Hebei University of Technology, China
Jing Wang,
Shanghai Jiao Tong University, China

****Correspondence:***
Xinying Jiang
jiangxinying@caep.cn
Wanguo Zheng
wgzheng_caep@sina.com

Specialty section:
This article was submitted to Optics and Photonics, a section of the journal Frontiers in Physics

Received: *19 April 2022*
Accepted: *23 May 2022*
Published: *30 June 2022*

Citation:
Jiang X, Xiao K, Yan X, Wang Z, Jiang X, Xue Q, Wu W, Chen J, Zhang C, Zheng J, Peng Z, Zheng K, Li P, Hu D, Zhu Q and Zheng W (2022) Diode-Pumped 50 Hz–10 J Nano-Second Nd:YAG Laser. Front. Phys. 10:923710. doi: 10.3389/fphy.2022.923710

INTRODUCTION

Diode-pumped re-frequency high-energy nano-second laser is one of the developing directions of the new generation of lasers and has a wide range of application prospects. It can be used for industrial applications and laboratory research, such as laser peening, pump source of Ti:sapphire femtosecond laser, high-energy density physics, strong field physics, high-energy and high-brightness X-ray source, or high-energy and high-brightness particle beams. Many industrial applications require high repetition of laser frequency to realize high processing rate.

In recent years, 10 Hz nano-second laser has developed rapidly, and the output energy had increased from 10 J to 100 J [1–7]. However, at that energy level, higher frequency just as 50 Hz or even 100 Hz was not realized before 2020. In 2018, we used Nd:YAG crystals as laser media and obtained 12 J–10 Hz laser output [8]. Taking the advantage of the low pumping intensity, the laser system has a large potential to increase the operation frequency to 50 Hz in 2020 [9]. In this paper, we introduce the details of the laser system to readers. We present the configuration of the laser, introduce the key problems of thermal management and ASE inhibition, and give the experimental results in this paper.

EXPERIMENTAL SETUP

Figure 1 shows the schematic diagram of the laser system. A Q switch cavity with a side face pumped Nd:YAG rod was the seed. Two side face pumped rods were used as pre-amplifiers. The maximal output energy was 375 mJ. The beam was shaped by a glass diaphragm to a square with the output energy of about 190 mJ. The main amplifier was composed of eight water-cooled laser amplifier modules which were pumped from the back end by 808 nm LD arrays.

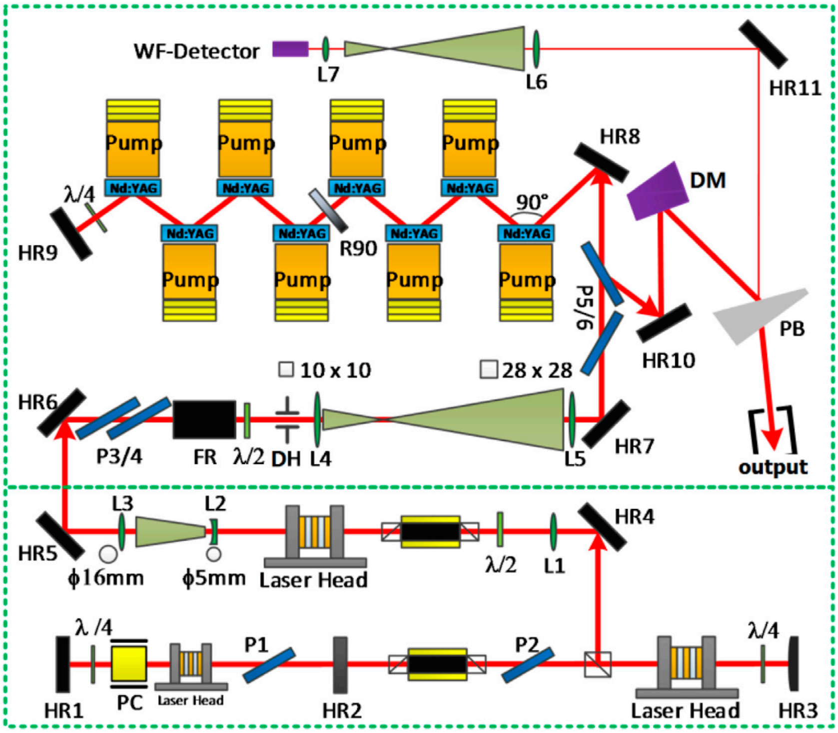

FIGURE 1 | Schematic diagram of the 10 J–50 Hz laser system. HR is the high-reflection mirror. P is the polarization mirror. L is the lens. λ/4 is the 1/4 wave plate. FR is the Faraday rotator. λ/2 is the 1/2 wave plate. DM is the deformable mirror. DH is the diaphragm. WF-Detector is the wave front detector. PB is the sampling mirror with obliquity.

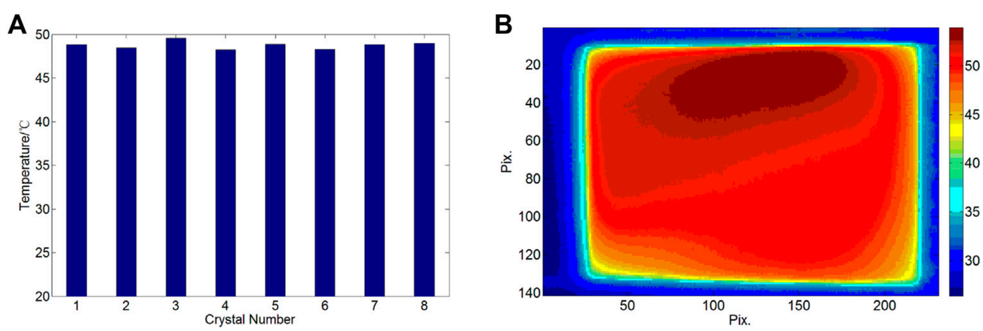

FIGURE 2 | (A) The average surface temperature. **(B)** A typical surface temperature distribution.

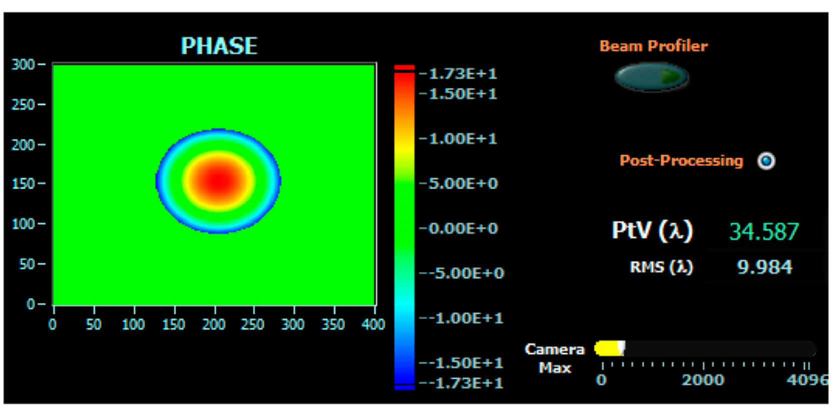

FIGURE 3 | Total defocus of the two pass amplifier.

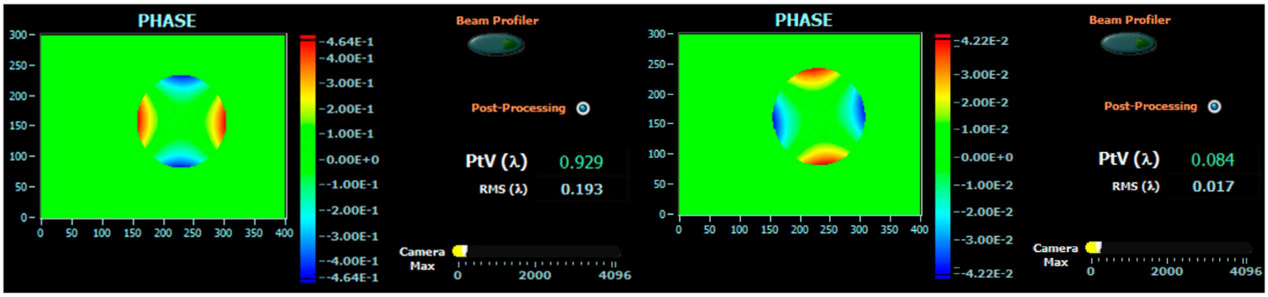

FIGURE 4 | Astigmatism of one amplifier module **(A)** before adjustment and **(B)** after adjustment.

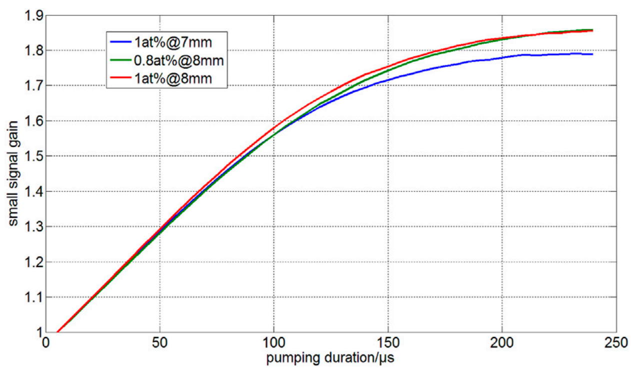

FIGURE 5 | Simulation results of different thicknesses and doping concentrations to a small signal gain.

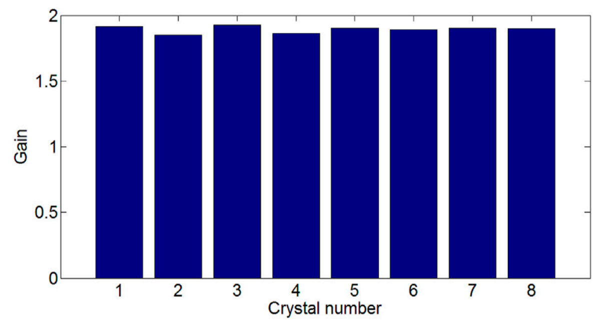

FIGURE 6 | Small signal gain of each amplifier module.

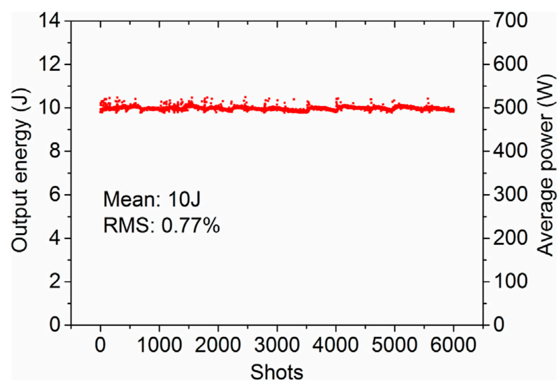

FIGURE 7 | Output energy and average power in 6000 shots.

The laser beam run double passes in the main amplifier and then output from the polaroid plate (P5). A deformable mirror (DM) was used to compress the phase aberration of the laser beam after the output polaroid plate (P5).

KEY ISSUES OF THE LASER SYSTEM

Thermal Management of the Amplifier

Under 50 Hz pumping, the thermal effect of the amplifier was significant. We present the thermal management in detail with theory and numerical simulation in our earlier paper [10]. The surface temperature of each crystal was measured, and the results are shown in **Figure 2**. The average surface temperature of each crystal was about 48–49°C. The surface temperature modulation in the pumping area of a typical surface was 1.05. The defocus of the double pass amplifier chain from thermal was as large as 35λ, which is shown in **Figure 3**. The defocus was pre-compressed by the image transfer lens (L4 and L5) before the laser seed injecting to the main amplifier. The focal length of L4 and L5 was 500 and 1500 mm, respectively, and we set the distance of them to 2400 mm to pre-compress the defocus. The astigmatism from each amplifier module was about 0.9λ. We adjusted the astigmatism at the laser head by mechanism. The residual astigmatism after adjustment was less than 0.1λ, which is shown in **Figure 4**. The depolarization of the amplifier chain was measured, and the result was 16% on a single pass. To compensate the depolarization, we put a 90° quartz rotator (R90) in the middle of the amplifier chain. We use 120 mJ energy as the measurement beam, and the minimum energy of the energy meter was 100 μJ. After compensation, the depolarization could not be measured by an energy meter, which means the depolarization must be lower than 0.1%.

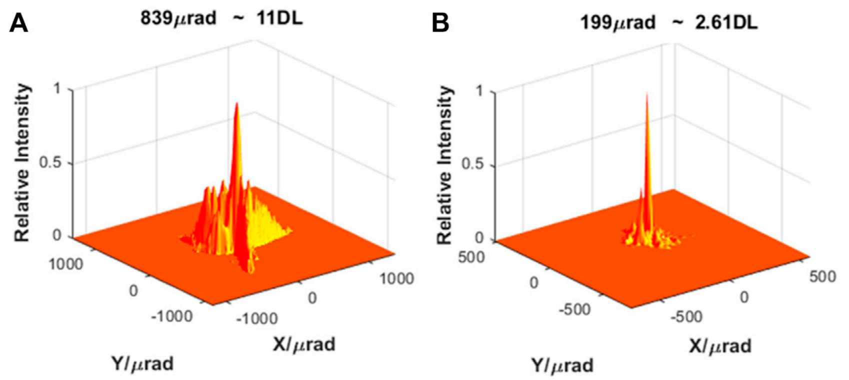

FIGURE 8 | Far field of the laser beam **(A)** before compensation and **(B)** after compensation.

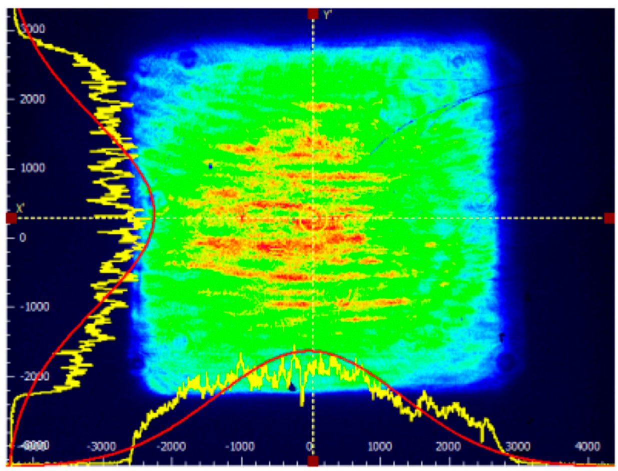

FIGURE 9 | Beam image in the near field.

ASE Control of the Laser Amplifier

The Nd:YAG crystal has a large emission cross area which makes the ASE very remarkable in a large area amplifier. The size of the Nd:YAG crystal was 60 mm × 40 mm × 8 mm, which was larger than that we used in 2018 [6]. Although the aperture was larger, the thickness was increased from 7 to 8 mm, which was a benefit to reduce ASE. The simulation results of different thicknesses and doping concentrations are shown in **Figure 5**. To obtain high energy conversion efficiency, we use a relatively high pumping power with a relatively short duration. The pumping current was 360 A, and the pumping duration was set to 140 μs with a rise edge of 20 μs. To absorb the ASE light, we use Cr^{4+}:YAG as the edge cladding. The absorption coefficient and the width of Cr^{4+}:YAG were 8/cm and 8 mm, respectively. In this condition, the small signal gain was measured and is shown in **Figure 6**.

On the contrary, the edge cladding was used as a thermal balance method to obtain a good beam quality. The principle has been described in [7]. **Figure 7** shows the near field of one pass of an amplifier without edge cladding and double pass of eight amplifiers with edge cladding.

OUTPUT PARAMETERS OF THE LASER

The output parameters of the laser were measured. The output energy was 10 J with the stability of 0.8% (RMS@6000shots). The output energy is shown in **Figure 7**. The far field was compensated by adaptive optics (AO). The far field of the laser before and after compensation is shown in **Figure 8**. The beam quality of the laser was 11 diffraction limited (DL) and 2.6 DL before and after compensation, respectively. The origin of the side-lobes was the marginal residual high-frequency component which could not be compressed by AO. The near field is shown in **Figure 9**. The overall outline of beam distribution was supergauss with thin modulation on the top due to polishing of the crystal. The total modulation of the near field was 1.9.

CONCLUSION

In this letter, a laser beam of energy 10 J with the repetition rate of 50 Hz was realized. For such a high repetition rate, the thermal effect was controlled by uniform pumping and cooling, adjustment of astigmatism and compensation of defocus, and compensation of AO. The beam quality less than 3DL was realized. This confirms the viability of active mirror Nd:YAG amplifier concept, which is scalability to the kilowatt level. Further increases in the average power to 1000 W are expected at the frequency of 100 Hz.

DATA AVAILABILITY STATEMENT

The original contributions presented in the study are included in the article/Supplementary Material, and further inquiries can be directed to the corresponding authors.

AUTHOR CONTRIBUTIONS

XJ was responsible for overall laser design and thermal management. KX was responsible for overall laser integration. XY was responsible for laser energy flow design. ZW was responsible for pump coupling design. XJ was responsible for overall structural design. QX was involved in the development and commissioning of deformation mirror. WW was responsible for laser head design. JC was responsible for switch power supply development. CZ was involved in the development of soft-edge light appendix with high threshold. JZ was responsible for fluid homogenization design. ZP was responsible for miscellaneous light management. KZ was involved in clean management. PL was involved in self-shock inhibition. DH was involved in optical transmission design. QZ gave beam quality control guidance. WZ gave overall guidance.

FUNDING

The research was supported in part by the National Natural Science Foundation of China (NSFC) (Grant No. 62105310).

REFERENCES

1. Bayramian A, Armstrong P, Ault E, Beach R, Bibeau C, Caird J, et al. The Mercury Project: A High Average Power, Gas-Cooled Laser for Inertial Fusion Energy Development. *Fusion Sci Technol* (2007) 52:383–7. doi:10.13182/fst07-a1517
2. Marrazzo S, Gonçalvès-Novo T, Millet F, Chanteloup JC. Low Temperature Diode Pumped Active Mirror Yb̃3+:YAG Disk Laser Amplifier Studies. *Opt Express* (2016) 24(12):12651–60. doi:10.1364/oe.24.012651
3. Yasuhara R, Kawashima T, Sekine T, Kurita T, Ikegawa T, Matsumoto O, et al. 213 W Average Power of 24 GW Pulsed Thermally Controlled Nd:glass Zigzag Slab Laser with a Stimulated Brillouin Scattering Mirror. *Opt Lett* (2008) 33(15):1711–3. doi:10.1364/ol.33.001711
4. Mason P, Divoký M, Ertel K, Pilař J, Butcher T, Hanuš M, et al. Kilowatt Average Power 100 J-Level Diode Pumped Solid State Laser. *Optica* (2017) 4(4):438–9. doi:10.1364/optica.4.000438
5. Mason P, Banerjee S, Smith J, Butcher T, Phillips J, Höppner H, et al. Development of a 100 J, 10 Hz Laser for Compression Experiments at the High Energy Density Instrument at the European XFEL. *High Pow Laser Sci Eng* (2018) 6:e65. doi:10.1017/hpl.2018.56
6. Liu T, Sui Z, Chen L, Li Z, Liu Q, Gong M, et al. 12 J, 10 Hz Diode-Pumped Nd:YAG Distributed Active Mirror Amplifier Chain with ASE Suppression. *Opt Express* (2017) 25(18):21981. doi:10.1364/oe.25.021981
7. Liu T, Feng T, Sui Z, Liu Q, Gong M, Zhang L, et al. 50 Mm-Aperture Nd:LuAG Ceramic Nanosecond Laser Amplifier Producing 10 J at 10 Hz. *Opt Express* (2019) 27(11):15595. doi:10.1364/oe.27.015595
8. Jiang X, Wang Z, Yan X, Xue Q, Dai W, Wu W, et al. LD End-Pumped 12J-10Hz Nd:YAG Pulse Laser. *Proc SPIE* (2019) 2019:113330. doi:10.1117/12.2543001
9. Jiang X, Xiao K, wang Z, Yan XW, Jiang X, Xue Q, et al. Progress of 10J-50Hz Nd:YAG Laser[C]. In: LOT2020; Shanghai (2020).
10. Kai-bo X, Zheng JG, Jiang XY, Jiang XJ, Wu WL, Yan XW, et al. Temperature Characteristics of High Repetition Rate Water-Cooled Nd:YAG Active Mirror Amplifier [J]. *Chin Phys Soc* (2021) 70(3):034203.

Conflict of Interest: The authors declare that the research was conducted in the absence of any commercial or financial relationships that could be construed as a potential conflict of interest.

Publisher's Note: All claims expressed in this article are solely those of the authors and do not necessarily represent those of their affiliated organizations, or those of the publisher, the editors, and the reviewers. Any product that may be evaluated in this article, or claim that may be made by its manufacturer, is not guaranteed or endorsed by the publisher.

frontiers | Frontiers in Physics

TYPE Original Research
PUBLISHED 22 July 2022
DOI 10.3389/fphy.2022.937976

OPEN ACCESS

EDITED BY
Shangran Xie,
Beijing Institute of Technology, China

REVIEWED BY
Xuezong Yang,
Hangzhou Institute for Advanced Study, China
Zhenxu Bai,
Hebei University of Technology, China

*CORRESPONDENCE
Eduardo Granados,
eduardo.granados@cern.ch

SPECIALTY SECTION
This article was submitted to Optics and Photonics,
a section of the journal
Frontiers in Physics

RECEIVED 06 May 2022
ACCEPTED 04 July 2022
PUBLISHED 22 July 2022

CITATION
Echarri DT, Chrysalidis K, Fedosseev VN, Heinke R, Marsh BA, Reich BB and Granados E (2022), Tunable diamond raman lasers for resonance photo-ionization and ion beam production.
Front. Phys. 10:937976.
doi: 10.3389/fphy.2022.937976

Tunable diamond raman lasers for resonance photo-ionization and ion beam production

Daniel T. Echarri [1,2], Katerina Chrysalidis [1], Valentin N. Fedosseev [1], Reinhard Heinke [1], Bruce A. Marsh [1], Bianca B. Reich [1] and Eduardo Granados [1]*

[1]CERN, Geneva, Switzerland, [2]Universidad de Navarra, Tecnun, Spain

Lasers with wide tunability and tailored linewidth are key assets for spectroscopy research and applications. We show that diamond, when configured as a Raman laser, provides agile access to a broad range of wavelengths while being capable of efficient and selective photo-excitation of atomic species and suitable spectroscopic applications thanks to its narrow linewidth. We demonstrate the use of a compact diamond Raman laser capable of efficient ion beam production by resonance ionization of Sm isotopes in a hot metal cavity. The ionization efficiency was compared with a conventional Ti: sapphire laser operating at the same wavelength. Our results show that the overall ion current produced by the diamond Raman laser was comparable -or even superior in some cases-to that of the commonly used Ti:sapphire lasers. This demonstrates the photo-ionization capability of Raman lasers in the Doppler broadening-dominated regime, even with the considerable differences in their spectral properties. In order to theoretically corroborate the obtained data and with an eye on studying the most convenient spectral properties for photo-ionization experiments, we propose a simple excitation model that analyzes and compares the spectral overlap of the Raman and Ti: Sapphire lasers with the Doppler-broadened atomic spectral line. We demonstrate that Raman lasers are a suitable source for resonance photo-ionization applications in this regime.

KEYWORDS
diamond, lasers, tunable lasers, Raman scattering, photo-ionization, resonant ionization, spectroscopy

1 Introduction

Over the years, the capability of light to interact with matter has been widely exploited. In the field of nuclear research, photo-ionization of atoms is one of the key processes for selective and efficient delivery of ion beams. Tunable lasers play a crucial role providing photons that resonantly match the electronic transitions of the atoms. By using multiple resonant steps, sometimes in conjunction with a last, non-resonant excitation step, the ionization potential (IP) can be surpassed and the atom thus ionized. Moreover, for efficient resonance laser ionization, the effective linewidth of the atomic transitions in the experimental environment requires a spectrally matched light source. Thus, lasers are a suitable tool for the research of molecular and atomic structures [1].

At CERN, experiments involving isotope production with the ISOL (Isotope Separation On-Line) method of extraction directly from a high energy proton beam-impacted production target, typically rely on several approaches for ionization, with resonance laser photo-ionization being one of the most convenient and widely applied techniques. This method is applied in what is called the resonance ionization laser ion source (RILIS) [2]. The laser sources are employed to selectively ionize the desired (radiogenic) elements in a hot cavity, after which the ions are extracted and guided through a mass separation system to select the particular isotope of interest. The main purpose of this infrastructure is to provide the Isotope Separator On-Line Device (ISOLDE) facility with pure ion beams for the subsequent study of radioactive isotopes and exotic particles at dedicated experimental setups [3]. Alternatively, atomic and nuclear structure effects can be directly investigated on very low production rates by performing laser spectroscopy directly in the ion source [4].

In general, lasers capable of fulfilling the demanding requirements for high precision atomic studies are hard or expensive to come by. For high efficiency in the ionization process and in non-linear frequency conversion techniques to enlarge the available wavelength range, lasers with a high repetition rate and a high peak power, are required. At the same time, the spectral laser linewidth should match the effective transition linewidth in the experimental environment to address the complete atomic ensemble. For applications at ISOLDE, nanosecond pulse lasers at tens of kHz repetition rate range exhibiting linewidths between 1–15 GHz (for Doppler broadened transitions in hot cavity ion sources at around 2000°C are suitable. Additionally, wide-range tunability is a key attribute, since it allows to access a large variety of transitions of most chemical elements [5]. In the RILIS laser setup, light covering the UV to blue and near-IR spectral regions is provided by solid-state Ti:sapphire (Ti:Sa) lasers, while the visible range and part of the UV range is covered by dye lasers [6]. In contrast to solid-state lasers, dye lasers maintenance is an operationally more challenging task and continuous operation is constrained by regularly required dye changes [7]. Overall, the laser system used at RILIS covers the UV to mid-IR spectrum well, except for the range around 532 nm, which is the wavelength used for pumping of the tunable lasers. Thus, the development of efficient and broadly tunable solid-state laser sources for the visible spectral range entails an interesting challenge since it would on the one hand offer the possibility to replace the spectral range provided by the dye lasers and on the other hand increase the total coverage of accessible wavelengths. The possibility to finally meet these requirements has recently enlivened the exploration of alternative solid-state light sources for ionization experiments.

A proposed solution consists of a continuously tunable diamond Raman laser capable of generating a frequency shift from a Ti:Sa pumping laser, gaining access to the visible spectral range [8]. Furthermore, a compact version of the resonator is able to diversify the spectral coverage by producing multiple Stokes orders while preserving the linewidth of the pump. This laser source was characterized and tested for resonant ionization spectroscopy experiments, by exciting the atomic transition $4s^2\,{}^1S_0 \rightarrow 4s4p^1P_1^0$ of calcium at 422.79 nm. The Ca^+ isotopes were produced inside an atomic beam unit in cross-beam geometry, where a time-of-flight spectrometer was used to measure the ion signal [9]. The results showed that the technology has great potential to cope with the demanding requirements of resonantly exciting atomic transitions of different elements. A pivotal feature here is that the laser operates in what is called the "coherent Raman scattering regime", where the achievable Stokes linewidth is approximately the same as for the pumping light [9].

More detailed evaluation shows that—even if the Raman resonator replicates the average linewidth of the Ti:Sa laser—the spectral lineshape and distribution of the axial longitudinal modes within the lasing bandwidth is substantially different. Thus, the performance of the Raman laser system to efficiently ionize atoms in the typical application environment required further investigation. Moreover, the arrangement of the cavity produces a specific spectral content, for instance a simple hemi-spherical setup compared to a z-fold design with a longer length, will generate substantially lower number of spectral modes but with an increased axial mode linewidth due to noise. Hence, studying the spectral performance of laser pulses with varied spectra would allow the construction of more efficient ionization sources.

In order to understand the interplay between the laser spectral features and the atomic transition of interest we have developed a computational model that simulates the excitation process of lasers with arbitrary spectral content. This enables us to compare the different laser technologies for producing the most convenient pulses. We complete the study by experimentally demonstrating the performance of Raman lasers for efficient ionization applications, showing a comparable performance in the ion current produced compared to the Ti:Sa laser when operating in the ionization saturation regime.

We also study the behaviour of Raman lasers considering their dependency on operating wavelength. The computational model also calculates the effect of the polarization angle in terms of accessibility to the maximum Raman gain [10]. In combination with the aforementioned spectral model, the behaviour of a Raman resonator can be predicted and optimized, being able to calculate key designing parameters for Raman laser construction, such as the lasing threshold or the slope efficiency.

Needless to say, the diamond Raman laser applicability is not reduced to spectroscopy experiments. The combination of outstanding optical and thermal properties makes them particularly interesting for a variety of applications; such as construction of high power lasers [11, 12], or integrated photonic devices [13, 14] at extended wavelength ranges [15, 16] providing wide tunability [17], and quantum applications [18, 19]. In fact, selective and efficient ionization is interesting in quantum technologies as it provides means for producing atomic quantum states with high fidelity [20, 21].

In this work, we present the different tools developed for Raman laser design and characterization, along with the latest improvements towards wavelength diversification thanks to efficient cascading, narrow linewidth preservation, and ionization efficiency depending on the spectral properties of the laser pulses. We compare the results from our mathematical model with results from photo-ionization experiments, where samarium (Sm) atoms were resonantly ionized in a two-step ionization scheme, consisting of a resonant first step at 433.9 nm and a second step for non-resonant ionization above the IP at 355 nm. With this setup saturated ion beam efficiency measurements were performed, to compare the performance of the Raman and Ti:Sa lasers for the excitation of $^{152}Sm^{+}$ isotopes, willing to verify the suitability of the new technology.

2 Widely tunable diamond Raman laser design

For constructing Raman lasers functional across a broad spectral range, it is important to consider the dependency of the Raman gain with the wavelength as well as the spectral response of the optical elements used in the resonator. We present a multi-Stokes Raman scattering simulator that takes this wavelength dependency into account, by appropriately modifying the standard coupled differential equations for steady-state Raman processes proposed in the literature [22]. For nanosecond pulses, this theory reproduces with enough accuracy the dynamic nonlinear Raman process. Mathematically we have that

$$\begin{aligned}\frac{dI_P}{dz} &= -\frac{\omega_P}{\omega_{s1}} g_{R1} I_P I_{s1} - \alpha_P I_L,\\ \frac{dI_{s1}}{dz} &= g_{R1} I_P I_{s1} - g_R \frac{\omega_{s1}}{\omega_{s2}} I_{s1} I_{s2} - \alpha_{s1} I_{s1},\\ \frac{dI_{s2}}{dz} &= g_{R2} I_{s1} I_{s2} - g_R \frac{\omega_{s2}}{\omega_{s3}} I_{s2} I_{s3} - \alpha_{s2} I_{s2},\end{aligned} \tag{1}$$

where I_P refers to the pump intensity, while I_{sx} defines the Stokes intensity with x donating the order of the Stokes. In the same way, ω is the angular frequency and g_R the Raman gain at the pumping frequency. Finally, g_{Rx} refers to the Raman gain associated to each Stokes order and α_x to the corresponding loss coefficients. Assuming that cavity losses predominate over the system, it is reasonable to consider the loss coefficients α_x from Eq. 1 to be negligible, especially since their effect is often not perceivable for diamond in the visible spectral range [22]. The Raman gain for higher Stokes orders g_{Ri} is calculated as follows [23],

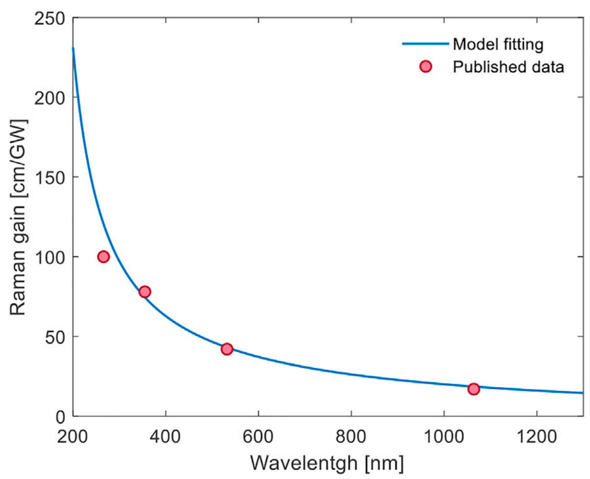

FIGURE 1
Wide-range fit of a diamond Raman gain model according to [25] (blue) on experimental data (red) from the literature [15, 24].

$$g_{Ri} = g_R(\omega_P)\frac{\omega_{si}}{\omega_P}, \tag{2}$$

where ω_{si} corresponds to the angular frequency of the higher Stokes orders and ω_P the angular frequency of the pump. To determine g_R for each of the simulated wavelengths a fit across a broad spectral range was computed based on the experimental data obtained from the literature [15, 24]. It is important to remark that the expected theoretical value for g_R in the UV was considerably higher than the measured one [15]. The resulting fit is depicted in Figure 1 and it is based on the wavelength dependant Raman gain formula found in [25]:

$$g_R(\omega_P) = \frac{A(\omega_P - B)}{(C - \omega_P^2)^2}, \tag{3}$$

where in our case for diamond, the value for each constant was $A = 976 \cdot 10^{48}$, $B = 251 \cdot 10^{12}$ and $C = 169 \cdot 10^{14}$.

The obtained Raman gain parameters were adjusted depending on the pump polarization state of both the pump and Stokes, by using the adequate Müller matrix for each particular case. Here, the light propagation occurs through the <110> crystallographic axis as explained in [10]. Under these conditions, the polarization angle that maximizes the cascading process is ±54.7° with respect to the [001] direction, since it produces Stokes orders with polarization states parallel to the <111> crystallographic axis, maximizing the gain. We refer to cascading as the process in which not only the photons from the pumping light are Raman shifted to produce a first Stokes, but

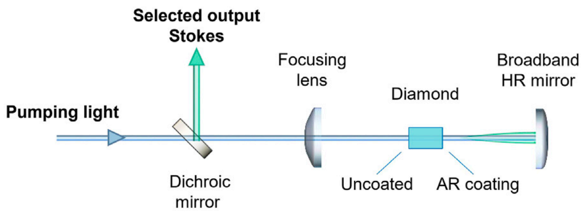

FIGURE 2
Schematic of the hemi-spherical diamond Raman cavity simulated in the Stokes generation mathematical tool, where all the elements depicted and the spacing between them are variable and considered in the simulator.

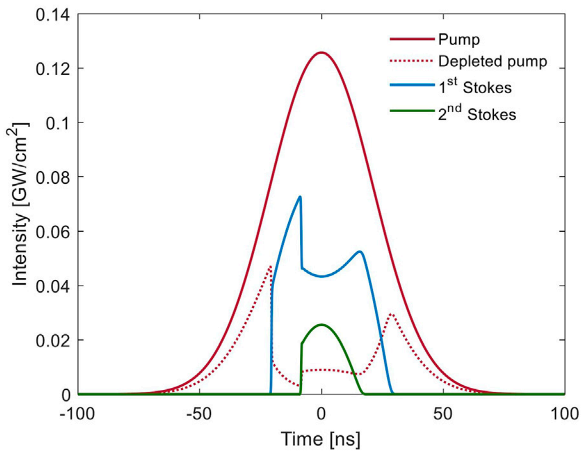

FIGURE 3
Example of the simulated depleted signal (dotted red) of a nanosecond laser pulse (solid red), along with the calculated first (blue) and second (green) Stokes generation.

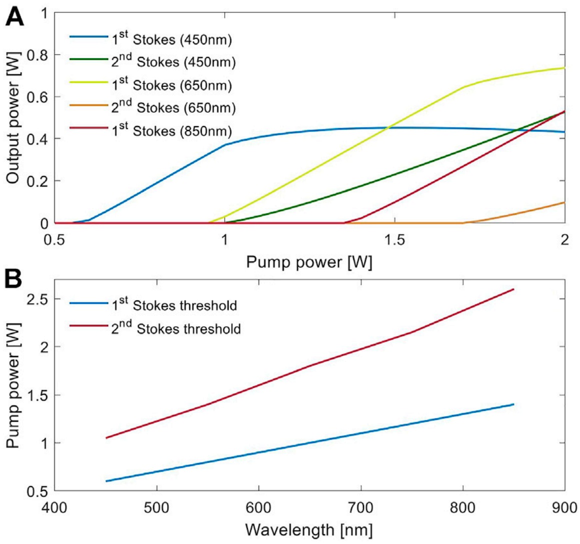

FIGURE 4
(A) Simulation results of Stokes output power for different pump laser wavelengths (450 nm, 650 and 850 nm) under same conditions and alongside a range of different pump powers. **(B)** Required pump power to produce first and second Stokes (lasing threshold) at a broad spectral range in the visible.

when this process is replicated in order to produce a second Stokes and higher Stokes orders consecutively.

In order to design a Raman converter that is wavelength agile and provides a useful output at a broad spectral range, we have opted for a minimalist hemi-spherical cavity design composed uniquely of a Raman medium and a curved retro-reflector as depicted in Figure 2. In this arrangement, the output coupler is the uncoated surface of the diamond, while the coatings of both the second diamond surface (anti-reflection) and the curved mirror (high reflector) are broadband and operating in the 450–850 nm range. The pump was focused into the diamond by means of a focusing lens, producing a spot size of approximately 50 μm diameter ($1/e^2$). The separation between pump and Stokes beams is provided by a dichroic mirror that can be chosen according to the pumping wavelength and is not part of the resonator. The spectral output produced (in terms of number of longitudinal modes) by such a resonator depends on the cavity length and the pumping conditions, which will be discussed in section 3 in more detail.

Specifically, the previously presented differential equations Eq. 1 are resolved for the cavity illustrated in Figure 2 by dividing the diamond bulk into differential slabs and neglecting dispersion and diffractive effects through the diamond thanks to its relatively small size compared to the Rayleigh length of the cavity modes. The pump light travels through the crystal twice, while the Stokes orders resonate in the cavity. We only considered here cascading up to the second Stokes order. Computationally, the equations were solved by employing a fixed-step finite differences method, with a grid fine enough to accurately reproduce the temporal dynamics of the Raman process. Regarding the boundary conditions of the diamond, in the anti-reflection coating we assumed non-perfect behaviour so the transmission was set to a value of 0.95. While for the uncoated side reflected light into the resonator was calculated by the Snell law in combination of the Sellmeier equation for diamond. Additionally, a loss factor was applied to the re-injected light since not all the reflected light in the uncoated surfaces necessarily resonates back. In particular the value for the re-injected pump light was negligible and this is why we considered that it just propagates twice through the crystal.

The simulated pumping pulse resembles the one used in the experiments produced by a gain-switched Ti:Sa laser described in section 4. For the simulated cavity parameters the length of the crystal is selected to be 5 mm, the output coupler corresponds to the uncoated side of the crystal and the high reflector concave mirror is assumed to be ideal (100% of reflectivity). A 50 ns pulse is focused into the Raman medium with an intensity exceeding 0.1 GW/cm^2, the corresponding temporal envelope is represented as a solid red line in Figure 3. Here it can also be appreciated the depleted pump (discontinuous red line), along with the produced first and second Stokes pulses. As the pump pulse increases in intensity, it reaches the lasing threshold and the first Stokes is produced. The growth rate of the Stokes pulse is fast thanks to the small resonator dimensions, quickly depleting the available pump. A similar dynamic is observed when the lasing threshold for the second Stokes is reached, represented by the pronounced depletion in the first Stokes lineshape. The fast dynamics observed in the temporal pulse shapes are a consequence of the relatively high losses and compactness of our laser resonator. The resulting Stokes pulses have non-Gaussian envelopes and a duration that is considerably shorter than the pump pulse. Such effect was experimentally observed also in [9].

The laser dynamics depend on the pump pulse intensity. In order to study the energy transfer dynamics, we simulated a scan scanned the pump power producing different cascading conditions, as shown in Figure 4, where we compare the produced Stokes output powers for three different pumping wavelengths (450, 650, and 850 nm) at the same pump intensity and maintaining the spot size. It is obvious that thanks to the wavelength dependency of the Raman gain, Raman lasers will be more efficient at shorter wavelengths, and they should require a lower power for reaching the lasing threshold. Particularly, Figure 4A shows the different output powers for the first and second Stokes orders depending on the pumping power at different wavelengths. The first Stokes output power is capped whenever the second Stokes lasing threshold is reached, which is also observed in Figure 3. Figure 4B illustrates the calculated lasing threshold of the Stokes as a function of the wavelength. The cascading process can be optimized in terms of necessary cavity reflectivity and pump intensity with the relatively simple model presented here.

The spectral content of the laser pulses plays a crucial role in the efficiency of the atomic photo-ionization process. In our laser, the spectral properties of each pulse strongly depend on the resonator length, round-trip reflectivity, and Raman gain. In particular, the number of longitudinal modes and the linewidth of each of them must be considered to assess the ultimate performance of Raman lasers for photo-ionization efficiency and spectroscopy applications.

3 Spectrum dependant excitation model

The interaction of light with atomic orbitals, and subsequent photo-ionization processes, has been widely studied in the literature, including the description of multi-step laser ionization processes [1]. The most simple and general case is to study the two-level atom interaction. Here we will refer to the two states as $|1\rangle$ and $|2\rangle$ with resonance frequency $\nu_{21} = (E_2 - E_1)/h$ and pumping frequency ν_P with detuning $\delta = \nu_P - \nu_{21}$. Under steady state conditions and following [26] the excited state population ρ is given by

$$\rho = \frac{S_0/2}{1 + S_0 + 4\delta^2/\xi^2}, \tag{4}$$

where ξ is the spontaneous decay rate of state $|2\rangle$ and S_0 is the resonant saturation parameter defined as $S_0 = I/I_S$ with the saturation intensity I_S given by

$$I_S = \frac{\pi hc}{3\lambda_P^3 \tau}. \tag{5}$$

Here λ_P is the center wavelength of the ionizing laser and τ the lifetime of the excited state. However, the calculation of ρ is not taking into account the effect of the spectral content in the ionization process. In this work, we aim at quantifying this effect by proposing a laser spectrum-dependant excitation model.

Our simulation tool calculates the spectral overlap of defined laser-like spectra with the spectrum produced by a heated cloud of Sm atoms (although the same formalism applies to any atomic species). This spectrum would have a Gaussian envelope stretched by the Doppler broadening of the atoms ruled by the oven temperature and given by [27].

$$\Delta\omega_{Doppler} = \frac{2\omega_0}{c}\sqrt{2\ln 2\frac{kT}{m_0}}, \tag{6}$$

where ω_0 is the central frequency of the Sm atom transition, k is the Boltzmann constant, T is the temperature of the oven, c is the speed of light and m_0 is the atomic mass of Sm. The Gaussian lineshape is given by the fact that each of the atoms presents a Lorentzian natural linewidth at a random frequency normally distributed across the whole spectrum defined by the Doppler effect. As determined by the central limit theorem, the summation of a high enough number of Lorentzian lineshapes results in a Gaussian one [28]. The computed Gaussian lineshape for Sm at the experiment temperature of 2000°C presented a full width half maximum (FWHM) linewidth of 1.81 GHz. Which lineshape would be defined as

$$A_{Sm}(\nu) = e^{-\frac{(\nu-\nu_0)^2}{\Delta\nu_{Doppler}}}, \tag{7}$$

where ν_0 is the central frequency of the transition and the lineshape is normalized in amplitude. Note that in general, in the excitation process, the atoms are individually ionized, and therefore during the saturation process the spectral shape of the absorption will vary accordingly. This is similar to what is known in laser systems as "spectral hole burning".

Along with the atoms spectral distribution, we also define the spectral modes of two ideal laser sources similar to the ones employed in the experiment, based on theoretical models [29]

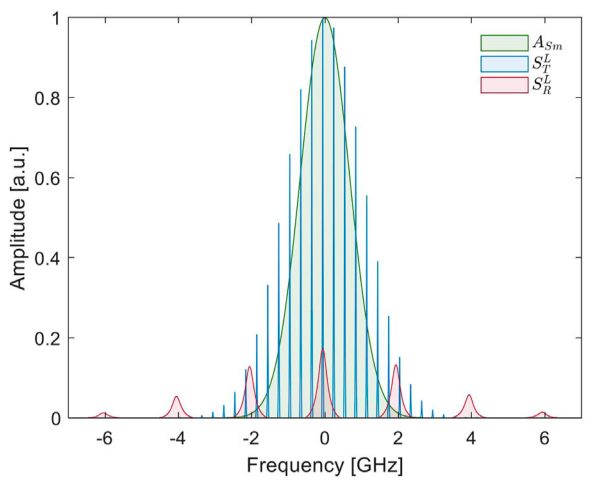

FIGURE 5
The different generated spectra for simulations, including the Sm Doppler broadened Gaussian and the Ti:Sa and Raman laser spectra, both presenting Lorentzian truncated modes.

and selecting envelope linewidths better matching the Doppler broadening than the real ones. The calculated spectrum to resemble the Raman laser behaviour was defined as a Gaussian envelope of 6.4 GHz FWHM linewidth with 300 MHz linewidth longitudinal modes separated by a free spectral range (FSR) of 2 GHz. For the laser modes modeled here, we generated the spectrum by summing truncated Lorentzian lineshapes, where the offset is determined by the lasing threshold as was proposed in [30]. For comparison purposes we generated a similar spectrum but with Gaussian axial mode lineshapes, in order to quantify the effect of the modes spectral distribution. Regarding the Ti:Sa laser representation, the generated envelope had a FWHM linewidth of 3.1 GHz with 20 MHz linewidth modes separated by a FSR of 300 MHz, as we assumed Fourier-limited modes. The resulting spectra can be observed in Figure 5, where we present together the Gaussian envelope for the Doppler broadened transition of the Sm atoms, and the spectra for the Raman and Ti:Sa laser with truncated Lorentzian modes.

To mathematically construct the laser spectrum $S(\nu)$ we first need to compute the product of the laser emission spectral bandwidth $A(\nu)$ with the cavity longitudinal modes. Since we evaluate the spectra for two different modal lineshapes, for the Gaussian lineshape axial modes $m_j^G(\nu)$ we will have a resulting laser spectral shape $S^G(\nu)$ of

$$\begin{aligned} S^G(\nu) &= A(\nu)\cdot\sum_j m_j^G(\nu) \\ &= A_0^G e^{-\frac{(\nu-\nu_0^e)^2}{2\gamma_e^2}}\cdot\sum_j e^{-\frac{\left(\nu-\nu_{0_j}^m\right)^2}{2\gamma_m^2}}, \end{aligned} \tag{8}$$

and for the Lorentzian lineshape axial modes $m_j^L(\nu)$ a resulting laser spectral shape $S^L(\nu)$ of

$$\begin{aligned} S^L(\nu) &= A(\nu)\cdot\sum\nolimits_j m_j^L(\nu) \\ &= A_0^L e^{-\frac{(\nu-\nu_0^e)^2}{2\gamma_e^2}}\left(\sum\nolimits_j \frac{\gamma_m/\pi}{\left(\nu-\nu_{0_j}^m\right)^2+\gamma_m^2}-T_L\right)^+ \end{aligned} \tag{9}$$

where γ_e is the half width half maximum (HWHM) linewidth of the envelope and ν_0^e the central frequency. γ_m is the HWHM linewidth of the mode, and the central frequency of the modes is defined as $\nu_{0_j}^m = \nu_0^m \pm j\Delta\nu_m$ with $j = 0, 1, 2 \ldots$ with $\Delta\nu_m$ equal to the corresponding free spectral range (FSR). T_L accounts for the lasing threshold of the longitudinal modes which we take as 0.1 in our simulations.

The super-index defines the distribution employed for the modes (G for Gaussian, L for Lorentzian), and the sub-index will define the specific laser (T for Ti:Sa, R for Raman). Thus, $S_R^L(\nu)$ will refer to the Raman laser spectrum with Lorentzian lineshape axial modes, whereas $S_R^G(\nu)$ will refer to Gaussian lineshape axial modes; correspondingly, $S_T^L(\nu)$ will refer to the Ti:Sa laser spectrum with Lorentzian and $S_T^G(\nu)$ will refer to the Ti:Sa laser spectrum with Gaussian lineshape axial modes.

In order to compare laser pulses with the same energy, we set $\int_\nu S_T(\nu) = \int_\nu S_L(\nu)$. The relative scaling of the Raman and Ti:Sa laser spectra is taken such max $(A_T(\nu)) = 1$, meaning that the amplitude of the spectral envelope of the Ti:Sa laser is at the threshold for the saturation of the ionization process.

The resulting ion current is then proportional to the integral of the overlap of the Raman and Ti:Sa lasers spectra with the Sm absorption distribution. To calculate the excitation ratio $\Theta_{R,T}^{G,L}$ approximated by the overlap we have

$$\Theta_{R,T}^{G,L} = \frac{\int_\nu A_{Sm}(\nu)\cdot S_{R,T}^{G,L}(\nu)\, d\nu}{\int_\nu A_{Sm}(\nu)\, d\nu}. \tag{10}$$

To obtain a relative performance of the excitation process and the theoretical saturation curves of each laser spectrum, a power scan of the overlap between their spectra (S_R^L, S_R^G, S_T^L and S_T^G) and the Sm Doppler broadened Gaussian envelope (A_{Sm}) was simulated. For this computation, the amplitude of all the simulated spectra were multiplied by a scaling factor k ranging from 0.1 to 100, which is a broad enough range to determine the saturation point and the behaviour of the lasers in experimental conditions, as will be seen in section 5. All the calculations were performed over 20,000 laser pulses with uniformly distributed ν_0^m values and therefore the average results for all of the simulated pulses were calculated at all the different powers. Note that for k values of less than 1, the result resembles non-saturated ionization conditions, whereas for $k > 1$, the saturation process starts for the Ti:Sa laser, although not necessarily for the Raman laser.

The model agrees well with the obtained experimental data in terms of the slope behaviour and saturation point for both lasers, as will be shown in section 5. For our particular case, we consider the saturation effect by capping the increment of the signal power

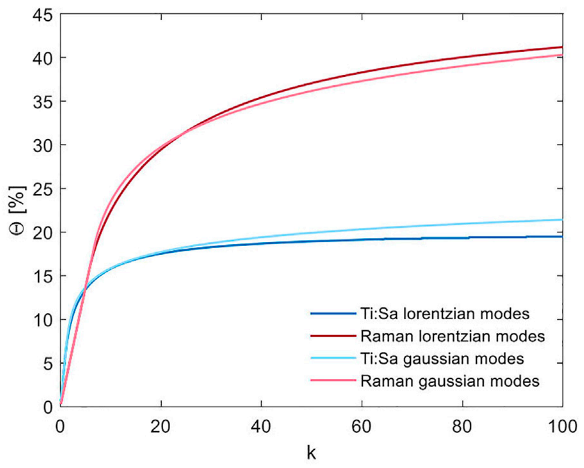

FIGURE 6
Saturation curves simulated by the model based on the overlap of the laser spectra with the Doppler Gaussian spectrum of the Sm atoms A_{Sm} (rate of ionized atoms) depending on the scaling factor k that emulates the laser power.

to a fixed spectral amplitude. After computing the ionization signal for a wide laser power range by applying a scaling factor to the laser spectra, the laser spectral function is capped to one to reproduce the effect of ionization saturation. We consider that this approximation is good enough to verify the points of interest in this work, although the effect of spectral hole burning is not considered in this model [30]. Thus, by introducing the aforementioned function capping $[S_{R,T}^{G,L}(\nu)\cdot k]_0^1$ (which limits the function between 0 and 1), the rate of ionized atoms defined in Eq. (10) will result in

$$\Theta_{R,T}^{G,L} = \frac{\int_{\nu} A_{Sm}(\nu)\cdot\left[S_{R,T}^{G,L}(\nu)\cdot k\right]_0^1 d\nu}{\int_{\nu} A_{Sm}(\nu)\, d\nu}. \tag{11}$$

Employing Eq. 11, we can then calculate the relative ionization efficiency for both lasers assuming Lorentzian and Gaussian axial modes. The results using the spectra shown in Figure 5 are depicted in Figure 6. Here, it can be seen that wider spectral modes, as the ones generated for the Raman spectrum, enhance by nearly a factor of two the excitation capability comparing equivalent laser powers, regardless of the assumption of axial mode spectral shape. Meaning that non-ideal, thus noisy, laser sources with broadened spectral modes are more suitable for excitation or ionization processes based on the spectral overlap approach presented in this work.

4 Experimental setup

In order to determine the ionization efficiency of the diamond Raman laser, its performance was compared with the ionization capabilities of a Ti:Sa laser, which is commonly used at RILIS. This comparison was carried out in a laser ionization setup similar to the one used at ISOLDE. After ionization of the Sm atoms with the ionization scheme and setup depicted in Figure 7 the Sm was mass separated and the ions detected by a Faraday-cup (FC).

The Offline-2 facility at CERN provides a testbed for the technology to be subsequently used in the ISOLDE facility and here our experiments took place. The frontend is equivalent to the one in the ISOLDE facility, details about this facility can be found in [3]. The process by which atoms are resonantly ionized can be followed by observing Figure 7A. The laser beams are focused into the ion source, where a cloud of atoms is formed in a hot cavity, which consists of a refractory metal tube, with an internal diameter of 3 mm and a length of 34 mm, for further details see [4]. The atoms are ionized by the photons. The produced ions are then extracted as a beam by an extraction electrode at a potential difference of 30 kV, and the beam is transported through a system of ion beam optics. This beam can be characterized by an instrumentation setup composed by a Faraday-cup and a beam scanner. Afterwards, an isotopically pure ion beam is obtained by selecting only the isotopes of interest ($^{152}Sm^{+}$) with a mass separator dipole magnet. Again, the ion beam intensity can be obtained from measurements with a Faraday-cup and the beam shape can be investigated with a beam scanner set.

The laser light in charge of the ionization process is delivered from an adjacent laser lab. The setup employed for this experiment is depicted in Figure 7B, while the two color ionization scheme followed to ionize the Sm atoms is illustrated in Figure 7C. The first step transition $4f\,^{6}6s^{2} \rightarrow 4f\,^{5}(6F\,^{\circ})5\,d6s^{2}$ is provided by the two different laser sources for comparison. On the one hand, we have a frequency-doubled grating tunable Ti:Sa laser presenting an output maximum power of 900 mW at 433.9 nm wavelength and 10 kHz repetition rate. It is arranged in a Z-fold geometry and the intra-cavity doubling was obtained with a Beta Barium Borate (BBO) crystal, cavity mirrors were conveniently coated for the operation range, for further information see [31]. On the other hand, we have the hemi-spherical diamond Raman cavity composed by a 6 mm diamond crystal acting as the Raman medium and a 50 mm ROC concave mirror. A half-wave-plate (HWP) was used to control the polarization of the pump, a 150 mm focusing lens to pump the diamond, and a dichroic crystal to separate the pump from the output first Stokes. The resonator was encompassed this way by the uncoated side of the crystal (approximate reflectivity of 17%) and the broad high reflectivity (~99%) concave mirror, presenting a consequent FSR of around 2 GHz. The laser presented a maximum output power of 400 mW at 433.9 nm and 10 kHz repetition rate. The Raman laser was pumped by a tunable Ti:Sa cavity frequency-doubled by a BiB_3O_6 (BiBO) crystal and producing a 1 W maximum pump power at

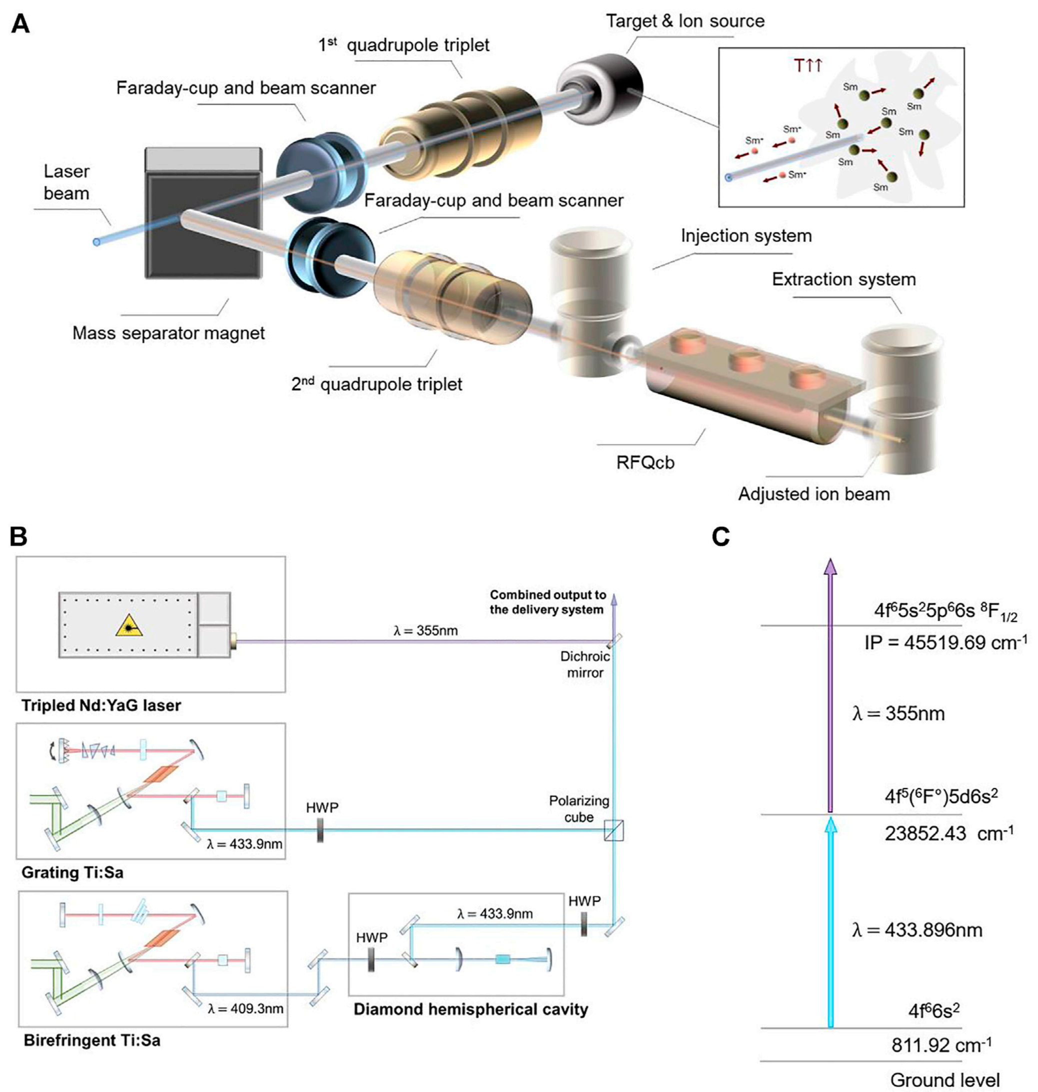

FIGURE 7
(A) Sketch of the Offline-2 beam line with Sm atoms heated in the hot cavity, which are consequently ionized by a laser beam, producing a pure ion beam after the mass separator. In the experiment the final measurements of the ions were performed in the second FC, meaning that the elements shown in transparent depiction were not used. **(B)** Laser setup presenting the Nd:YAG laser for non-resonant ionization into the continuum, the grating Ti:Sa used for generating the first step and the diamond Raman laser, pumped by the birefringent Ti:Sa, also used for the first step. Additionally, the power control system for adjustment of the pump laser power composed by half-wave-plates and a polarizing cube is shown. The first and second step laser beams were combined with a dichroic mirror. **(C)** The two steps color scheme employed for the experiment including the resonant first step and the non-resonant second step surpassing the ionization potential.

409.3 nm. Frequency stability was equal and below 0.005 cm^{-1} for both Ti:Sa lasers, and consequently identical for the Raman laser. For further details regarding the Raman resonator see [9]. Both lasers performed separately the first resonant excitation step of the Sm atoms. In order to be able to measure the ion production saturation curves for these lasers, a second non-resonant step was required. For this purpose, a high power frequency-tripled Q-switched *InnoSlab* Nd:YAG laser from Edgewave © was utilized, with a maximum power of 10 W at 355 nm wavelength. The output was synchronized in time and optimized for each of the two lasers to be able to suitably perform the ionization scheme presented in Figure 7C.

The beam characterization was performed by measuring on-line the center wavelength and linewidth (of the spectral envelope of the modes) of the lasers using a *HighFinesse/Ångstrom WS/6* wavemeter with a resolution better than < 0.066 cm^{-1}. The obtained data was checked by measuring the generated ion current while performing a frequency sweep, obtaining the resulting linewidth of the convolution between the lasers' and the transitions linewidth, since the measurement was taken below

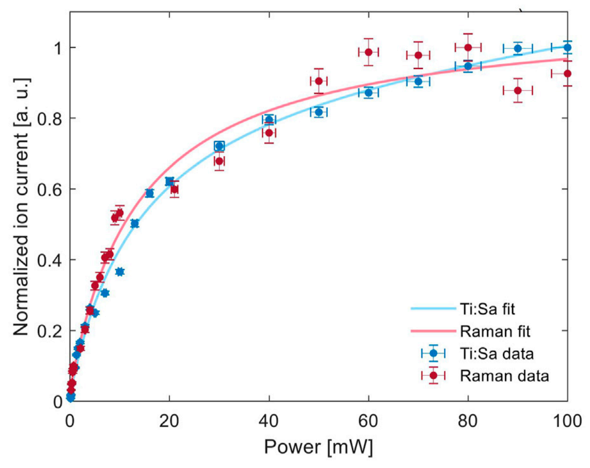

FIGURE 8
Normalized values of the measured ion current for the Raman and the Ti:Sa lasers depending on the output power of each laser along with their corresponding fits and the obtained saturation point.

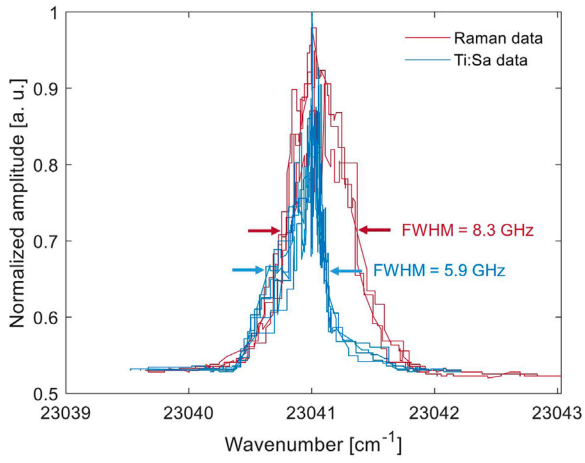

FIGURE 9
Measured spectra for the excitation of the transition while performing a frequency sweep with the Raman and Ti:Sa lasers wavelength and the resulting linewidths for both convolutions.

the saturation point. In addition, the spot size of each laser was measured by utilizing a *Basler acA1920-40 gm* CMOS camera and post-analysis of the image.

5 Results

As mentioned before, in this experiment ion beams were produced by using the presented two lasers in combination with a frequency-tripled Nd:YAG laser. The generated ion current of ^{152}Sm ions in the Faraday-cup was measured for different output powers of the Raman and Ti:Sa resonators within a range of ~0.15–100 mW. The obtained results are depicted in Figure 8, along with their corresponding fits.

For comparison purposes and to corroborated the mathematical model presented here, it is known from the literature [32] that the measured ion current $F(p)$ in an ionization process can be approximated as

$$F(P) \propto I_0 + C_1 \frac{1}{1 + (P/P_S)} + C_2 P, \tag{12}$$

where p is the absorbed laser power, P_S the saturation power, I_0 the background ion current, C_1 is a constant and $C_2 P$ the linear term for the non-resonant photo-ionization contribution. Which for our measurements $I_0 = 339.4$ for the Raman fit, $I_0 = 158.1$ for the Ti:Sa fit, $C_1 = -329.7$ for the Raman fit, $C_1 = -154.7$ for the Ti:Sa fit, $P_S = 13.54$ mW for the Raman fit, $P_S = 13.97$ mW for the Ti:Sa fit, $C_2 = 0.0286$ for the Raman fit and $C_2 = 0.2566$ for the Ti:Sa fit. The obtained curves follow the predicted behaviour in the simulation as can be observed in Figures 8A,B. However, the measurements were performed under unstable conditions, meaning that the obtained values for each laser can not be compared in terms of absolute ion current. Charging and discharging effects of the ion optics could be observed through instabilities in the delivered ion beam, leading to the total ion current changing over time. This problem has been possible to solve only after the experiment, meaning that the total observed ion current in each of the data sets is different. The dataset depicted here was selected among multiple different measurements, as it presented the smallest deviations between the first and last point measured at the same power of the laser for which the saturation was measured. Thus, for comparison purposes we normalized the obtained data by the maximum ion current measured ofr each laser as can be seen in Figure 8. The values obtained here and in the fits parameters provide then comparable information, as the saturation power P_S is independent of the absolute measured ion current. The presented results not only demonstrate that the diamond Raman laser is a suitable tool for efficient photo-ionization, but the performance is at least comparable to the current technology. To provide further evidences about the spectral advantage that the model suggests, additional research is required under more stable conditions with constant ion beam intensities.

Regarding the spectroscopic measurements of the Sm transition line using both lasers, Figure 9 shows a comparison resulting from frequency sweep scans, representing the convolution between the lasers' spectral envelopes and the Sm transition's linewidth. For Gaussian linewidths the total measured linewidth is approximately $\gamma_T = \sqrt{\Delta\omega_{Doppler}^2 + \gamma_e^2}$. Which is 8.3 GHz for the Raman convolution, this is around 8.1 GHz for the Raman linewidth and 5.9 GHz for the Ti:Sa convolution, meaning that the laser linewidth itself is around 5.6 GHz.

Moreover, the model assumes that the beam spot size is identical for both laser sources. The ion current was optimized for each of the laser beams by optimization of the focal position inside the ion source. The spot size measurements showed that when removing the ion source after the experiment and placing the camera in the same position, the spot size of the Raman laser was around 50% bigger than the Ti:Sa in the horizontal axis. Nevertheless, the area of interaction is smaller than both beams spot size (3 mm of interaction against over 5 mm of beam size), meaning that performing a fair comparison of the ionization efficiency for both lasers, within the experiment and with respect to the theoretical results, is more complex. In spite of these difficulties, the results appear to be promising and suggest that the presented simple model is a convenient tool for laser source-selection and optimization of their spectral characteristics.

6 Conclusion

In this work we consider the aspects that affect diamond Raman laser performance as resonance ionization sources for ion beam production. We presented two mathematical tools that try to bring some detailed explanation into what was observable during not only this experiment, but also previous studies. The main results are the demonstration of the wide and continuous tunability of these kind of lasers, which at the same time preserve the pump's spectral linewidth and exhibit a theoretically more convenient modal distribution for atomic photo-ionization than some other conventional sources. These findings could in consequence lead to a consideration of alternative photonic sources for nuclear and quantum applications which are better matched to the requirements of excitation of the electronic transitions.

The herein presented models show that laser cavities with broader spectral modes, which have specific spectral features that have an impact in the efficiency of resonance ionization processes. This is due to the fact that the better the spectral overlap with the transition is, the better the excitation capability becomes, suggesting that a rather noisy pulse will better match the Doppler-broadened transition than a source with a cleaner spectral profile. Since the modal lineshape is broadened and the effective overlap area is increased. This is particularly appreciable when ionizing in the saturation regime, where the spectral overlap integral is two times higher for the proposed noisy spectrum than the cleaner one. The Stokes generation simulator provides useful designing approaches for Stokes generation and cascading efficiency maximization, such as the optimal pump polarization angle or the most suitable parameters to reduce the lasing threshold.

In fact, the presented results provide useful information for the design of optimal Raman resonators, as key parameters to be considered when efficient Stokes generation and cascading are desired have been proposed. Moreover, parametric simulations such as the ones depicted in section 2, suggest that it is overall more efficient to perform frequency alterations, like frequency doubling, to the pumping light rather than to the Raman shifted output, which is an important aspect to consider when developing a Raman laser system.

The experiment showed that the presented hemi-spherical diamond Raman cavity followed the models predictions, being able to efficiently ionize Sm atoms. Since the Raman laser can extend the Ti:Sa laser spectral coverage while preserving the linewidth and its continuous tunability, the technology serves as an all-solid-state solution to less convenient laser sources for nuclear and atomic experiments. Moreover, the results suggest that the overall ionization performance of the current light sources can be improved by selecting light sources with particular spectral properties, meaning that other fields such as quantum technologies, could benefit from this enhancement. Particularly, its spectral properties could improve the fidelity of the quantum states of ions as it can perform atomic excitation with higher probability. The technology can also bridge in a simple manner the gap between 450 and 650 nm, which is otherwise hard to reach by using other available solid-state light sources based on nonlinear frequency conversion. Allowing atomic manipulation of desired isotopes like $^{133}Ba^{+}$ [21] in a simplified way. In conclusion, this work provides evidence of the capabilities of diamond Raman lasers in the field of efficient resonance photo-ionization.

Data availability statement

The raw data supporting the conclusion of this article will be made available by the authors, without undue reservation.

Author contributions

The manuscript was written and prepared by DE and EG. The mathematical model conception and development was performed by DE and EG. All the authors contributed to the preparation and installation of the laser setup, while the design and installation of the Raman resonator was performed by DE and EG. The beamline and hot cavity preparation was performed by KC and RH. All authors contributed to manuscript revision, read, and approved the submitted version.

Funding

This project has received funding from the European Union's Horizon 2020 research and innovation programme under grant agreement No 861198–LISA–H2020-MSCA-ITN-2019 and it was also partially funded by CERN (Knowledge Transfer Fund—Singular Light project).

Conflict of interest

The authors declare that the research was conducted in the absence of any commercial or financial relationships that could be construed as a potential conflict of interest.

Publisher's note

All claims expressed in this article are solely those of the authors and do not necessarily represent those of their affiliated organizations, or those of the publisher, the editors and the reviewers. Any product that may be evaluated in this article, or claim that may be made by its manufacturer, is not guaranteed or endorsed by the publisher.

References

1. Letokhov VS. *Lasers in atomic, molecular, and nuclear physics*. Singapore: World Scientific Publishing Co. Pte. Ltd. (1987). p. 422.

2. Marsh B Resonance ionization laser ion sources. In: Bailey R. editor. *CAS - CERN accelerator school : Ion sources* (2013) 61. doi:10.5170/CERN-2013-007.203.61

3. Catherall R, Andreazza W, Breitenfeldt M, Dorsival A, Focker GJ, Gharsa TP, et al. The ISOLDE facility. *J Phys G: Nucl Part Phys* (2017) 44:094002. doi:10.1088/1361-6471/aa7eba

4. Fedosseev V, Chrysalidis K, Goodacre TD, Marsh B, Rothe S, Seiffert C, et al. Ion beam production and study of radioactive isotopes with the laser ion source at ISOLDE. *J Phys G: Nucl Part Phys* (2017) 44:084006. doi:10.1088/1361-6471/aa78e0

5. Demtröder W. *Laser spectroscopy*. Germany: Springer Science & Business Media (2002). 986.

6. Rothe S, Marsh BA, Mattolat C, Fedosseev VN, Wendt K. A complementary laser system for ISOLDE RILIS. *J Phys : Conf Ser* (2011) 312:052020. doi:10.1088/1742-6596/312/5/052020

7. Sinha S, Sasikumar S, Ray AK, Dasgupta K. The effect of dye photodegradation on the performance of dye lasers. *Appl Phys B* (2004) 78:401–8. doi:10.1007/s00340-003-1383-4

8. Chrysalidis K, Fedosseev VN, Marsh BA, Mildren RP, Spence DJ, Wendt KDA, et al. Continuously tunable diamond Raman laser for resonance laser ionization. *Opt Lett* (2019) 44:3924. doi:10.1364/OL.44.003924

9. Echarri DT, Chrysalidis K, Fedosseev VN, Marsh BA, Mildren RP, Olaizola SM, et al. Broadly tunable linewidth-invariant Raman Stokes comb for selective resonance photoionization. *Opt Express* (2020) 28:8589. doi:10.1364/OE.384630

10. Echarri DT, Mildren RP, Olaizola SM, Granados E. Cascaded Stokes polarization conversion in cubic Raman crystals. *Opt Express* (2021) 29:291. doi:10.1364/OE.413098

11. Williams RJ, Kitzler O, Bai Z, Sarang S, Jasbeer H, McKay A, et al. High power diamond Raman lasers. *IEEE J Sel Top Quan Electron* (2018) 24:1–14. doi:10.1109/JSTQE.2018.2827658

12. Yang X, Kitzler O, Spence DJ, Bai Z, Feng Y, Mildren RP, et al. Diamond sodium guide star laser. *Opt Lett* (2020) 45:1898. doi:10.1364/OL.387879

13. Hausmann BJM, Bulu I, Venkataraman V, Deotare P, Lončar M. Diamond nonlinear photonics. *Nat Photon* (2014) 8:369–74. doi:10.1038/nphoton.2014.72

14. Latawiec P, Venkataraman V, Burek MJ, Hausmann BJM, Bulu I, Lončar M, et al. On-chip diamond Raman laser. *Optica* (2015) 2:924. doi:10.1364/OPTICA.2.000924

15. Granados E, Spence DJ, Mildren RP. Deep ultraviolet diamond Raman laser. *Opt Express* (2011) 19:10857. doi:10.1364/OE.19.010857

16. Sabella A, Piper JA, Mildren RP. Diamond Raman laser with continuously tunable output from 3.38 to 3.80 *μm*. *Opt Lett* (2014) 39:4037. doi:10.1364/OL.39.004037

17. Yang X, Bai Z, Chen D, Chen W, Feng Y, Mildren RP, et al. Widely-tunable single-frequency diamond Raman laser. *Opt Express* (2021) 29:29449. doi:10.1364/OE.435023

18. Granados E, Granados C, Ahmed R, Chrysalidis K, Fedosseev VN, Marsh BA, et al. Spectral synthesis of multimode lasers to the Fourier limit in integrated fabry–perot diamond resonators. *Optica* (2022) 9:317. doi:10.1364/OPTICA.447380

19. Granados E, Stoikos G, Echarri DT, Chrysalidis K, Fedosseev VN, Granados C, et al. Tunable spectral squeezers based on monolithically integrated diamond Raman resonators. *Appl Phys Lett* (2022) 120:151101. doi:10.1063/5.0088592

20. Noek R, Vrijsen G, Gaultney D, Mount E, Kim T, Maunz P, et al. High speed, high fidelity detection of an atomic hyperfine qubit. *Opt Lett* (2013) 38:4735. doi:10.1364/OL.38.004735

21. Christensen JE, Hucul D, Campbell WC, Hudson ER. High-fidelity manipulation of a qubit enabled by a manufactured nucleus. *Npj Quan Inf* (2020) 6:35. doi:10.1038/s41534-020-0265-5

22. Pask H. The design and operation of solid-state Raman lasers. *Prog Quan Electronics* (2003) 27:3–56. doi:10.1016/S0079-6727(02)00017-4

23. von der Linde D, Maier M, Kaiser W. Quantitative investigations of the stimulated Raman effect using subnanosecond light pulses. *Phys Rev* (1969) 178:11–7. doi:10.1103/PhysRev.178.11

24. Savitski VG, Reilly S, Kemp AJ. Steady-state Raman gain in diamond as a function of pump wavelength. *IEEE J Quan Electron* (2013) 49:218–23. doi:10.1109/JQE.2012.2237505

25. Lisinetskii VA, Rozhok SV, Bus'ko DN, Chulkov RV, Grabtchikov AS, Orlovich VA, et al. Measurements of Raman gain coefficient for barium tungstate crystal. *Laser Phys Lett* (2005) 2:396–400. doi:10.1002/lapl.200510007

26. Citron ML, Gray HR, Gabel CW, Stroud CR. Experimental study of power broadening in a two-level atom. *Phys Rev A (Coll Park)* (1977) 16:1507–12. doi:10.1103/PhysRevA.16.1507

27. Haken H, Wolf HC, Brewer WD. *The physics of atoms and quanta*. Germany: Springer (2005). doi:10.1007/3-540-29281-0

28. Laplace P. *Théorie analytique des probabilités*. Paris: Courcier (1812).

29. Duarte F. Tunable lasers handbook. In: Duarte F, editor. *Tunable lasers handbook*. San Diego: Academic Press (1995). Optics and Photonics. doi:10.1016/B978-0-12-222695-3.50013-1

30. Svelto O, Hanna DC. *Principles of lasers*. New York: Plenum Press (2010). doi:10.1007/978-1-4419-1302-9

31. Teigelhöfer A, Bricault P, Chachkova O, Gillner M, Lassen J, Lavoie JP, et al. Grating tuned ti:sa laser for in-source spectroscopy of rydberg and autoionizing states. *Hyperfine Interact* (2010) 196:161–8. doi:10.1007/s10751-010-0171-x

32. Mostamand M. *Laser developments and study of Rydberg and autoionizing Rydberg states in Tm, La and at using resonant ionization laser spectroscopy*. Ph.D. thesis. University of Manitoba Winnipeg (2020).